

**The role of chromatin structure and DNA end
resection in the growth state dependence of
alternative end joining (alt-EJ)**

**Inaugural-Dissertation
zur
Erlangung des Doktorgrades
Dr. rer. nat.**

**der Fakultät für Biologie
an der
Universität Duisburg-Essen**

**vorgelegt von
Pelin Küçük Tetik
aus Trabzon, Türkei
März, 2019**

Die der vorliegenden Arbeit zugrunde liegenden Experimente wurden am Institut für Medizinische Strahlenbiologie am Universitätsklinikum Essen durchgeführt.

1. Gutachter: Prof. Dr. George Iliakis

2. Gutachter: Prof. Dr. Dominik Boos

Vorsitzender des Prüfungsausschusses: Prof. Dr. Christian Johannes

Tag der mündlichen Prüfung: 10.07.2019

DuEPublico

Duisburg-Essen Publications online

UNIVERSITÄT
DUISBURG
ESSEN
Offen im Denken

ub | universitäts
bibliothek

Diese Dissertation wird über DuEPublico, dem Dokumenten- und Publikationsserver der Universität Duisburg-Essen, zur Verfügung gestellt und liegt auch als Print-Version vor.

DOI: 10.17185/duepublico/70293
URN: urn:nbn:de:hbz:464-20190725-064433-1

Alle Rechte vorbehalten.

The biggest battle is the war against ignorance.

Mustafa Kemal Atatürk (1881-1938)

TABLE OF CONTENTS

LIST OF ABBREVIATIONS	7
LIST OF FIGURES	12
LIST OF TABLES	18
1. INTRODUCTION	19
1.1. Mammalian cell cycle phases	20
1.2. DNA damage induction by ionizing radiation	22
1.3. Recognition, signaling and repair of DSBs in eukaryotic cells	23
1.3.1. Homologous recombination repair (HRR)	24
1.3.2. Canonical non-homologous end joining (C-NHEJ)	27
1.3.2.1. DNA-PK	29
1.3.3. Alternative end joining (Alt-EJ)	31
1.4. Chromatin structure, regulation and modifications	34
1.5. DNA end resection at DSBs	36
2. AIM OF THE STUDY	39
3. MATERIALS AND METHODS	40
3.1. Materials	40
3.2. Methods	51
3.2.1. Cell culture.....	51
3.2.2. Induction of growth arrest	51
3.2.3. X-ray irradiation	52
3.2.4. Hypotonic treatment	52
3.2.5. Drug treatments	52
3.2.6. Flow cytometry	53
3.2.7. Clonogenic survival assay	54

3.2.8. Pulsed-field gel electrophoresis (PFGE)	54
3.2.9. Immunofluorescence staining	55
3.2.10. SDS-PAGE and western blotting.....	56
4. RESULTS	57
4.1. Growth state dependence of alt-EJ	57
4.1.1. Standardization of growth conditions	57
4.1.2. DSB repair in proliferating and quiescent c-NHEJ deficient MEFs.....	64
4.2. Modification of the chromatin structure	70
4.2.1. The effects of hypotonic treatment	72
4.2.2. The effects of DNA methylation inhibitor 5'-aza-2'-deoxycytidine (AzadC)	75
4.2.3. The effects of Histone Deacetylase (HDAC) inhibitors	77
4.3. The role of DNA-PKcs in the DSB repair pathways	83
4.3.1. DNA end resection in DNA-PKcs deficient cells.....	83
4.3.2. Repair efficiency of Ku80 ^{-/-} DNA-PKcs ^{-/-} double mutant MEFs	87
4.3.3. The effects of inhibition of PARP-1 and DNA ligases 1 and 3 on DSB repair in DNA-PKcs deficient cells.....	89
4.3.4. Chromatin structure and transcription related markers in different growth states	91
4.4. Alt-EJ in CHO cells expressing different mutant forms of DNA-PKcs	95
4.4.1. The effects of different DNA-PKcs levels on DSB repair	100
4.4.2. Different responses of DNA-PKcs knockout and kinase dead mutants	101
4.4.3. The effects of phospho-mimicking mutations of DNA-PKcs on DSB repair	103
4.4.4. The effects of phospho-ablating mutations in the autophosphorylation sites of DNA-PKcs on DSB repair	104
4.4.5. The role of DNA end resection in alt-EJ in DNA-PKcs mutants	106
4.5. The role of 53BP1 in DSB repair pathway choice	111

5.	DISCUSSION.....	116
5.1.	Global chromatin relaxation is not sufficient to promote alt-EJ in quiescent cells	116
5.2.	Rescued alt-EJ in quiescence by DNA-PKcs deficiency may not be related to DNA end resection in rodent cells	121
5.3.	Mutations in the autophosphorylation sites or kinase inactivation may not mimic DNA-PKcs deficient phenotype	124
5.4.	c-NHEJ could still operate in the absence of 53BP1	126
6.	SUMMARY	128
7.	ZUSAMMENFASSUNG	130
8.	REFERENCES	132
9.	SUPPLEMENTARY DATA	146
10.	ACKNOWLEDGEMENTS.....	183
11.	CURRICULUM VITAE.....	184
12.	DECLARATIONS.....	187

LIST OF ABBREVIATIONS

~	Approximately
°C	Degree Celsius
γH2AX	phosphorylated H2AX at S139
53BP1	p53 binding protein
A	Amper
aa	Amino acid
Ab	Antibody
ADP	Adenosine diphosphate
alt-EJ	Alternative end joining
ATM	Ataxia telangiectasia mutated kinase
ATP	Adenosine triphosphate
ATR	ATM and Rad3 related kinase
AzadC	5'-aza-2'-deoxycytidine
BLM	Bloom syndrome protein
bp	base pair
BRCA1/2	Breast cancer susceptibility protein 1/2
BSA	Bovine serum albumin
Cdk/s	Cyclin-dependent kinase/s
Chk1/2	Checkpoint kinase 1
CHO	Chinese hamster ovary cell line
c-NHEJ	classical non-homologous end joining
CO ₂	Carbon dioxide
CtIP	C-terminal binding protein interacting protein
CSR	Class switch recombination
d	day
D-loop	Displacement loop
DAPI	4',6-diamidino-2-phenylindole
DDR	DNA damage response
DEQ	Dose equivalent

dH ₂ O	Distilled water
DMEM	Dulbecco's modified eagle's medium
DMSO	Dimethyl sulfoxide
DNA	Deoxyribonucleic acid
DNA2	DNA replication ATP-dependent helicase/nuclease 2
DNA-PK	DNA-dependent protein kinase
DNA-PKcs	Catalytic subunit of DNA-PK
DR	Dose response
dsDNA	Double stranded DNA
EDTA	Ethylene diamine tetraacetic acid
EdU	5-ethynyl-2'-deoxyuridine
et al.	et alii
EtBr	Ethidium bromide
EtOH	Ethyl Alcohol
Exo1	Exonuclease 1
eV	Electronvolt
FACS	Fluorescence activated cell sorting
FBS	Fetal bovine serum
FDR	Fraction of DNA released
G _{0/1/2}	Gap 0/1/2 phases
Gy	Gray
h	hour
HAT	Histone acetyltransferase
HDAC	Histone deacetylase
HEPES	4-(2-hydroxyethyl)-1-Piperazineethanesulfonic acid
HJ	Holliday junction
HMT	Histone methyltransferase
HP1	Heterochromatin protein 1
HRR	Homologous recombination repair
IF	Immunofluorescence

IR	Ionizing radiation
IRIF	Ionizing radiation induced foci
K	Lysine
k	Kilo (10^3)
KAP1	KRAB (Krüppel-associated box) domain-associated protein 1
kDa	kilo dalton
keV	kilo electronvolt
LASER	Light amplification by stimulated emission of radiation
LET	Linear energy transfer
Lig1/3/4	DNA Ligase 1/3/4
LIF	Leica image format
LMA	Low melting agarose
LRR	leucine rich region
m	mouse
M	Mega (10^6)
M	Mitosis phase
ml	Milliliter
mm	Millimeter
mM	millimolar
Mab	Monoclonal antibody
MDC1	Mediator of DNA damage checkpoint protein 1
MEF	Mouse embryonic fibroblasts
MEM	Minimal essential medium
min	minute/s
MMEJ	Microhomology mediated end joining
MMSET	Multiple myeloma SET domain
Mre11	Meiotic recombination 11
MRN complex	Mre11/Rad50/Nbs1 complex
Nbs1	Nibrin
NEA	Non-Essential Amino Acids

NLS	N-lauryl sarcosine
ng	nanogram
NHEJ	Non-homologous end joining
nM	nanomolar
Pab	Polyclonal antibody
PARP-1	Poly (ADP-ribose) polymerase 1
PBS	Phosphate-buffered saline
PE	Plating efficiency
PFA	Paraformaldehyde
PFGE	Pulsed-field gel electrophoresis
PI	Propidium iodide
PI3K	Phosphoinositide 3-kinase
PIKK	Phosphoinositide 3-kinase-related protein kinase
PMT	Photomultiplier tube
PTIP	PAX transactivation activation domain-interacting protein
PTM	Post-translational modification
Q	Glutamine
r	rabbit
Rad51/54	Radiation protein 51/54
RAP	Receptor-associated protein
RIF1	RAP1-interacting factor 1
RIPA	Radio-immuno-precipitation buffer
RK	Repair kinetics
RNF8/168	Ring finger protein 8/168
RPA	Replication protein A
rpm	rounds per minute
RT	Room temperature
SD	Serum deprived
SDSA	Synthesis dependent strand annealing
S	Serine

S	Synthesis phase
SI	International System of Units
SQ/TQ	Serine or threonine residues that precede glutamine residues
SSA	Single strand annealing
SSB	Single strand break
ssDNA	Single stranded DNA
T	Threonine
TSA	Trichostatin A
VPA	Valproic Acid
Wrn	Werner syndrome protein
WT	Wild type
Xlf	Xrcc4-like factor
XRCC1/2/3/4	X-ray cross-complementing protein 1/2/3/4
Y	Tyrosine

LIST OF FIGURES

Figure 1. Regulation of the cell cycle by cyclins and CDKs.....	22
Figure 2. Cell cycle dependence of HRR.	25
Figure 3. DSB repair by HRR.	27
Figure 4. c-NHEJ activity throughout the cell cycle.	28
Figure 5. DSB repair by c-NHEJ.....	29
Figure 6. DSB repair in WT, c-NHEJ and HRR deficient CHO cells.....	32
Figure 7. Cell cycle and growth state dependence of alt-EJ.....	33
Figure 8. DSB repair by alt-EJ.	34
Figure 9. Growth curves of MEFs.....	57
Figure 10. Cell cycle distribution of MEFs growing into plateau phase.....	60
Figure 11. Cell cycle distribution of MEFs after serum deprivation.....	62
Figure 12. Ki67 levels in MEFs after serum deprivation.	64
Figure 13. Repair efficiency of WT MEFs in p53 proficient and p53 deficient genetic background.	65
Figure 14. Repair efficiency of H2AX deficient MEFs.	65
Figure 15. Repair efficiency of Lig4 ^{-/-} , Ku70 ^{-/-} and DNA-PKcs ^{-/-} MEFs in different growth states.	66
Figure 16. γ H2AX foci kinetics after 1 Gy of IR in WT and Lig4 ^{-/-} MEFs in exponential and SD state.....	68
Figure 17. 53BP1 foci kinetics after 1 Gy of IR in WT and Lig4 ^{-/-} MEFs in exponential and SD state.....	69
Figure 18. Survival curves of WT and Lig4 ^{-/-} MEFs in exponential and SD state.....	70
Figure 19. H3K9me3 and H3K9Ac levels in WT and Lig4 ^{-/-} cells in exponential and SD state.	72
Figure 20. Effects of hypotonic treatment for 24 h in WT and Lig4 ^{-/-} MEFs.	74

Figure 21. Repair kinetics of WT and Lig4 ^{-/-} MEFs after post-IR hypotonic treatment.	75
Figure 22. H3K9me3 levels in Lig4 ^{-/-} MEFs after AzadC treatment in exponential and SD state.	76
Figure 23. Repair kinetics of WT and Lig4 ^{-/-} MEFs treated with AzadC.	77
Figure 24. Hyperacetylation in WT and Lig4 ^{-/-} MEFs after TSA treatment in exponential and SD state.....	78
Figure 25. Repair kinetics of WT and Lig4 ^{-/-} MEFs treated with TSA.....	79
Figure 26. Acetylation status of Lig4 ^{-/-} MEFs after 2 to 12 h TSA treatment.....	80
Figure 27. Repair kinetics of Lig4 ^{-/-} MEFs in SD state with increasing concentrations of TSA.	81
Figure 28. Lig4 ^{-/-} MEFs treated with VPA alone or in combination with TSA.	82
Figure 29. RPA levels induced by 20 Gy of IR in WT, Lig4 ^{-/-} , DNA-PKcs ^{-/-} , Ku80 ^{-/-} DNA-PKcs ^{-/-} and Ku80 ^{-/-} MEFs in exponential and SD state.....	85
Figure 30. Cell cycle distribution of WT, Lig4 ^{-/-} , DNA-PKcs ^{-/-} , Ku80 ^{-/-} DNA-PKcs ^{-/-} and Ku80 ^{-/-} MEFs in exponential and SD state.....	86
Figure 31. Total CtIP levels in WT, Lig4 ^{-/-} and DNA-PKcs ^{-/-} cells in exponential and SD state.	87
Figure 32. Repair kinetics of Ku80 ^{-/-} , DNA-PKcs ^{-/-} and Ku80 ^{-/-} DNA-PKcs ^{-/-} double mutant MEFs in exponential and SD state.	88
Figure 33. Repair kinetics of WT, DNA-PKcs ^{-/-} , Lig4 ^{-/-} and Ku80 ^{-/-} MEFs after PJ34 and L67 treatment.	90
Figure 34. Flow cytometric analysis of heterochromatin and euchromatin related markers in WT, Lig4 ^{-/-} , DNA-PKcs ^{-/-} and Ku80 ^{-/-} MEFs in exponential and SD state.....	92
Figure 35. Cell cycle distribution of WT, Lig4 ^{-/-} , DNA-PKcs ^{-/-} and Ku80 ^{-/-} MEFs in exponential and SD state.....	94
Figure 36. Total HP1 and KAP1 levels in WT, Lig4 ^{-/-} , DNA-PKcs ^{-/-} and Ku80 ^{-/-} cells in exponential and SD state.	95
Figure 37. Schematic diagram of DNA-PKcs structure with major domains (red) and mutations in the corresponding CHO mutants (blue).....	96

Figure 38. Cell cycle distribution of V3 CHO mutants in exponential and SD state.	97
Figure 39. Survival curves of V3 CHO mutants in exponential and SD state.	99
Figure 40. Repair kinetics of A5 and A36 cells in exponential and SD state.	100
Figure 41. Repair kinetics of A5 and A36 cells in SD state treated with 5 μ M NU7441 for 1 h.	101
Figure 42. Repair kinetics of VectA and K>R31 cells in exponential and SD state.	102
Figure 43. Repair kinetics of VectA and K>R31 cells in SD state treated with 5 μ M NU7441 for 1 h.	102
Figure 44. Repair kinetics of ND5 and JKD2 cells in exponential and SD state.	103
Figure 45. Repair kinetics of ND5 and JKD2 cells in exponential and SD state treated with 5 μ M NU7441 for 1 h.	104
Figure 46. Repair kinetics of PQR and GG6 cells in exponential and SD state.	105
Figure 47. Repair kinetics of PQR and GG6 cells in SD state treated with 5 μ M NU7441 for 1 h.	106
Figure 48. RPA levels induced by 20 Gy of IR in A36, VectA, K>R31, PQR and GG6 cells in exponential and SD state.	107
Figure 49. RPA levels induced by 20 Gy of IR in G ₁ and G ₂ phases in A36, VectA and K>R31 cells in exponential and SD state.	109
Figure 50. RPA levels induced by 20 Gy of IR in G ₁ and G ₂ phases in PQR and GG6 cells in exponential and SD state.	110
Figure 51. Cell cycle distribution of A36, VectA, K>R31, PQR and GG6 cells in exponential and SD state.	111
Figure 52. Repair kinetics of WT and 53BP1 ^{-/-} mESCs in exponential and SD state.	112
Figure 53. Cell cycle distribution and Ki67 levels in WT and 53BP1 ^{-/-} mESCs.	113
Figure 54. Repair kinetics of WT and 53BP1 ^{-/-} mESCs in exponential and SD state treated with 5 μ M NU7441 for 1 h.	114
Figure 55. RPA levels induced by 20 Gy of IR in WT and 53BP1 ^{-/-} mESCs in exponential and SD state.	115

Figure 56. Cell cycle distribution of WT and 53BP1^{-/-} mESCs in exponential and SD state. 115

Supplementary Figure 1. RPA levels induced by 20 Gy of IR in WT cells in exponential and SD state. 146

Supplementary Figure 2. RPA levels induced by 20 Gy of IR in Lig4^{-/-} cells in exponential and SD state. 147

Supplementary Figure 3. RPA levels induced by 20 Gy of IR in DNA-PKcs^{-/-} cells in exponential and SD state. 148

Supplementary Figure 4. RPA levels induced by 20 Gy of IR in Ku80^{-/-} DNA-PKcs^{-/-} cells in exponential and SD state. 149

Supplementary Figure 5. RPA levels induced by 20 Gy of IR in Ku80^{-/-} cells in exponential and SD state. 150

Supplementary Figure 6. DNA end resection in G₁ and G₂ phases in WT cells in exponential state. 151

Supplementary Figure 7. DNA end resection in G₁ and G₂ phases in WT cells in SD state. .152

Supplementary Figure 8. DNA end resection in G₁ and G₂ phases in Lig4^{-/-} cells in exponential state. 153

Supplementary Figure 9. DNA end resection in G₁ and G₂ phases in Lig4^{-/-} cells in SD state. 154

Supplementary Figure 10. DNA end resection in G₁ and G₂ phases in DNA-PKcs^{-/-} cells in exponential state. 155

Supplementary Figure 11. DNA end resection in G₁ and G₂ phases in DNA-PKcs^{-/-} cells in SD state. 156

Supplementary Figure 12. DNA end resection in G₁ and G₂ phases in Ku80^{-/-} DNA-PKcs^{-/-} cells in exponential state. 157

Supplementary Figure 13. DNA end resection in G₁ and G₂ phases in Ku80^{-/-} DNA-PKcs^{-/-} cells in SD state. 158

Supplementary Figure 14. DNA end resection in G₁ and G₂ phases in Ku80^{-/-} cells in exponential state. 159

Supplementary Figure 15. DNA end resection in G ₁ and G ₂ phases in Ku80 ^{-/-} cells in SD state.	160
Supplementary Figure 16. Chromatin structure and transcription related markers in WT MEFs.	161
Supplementary Figure 17. Chromatin structure and transcription related markers in Lig4 ^{-/-} MEFs.	162
Supplementary Figure 18. Chromatin structure and transcription related markers in DNA-PKcs ^{-/-} MEFs.	163
Supplementary Figure 19. Chromatin structure and transcription related markers in Ku80 ^{-/-} MEFs.	164
Supplementary Figure 20. RPA levels induced by 20 Gy of IR in A36 cells in exponential and SD state.	165
Supplementary Figure 21. RPA levels induced by 20 Gy of IR in VectA cells in exponential and SD state.	166
Supplementary Figure 22. RPA levels induced by 20 Gy of IR in K>R31 cells in exponential and SD state.	167
Supplementary Figure 23. RPA levels induced by 20 Gy of IR in PQR cells in exponential and SD state.	168
Supplementary Figure 24. RPA levels induced by 20 Gy of IR in GG6 cells in exponential and SD state.	169
Supplementary Figure 25. DNA end resection in G ₁ and G ₂ phases in A36 cells in exponential state.	170
Supplementary Figure 26. DNA end resection in G ₁ and G ₂ phases in A36 cells in SD state.	171
Supplementary Figure 27. DNA end resection in G ₁ and G ₂ phases in VectA cells in exponential state.	172
Supplementary Figure 28. DNA end resection in G ₁ and G ₂ phases in VectA cells in SD state	173
Supplementary Figure 29. DNA end resection in G ₁ and G ₂ phases in K>R31 cells in exponential state.	174

Supplementary Figure 30. DNA end resection in G ₁ and G ₂ phases in K>R31 cells in SD state.	175
Supplementary Figure 31. DNA end resection in G ₁ and G ₂ phases in PQR cells in exponential state.....	176
Supplementary Figure 32. DNA end resection in G ₁ and G ₂ phases in PQR cells in SD state.	177
Supplementary Figure 33. DNA end resection in G ₁ and G ₂ phases in GG6 cells in exponential state.....	178
Supplementary Figure 34. DNA end resection in G ₁ and G ₂ phases in GG6 cells in SD state.	179
Supplementary Figure 35. RPA levels induced by 20 Gy of IR in WT mESCs in exponential and SD state.....	180
Supplementary Figure 36. RPA levels induced by 20 Gy of IR in 53BP1 ^{-/-} mESCs in exponential and SD state.....	181
Supplementary Figure 37. RPA levels induced by 20 Gy of IR in CHO cells in exponential and SD state.....	181

LIST OF TABLES

Table 1: Laboratory apparatus	40
Table 2: Disposable products	41
Table 3: Chemicals	42
Table 4: Cell lines and growth medium	45
Table 5: Solutions	46
Table 6: Antibodies and dilutions.....	48
Table 7: Software.....	50

1. INTRODUCTION

Each cell in the human body confronts thousands of DNA lesions per day (Tubbs and Nussenzweig 2017). DNA double strand breaks (DSBs) are one of the most severe lesions induced by exogenous agents such as ionizing radiation (IR) and chemotherapeutics or endogenous cellular processes such as replication stress, meiosis and V(D)J rearrangements (Helleday et al. 2007, Mehta and Haber 2014). Unrepaired or misrepaired DSBs may lead to genomic rearrangements and eventually cell death or cancer (Rothkamm and Löbrich 2002). Therefore, eukaryotic cells evolved specific pathways to repair DSBs and maintain genome integrity. Canonical (or classical) non-homologous end joining (c-NHEJ) and homologous recombination repair (HRR) represent the most prominent pathways in eukaryotic DSB repair (Chapman et al. 2012).

c-NHEJ is active throughout the cell cycle and error-prone due to the direct ligation of DSB ends in the close proximity without homology requirement. HRR is active only in late S and G₂ phases of the cell cycle, where a homologous sister chromatid is available as template; therefore it is generally error-free (Davis and Chen 2013). However, it has also been shown that cells deficient for c-NHEJ and HRR factors are still able to repair the majority of DSBs in an error-prone manner and with slower kinetics. This newly identified pathway is known as alternative end joining (alt-EJ) and it has been studied intensively in the recent years (Iliakis et al. 2004, Bennardo et al. 2008, Chiruvella et al. 2013). However, there are still many open questions to be answered regarding the regulation of this pathway.

Our previous data has shown that, cells deficient for c-NHEJ factors such as Ku70/80, DNA Ligase 4 (Lig4), X-ray repair cross-complementing protein 4 (XRCC4) show an abrogated repair in G₀, indicating that alt-EJ is a growth state dependent pathway (Iliakis 2009). In the present study, we confirmed the growth state dependence of alt-EJ, using c-NHEJ deficient mouse embryonic fibroblasts (MEFs) and we focused on the potential mechanisms underpinning this response.

Many studies have shown that compact (condensed) chromatin structure is a barrier for DSB repair. In order to facilitate DSB repair chromatin relaxation (decondensation) is required (Ziv

et al. 2006, Falk et al. 2007, Price and D'Andrea 2013, House et al. 2014). Based on this knowledge, we hypothesized that the growth state dependence of alt-EJ may be a consequence of more compact chromatin structure in non-cycling (G_0) cells in comparison to cycling (exponential) cells (Leitch 2000). On the other hand, DNA-PKcs mutants represent a notable exception to the strong growth state dependence of alt-EJ demonstrated in a variety of c-NHEJ mutants. DNA-PKcs has a pivotal role in c-NHEJ and therefore chemical inhibition or mutation of DNA-PKcs severely compromises c-NHEJ and DSB repair shifts to alt-EJ (Iliakis et al. 2004). Interestingly, cells deficient for DNA-PKcs are able to repair DSBs regardless of the growth state, unlike other c-NHEJ mutants. An intriguing finding from our laboratory in this direction was that DNA-PKcs deficient human malignant glioblastoma cells (M059J) has extensive DNA end resection, compared to their wild type counterparts (M059K) in G_2 phase of the cell cycle. Moreover, as there are numerous reports suggesting that DNA end resection is influenced by chromatin structure (Chen and Symington 2013, Liu and Huang 2016, Hauer and Gasser 2017), this finding led us focus on DNA-PKcs and its role in the DSB repair pathway choice in context of chromatin and DNA end resection.

1.1. Mammalian cell cycle phases

Cell division is evolutionarily conserved process in all living organisms for the continuity of life and generations. A cell divides to reproduce by performing a series of events to duplicate its contents and produces two genetically identical daughter cells. Every round of division is known as the cell cycle and it is mainly divided in two phases; *interphase* and *mitosis*. Interphase consists of 3 sequential phases as G_1 , S and G_2 , where cells grow and double their content. G_1 and G_2 are the *gap phases* during which RNA and protein synthesis occur. The gap between mitosis and S phase is named as G_1 and between S phase and mitosis is named as G_2 (Figure 1). Gap phases also provide time for cells to monitor the internal and external conditions in order to proceed cycling. There are two important control systems in G_1 and G_2 phases, known as *checkpoints*, where cells can be arrested until the conditions are favorable. G_1 checkpoint mainly depends on the extracellular conditions and in case of unfavorable environment, such as lack of growth factors; cells enter a resting state known as G_0 or *quiescence*. Cells can remain in G_0 phase for days or permanently for their whole lifetime. External stimulation can induce cells to

reenter the cycle and passing through a *restriction point*, cells commit to replicate their DNA. G₂ checkpoint controls whether DNA is completely replicated in S phase, ensuring the genetic information passes throughout the generations faithfully. G₁ and G₂ checkpoints also monitor DNA damage induced by radiation or chemicals, and allow time for cells to repair the damage. If the damage cannot be repaired, cells commit to suicide with a programmed cell death mechanism known as *apoptosis*. S phase (S for synthesis) is where DNA is replicated and M phase (M for mitosis) is where DNA is tightly packaged in chromosomes and segregated in two daughter cells. In order to ensure proper chromosome segregation another major checkpoint is operated during the M phase. There are additional cell cycle control mechanisms in S phase to ensure precise DNA replication (Lodish et al. 2000, Alberts et al. 2002, Harper and Brooks 2005).

Progression of cells through the cell cycle is governed by cyclins and cyclin-dependent kinases (CDKs). Upon stimulation of the cell by growth factors, cyclin D synthesis is induced and synthesis continues as long as growth factors are present. Cyclin D is rapidly degraded, so if growth factors are removed, intracellular concentrations of cyclin D rapidly decline and cell enters G₀ phase. If that is not the case, Cyclin D activates CDK4 and CDK6 and drives cell through the restriction point. Phosphorylation of the retinoblastoma protein (Rb) leads to the release of E2F transcription factor. E2F mediates the transcription of cyclin A and cyclin E (Alberts et al. 2002). Transition from G₁ to S phase and initiation of DNA synthesis are mediated by CDK2-cyclin E complex. Cyclin A activates CDK2 and CDK1, during the progression in S and G₂ phases, respectively. Finally, cell progress into mitosis with the interaction of CDK1 and cyclin B. Given the importance in the cell cycle control, CDKs are also regulated by CDK inhibitors to ensure the appropriate activity (Cooper 2000, Kastan and Bartek 2004, Satyanarayana and Kaldis 2009, Suryadinata et al. 2010). Figure 1 illustrates the cell cycle and its regulation with cyclins and CDKs.

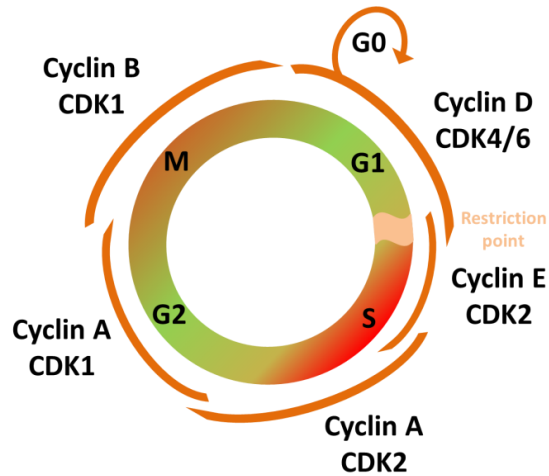


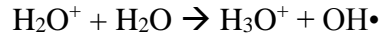
Figure 1. Regulation of the cell cycle by cyclins and CDKs.

Cyclin-CDK complexes regulate the progression through the cell cycle. See text for more information.

Cell cycle is tightly regulated and it is protected from external and internal threats by several mechanisms in order to maintain genome stability. Dysfunction of these mechanisms can result in the inheritance of DNA damage and eventually malignant transformation and cancer.

1.2. DNA damage induction by ionizing radiation

Ionizing radiation (IR) is defined as energy sufficient (~ 33 electronvolts (eV)) to eject one or more orbital electrons from an atom or molecule. The density of radiation is described as *linear energy transfer (LET)*, depending on the average energy deposited along the track (keV/ μm) of a particle to the material, which radiation passes through. Sparsely ionizing radiation such as X-rays and γ -rays that produce only a few interactions per track are characterized as *low-LET*. Low-LET radiations are indirectly ionizing, because they give up their energy to produce secondary electrons in order to generate damage. α -particles and protons, which produce dense ionizations along their tracks are referred to as *high-LET*. High-LET radiations are directly ionizing and they cause immediate damage in the absorbing material (Hill 1999, Hall and Giaccia 2006). In this study, only low-LET IR (X-rays) was used in order to generate DNA damage. Chemical mechanistic of low-LET IR effects in cells can be explained by the interaction of radiation with a water molecule as formulated below:



An electron ejected from the water molecule upon the interaction with IR leaves a charged ion radical, which in turn interacts with another water molecule to form highly reactive hydroxyl radical. This free radical diffuses to DNA and can form a plethora of different lesions, such as base or sugar backbone damages, DNA-protein cross-links or single strand breaks (SSB). Subsequent clustering of DNA lesions may lead to double strand breaks (DSB). In our study, we focused on IR induced DSBs and the mechanistic underpinnings of the repair mechanisms. As a parameter of absorbed radiation dose Gray (Gy), which corresponds to Joule per kilogram (J/kg) as defined by the International System of Units (SI) is used throughout this thesis (Hall and Giaccia 2006, Murmann-Konda 2016).

DSBs are severe lesions due to the difficulties in repair because of the lack of an intact template strand. Each Gy of IR induces around 20-40 DSBs in a single cell. If left unrepaired or misrepaired, DSBs can cause genomic instability and cancer development (Hill 1999, Hall and Giaccia 2006, Mladenov and Iliakis 2011). Therefore, eukaryotic cells evolved three different DSB repair pathways; homologous recombination repair (HRR), canonical non-homologous end joining (c-NHEJ) and alternative end joining (alt-EJ), which are discussed in detail in section 1.3.

1.3. Recognition, signaling and repair of DSBs in eukaryotic cells

Formation of DSBs in the cells induces several downstream pathways to initiate recognition and signaling cascades, which all together can be termed as DNA damage response (DDR) (Kastan and Bartek 2004). MRN complex, which is comprised of Mre11/Rad50/Nbs1 is among the sensor proteins that are instantly recruited to the DSB site. MRN complex contributes to the recruitment and activation of ATM (ataxia telangiectasia mutated), which is one of the key regulators of the crucial phosphorylation events in DDR. During replication stress and/or DNA damage, which involves the formation of ssDNA (single-stranded DNA) by DNA end resection; Replication protein A (RPA) activates another important kinase ATR (ataxia-telangiectasia and Rad3 related) in association with ATRIP (ATR-interacting protein). ATM and ATR are the

signal transducers, which belong to the phosphatidylinositol-3-kinase-related kinase (PIKK) family. Upon activation, they phosphorylate the histone variant H2AX at Serine 139 residue. DNA-PKcs (catalytic subunit of DNA dependent protein kinase) is also a member of PIKK family that can phosphorylate H2AX, however DNA-PKcs has a small pool of targets and it specifically activates the c-NHEJ pathway, upon recruitment to the break site by the sensor protein Ku70/80 (Lopez-Contreras and Fernandez-Capetillo 2012, Demond 2016).

The phosphorylated form of H2AX is referred to as γ H2AX and with the direct recognition by MDC1 (mediator of DNA damage checkpoint protein 1), it provides a central signaling platform for the recruitment of DNA repair proteins. γ H2AX can be visualized as spots, termed IRIF (ionizing radiation induced foci). It is highly specific molecular marker in the detection of DSBs, and the removal of γ H2AX from the break sites by phosphatases corresponds to accomplished DSB repair (Rossetto et al. 2012, Turinetto and Giachino 2015). Furthermore, H2AX and H2A are also ubiquitinated in concert with methylation of histone H4 in the Lysine 20 (H4K20) promote another IRIF forming DDR factor 53BP1 (p53-binding protein 1) to colocalize with γ H2AX. This is mediated by MDC1, which recruits E3 ubiquitin ligases RNF8 and RNF168 (Ring finger protein 8/168) to the break sites (Lopez-Contreras and Fernandez-Capetillo 2012, Kumar et al. 2013, Demond 2016). Recent data has shown that MMSET (Multiple myeloma SET domain), which is a histone methyltransferase (HMT) is recruited to the damage sites upon γ H2AX-MDC1 interaction and regulates the methylation of H4K20 (Pei et al. 2011). Another important sensor protein is PARP-1 (Poly [ADP-ribose] polymerase 1) which shifts DSB repair pathway to alt-EJ, in the absence of c-NHEJ factors (Wang et al. 2006, Soni et al. 2014). However, how a cell decides which DSB repair pathway to use is still a matter of debate. There are many factors, which may be decisive in the repair pathway choice, such as DSB complexity, cell cycle, growth factors, chromatin structure and etc., which require further investigations for the elucidation of the underlying mechanisms (Ziv et al. 2006, Falk et al. 2007, Iliakis 2009, Singh et al 2012, Schipler and Iliakis 2013, Price and D'Andrea 2013, House et al. 2014).

1.3.1. Homologous recombination repair (HRR)

Homologous recombination repair (HRR) depends on the recognition and pairing of broken DNA ends, using intact homologous sequences. Beside its indispensable role in DSB repair,

HRR is required for the genomic diversity in eukaryotes with its function in the meiotic cross-over. HRR has the greatest impact among the DSB repair pathways, in terms of preservation of genome stability with its role in the recovery of stalled or collapsed replication forks, as well as in telomere maintenance. HRR is an error-free process, because the repair is performed by copying the information from the undamaged homologous sister chromatid. Since a sister chromatid is only available in late S and G₂ phases of the cell cycle, HRR is strictly cell cycle dependent and a rather slow process (Hall and Giaccia 2006, Wang et al. 2006). Cell cycle dependent activity of HRR is illustrated in Figure 2.

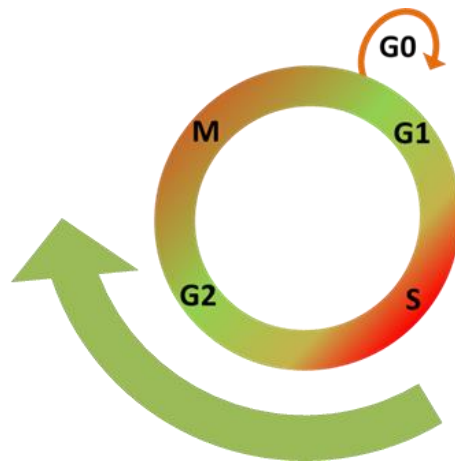


Figure 2. Cell cycle dependence of HRR.

HRR is only active in late S and G phases of the cell cycle due to requirement of a homologous sister chromatid.

HRR can be conceptually divided into three steps as recognition and processing of DSB, which involves an extensive DNA end resection process (1), homology search and strand invasion (2) and resolution of DSB (3). Recognition of DSBs is modulated by MRN complex with the recruitment of ATM and ATR to the damage sites. Phosphorylation of histone H2AX by ATM and ATR then recruits BRCA1 (Breast cancer susceptibility protein 1) to regulate the nuclease activity of MRN complex. In association with CtIP (C-terminal binding protein interacting protein) MRN complex initiates DNA end resection. Exo1 (Exonuclease 1) and DNA2 (DNA replication ATP-dependent helicase/nuclease 2) nucleases; and WRN (Werner syndrome protein) and BLM (Bloom syndrome protein) helicases facilitate the extension of DNA end resection process, which is required for HRR (for more detail see section 1.5). 3' ssDNA generated by DNA end resection is coated by replication protein A (RPA), which eliminates the

formation of secondary structures. RPA is subsequently replaced by Rad51 recombinase and strand exchange with the undamaged chromatid can be facilitated with the aid of BRCA2, Rad52 and the Rad51 paralogs Rad51-B, Rad51-C, Rad51-D, XRCC2 and XRCC3. Thus, formed nucleofilament catalyzes the formation of a joint heteroduplex molecule between damaged and undamaged DNA, providing the substrate for DNA synthesis following the unwinding of double stranded DNA molecule with the ATPase activity of Rad54. The branch point of the crossed DNA strands is called *Holliday junction (HJ)* (Hall and Giaccia 2006, Heyer 2007, Tamulevicius et al. 2007, San Filippo et al. 2008, Dueva and Iliakis 2013). DNA pairing and annealing steps in HRR can occur via different subpathways. The double Holliday junction (dHJ) pathway involves generation of a displacement loop (D-loop) with the invasion of a sister chromatid by the 3' DNA end formed by resection and the extension of D-loop by DNA synthesis. In the synthesis-dependent strand annealing (SDSA) pathway, D-loop collapses and leads to the gene conversion without crossovers. The single-strand annealing (SSA) occurs with annealing of two complementary strands formed by DNA end resection and it involves the deletion of non-complementary flaps (Morrical 2015). Figure 3 summarizes the central steps involved in HRR.

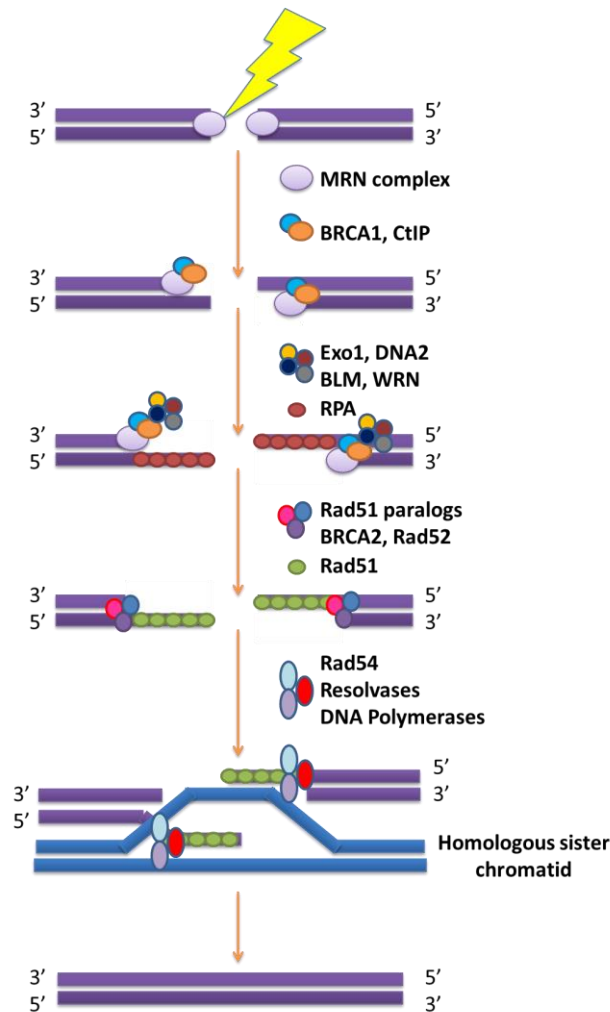


Figure 3. DSB repair by HRR.

Recognition of DSBs by MRN complex is followed by DNA end resection that requires CtIP and BRCA1. Resection is then extended by Exo1, DNA2, WRN and BLM. Homology search and strand invasion steps are operated by Rad51 and its paralogs. HRR is completed with resolution of DSBs with the aid of Rad54 and resolvases, and gap filling DNA synthesis carried out by DNA polymerases.

1.3.2. Canonical non-homologous end joining (C-NHEJ)

In contrast to template dependent, error-free nature of HRR, c-NHEJ involves the simple religation of the broken DNA termini without homology requirement. Therefore, it can take place throughout the cell cycle and even in G_0 as schematized in Figure 4. c-NHEJ efficiently restores DNA integrity with fast kinetics, however, in an error-prone manner (Mladenov and Iliakis 2011).

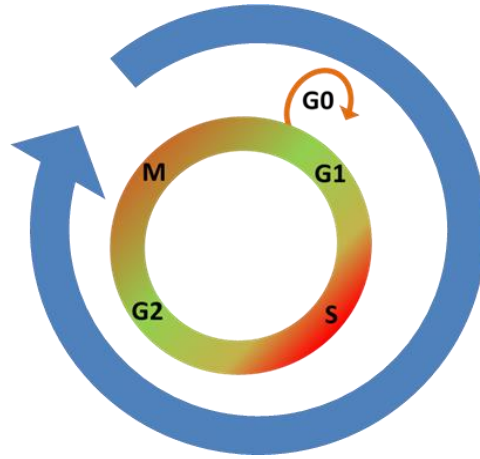


Figure 4. c-NHEJ activity throughout the cell cycle.

c-NHEJ is active throughout the cell cycle and in quiescence.

In c-NHEJ, DSBs are recognized by the Ku70/Ku80 heterodimer, which encircles the DNA and binds to DSBs with very high affinity. In addition to potential DSB end protection function, the Ku70/Ku80 heterodimer recruits DNA-PKcs in order to form DNA-PK holoenzyme complex. Formation of DNA-PK complex stimulates the kinase activity of DNA-PKcs and leads to the phosphorylation of a variety of substrates that promote DNA end resection to provide ligatable DSB ends. However, this resection only generates small microhomologies, around ≤ 4 nucleotides, and requires the activation of Artemis by DNA-PKcs. Extensive DNA end resection is prevented by Ku (Chang et al. 2017). Artemis has the 5' to 3' endonuclease activity on hairpins and single-stranded overhangs generated during V(D)J (V for variable, D for diversity and J for joining) and class switch recombination (CSR); which makes c-NHEJ an indispensable process in the diversity of immune response. However, this aspect of c-NHEJ may not be essential in the ligation of blunt ends or ends with compatible termini. DNA polymerases μ and λ are also recruited to the break site upon DNA-PKcs phosphorylation in order to prepare DSB ends for ligation. Final step of c-NHEJ is the ligation of the separated ends, which is also regulated by the DNA-PK complex and mediated by DNA Ligase 4 (Lig4), X-ray cross-complementing protein 4 (XRCC4) and Xrcc4-like factor (XLF) (Davis and Chen 2013, Hall and Giaccia 2006, Murmann-Konda 2016, Mladenov et al. 2016). C-NHEJ pathway is illustrated in Figure 5.

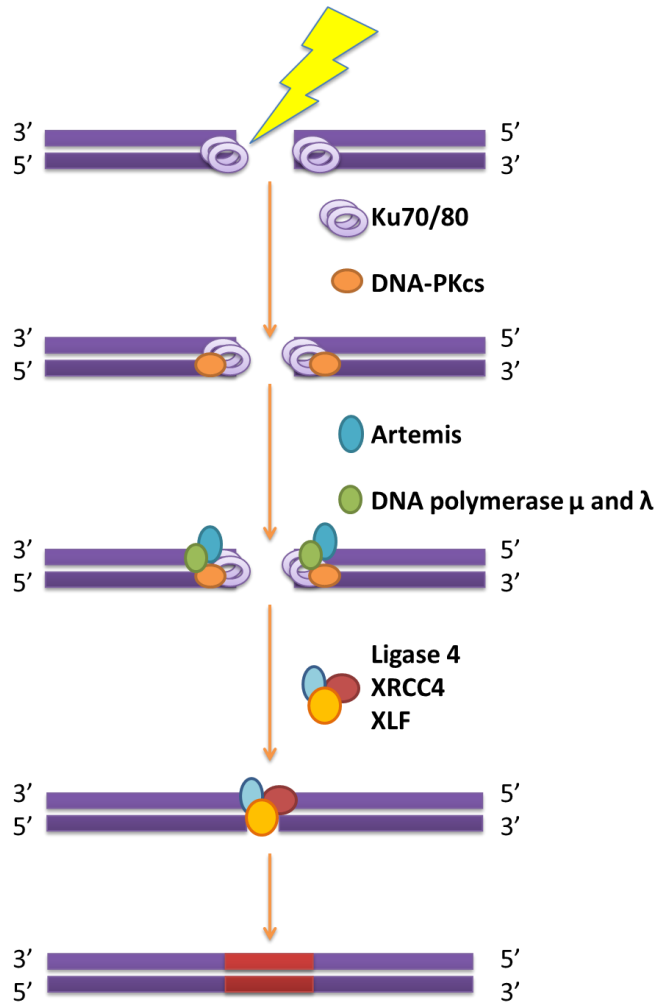


Figure 5. DSB repair by c-NHEJ.

DSBs are recognized by Ku70/80 heterodimer, which then recruits DNA-PKcs to form DNA-PK holoenzyme. A very limited DNA end resection, which provides ligatable ends is operated by Artemis. Ligation is carried out by Lig4/XRCC4/XLF complex and DNA sequence alterations are generated due to the direct ligation of DSBs.

1.3.2.1. DNA-PK

DNA-PK is a serine/threonine protein kinase, comprised of Ku70, Ku80 and the catalytic subunit of DNA dependent protein kinase (DNA-PKcs) and it plays a central role in c-NHEJ as mentioned above. Ku is a heterodimeric protein, consisting 70 kDa and 80 kDa subunits, which forms a ring structure to encircle duplex DNA with very high affinity but without sequence specificity. Once bound to DNA, it recruits DNA-PKcs and promotes its kinase activity. In the absence of DNA-PKcs, Ku interacts with the extreme termini of DNA ends. In the presence of

DNA-PKcs, Ku translocates inwards (Walker et al. 2001). DNA-PKcs is a ~460 kDa protein containing a leucine rich region (LRR) in the N-terminal and phosphatidylinositol 3 (PI3) kinase domain, Ku interacting domain and FAT and FATC domains in the C-terminal. DNA-PKcs preferentially targets serines and threonines that are followed by glutamine residues (SQ/TQ motif) and it also commonly phosphorylates itself. Autophosphorylation of DNA-PKcs has at least three critical functions: (1) regulation of DNA end resection, (2) kinase inactivation and (3) dissociation of the catalytic subunit from Ku-bound DNA. Two major autophosphorylation clusters related to these functions are termed ‘ABCDE’ and ‘PQR’, located in residues 2609-2647 and 2023-2056, respectively. Nevertheless, it has been reported that ABCDE but not PQR site is phosphorylated by ATM, suggesting that other kinases can be involved in the phosphorylation of DNA-PKcs (Chen et al. 2007, Meek et al. 2008). Functional studies have shown that, phospho-ablation of ABCDE site by alanine substitution, imparts a severe radiosensitive phenotype. However, phospho-ablation of PQR site only modestly affects the radiosensitivity. Mutations in either of these sites results in dysregulated DNA end resection. In WT status, autophosphorylation of ABCDE sites promotes DNA end resection, whereas it is suppressed by autophosphorylation of PQR. Studies have shown that alanine substitution reversed the function of each site on resection, suggesting that DNA-PKcs may have an impact on DSB repair pathway choice through regulating DNA end resection (Meek et al. 2008, Neal and Meek 2011, Neal et al. 2014).

Other relevant phosphorylation sites are T3950, termed ‘T’, which is the activation loop of the kinase and S56 and S72 at the extreme N-terminus of DNA-PKcs, termed ‘N’. Phosphorylation of these sites results in kinase inactivation, but does not affect complex stability. Recently identified other phosphorylation sites are T946 and S1004, termed ‘JK’ is assumed to serve as a switch between c-NHEJ and HRR. Phospho-mimicking JK by aspartic acid substitution, affects neither DNA end resection nor kinase activity, but still blocks c-NHEJ and promotes HRR (Neal and Meek 2011, Neal et al. 2014). Dr. Kathryn Meek’s laboratory suggested a model for the role of these phosphorylation sites during DSB repair. According to the model, upon DNA binding, a clamping of the DNA-PK complex is induced. Phosphorylation of PQR and JK sites stabilizes this conformation and allows the initiation of c-NHEJ. Phosphorylation of ABCDE sites promotes flattening of the complex, which has been shown to facilitate the activation of Artemis and recruitment of XRCC4/Lig4 and eventual complex dissociation.

Catalytic activity is maintained through phosphorylation of N and T sites, by blocking kinase inactivation (Goodarzi et al. 2006, Neal et al. 2014). Since DNA bound DNA-PKcs effectively blocks the access to DNA ends, its dissociation is crucial for the end processing. However, DNA ends are protected by DNA-PKcs until two broken ends find each other and are properly aligned in a synaptic complex. Upon autophosphorylation DNA-PKcs dissociates from the complex and DNA ends can be processed for ligation (Meek et al. 2008, Neal and Meek 2011, DeFazio et al. 2002, Weterings and Chen 2007).

1.3.3. Alternative end joining (Alt-EJ)

DSB repair had been shown to occur using a fast component acting from 5 to 30 minutes and a slow component acting from 2 to 30 hours. In cells with defects in c-NHEJ, mainly the fast component is compromised and the contribution of the slow component to the repair increases (Iliakis and Nüsse 1983, DiBiase et al. 2000). It was also shown that, repair kinetics of c-NHEJ mutant cells remained the same when these cells were depleted for the genes of Rad52 epistasis group, which are essential for HRR activity; therefore the slow component of repair cannot be attributed to HRR (Wang et al. 2001, Symington 2002). Previous study from our laboratory has shown that in the absence of c-NHEJ factors, DSB repair still operates with relatively slow kinetics and the efficiency of repair fluctuates throughout the cell cycle. Moreover, in the absence of HRR factors, DSB repair operates as efficiently as wild type cells. In the aforementioned study, wild type (V79) and c-NHEJ or HRR deficient Chinese hamster ovary (CHO) cells were exposed to 20 Gy of IR to induce DSBs. HRR deficient cells were depleted of XRCC2 (Irs1) or XRCC3 (Irs1-SF) and c-NHEJ deficient cells were depleted of Ku80 (Xrs5), DNA-PKcs (XR-C1-3) or XRCC4 (XR-1). Repair efficiency was measured by Pulsed-Field Gel Electrophoresis (PFGE, see chapter 3.2.8) in either asynchronous cells or cells sorted in G₁ or G₂ phase of the cell cycle. These experiments revealed that in wild type and HRR deficient cells DSB repair is efficient regardless of cell cycle phase. This is suggesting that the contribution of HRR in DSB repair at high radiation doses is very small as HRR is expected to operate only in late S and G₂ phases of the cell cycle. On the other hand, c-NHEJ mutants exhibited slower repair kinetics in all sort of cell populations, in comparison to wild type cells. Moreover, repair efficiency diminished in G₁ sorted cells; whereas G₂ sorted cells exhibited enhanced DSB repair.

These findings revealed the presence of a cell cycle dependent backup pathway (Figure 6) (Wu et al. 2008).

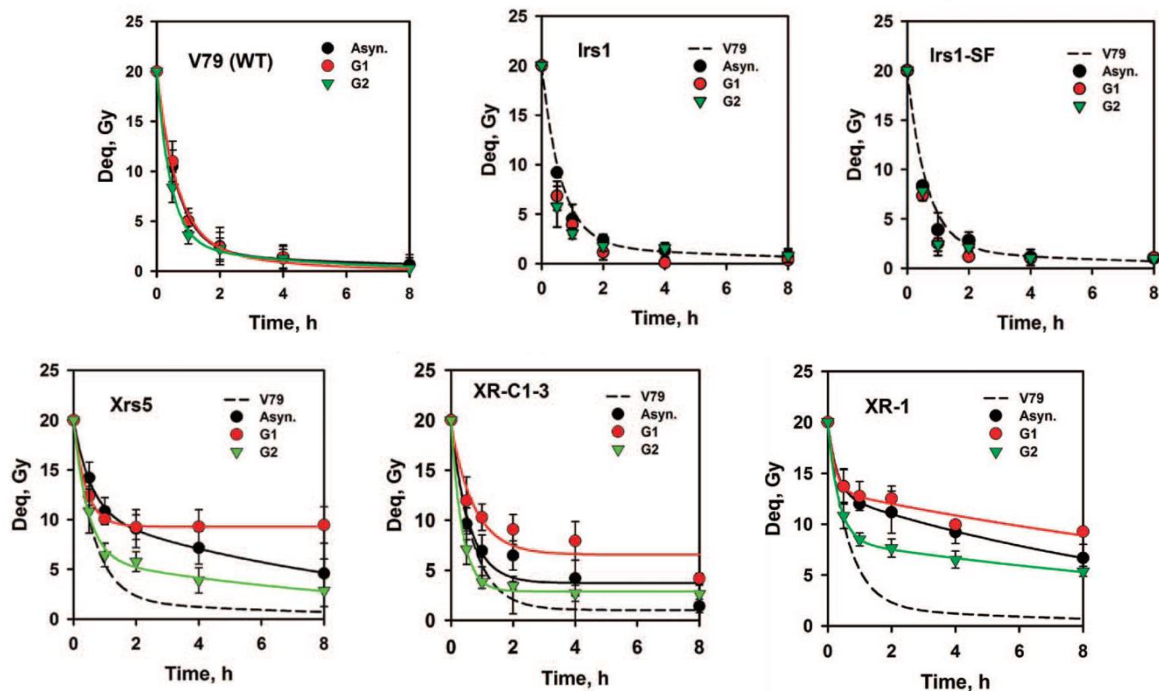


Figure 6. DSB repair in WT, c-NHEJ and HRR deficient CHO cells

DSB repair measured by PFGE following exposure to 20 Gy IR in CHO cell lines wild type (V79), HRR mutants deficient for XRCC2 (Irs1) and deficient for XRCC3 (Irs1-SF); c-NHEJ mutants deficient for Ku80 (Xrs5), deficient for DNA-PKcs (XR-C1-3) and deficient for XRCC4 (XR-1), respectively. HRR mutants exhibited similar repair efficiency to wild type controls. C-NHEJ mutants showed fluctuations in repair efficiency. See text for more information. Figure adapted from Wu et al. 2008.

Extensive studies made it clear that in the absence of c-NHEJ and HRR, cells are able to repair the majority of DSBs using an alternative pathway with relatively slow kinetics and in an error-prone manner (Nevaldine et al. 1997, Kabotyanski et al. 1998, Wang et al. 2001, Wang et al. 2003, Wu et al. 2008). This newly identified however evolutionarily old pathway is named as ‘*alternative end joining (alt-EJ)*’ and many efforts have been made to elucidate its molecular mechanisms. Due to its backup function in the absence of c-NHEJ, this pathway is referred to as backup-NHEJ (Kabotyanski et al. 1998, Wang et al. 2003, Windhofer et al. 2007, Rosidi et al. 2008, Wu et al. 2008, Iliakis 2009, Singh 2010, Mladenov et al. 2013, Soni et al. 2014) and considering the utilization of microhomologies, it is referred to as microhomology-mediated end joining (MMEJ) (Truong et al. 2013), as well. Similar to c-NHEJ, alt-EJ is active throughout

the cell cycle; however, the activity is enhanced in G₂ phase as shown in Figure 6 (Wang et al. 2001, Wu et al. 2008). Interestingly, alt-EJ has been found to be strongly growth state dependent, indicated by dramatic reduction in repair efficiency upon growth arrest in G₀ (Windhofer et al. 2007). Cell cycle and growth state dependence of alt-EJ is illustrated in Figure 7. In this study we focused on the growth state dependence of alt-EJ and the mechanisms underpinning this response.

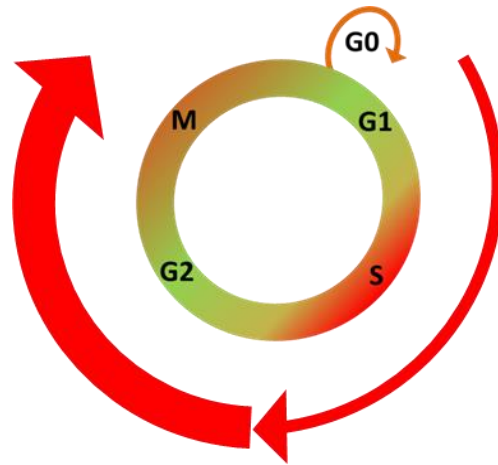


Figure 7. Cell cycle and growth state dependence of alt-EJ.

Alt-EJ is active throughout the cell cycle with an enhanced activity in G₂ and it is strongly growth state dependent with a dramatic abrogation in G₀.

In alt-EJ, PARP-1 acts as DSB sensor and the initiator of the pathway. In contrast to c-NHEJ, alt-EJ predominantly requires DNA end resection in order to generate 15-100 nucleotide 3' overhangs. This resection activity is regulated by the nuclease function of MRN complex (Mre11/Rad50/Nbs1), which is stimulated by phosphorylated CtIP. Annealing of 3' ssDNA overhangs is stabilized by DNA Polymerase θ , which is encoded by the POLQ gene and the ligation of the separated ends is mediated by DNA Ligase 1 and 3 (Lig1 and Lig3) (Chang et al. 2017). Histone H1 is another factor involved in alt-EJ. It functions as an accessory factor of Lig3 and it enhances the activity of PARP-1. It also promotes alt-EJ by inhibiting HRR and c-NHEJ (Rosidi et al. 2008).

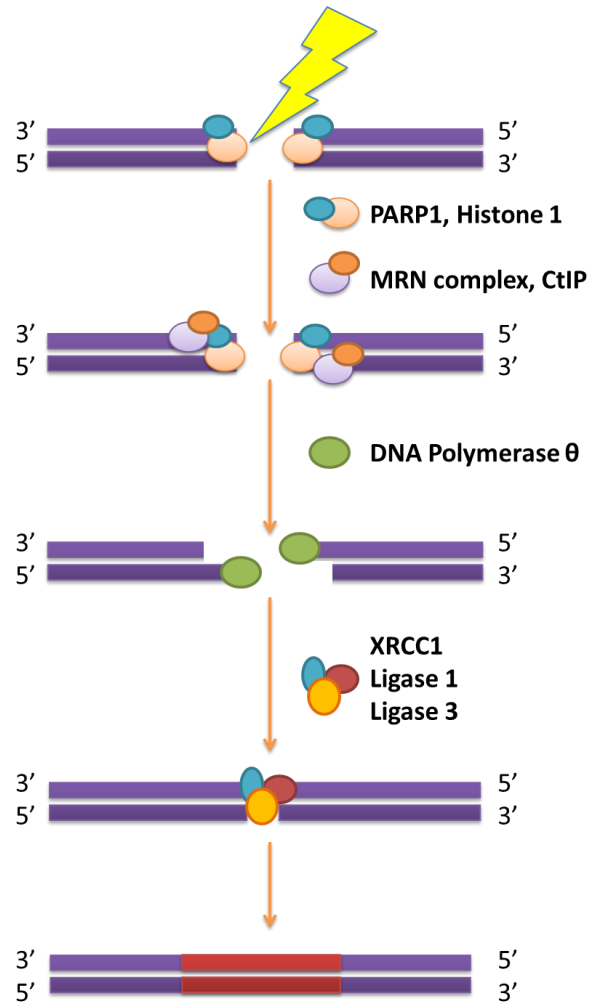


Figure 8. DSB repair by alt-EJ.

In alt-EJ, DSBs are recognized by PARP-1 and a short track DNA end resection is carried out by MRN complex and CtIP. DNA Polymerase θ plays role in the alignment of microhomologies and following ligation carried out by Lig1 and Lig3, extensive DNA sequence alterations are generated.

1.4. Chromatin structure, regulation and modifications

In eukaryotic cells, DNA fiber is tightly folded and packed in complex with an equal mass of proteins, in the form of *chromatin*, which is further organized into chromosomes. The compaction ratio of the DNA in an interphase chromosome is approximately 1000-fold, while this ratio for a mitotic chromosome is nearly 10,000-fold. The proteins that help DNA to form chromatin structure are classified as *histones* and *non-histone proteins*. The most basic organization in the chromatin consists of a ~146 bp DNA segment wrapped around homodimers

of H2A, H2B, H3 and H4 type histones to form the *nucleosome* core. Each nucleosome is linked together by the linker histone H1 and packed into a solenoid arrangement to form the 30 nm chromatin fiber (Lodish et al. 2000, Alberts et al. 2002).

Chromatin has a dynamic structure and post-translational modifications (PTMs) in the N-terminal tails of the four histones in the nucleosome core profoundly affect its structure. PTMs play the major role in the formation of *euchromatin*, which is less condensed and transcriptionally active; and *heterochromatin*, which is highly condensed, transcriptionally silent and generally rich in repetitive DNA sequences. First identified histone modification is the acetylation of the Lysine (K) residues. Histone acetylation is regulated by the opposing actions of histone acetyltransferases (HATs) and histone deacetylases (HDACs). HATs catalyze the transfer of acetyl groups to lysine residues, which neutralize the positive charge of lysines and attenuate the histone-DNA interaction. HDACs remove the acetyl groups from lysines and lead to a more compact chromatin structure through tightening the histone-DNA interaction. Therefore, the interplay between HATs and HDACs regulates the acetylation status of histones, thus accessibility and function. Acetylation of histone H3 in the K9 (H3K9Ac), K27 (H3K27Ac) and histone H4 in the K20 (H3K20Ac) residues has been extensively studied and correlated with chromatin relaxation (Eberharter and Becker 2002, Bannister and Kouzarides 2011). Another well-known histone modification is the methylation of lysines catalyzed by histone methyltransferases (HMTs). Lysines can be mono- di- or tri-methylated and the methylation is generally accepted to contribute in chromatin compaction. Histone methylation was known as a stable modification for many years; however, histone demethylases have been discovered and shown to reverse the action of HMTs (Bannister and Kouzarides 2011). Mostly studied histone methylations occur as the trimethylated forms of histone H3 in the K9 (H3K9me3), K27 (H3K27me3) and histone H4 in the K20 (H4K20me3). These markers have been related to chromatin compaction (Sims et al. 2003). Histones can also be phosphorylated on serine (S), threonine (T) and tyrosine (Y) residues. The phosphorylation status of histones is controlled by the dynamic regulation between kinases and phosphatases, which add and remove phosphate groups from ATP to the target residue, respectively. Addition of a phosphate group adds negative charge to histones. Although, phosphorylation of histone H3 in the S10 residue is well documented and associated with chromatin compaction during mitosis and meiosis; it has also

been shown to be involved in chromatin relaxation linked to transcriptional activation (Rossetto et al. 2012). One of the most important phosphorylation events is the formation of γ H2AX, as discussed in section 1.3. In addition to its role in DDR, there is evidence indicating that it is also involved in chromatin relaxation upon formation of DSBs (Price and D'Andrea 2013, House et al. 2014, Turinetto and Giachino 2015).

In addition, it has been shown that non-histone proteins such as KAP-1 [KRAB (Krüppel-associated box) domain-associated protein 1] and HP1 (heterochromatin protein 1) generate a heterochromatic barrier to DSB repair. Specific modifications of these proteins in an ATM dependent manner are required to allow chromatin relaxation and promote DSB repair (Lemaître and Soutoglou 2014). There are several other types of histone modifications such as ubiquitination, ADP ribosylation, succinylation, neddylation, sumoylation, deamination and etc. However in this study we focused mostly on acetylation and methylation of histones, as mentioned above in detail. Based on the broad range of studies in the literature, chromatin structure seems to play an important role in DSB repair. In addition, it has been reported that PTMs may exhibit differential patterns depending on growth state or cell cycle phase (Bártová et al. 2008, Ma et al. 2015). Therefore, we hypothesized that growth state dependence of alt-EJ may be associated with the chromatin structure and influencing chromatin modifications may have an impact on this response.

1.5. DNA end resection at DSBs

DNA end resection is highly complex and regulated process, which catalyzes the nucleolytic degradation of the broken ends in the 5' to 3' direction, providing a 3' ssDNA overhang as a template for DNA synthesis. This reaction occurs more prominently in S and G₂ phases of the cell cycle, shunting DSB repair to HRR, where a homologous sister chromatid is available. Among the first set of proteins to localize to the sites of DSB, MRN complex (Mre11/Rad50/Nbs1) plays a central role. Mre11 subunit possesses the catalytic function; while both Rad50 and Nbs1 enhance the nuclease activity of Mre11. Nbs1 interacts directly with CtIP, which is required for the initiation of resection. The tumor suppressor and E3 ubiquitin ligase, BRCA1, physically interacts with and polyubiquitinates CtIP to promote its recruitment to the break sites (Huertas 2010, Liu and Huang 2016). MRN-CtIP complex promotes a short-track

DNA end resection, which is then extended by the recruitment of Exo1 and DNA2 endonucleases. Limited DNA end resection mediated by MRN-CtIP has been shown to promote alt-EJ, however it is not sufficient to promote HRR (Truong et al. 2013, Xiong et al. 2015). In order to catalyze the extensive DNA end resection, Exo1 and DNA2 collaborate with BLM and WRN helicases, which generate 5' and 3' ssDNA by unwinding of broken DNA ends. RPA enhances the activity of Exo1 and DNA2 on the 5' strand and allows resection to occur only in the 5' to 3' direction (Paudyal and You 2016).

DNA end resection is controlled in a cell cycle dependent manner to prevent HRR in G₀/G₁ phase and to avoid strand exchange between homologous chromosomes, which can lead to loss of heterozygosity. CDK2-dependent phosphorylation of CtIP at the site S327, which induces its interaction with BRCA1 in S/G₂ is an important determinant in the cell cycle dependent regulation of DNA end resection. Another important factor in the cell cycle dependent regulation of DNA end resection is 53BP1, which plays role as a negative regulator. 53BP1, along with its interaction partners RIF1 (RAP1-interacting factor 1) and PTIP (Pax transactivation domain-interacting protein) prevents DNA end resection in G₁ in an ATM phosphorylation dependent manner. BRCA1 inhibits ATM-dependent 53BP1 phosphorylation in S/G₂ phases and favors DNA end resection by directly interacting with CtIP and MRN complex (Daley et al. 2015, Paudyal and You 2016). 53BP1 is also important in the DDR signaling, which involves its colocalization with γ H2AX (Anderson et al. 2001, Ward et al 2003). Binding of Ku to dsDNA ends with high affinity also generates a barrier to DNA end resection. Increasing evidence suggests that MRN, in complex with CtIP and BRCA1, removes Ku from DNA ends in S/G₂ (Daley and Sung 2014).

As mentioned above and in section 1.3.1, HRR is strictly cell cycle dependent and it is regulated to occur only in the presence of homologous sister chromatids. Available data suggests that DNA end resection, which is governed by CDKs throughout the cell cycle, is the decisive factor in this regulation (Aylon et al. 2004). As suggested by several studies, alt-EJ seems to utilize short-track DNA end resection, which is distinct from the extensive DNA end resection required to promote HRR (Zou et al. 2006). Starting from this point, we also hypothesized that growth

state dependence of alt-EJ may be a consequence of cell cycle dependent regulation of DNA end resection.

2. AIM OF THE STUDY

The main purpose of this study is to determine the mechanistic underpinnings of the growth state dependence of alt-EJ. Therefore, we focused on two prime candidates; chromatin structure and DNA end resection, which are known to play a role not only in DSB repair pathway choice, but also in the efficiency of each individual pathway. For this purpose, we first confirmed the growth state dependence of alt-EJ using MEF cells that are deficient for c-NHEJ factors. In order to investigate the role of the chromatin structure in the growth state dependence, we applied various chromatin relaxing treatments in G₀ phase where alt-EJ is abrogated. We also placed particular emphasis on DNA-PKcs deficiency, as DNA-PKcs deficient cells represent an exception to the growth state dependence of alt-EJ. Considering the high affinity of DNA-PKcs to DSB ends, we first hypothesized that the absence of DNA-PKcs might increase accessibility of DNA ends for resection, and thus alternative pathways may repair DSBs efficiently. To test this hypothesis, we employed a Ku80^{-/-} DNA-PKcs^{-/-} double mutant cell line, in addition to DNA-PKcs^{-/-} single mutant. We also employed several Chinese hamster ovary (CHO) mutants of DNA-PKcs to dissect the possible roles of distinct DNA-PKcs properties in alt-EJ. For the further investigations in the role of DNA end resection in the growth state dependence of alt-EJ, we also tested 53BP1 deficient mouse embryonic stem cells (mESCs), as 53BP1 is a negative regulator of DNA end resection. In summary, the overall aim of this study was to investigate the role of the chromatin structure and DNA end resection in the growth state dependence of alt-EJ.

3. MATERIALS AND METHODS

3.1. Materials

Table 1: Laboratory apparatus

Apparatus	Provider
Analytical Digital Balance Scale, BP 110	Sortorius, Gottingen, Germany
Centrifuge, Biofuge Fresco	Heraeus, Germany
Centrifuge, Multifuge 3S-R	Heraeus, Germany
Centrifuge, Rotanta 460R	Hettich, Germany
Confocal laser scanning microscope TCS SP5	Leica Microsystems, Germany
Cooling unit, DC10-K20	Thermo Fischer Scientific, Germany
Coulter counter, Multisizer 4e	Beckman Coulter, Germany
Electrophoresis chambers, Horizon	Life Technologies, USA
Electrophoresis Power Supply, EPS 301	Amersham, GE Healthcare, USA
Flow cytometer Gallios	Beckman Coulter, Germany
FluorImager, Typhoon 9400	Molecular Dynamics, Germany
Heating unit	Oehmen, Germany
Infrared imaging system, Odyssey	LI-COR, USA
Inverted microscope LH50A	Olympus, Germany
Laminar flow hood, HeraSafe	Heraeus, Germany
Magnetic stirrer, MR Hei-Standard	Heidolph, Germany
MCO-18 O ₂ /CO ₂ incubators	Sanyo, Germany
Micro Centrifuge, IR	Carl Roth, Germany
Minishaker MS1	IKA, Germany

pH-Mater, InoLab	WTW GmbH, Germany
Pipetaid	Falcon, BD Biosciences, Germany
Pipettes, Rainin Pipet-Lite	Mettler Toledo, Germany
Power supply, PowerPac Basic	Bio-Rad, Germany
PTB dosimeter	Physikalisch-Technische Bundesanstalt, Germany
Rocky shaker	Oehmen, Germany
SDS PAGE equipment	Bio-Rad, Munich, Germany
Sonicator, RK225H	Sonorex, Bandelin, Germany
Thermo-mixer	Eppendorf, Germany
UV/VIS Spectrophotometer, UV-2401 PC	Shimadzu, Japan
Vacuum gas pump	VWR, Germany
Vortexer, IKA MS 3 basic	IKA, Germany
Water bath, GFL 1092	Oehmen, Germany
Weighing balance, 572-43	Kern, Germany
Weighing balance, VWR-124	Sartorius, Germany
Wet transfer system	Bio-Rad, USA
X-ray control unit, Xrad320	PXi, USA
X-ray generator, ISOVOLT Titan	General Electrics, USA
X-ray tube, MXR320	Comet, Switzerland

Table 2: Disposable products

Disposable Product	Provider
Culture dishes (35 mm)	Thermo Scientific, Germany
Culture dishes (60 and 100 mm)	Greiner, Germany

Filter tips (various)	Greiner, Germany
Falcon tubes (15 and 50 ml)	Greiner, Germany
Glass flasks, beakers and cylinders	Schott Duran, Germany
Glass cover slips (Ø 20 mm)	VWR, Germany
Glass tubes (3 mm)	CM Scientific Ltd., UK
Blotting stacks, Nitrocellulose and PVDF	Invitrogen, Life Technologies, Germany
Microscope slides, cut color frosted white	VWR, Germany
Non-cap tubes (12 ml)	Greiner, Germany
Parafilm	Bremis, USA
Pipette tips	Starlab, Germany
Reaction tubes (1.5 and 2 ml)	Greiner, Germany
Serological pipettes (2, 5, 10, 25 ml)	Sarstedt, Germany

Table 3: Chemicals

Chemicals	Provider
4',6-diamidino-2-phenylindole (DAPI)	Serva, Germany
5-Ethenyl-2'-deoxyuridine (EdU)	Santa Cruz, USA
5'-aza-2'-deoxycytidine	MedChem Express, USA
β-Mercaptoethanol	Sigma-Aldrich, Germany
Agarose, SEAKEM LE	Lonza, Germany
Ammonium persulfate (APS)	Roth, Germany
Ascorbic Acid	Roth, Germany
Blasticidin	InvivoGen, Germany
Boric acid	Roth, Germany

Bovine serum albumin (fraction V) (BSA)	Sigma-Aldrich, Germany
Bromophenol blue	Sigma-Aldrich, Germany
Click-iT® EdU Alexa Fluor®647 Imaging Kit	Life Technologies, Germany
Copper(II) sulfate pentahydrate	Sigma-Aldrich, Germany
Crystal Violet	Merck Millipore, Germany
Cy5 dye	Thermo Scientific, Germany
Dimethyl sulfoxide (DMSO)	Sigma-Aldrich, Germany
Dulbecco's Modified Eagle Medium	Gibco, Life Technologies, Germany
Dulbecco's Modified Eagle Medium: Nutrient Mixture F-12	Gibco, Life Technologies, Germany
Ethanol	Sigma-Aldrich, Germany
Ethidium bromide (EtBr)	Roth, Germany
Ethylenediaminetetraacetic acid (EDTA)	Roth, Germany
Fetal bovine serum (FBS)	Gibco, Life Technologies, Germany
Fetal bovine serum (FBS)	Capricorn Scientific, Germany
Formaldehyde	Merck Millipore, Germany
Gelatin from cold water fish skin	Sigma-Aldrich, Germany
Glycine	Roth, Germany
HEPES	Roth, Germany
Hydrochloric acid (HCl)	Roth, Germany
Isopropanol	Sigma-Aldrich, Germany
L67	Specs, Netherlands
Low melting agarose	Roth, Germany
Mc Coy's 5A medium	Sigma-Aldrich, Germany

Methanol	Sigma-Aldrich, Germany
Minimum Essential Medium	Gibco, Life Technologies, Germany
N-lauroyl sarcosine (NLS)	Merck Millipore, Germany
Non-essential amino acids (NEAA)	Biochrom, Germany
Non-fat dry milk	Roth, Germany
NU7441 (DNA-PKcs inhibitor)	Tocris Bioscience, USA
Page Ruler, Prestained Protein Ladder	Fermentas, Thermo Scientific, Germany
Paraformaldehyde (PFA)	Roth, Germany
Penicillin	Sigma-Aldrich, Germany
Phosphatase inhibitor cocktail	Thermo Scientific, Germany
Phosphate-buffered saline (PBS)	Roth, Germany
PJ34	Calbiochem, Germany
PromoFluor Antifade	PromoKine, Germany
Propidium iodide (PI)	Sigma-Aldrich, Germany
Protease, from <i>Streptomyces griseus</i>	Sigma-Aldrich, Germany
Protease inhibitor cocktail	Sigma-Aldrich, Germany
RIPA buffer	Thermo Scientific, Germany
RNase A	Sigma-Aldrich, Germany
Rotiphorese® Gel 30 (37,5:1), 30% acrylamide/bis-acrylamide solution	Roth, Germany
Sodium azide	Roth, Germany
Sodium bicarbonate (NaHCO ₃)	Roth, Germany
Sodium chloride (NaCl)	Roth, Germany
Sodium dodecyl sulfate (SDS)	Roth, Germany

Sodium hydroxide (NaOH)	Roth, Germany
Streptomycin	Sigma-Aldrich, Germany
Sucrose	Sigma-Aldrich, Germany
Tetramethylethylenediamine (TEMED)	Sigma-Aldrich, Germany
Tris(hydroxymethyl)aminomethane (Tris)	Roth, Germany
Triton X-100	Roth, Germany
Trypsin	Biochrom, Germany
Trichostatin A (TSA)	Selleckchem, USA
Tween 20	Roth, Germany
Valproic Acid (VPA)	Sigma-Aldrich, Germany

Table 4: Cell lines and growth medium

Cell line	Cell type	Growth medium
WT	MEFs	DMEM
WT (p53 ^{-/-})	MEFs	DMEM
WT (H2AX ^{-/-} , p53 ^{-/-})	MEFs	DMEM
Lig4 ^{-/-} (p53 ^{-/-})	MEFs	DMEM
Ku70 ^{-/-}	MEFs	MEM
Ku80 ^{-/-}	MEFs	DMEM
DNA-PKcs ^{-/-}	MEFs	MEM
Ku80 ^{-/-} , DNA-PKcs ^{-/-}	MEFs	MEM
A36	CHO	McCoy's 5A + 2.5µg/ml Blasticidin
A5	CHO	McCoy's 5A + 2.5µg/ml Blasticidin
VectA	CHO	McCoy's 5A + 2.5µg/ml Blasticidin

KR31	CHO	McCoy's 5A + 2.5µg/ml Blasticidin
ND5	CHO	McCoy's 5A + 2.5µg/ml Blasticidin
JKD2	CHO	McCoy's 5A + 2.5µg/ml Blasticidin
PQR	CHO	McCoy's 5A + 2.5µg/ml Blasticidin
GG6	CHO	McCoy's 5A + 2.5µg/ml Blasticidin
WT	mESCs	DMEM F12 + 1% NEA + 55µM β-Mercaptoethanol
53bp1 ^{-/-}	mESCs	DMEM F12 + 1% NEA + 55µM β-Mercaptoethanol

Table 5: Solutions

Solution	Compounds	Application
PBS (1x)	137 mM NaCl 10 mM Na ₂ HPO ₄ 2.7 mM KCl 1.76 mM KH ₂ PO ₄ dH ₂ O pH 7.4	Various
3% PFA (Fixation solution)	3% PFA 2% Sucrose 1x PBS pH 7.4	Flow cytometry
2% PFA (Fixation solution)	2% PFA 2% Sucrose 1x PBS	Immunofluorescence
Permeabilization solution	1x PBS 0.2% Triton X-100 before use	Flow cytometry

Permeabilization solution	100 mM Tris, pH 7.4 50 mM EDTA dH ₂ O 0.5% Triton X-100 before use	Immunofluorescence
PBG (Blocking buffer)	0.2% Gelatin 0.5% BSA (fraction V) 1x PBS pH 7.4	Flow cytometry, Immunofluorescence
HEPES buffered medium	5 mM NaHCO ₃ 20 mM HEPES Serum-free growth medium	PFGE
Lysis Buffer	10 mM Tris, pH 7.6 100 mM EDTA 50 mM NaCl 2% NLS dH ₂ O 0.2 mg/ml Protease before use	PFGE
Washing Buffer	10 mM Tris, pH 7.6 100 mM EDTA 50 mM NaCl dH ₂ O	PFGE
RNase Buffer	10 mM Tris, pH 7.6 100 mM EDTA 50 mM NaCl dH ₂ O 0.1 mg/ml RNase before use	PFGE

5X TBE	890 mM Tris 890 mM Boric Acid 10 mM EDTA dH ₂ O	PFGE
Bradford Solution	0.5 mg/ml Coomassie 25% EtOH 42.5% Phosphoric Acid dH ₂ O	SDS-PAGE
SDS-PAGE Buffer (10X)	0.025M Tris 0.192M Glycine 0.1% SDS dH ₂ O	SDS-PAGE
Transfer Buffer	0.025M Tris 0.175M Glycine 20% Methanol dH ₂ O	Western blot
TBS (1X)	50 mM Tris, pH 7.6 150 mM NaCl	Western blot

Table 6: Antibodies and dilutions

Antibody	Host species	Type	Dilution	Provider
53BP1 (H300)	rabbit	polyclonal	1:300	Santa Cruz Biotechnology
γ H2AX [3F2]	mouse	monoclonal	1:300	Abcam
H3K9ac	rabbit	polyclonal	1:500	Abcam
H3K9me3	rabbit	polyclonal	1:500	Abcam
Ki67	rabbit	polyclonal	1:500	Abcam
RPA	mouse	monoclonal	1:300	IFMSB, UK-Essen

CtIP	mouse	monoclonal	1:200	Santa Cruz Biotechnology
GAPDH	mouse	monoclonal	1:1000	Millipore
H3K9me2	mouse	monoclonal	1:500	Abcam
H3K27Ac	rabbit	monoclonal	1:300	Cell Signaling
H3K27me3	rabbit	monoclonal	1:300	Cell Signaling
H4K20me1	rabbit	polyclonal	1:300	Abcam
H4K20me2/3	mouse	monoclonal	1:200	Abcam
KAP1	mouse	monoclonal	1:300	Abcam
HP1	mouse	monoclonal	1:100	Santa Cruz Biotechnology
Alexa Fluor 488 Anti-mouse	goat	polyclonal	1:400	Invitrogen
Alexa Fluor 488 Anti-rabbit	goat	polyclonal	1:400	Invitrogen
Alexa Fluor 647 Anti-mouse	goat	polyclonal	1:400	Abcam
Alexa Fluor 647 Anti-rabbit	goat	polyclonal	1:400	Invitrogen
Alexa Fluor 568 Anti-rabbit	goat	polyclonal	1:400	Invitrogen
IRDye 680LT	goat	polyclonal	1:20000	Li-COR Biosciences
IRDye 800CW	goat	polyclonal	1:10000	Li-COR Biosciences

Table 7: Software

Software	Provider
ImageQuant 5.0	GE Healthcare, Germany
ImarisXT 8.0	Bitplane AG, Switzerland
Kaluza 1.2	Beckman Coulter, USA
LasAF	Leica Microsystems, Germany
Microsoft Office 2010	Microsoft, USA
MultiCycle AV DNA Analysis	Phoenix Flow Systems, USA
Odyssey® Infrared Imaging System	LI-COR Biosciences, USA
SigmaPlot 12.5	Systat Software Inc. USA

3.2. Methods

3.2.1. Cell culture

Cell lines were maintained in a humidified incubator with 5% CO₂ at 37°C. Cells were cultured as monolayers either in 100 mm or 60 mm cell culture dishes with 15 ml or 5ml of growth medium, respectively. All growth medium were supplemented with 10% fetal bovine serum (FBS), 100 µg/ml penicillin and 100 µg/ml streptomycin. The growth medium used for mESCs was supplemented additionally with 1% non-essential amino acids (NEA) and 55 µM β-Mercaptoethanol. The growth medium used for CHO cells was additionally supplemented with 2.5 µg/ml Blastidicin.

For passaging cells, growth medium was aspirated from the petri dish, the cell monolayer was washed once with 1x phosphate buffered saline (PBS) and subsequently with 0,05% Trypsin-EDTA. The dishes were incubated at 37°C for 3-5 min in order to detach the cells from the surface with the enzymatic activation of Trypsin. The detached cells were collected in 10 ml fresh growth medium containing 10% FBS. 0.5 ml cell suspension was used to determine the cell number with the automated particle analyzer (Beckman Coulter Multisizer 4e). The cells were plated at concentrations of 0.2-0.5x10⁶ cells in 100 mm dishes and passaged every 2nd day. Full confluence was avoided in order to keep the cells in the exponential phase of growth. In order to generate a growth curve, suspension of 0.01x10⁶ cells/ml was prepared and 0.05x10⁶ cells were distributed in 60 mm dishes. Cells were collected and counted as described above every 24 h for 10-14 days and cell numbers were plotted against the time (days) in a logarithmic scale. Corresponding growth medium and other supplements for cell culture are listed in Table 4.

3.2.2. Induction of growth arrest

In order to obtain a non-proliferating cell population in G₀, either cells were kept growing till reaching a high density and enter a plateau phase, or cells were deprived of serum. For growing cell into plateau, 0.1-0.2x10⁶ cells were plated into 60 mm culture dishes and grown for 7 to 10 days in complete growth medium containing 10% FBS. Identical plating conditions were applied for serum deprivation (SD) and cells were grown for 3 days. Subsequently, growth

medium was aspirated and cell monolayer was washed twice with 5 ml of PBS. Serum free medium was given and cells were incubated for another 3 days.

3.2.3. X-ray irradiation

Irradiation of cells was carried out at room temperature (RT) using an X-ray machine (X-ray tube: MXR320 (Comet), X-ray generator: ISOVOLT Titan (General Electrics), control unit: Xrad320 (PXi)) operating at 320kV and 10 mA with 1.65 mm aluminum filter. Cells in 60 mm culture dishes were exposed to X-rays at a distance of 50 cm from the source and a dose rate of ~3.7 Gy/min and cells in 100 mm dishes were exposed to X-rays at a distance of 75 cm and a dose rate of ~1.6 Gy/min. Homogeneous irradiation was ensured by rotation of the radiation table. Dosimetry was performed with a PTB dosimeter (Physikalisch-Technische Bundesanstalt, Braunschweig, Germany) that was used to calibrate an in-field ionization monitor. Immediately after irradiation, cells were placed back in the 37°C incubator until the collection of time points, according to the experiment protocol. Control samples which were not exposed to irradiation were treated equally.

3.2.4. Hypotonic treatment

In order to relax the chromatin structure, we applied hypotonic treatment. Hypotonic medium was prepared by diluting standard growth medium with sterile dH₂O in 1:1 ratio. For exponentially growing cells, hypotonic medium was supplemented with 10% FBS and for SD cells hypotonic medium without serum was used. 24 h prior to the experiments, growth medium was replaced with pre-warmed hypotonic medium. Post-IR hypotonic treatment was applied immediately after IR.

3.2.5. Drug treatments

Cells were treated with 5'-aza-2'-deoxycytidine (AzadC) in order to induce hypomethylation and thus relax the chromatin structure. 100 mM stock AzadC was prepared by dissolving 0.023 g AzadC in 1 ml DMSO. Cells were treated with 0.25, 0.5 and 1 μM AzadC for 24 h. In order to inhibit HDACs and thus relax the chromatin structure, cells were treated with Trichostatin A (TSA) or Valproic acid (VPA). 5 mM stock TSA was prepared by dissolving 1 mg TSA in

0.6614 ml DMSO. Cells were treated with 0.5, 2.5, 5, 7.5, 10 and 20 μM TSA for 1 h prior to irradiation. 100 mM stock VPA was prepared by dissolving 0.2 g VPA in 12 ml dH_2O . Cells were treated with 1 mM VPA for 72 h prior to irradiation.

Cells were also treated with NU7441 (5 μM) to inhibit DNA-PKcs, with PJ34 (5 μM) to inhibit PARP-1 and with L67 (100 μM) to inhibit Ligase 1&3, 1 h before irradiation. All inhibitors except VPA were dissolved in DMSO and accordingly, DMSO was added to control cells. For VPA treatment, control cells were treated with dH_2O .

3.2.6. Flow cytometry

Flow cytometry, also known as fluorescence activated cell sorting (FACS), was performed to analyze cell cycle distribution. It was also used to measure Ki67 levels in order to analyze the proliferation status of the cells; histone and non-histone proteins to assess the chromatin structure and RPA levels to measure DNA end resection. In order to prepare cells for analysis of cell cycle distribution, cells were labeled with 10 μM EdU for 30 min at 37°C. EdU labeled cells were collected by trypsinization and centrifuged at 1500 rpm for 5 min at 4°C. Cell pellet was resuspended in 0.5 ml ice cold permeabilization solution on ice for 5 min. After centrifugation, cells were fixed in 3% PFA solution at RT for 15 min. If the experiment required antibody staining, fixation was followed by blocking with 0.5 ml PBG solution overnight at 4°C. Solutions for FACS are shown in Table 5. For antibody staining, PBG was aspirated after centrifugation and the cells were incubated with the primary antibody for 2 h at RT. Cells were washed with PBS before the Alexa Fluor dye conjugated second antibody was added for 2 h at RT in the dark. Antibodies and their dilutions are shown in Table 6. In order to stain EdU labeled cells, Click-iT EdU reaction was performed according to manufacturer's instructions. Cells were then stained with 0.5 ml Propidium iodide (PI) staining solution (40 $\mu\text{g}/\text{ml}$ PI, 62 $\mu\text{g}/\text{ml}$ RNase in 1X PBS) for 30 min in a 37°C water bath. Flow cytometry measurements were performed using the Beckman Coulter Gallios® flow cytometer. In total 5×10^4 cells per condition were analyzed. Data analysis was performed using Kaluza 1.2 and MultiCycle AV software. Quantitative values were obtained by normalization of the mean signal intensity of the stained samples to unstained control samples, which were only treated with secondary antibody as negative controls.

3.2.7. Clonogenic survival assay

Clonogenic survival assay was conducted to measure the capacity of the cells to produce progeny after exposure to IR. This reflects radiosensitivity to killing. To allow the formation of colonies from a single cell, cells were plated in low numbers aiming about 30 – 100 colonies/dish. As cell killing was expected to increase with the increasing IR dose, cells were plated at increasing numbers with increasing IR dose. Both exponential and SD cells were plated in growth medium supplemented with 10% FBS immediately after IR exposure. 3 replicates for each IR dose, along with non-irradiated controls, were incubated for ~7 days in a humidified incubator at 37°C and 5% CO₂. Colonies were stained with 1% Crystal Violet in 70% Ethanol and counted. Only colonies that comprised 50 or more cells were scored.

3.2.8. Pulsed-field gel electrophoresis (PFGE)

Pulsed-field gel electrophoresis (PFGE) method was performed to detect IR induced DSBs with the physical separation of fragmented DNA. To evaluate the induction of DSBs at different radiation doses, cells were collected and resuspended in ice cold serum-free HEPES buffered medium to reach a final concentration of 6×10^6 cells/ml. This cell suspension was then mixed with an equal volume of serum-free HEPES buffered medium containing 1% low melting agarose. The cell-agarose suspension was then pipetted into glass tubes with a diameter of 3 mm and placed on ice for polymerization. Solidified cell-agarose suspension was extruded from glass tubes and cut into 5 mm long cylindrical pieces (plugs). Subsequently, agarose plugs were placed in a 35 mm petri dish containing 2 ml cold serum-free HEPES buffered medium and exposed to 10, 20 and 30 Gy of IR along with non-irradiated controls on ice. Plugs were immediately placed in cold lysis buffer and incubated at 4°C until repair kinetics plugs were collected for all time points. For the evaluation of DSB repair kinetics, attached cells in the culture dishes were exposed to 20 Gy of IR and incubated at normal cell culture conditions to allow cells to repair IR induced DSBs, until the collection of time points. After each repair time interval, cells were collected and embedded in agarose plugs and placed in cold lysis buffer as described above. For determination of the background-DNA-released, plugs were prepared from otherwise identically treated non-irradiated cells at different time points. All collected plugs in cold lysis buffer were initially incubated at 4°C for at least 30 min and then at 50°C water bath

for 18h. After lysis, plugs were washed with washing buffer in a 37°C water bath for 2 h. Then, plugs were treated with RNase A solution at 37°C for another 2 h. Subsequently, plugs were loaded in 0.5% agarose gels prepared in 0.5X TBE buffer and electrophoresis was carried out in Horizon 20x25 boxes with cooled circulating 0.5X TBE buffer to ensure a stable temperature of approximately 6°C for 40 h using alternating cycles of 50 V (1.25 V/cm) for 900 sec in the (forward) direction of DNA migration and 200 V (5 V/cm) for 75 sec in the reverse direction. Following electrophoresis gels were stained with 8 µg/ml EtBr for 6 h and washed in dH₂O overnight to remove the excess EtBr. Solutions for PFGE are shown in Table 5. Gels were scanned with Typhoon 9400 imaging device and analyzed using ImageQuant 5.0 software. The fraction of DNA released (FDR) from the well into the lane reflects the DSBs in present in the cellular genome and is plotted as a function of dose to obtain a dose response (DR) curve. FDR shows a linear increase with the dose of IR, however the dose response can vary depending on the cell type and cell cycle phase (Iliakis et al. 1991). Therefore using DR curves for each set of plugs, we calculated a dose equivalent (DEQ) in Gy for the repair kinetics (RK) data points and plotted this parameter against repair time. Curve fitting was performed in Sigma Plot 12.5 software using an exponential decay algorithm, assuming a fast and a slow repair component.

3.2.9. Immunofluorescence staining

For immunofluorescence staining, cells were plated in petri dishes containing a 20 mm glass coverslip. For the analysis of IR induced foci (IRIF) formation, cells were exposed to 1 Gy of IR and incubated at normal cell culture conditions until the collection of time points at 1, 2, 4, 8 and 24 h. Subsequently, medium was aspirated and dishes were washed gently with 3 ml PBS. Coverslips were then transferred into 35 mm dishes containing 2 ml of 2% PFA solution and incubated at RT for 15 min. PFA was aspirated and 2 ml of Permeabilization solution was added to the dishes and incubated at RT for 5 min. After removal of Permeabilization solution dishes were washed gently with PBS and 2 ml of PBG solution was given for blocking overnight at 4°C. Solutions for immunofluorescence staining are shown in Table 5. After blocking, primary antibodies were diluted in PBG according to the dilution factor indicated in Table 6 and coverslips were incubated for 1.5 h with 100 µl of primary antibody on parafilm at RT. The coverslips were then transferred back into the 35 mm dishes and washed three times with PBS

for 5 min. Secondary antibodies conjugated with Alexa Fluor dyes were diluted in PBG and cells were incubated for 1 h with secondary antibody on parafilm, in the dark at RT. After the incubation coverslips were washed once with PBS and incubated for 30 min with 50 ng/ml DAPI (4',6 diamidino-2-phenylindole) for staining of DNA. Finally, coverslips were mounted on microscopic slides with PromoFluor and stored overnight in the dark for at least 24 h before analysis by confocal laser scanning microscopy.

3.2.10. SDS-PAGE and western blotting

In order to extract proteins, cells were collected and pelleted by centrifugation. Cell pellet was resuspended using 50-100 μ l of RIPA lysis and extraction buffer containing 1% Protease inhibitors and 2% Phosphatase inhibitors. Cell mixture was sonicated and incubated on ice for 15 min. Following 15 min centrifugation at 13000 rpm at 4°C, supernatant was transferred into a new Eppendorf tube. Bradford assay was performed to determine the total protein concentration of the samples. A standard curve was generated using 0.1, 0.2, 0.4, 0.6, 0.8, 1, 1.2 and 2 mg/ml concentrations of Bovine Serum Albumin (BSA), along with blank samples. Using a spectrophotometer, protein concentration of the standards and samples were measured. 50-100 μ g sample was mixed with 2X Laemmli solution containing β -Mercaptoethanol in 1:20 ratio and heated at 96°C for 3 min to allow denaturation of proteins. Samples were subjected to electrophoresis in SDS polyacrylamide gels for approximately 2 h at 100 Volts. SDS polyacrylamide gels were cast into Bio-Rad gel stands and consisted of a 5% stacking gel and 10% resolving gel. Proteins were transferred from gels to nitrocellulose membranes using Bio-Rad wet transfer system in 20% Methanol containing transfer buffer at 100 Volts for 2 h. Membranes were blocked in 5% non-fat dry milk in TBS-T (0.05% Tween20 in 1X TBS) for 1 h and then incubated with primary antibody overnight. After washing in TBS-T 3 times for 5 minutes, membranes were incubated in secondary antibodies for 1.5 h. Membranes were washed in TBS-T for another 3 times prior to scanning in The Odyssey® Infrared Imaging System. Solutions for SDS-PAGE and western blotting are shown in Table 5.

4. RESULTS

4.1. Growth state dependence of alt-EJ

4.1.1. Standardization of growth conditions

We studied alt-EJ in MEFs deficient for c-NHEJ factors Lig4, DNA-PKcs and Ku70. Before we started our investigations on the growth state dependence of alt-EJ in MEFs, we determined the optimal growth conditions for the cells. Unless stated otherwise, we grew cells in an exponential phase of growth, where they actively progress through the cell cycle and divide at certain period of time. We generated growth curves for each cell line and estimated the doubling times. Growth curves of MEFs are shown in Figure 9.

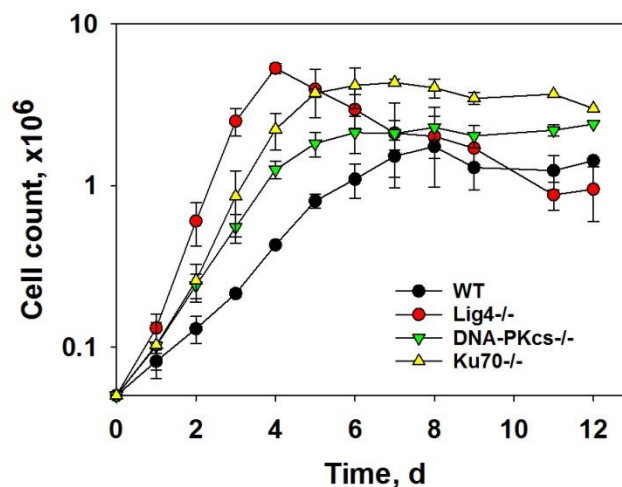
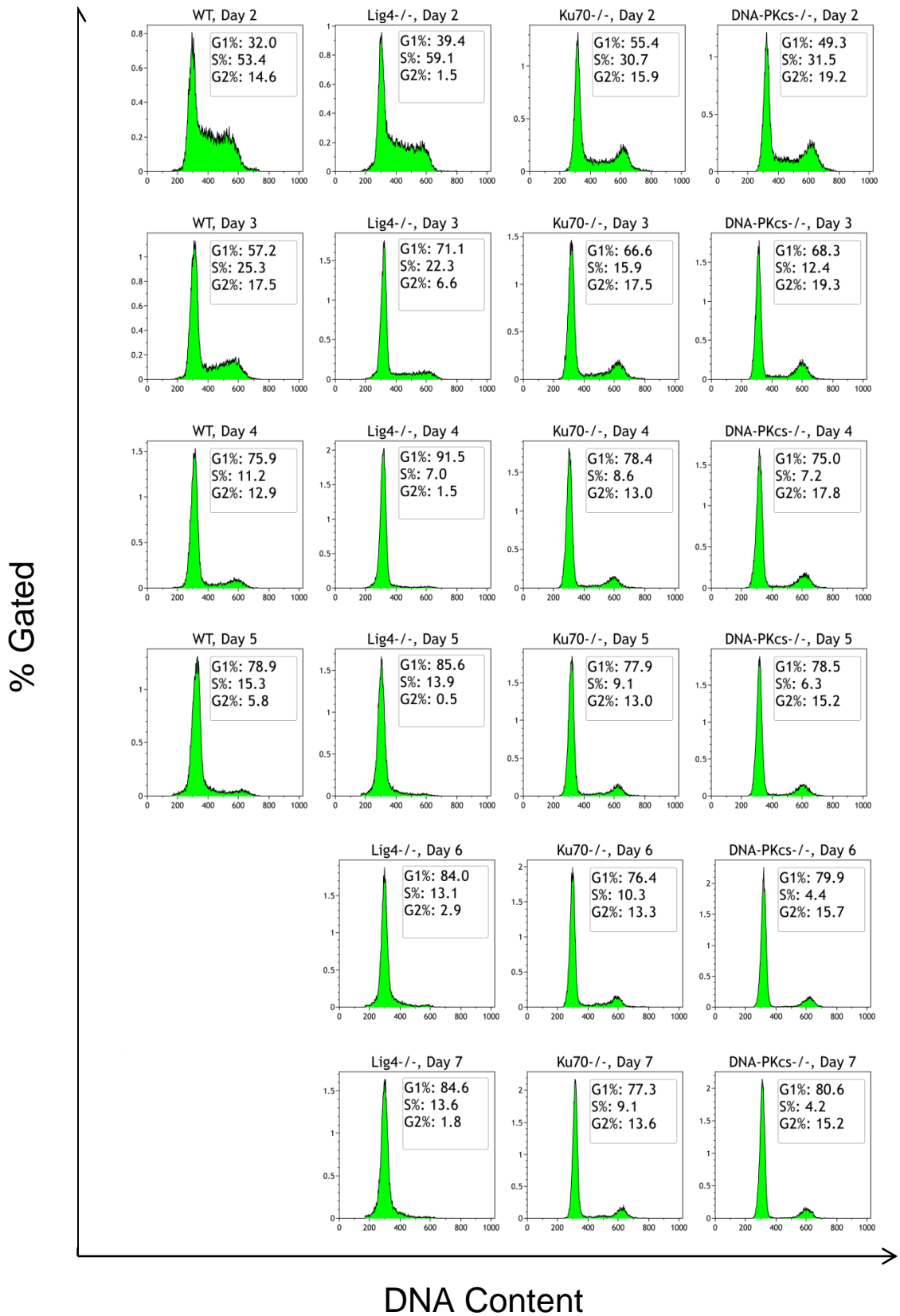


Figure 9. Growth curves of MEFs.

WT MEFs were used as controls for c-NHEJ. Lig4^{-/-}, DNA-PKcs^{-/-} and Ku70^{-/-} MEFs were used as c-NHEJ mutants in order to study alt-EJ. Doubling time for WT MEFs was 29.1 h, for Lig4^{-/-} MEFs 13.1 h, for DNA-PKcs^{-/-} MEFs 18.1 h and for Ku70^{-/-} MEFs 14.8 h. Results shown are the average of three independent experiments and error bars represent standard deviation.

For the analysis of DSB repair in different growth states, we kept cells either in asynchronous cultures in an exponential phase of growth or arrested in a quiescent state (G₀). Attempts to induce growth arrest by growing cells to high densities until reaching the plateau phase failed because of cell detachment from the growth surface. Figure 10 shows the cell cycle distribution

of MEFs while growing into plateau phase. WT cells could survive only until the 5th day of growth, where 15.3% of cells were still in S phase. Lig4^{-/-} cells still had 13.6% of S phase cells on the 7th day of growth. This protocol required incubation of the cells for more than 7 days. On the other hand, cells that were deprived of serum showed a lower proportion of S phase cells in a shorter period of time, as seen in Figure 11. In the serum deprivation method, we allowed cells to grow for 2 to 3 days in culture, depending on the cell number seeded, and subsequently replaced the medium with serum-free medium. We measured the cell cycle distribution at every 24 h and observed that cells accumulate in G₀/G₁ in ~24 h. With this approach, we removed the growth factors and other substances that stimulate cell cycle progression from an exponentially growing culture and thus induced a *quasi* G₀/G₁ state without reaching high cell densities. Therefore, in the experiments to be described here, unless indicated otherwise, growth arrested cells were generated by serum deprivation. We found this method more convenient for generating G₀/G₁ cells for our experiments and this condition is indicated as ‘SD’ for serum deprivation.



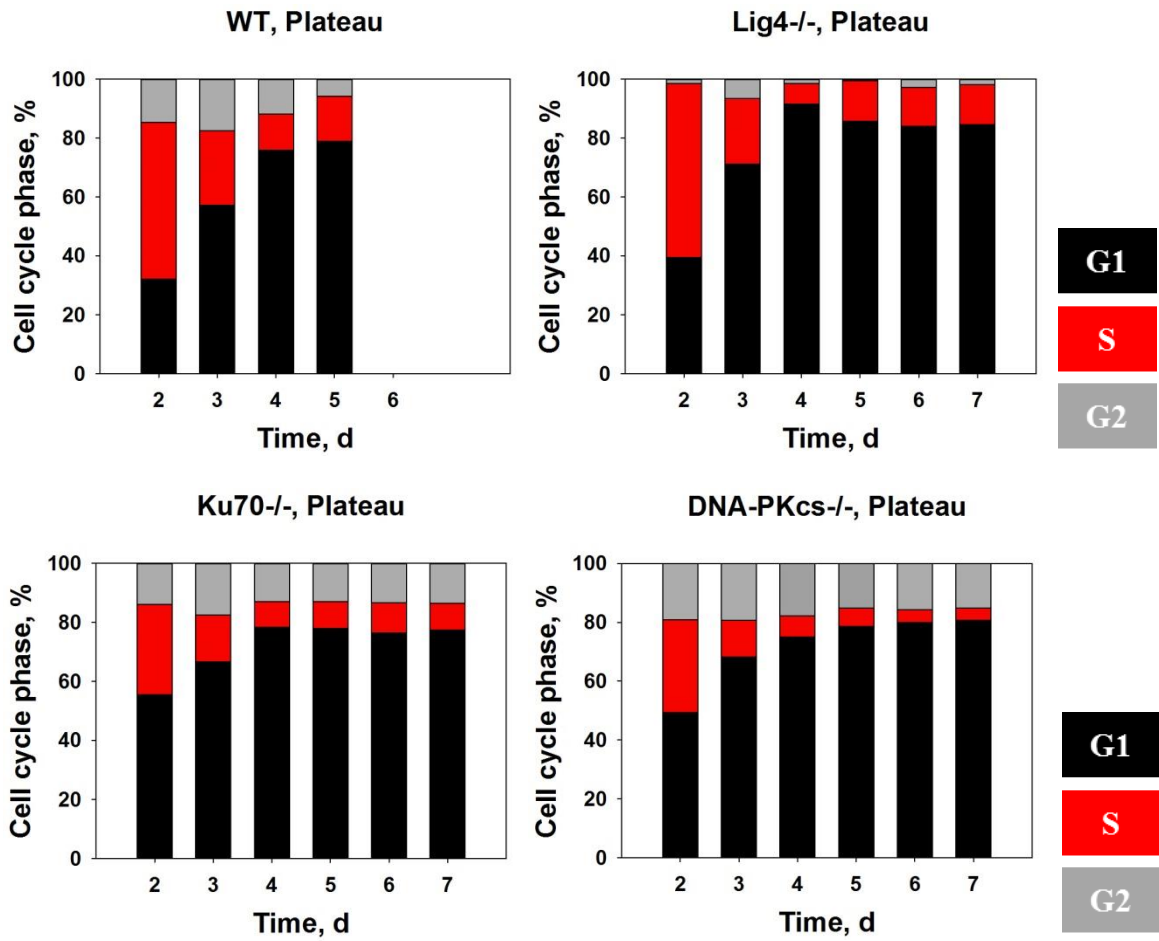
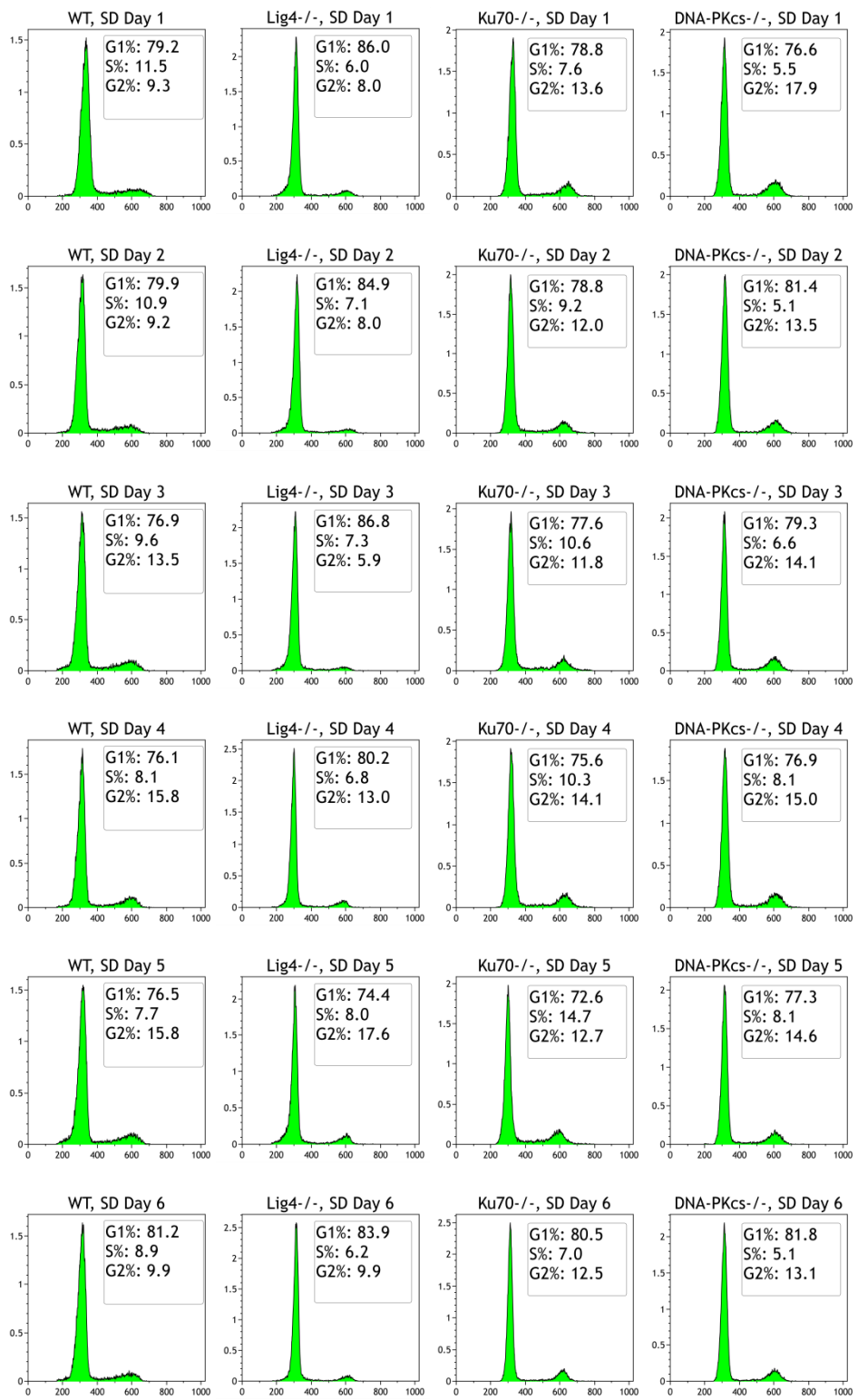


Figure 10. Cell cycle distribution of MEFs growing into plateau phase.

Representative PI histograms indicate DNA content of 1×10^4 cells measured by flow cytometry (previous page). Black bars represent G1, red bars represent S and grey bars represent G2 gated populations. Quantitative data is from one out of at least three independent experiments with similar results.

% Gated



DNA Content

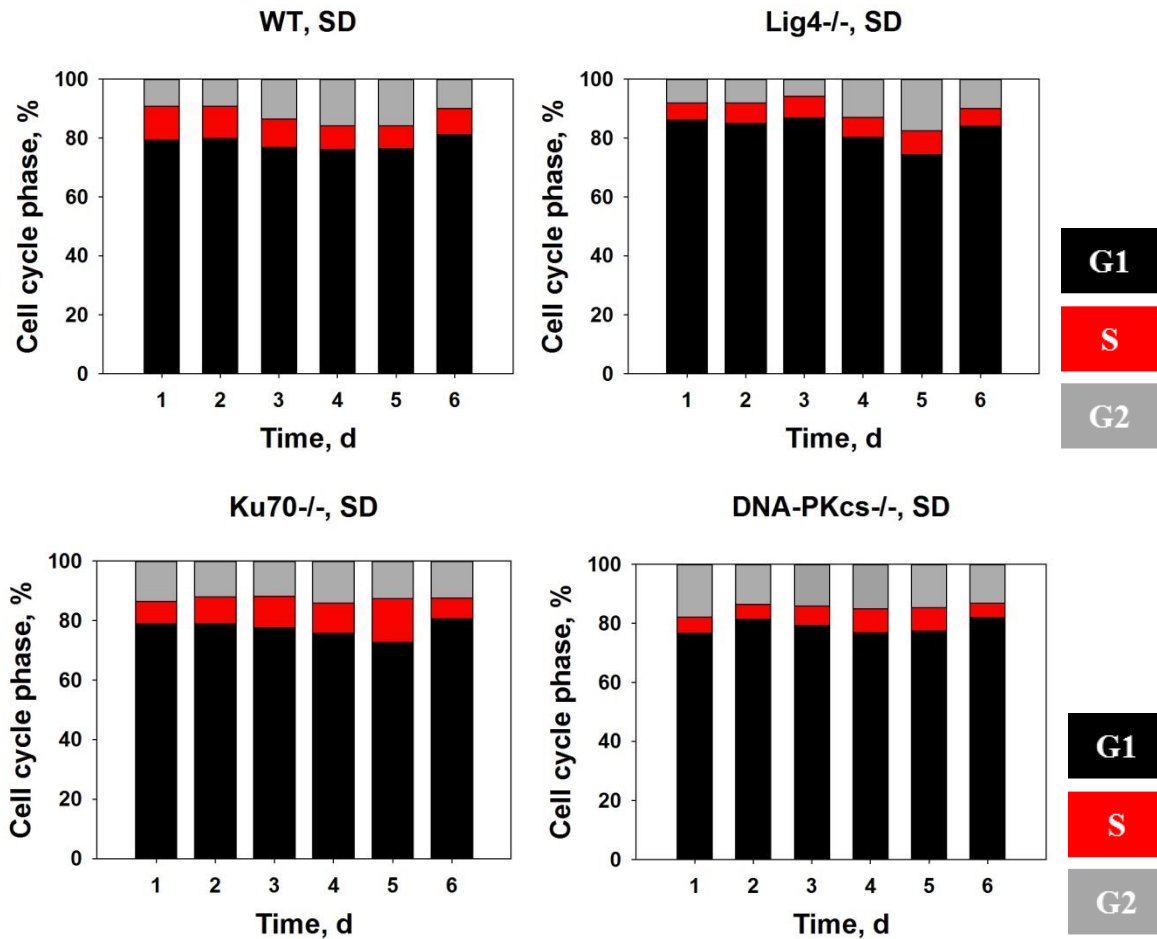
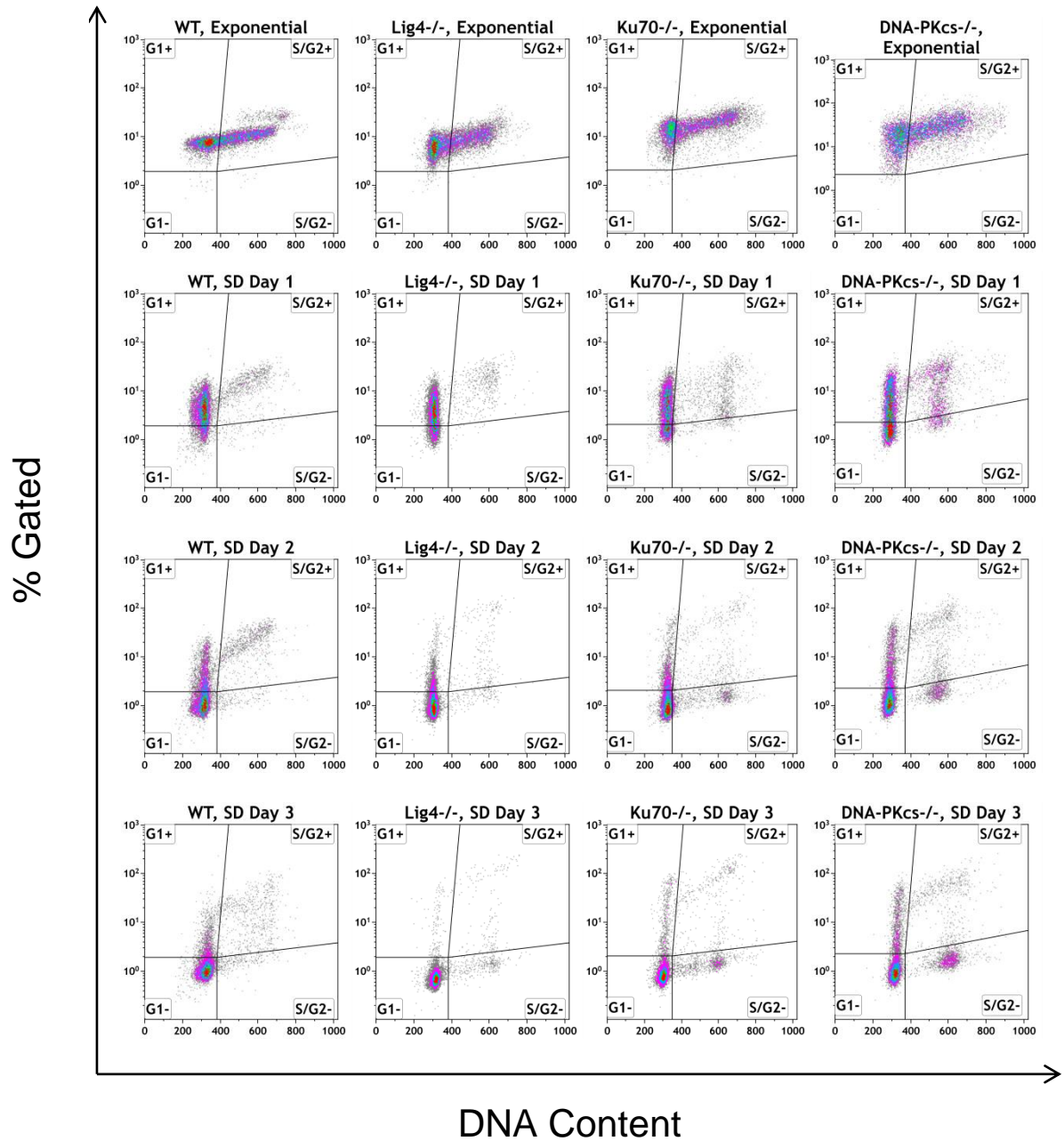


Figure 11. Cell cycle distribution of MEFs after serum deprivation.

Representative PI histograms indicate DNA content of 1×10^4 cells measured by flow cytometry (previous page). Black bars represent G1, red bars represent S and grey bars represent G2 gated populations. Quantitative data is from one out of at least three independent experiments with similar results.

In order to confirm that cells are in non-proliferating, quiescent state after serum deprivation, we also measured Ki67 levels, a widely used indicator of proliferative activity. Although approximately 80% of the cells were in G₁ phase in the first day of serum deprivation, as seen in Figure 11, these cells still expressed Ki67, indicating that they were in proliferative state. However, Ki67 levels dropped gradually and reached a minimum at 3 days of serum deprivation (Figure 12). Therefore, unless indicated otherwise, in the following experiments, growth arrested cells were generated by 3 days of serum deprivation.



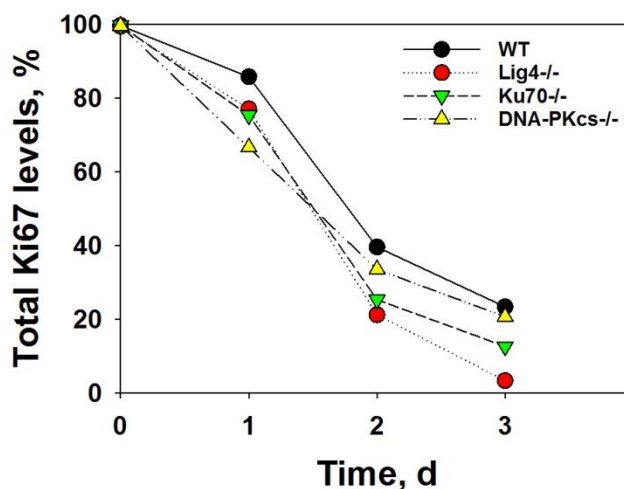


Figure 12. Ki67 levels in MEFs after serum deprivation.

Decrease in the Ki67 levels within 3 days of serum deprivation. Day 0 indicates the exponential phase of growth and the day of serum deprivation. Dot plots indicate the distribution of Ki67 signal in 5×10^4 cells measured by flow cytometry (previous page). Gates were defined according to unstained negative controls. Results shown are from one out of at least two independent experiments with similar results.

4.1.2. DSB repair in proliferating and quiescent c-NHEJ deficient MEFs

After standardizing the conditions for generating quiescent, *quasi G₀* cells, we performed PFGE experiments to measure DSB repair in different growth states. Along with c-NHEJ deficient cells we utilized c-NHEJ wild type (WT) cells as controls. Due to the fact that Lig4 deficiency causes embryonic lethality in mice, Lig4^{-/-} MEF cells are also deficient for p53 in order to rescue the apoptotic phenotype (Frank et al. 2000). Therefore we first tested WT p53^{+/+} and WT p53^{-/-} cells. Our data showed that WT MEFs are able to repair DSBs induced by 20 Gy of IR efficiently within 4 h, either in the exponential or SD state of growth, regardless of p53 status. Therefore, in the further experiments we used p53^{-/-} WT cells as controls (Figure 13).

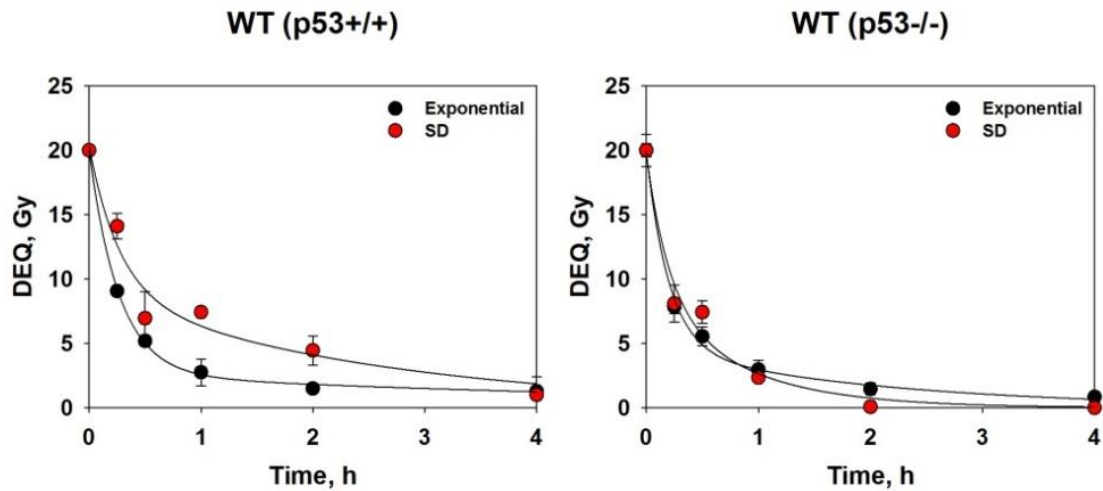


Figure 13. Repair efficiency of WT MEFs in p53 proficient and p53 deficient genetic background.

DSB repair was measured by PFGE after 20 Gy of IR in exponential and SD state. Results were obtained in one experiment and error bars represent standard deviation calculated from four determinations.

Considering the importance of γ H2AX formation in the DNA damage response, we also assessed the contribution of H2AX in DSB repair. PFGE experiments showed that although very important for DSB signaling, H2AX deficiency did not influence the repair upon 20 Gy of IR and regardless of growth state, H2AX^{-/-} cells repaired DSBs as efficiently as WT cells (Figure 14).

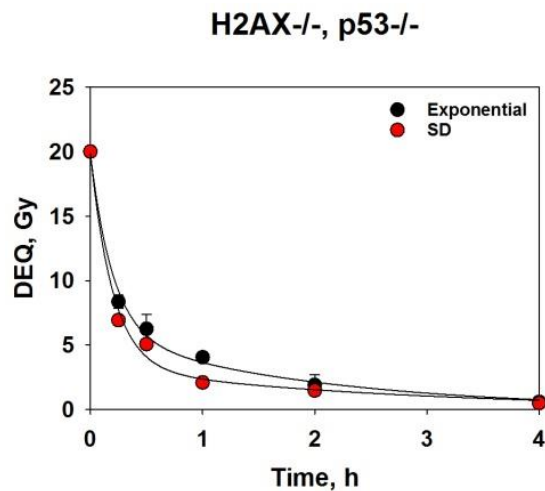


Figure 14. Repair efficiency of H2AX deficient MEFs.

DSB repair was measured by PFGE after 20 Gy of IR in exponential and SD state. Results were obtained in one experiment and error bars represent standard deviation calculated from four determinations.

Furthermore, we showed that c-NHEJ deficient MEFs, which are mutants of $Lig4^{-/-}$, $Ku70^{-/-}$ and $DNA-PKcs^{-/-}$ were also able to repair the majority of DSBs in the exponential phase of growth, in line with the previous reports (Iliakis et al. 2004, Bennardo et al. 2008, Chiruvella et al. 2013). However, while $Lig4^{-/-}$ and $Ku70^{-/-}$ MEFs showed a strong abrogation of repair in SD state, $DNA-PKcs^{-/-}$ MEFs showed only a small reduction in repair efficiency (Figure 15).

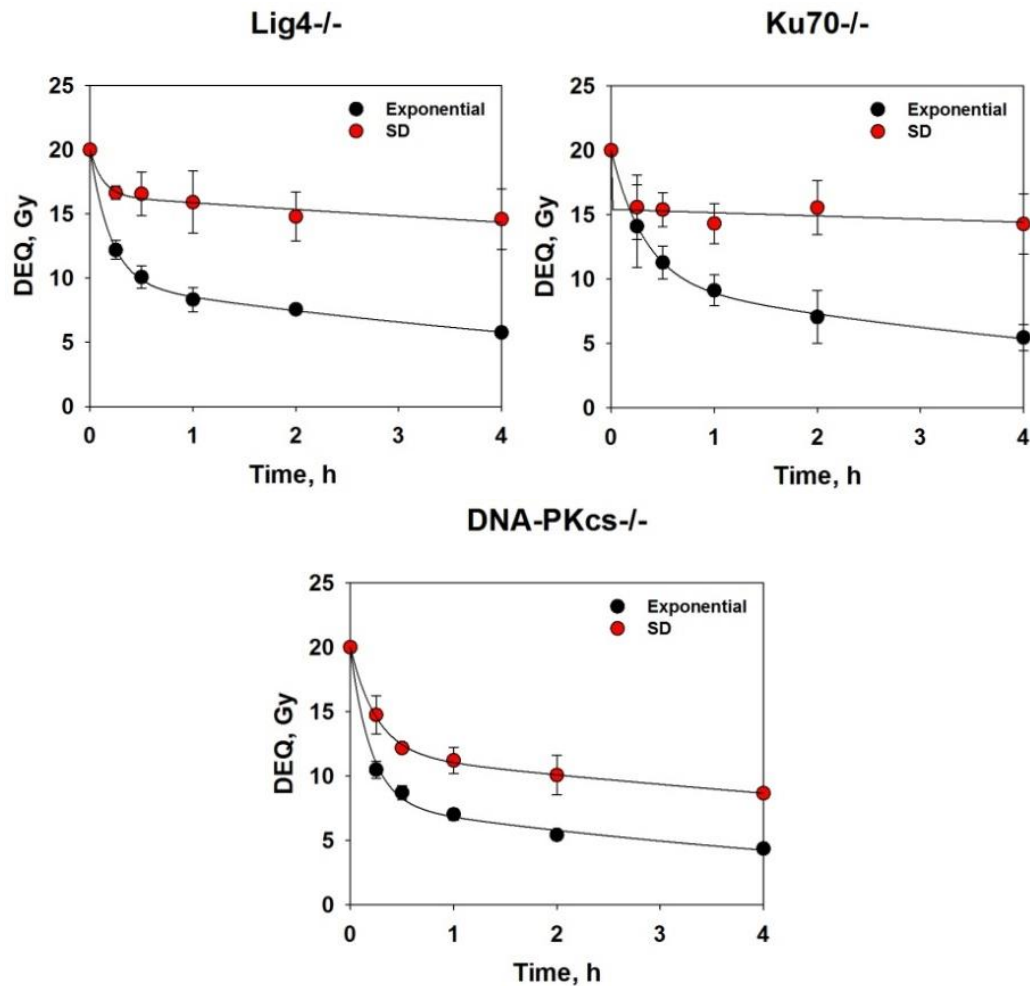


Figure 15. Repair efficiency of $Lig4^{-/-}$, $Ku70^{-/-}$ and $DNA-PKcs^{-/-}$ MEFs in different growth states.

DSB repair was measured by PFGE after 20 Gy of IR in exponential and SD state. Results shown are the average of three independent experiments and error bars represent standard deviation calculated from twelve determinations.

In order to elucidate the underpinning mechanisms of the growth state dependence of alt-EJ with further investigations, we used $Lig4^{-/-}$ MEFs, which typically represent the growth state dependent phenotype. We aimed to confirm our PFGE results using confocal laser scanning

microscopy to measure γ H2AX and 53BP1 foci kinetics in Lig4^{-/-} MEFs after 1 Gy of IR exposure (Figure 16 and Figure 17). Although, γ H2AX and 53BP1 foci formation reached the maximum level at 1 hour; the disappearance of foci, which indicates DSB repair, followed similar patterns as those observed in PFGE experiments. In exponentially growing Lig4^{-/-} MEFs, disappearance of γ H2AX and 53BP1 foci was slower than wild type cells, however repair was efficient. In SD state, γ H2AX and 53BP1 foci remained unresolved in Lig4^{-/-} MEFs. The slower kinetics of γ H2AX and 53BP1 foci decay, in comparison to PFGE kinetics may be explained by the requirement of longer period of time for the biochemical events required for the resolution of the focus than for the physical rejoining of the DSBs detected by PFGE (Kinner et al. 2008). Another important aspect would be the different dose range used in microscopy (1 Gy) and PFGE (20 Gy), which may possibly affect the repair kinetics. Figure 16 and Figure 17 show respectively, the γ H2AX and 53BP1 kinetics of Lig4^{-/-} MEFs in exponential and SD state along with WT controls.

Immunofluorescence staining of γ H2AX after 1 Gy of IR

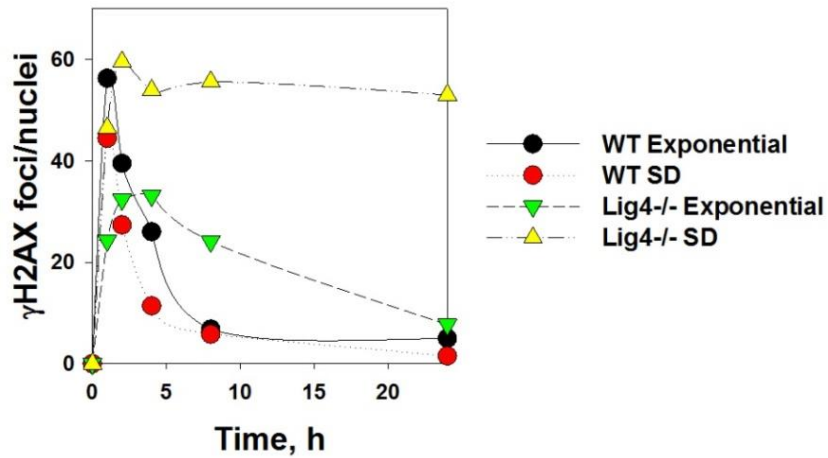
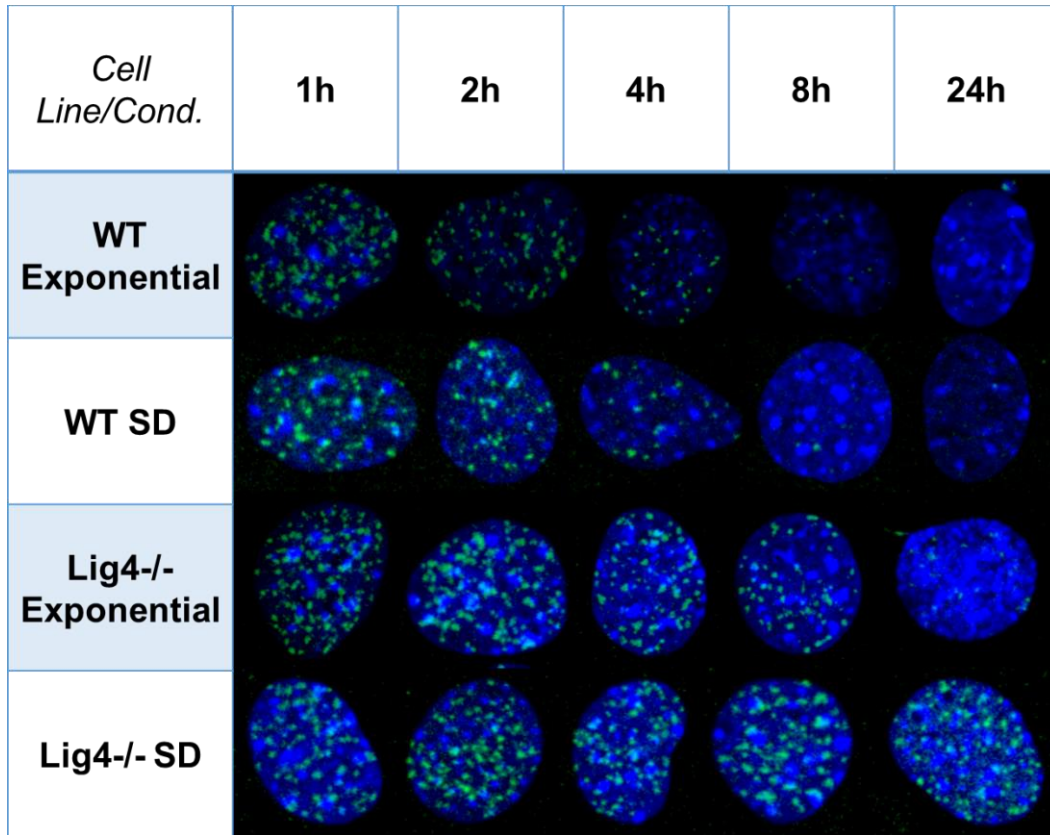


Figure 16. γ H2AX foci kinetics after 1 Gy of IR in WT and Lig4^{-/-} MEFs in exponential and SD state.

Representative images of immunofluorescence staining of γ H2AX (upper panel). γ H2AX foci was stained with Alexa Fluor 488 (green). DNA was stained with DAPI (blue) to visualize the nuclei. Results shown in the graph (lower panel) are from one out of two independent experiments with similar results. Average of γ H2AX foci per nucleus was counted in 50 cells per time point.

Immunofluorescence staining of 53BP1 after 1 Gy of IR

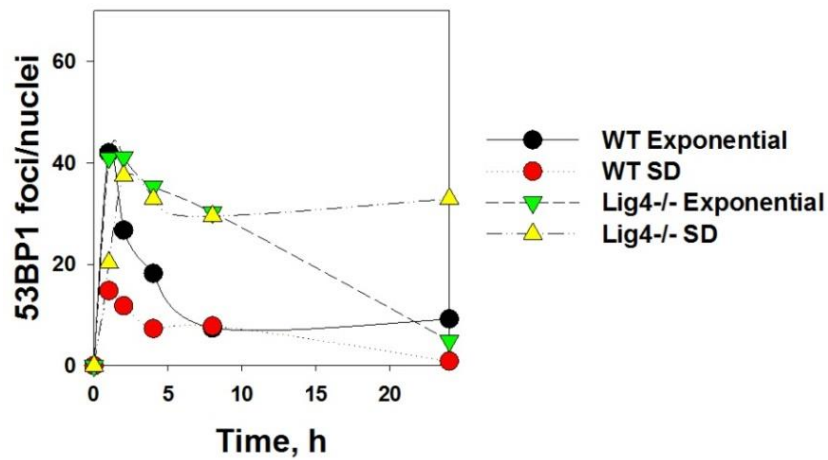
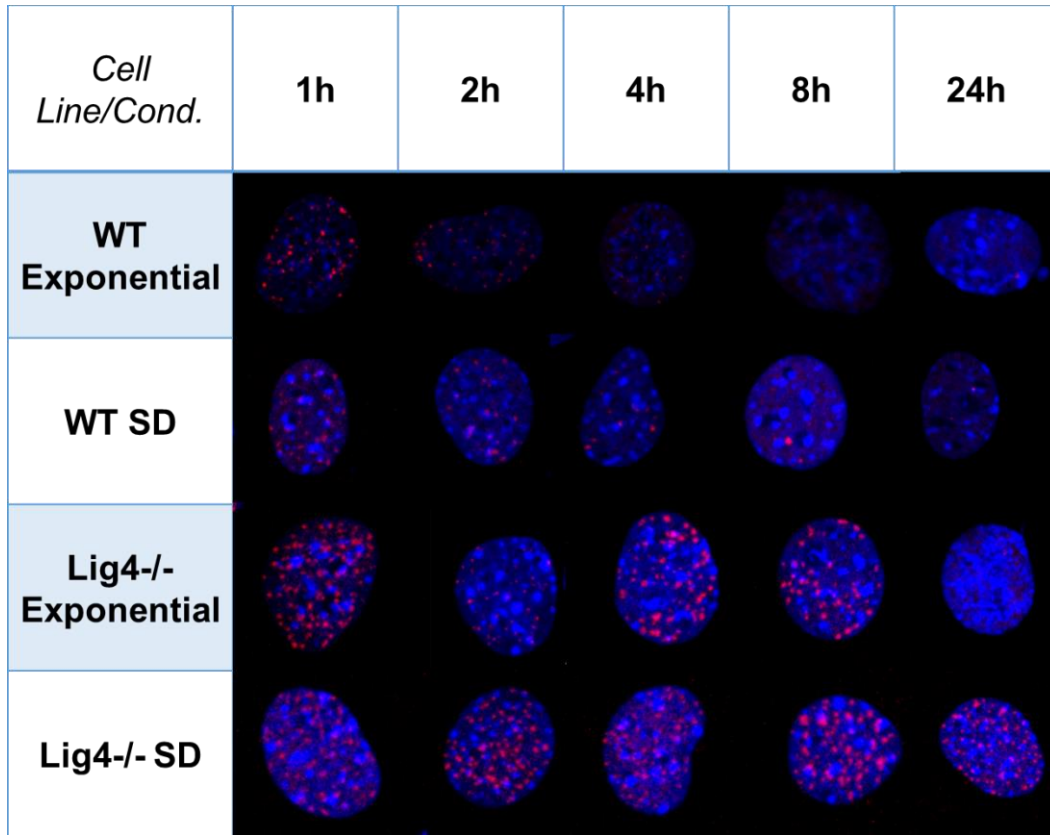


Figure 17. 53BP1 foci kinetics after 1 Gy of IR in WT and Lig4^{-/-} MEFs in exponential and SD state.

Representative images of immunofluorescence staining of 53BP1 (upper panel). 53BP1 foci was stained with Alexa Fluor 568 (red). DNA was stained with DAPI (blue) to visualize the nuclei. Results shown in the graph (lower panel) are from one out of two independent experiments with similar results. Average of 53BP1 foci per nucleus was counted in 50 cells per time point.

We also tested how alt-EJ contributes to the survival of MEFs. As seen in Figure 18, WT cells were highly radioresistant irrespectively of growth state. Although Lig4^{-/-} cells were found quite radiosensitive, alt-EJ still contributed to the survival of irradiated cells and radiosensitivity dramatically increased when cells were in SD state, as a consequence of growth state dependence of alt-EJ.

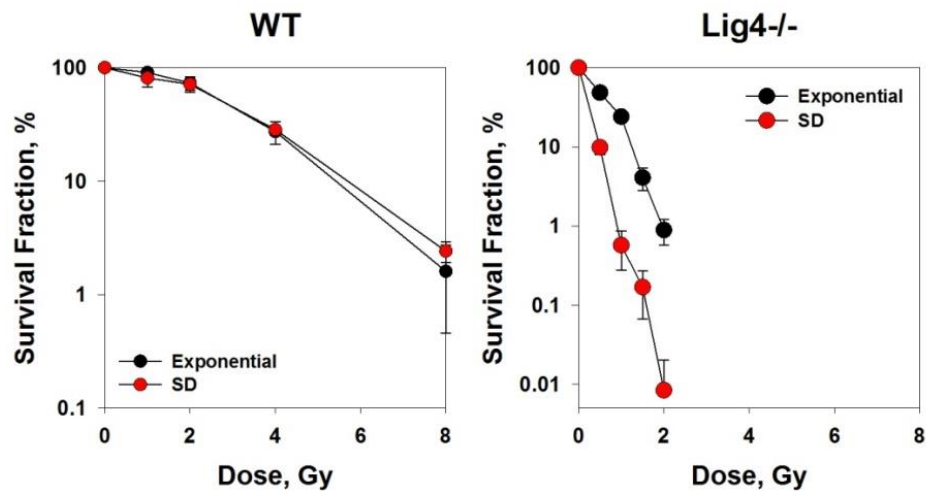


Figure 18. Survival curves of WT and Lig4^{-/-} MEFs in exponential and SD state.

Survival fraction was measured by clonogenic survival assay. Plating efficiency for WT cells in exponential state was 53%, in SD state 26%; for Lig4^{-/-} cells in exponential state 48%, in SD state 30%. Results shown are the average of two independent experiments and error bars represent standard deviation calculated from six determinations.

4.2. Modification of the chromatin structure

In order to elucidate the mechanism behind the growth state dependence of alt-EJ, we hypothesized that the more compact chromatin in G₀ cells may suppress alt-EJ, while it may be facilitated by the more relaxed chromatin in exponential phase. Highly compact chromatin is a conserved feature of quiescent cells in eukaryotes from *Saccharomyces cerevisiae* to humans (Sawicki 1979, Leitch 2000, McKnight et al. 2015, Swygert et al. 2019). It was shown that chromatin compaction is required to ensure quiescent state and chromatin modifications may play a determining role in the transition between quiescence and proliferative state (Srivastava et al. 2010, Li and Dilworth 2016, Liu et al. 2016). Moreover, it is well established that DSB repair is influenced by chromatin structure and upon formation of DSBs, many chromatin

remodeling events take place (Ziv et al. 2006, Falk et al. 2007, Goodarzi et al. 2010, Xu and Price 2011, Price and D'Andrea 2013, House et al. 2014, Taty-Taty et al. 2016, Hauer and Gasser 2017, Seeber and Gasser 2017). Starting from this point, we first aimed to confirm that the chromatin compaction status varies depending on the growth state. Using flow cytometry, we measured H3K9me3 and H3K9Ac levels in WT and Lig4^{-/-} MEFs in exponential and SD state. SD cells showed significantly higher levels of heterochromatin marker H3K9me3 (one tailed T-test, $P= 0.0395$ for WT, $P= 0.00785$ for Lig4^{-/-}), indicating more compact chromatin structure. Unexpectedly, euchromatin marker H3K9Ac levels were also found slightly higher in SD cells. However this difference did not reach statistical significance (one tailed T-test, $P= 0.347$ for WT, $P= 0.343$ for Lig4^{-/-}) (Figure 19). Using additional markers, we confirmed these findings, suggesting that chromatin structure is more compact in SD state in WT and Lig4^{-/-} MEFs (see chapter 4.3.4). Subsequently, we applied a variety of treatments to induce chromatin relaxation in SD state to investigate whether this relaxation would promote alt-EJ. These experiments are presented in the following chapters.

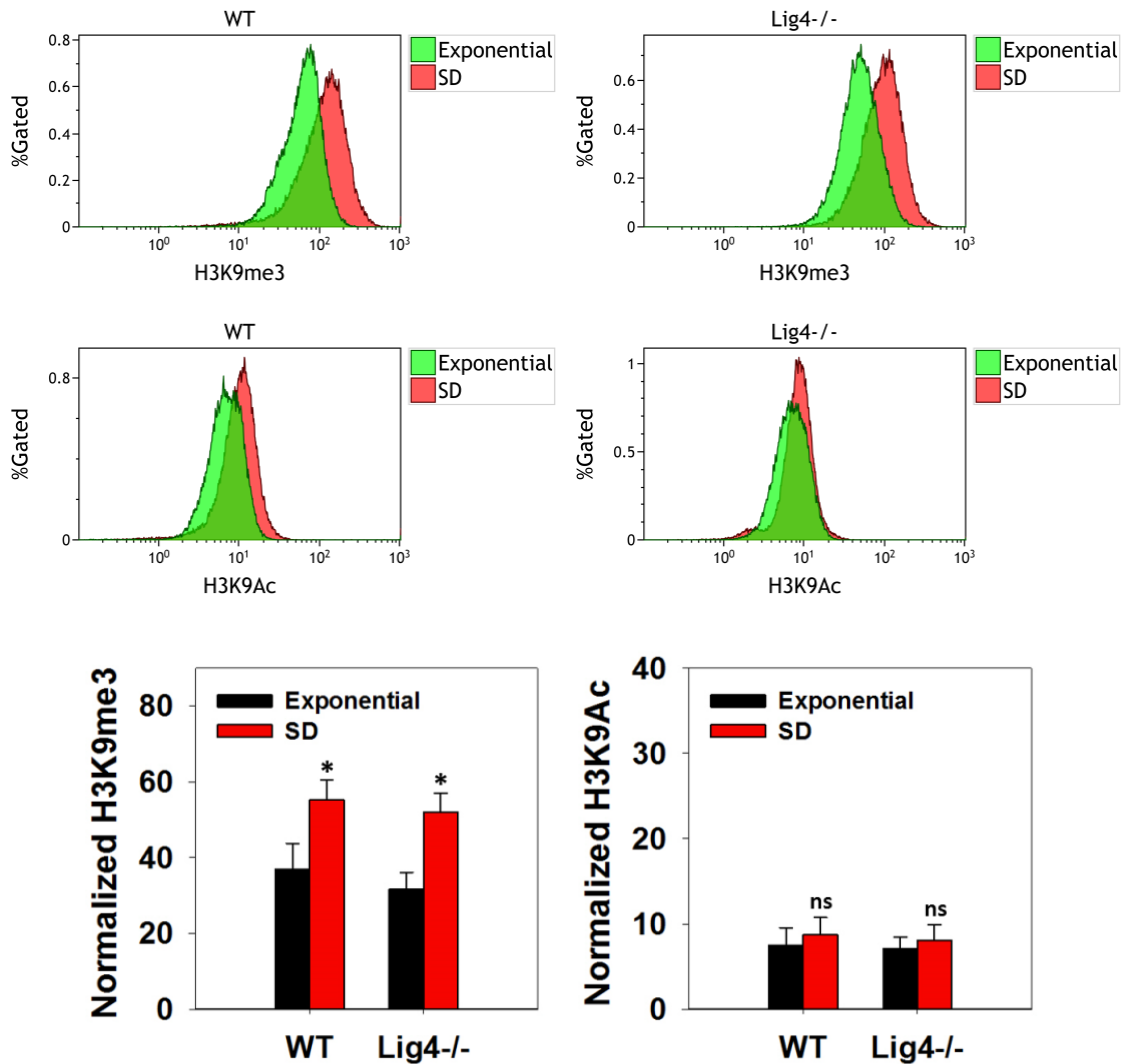


Figure 19. H3K9me3 and H3K9Ac levels in WT and Lig4^{-/-} cells in exponential and SD state.

Representative histogram plots indicate the mean fluorescence intensity of corresponding marker in 5×10^4 cells measured by flow cytometry (upper panel). Quantitative data is the average of at least four independent experiments and error bars represent standard error of the median (lower panel).

4.2.1. The effects of hypotonic treatment

Based on our question whether chromatin relaxation would promote alt-EJ, we treated cells with hypotonic medium for 24 h, which was previously shown to result in global chromatin relaxation (Delpire et al. 1985, Albiez et al. 2006, Srivastava et al. 2010, Goodarzi et al. 2010, Xu and Price 2011, Hübner et al. 2013, Hübner et al. 2015, Taty-Taty et al. 2016, Seeber and Gasser 2017). We prepared hypotonic medium by diluting the standard growth medium with equal

volume of sterile water and incubated the cells in hypotonic medium for 24 h. We measured H3K9me3 and H3K9Ac levels after hypotonic treatment to assess the alterations in the chromatin structure. However as seen in Figure 20 (upper panel), neither methylation nor acetylation levels were affected by hypotonic treatment. Nevertheless, considering that the global chromatin relaxation may not necessarily affect the levels of histone markers, we performed PFGE experiments under hypotonic conditions to test for possible modulation of alt-EJ. As seen in Figure 20 (lower panel), WT cells were not affected by hypotonic treatment. *Lig4*^{-/-} cells in SD state showed a slight decrease in repair efficiency, contrary to our expectations, and in exponential state the decrease was more prominent.

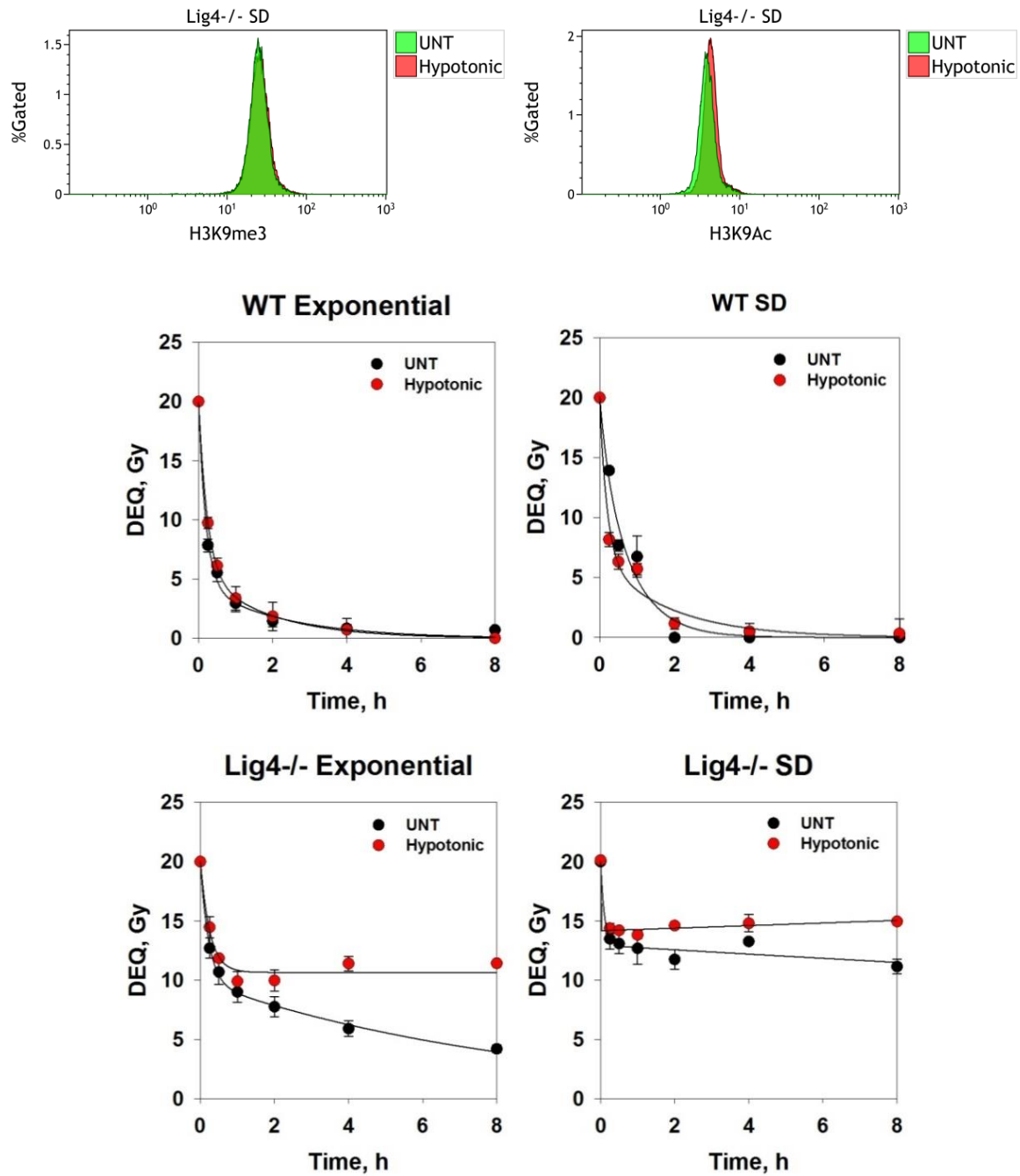


Figure 20. Effects of hypotonic treatment for 24 h in WT and $Lig4^{-/-}$ MEFs.

Histogram plots indicate the mean fluorescence intensity of corresponding marker in 5×10^4 cells measured by flow cytometry after 24 h of hypotonic treatment (upper panel). DSB repair was measured by PFGE after 20 Gy of IR in exponential and SD state following hypotonic treatment for 24 h. Quantitative data is from one out of at least two independent experiments with similar results and error bars represent standard deviation calculated from four determinations (lower panel).

Speculating that cells may be adapted to hypotonic environment within 24 h and that global chromatin relaxation may be reversible, we also tested the effect of short incubation time in hypotonic medium. In this approach, growth medium of the cells was replaced with hypotonic medium immediately after IR exposure (post-IR) and PFGE was performed as previously described. However, similar to 24 h treatment, post-IR hypotonic treatment did not promote the abrogated alt-EJ in $Lig4^{-/-}$ MEFs in SD state (Figure 21).

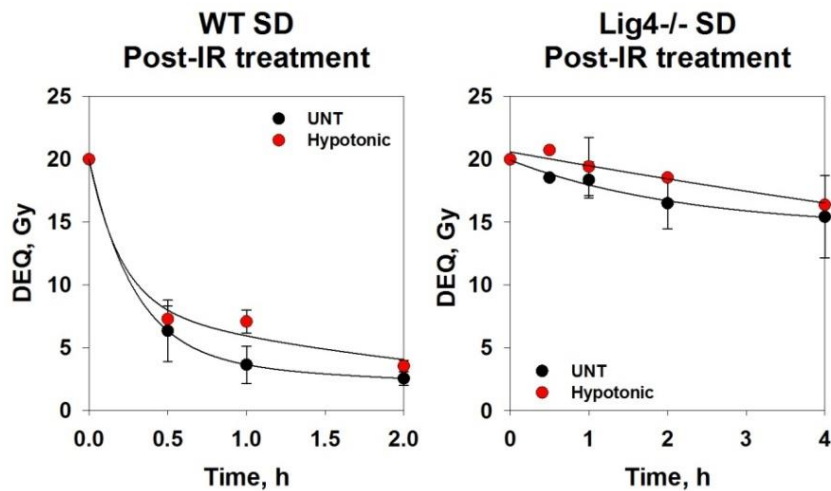


Figure 21. Repair kinetics of WT and $Lig4^{-/-}$ MEFs after post-IR hypotonic treatment.

DSB repair was measured by PFGE after 20 Gy of IR and post-IR hypotonic treatment. Results shown are from one (for WT MEFs) and one out of two (for $Lig4^{-/-}$ MEFs) independent experiments with similar results and error bars represent standard deviation calculated from four determinations.

4.2.2. The effects of DNA methylation inhibitor 5'-aza-2'-deoxycytidine (AzadC)

5'-aza-2'-deoxycytidine (AzadC), also known as Decitabine is a deoxycytidine analog that is incorporated into DNA during replication and it inhibits DNA methyltransferases. Inhibition of DNA methyltransferases results in hypomethylation of DNA, which leads to relaxation of chromatin structure (Haaf 1995, Christmann 2002). We treated $Lig4^{-/-}$ MEFs in exponential and SD state with increasing concentrations of AzadC for 24 h. Since AzadC requires DNA replication to perform its action, cells were deprived of serum only for 24 h and AzadC was administered simultaneously with serum-free medium, while cells were still in exponential state. Since global hypomethylation may also affect histone methylation due to chromatin relaxation, we measured H3K9me3 levels after AzadC treatment. However, AzadC treatment slightly

increased H3K9me3 levels and this trend was similar in exponential and SD state. Although AzadC treatment caused an increase in the G_2 population in both exponential and SD state, probably due to the activation of G_2 checkpoint, we showed that H3K9me3 levels followed similar trend in G_1 gated cells, as well. Thus, the increase in H3K9me3 levels was not a result of elevated DNA content due to accumulation of cells in G_2 after AzadC treatment (Figure 22).

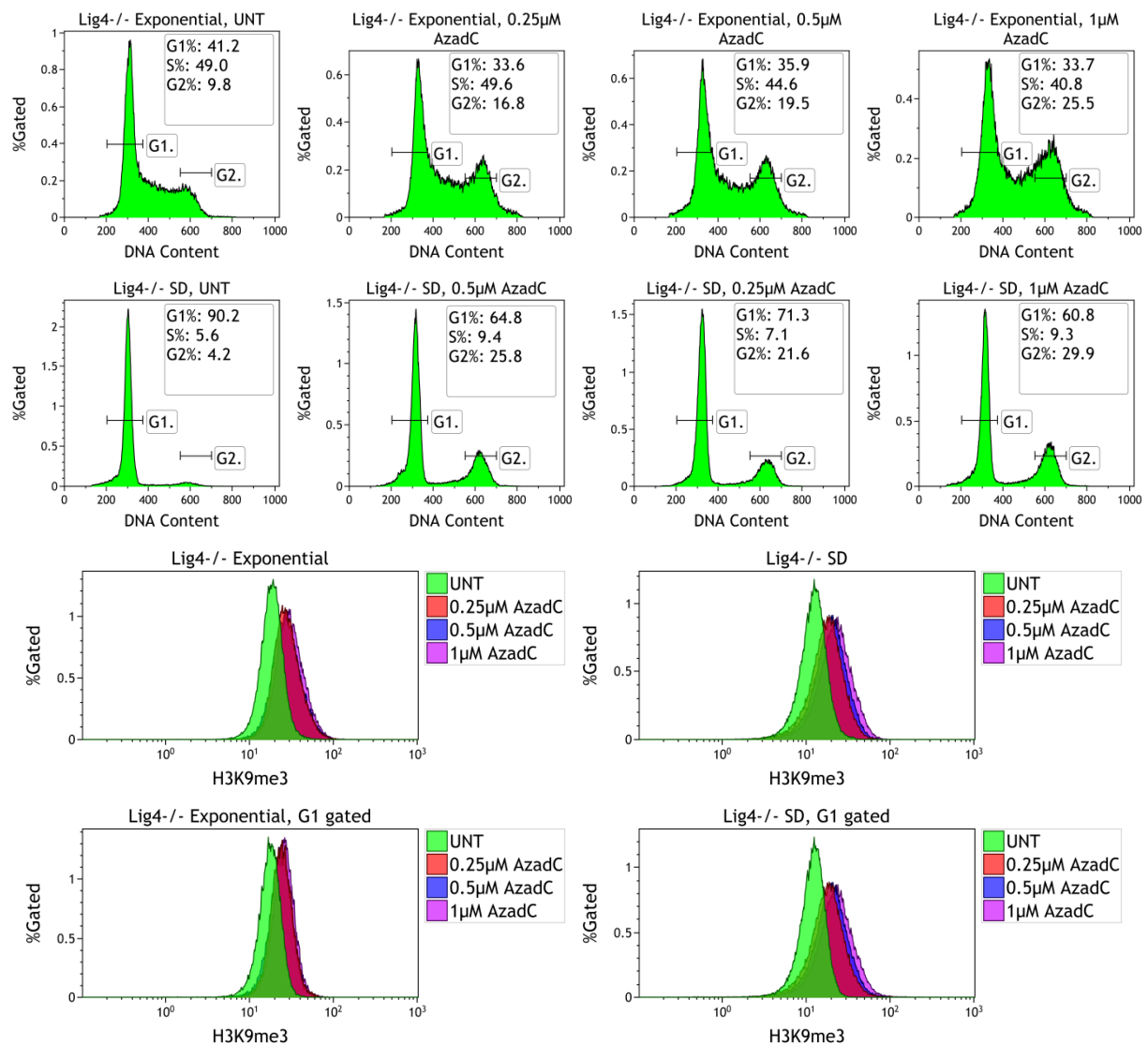


Figure 22. H3K9me3 levels in $Lig4^{-/-}$ MEFs after AzadC treatment in exponential and SD state.

$Lig4^{-/-}$ MEFs were treated with 0.25, 0.5 and 1 μ M AzadC for 24 h. DMSO was added to untreated controls. PI histograms indicate the cell cycle distribution after AzadC treatment (upper panel). Histogram plots indicate the mean fluorescence intensity of H3K9me3 in 5×10^4 cells measured by flow cytometry in whole cell population (middle panel) and in the G_1 gated population (lower panel). Results shown are from one experiment.

Komashko and Farnham showed that inhibition of DNA methylation by 5-azacytidine induced a global increase in H3K9me3 and H3K27me3 levels, in line with our findings (Komashko and Farnham 2010). Therefore, we performed PFGE experiments in Lig4^{-/-} MEFs in SD state with or without 0.5 μM AzadC treatment for 24 h. The results showed that AzadC treatment did not rescue the abrogated repair in Lig4^{-/-} MEFs (Figure 23).

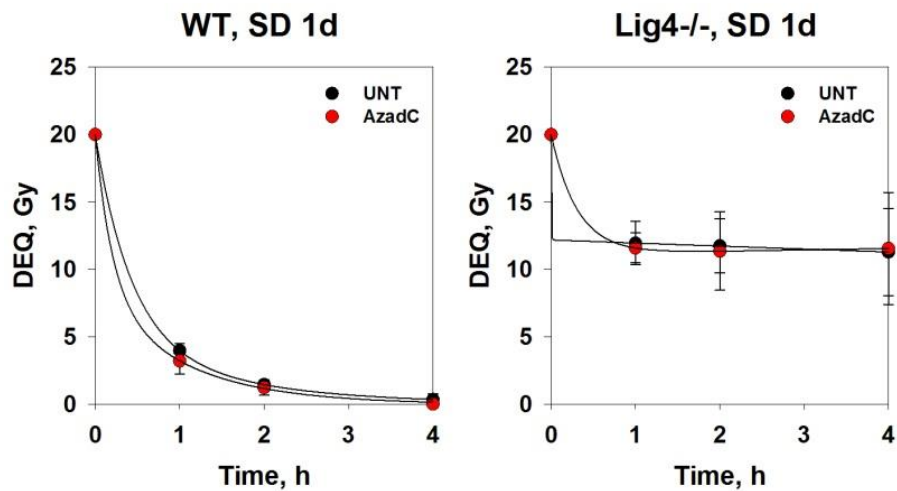


Figure 23. Repair kinetics of WT and Lig4^{-/-} MEFs treated with AzadC.

WT and Lig4^{-/-} MEFs were treated with 0.5 μM AzadC for 24 h. DMSO was added to untreated controls. DSB repair was measured by PFGE after 20 Gy of IR following AzadC treatment. Results shown for WT are from one experiment and for Lig4^{-/-} are the average of two independent experiments and error bars represent standard deviation calculated from three and six determinations, respectively.

4.2.3. The effects of Histone Deacetylase (HDAC) inhibitors

Trichostatin A (TSA) is a well-known non-specific histone deacetylase (HDAC) inhibitor that suppresses histone deacetylation (Tóth et al. 2004, Bulger 2005, Shogren-Knaak et al. 2006). As the addition of negatively charged acetyl groups to the lysine residues neutralizes the positive charge on histone tails, acetylation weakens the DNA binding affinity of histones. Acetylation status of histones is mediated by the balance between histone acetyl-transferases (HATs) and HDACs. Therefore, inhibition of HDACs results in hyperacetylation of histones that leads to chromatin relaxation (Eberharter and Becker 2002, Bannister and Kouzarides 2011). In order to induce chromatin relaxation, we treated WT and Lig4^{-/-} MEFs with 0.5 μM TSA for 1 h, in

exponential and SD state. TSA treatment induced hyperacetylation of H3K9, indicating chromatin relaxation, as shown in Figure 24.

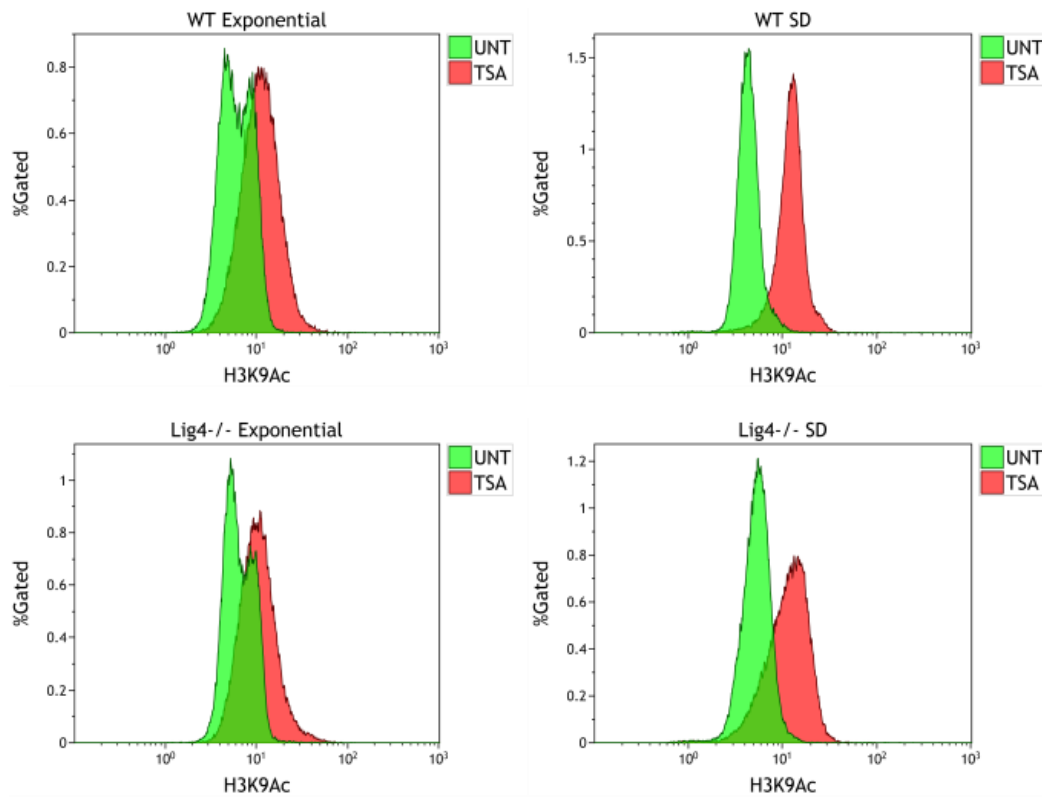


Figure 24. Hyperacetylation in WT and Lig4^{-/-} MEFs after TSA treatment in exponential and SD state.

WT and Lig4^{-/-} MEFs were treated with 0.5 μ M TSA for 1 h. DMSO was added to untreated controls. Results shown are from one experiment and indicate the mean fluorescence intensity of H3K9Ac in 5×10^4 cells measured by flow cytometry.

We performed PFGE experiments with WT and Lig4^{-/-} MEFs treated with 0.5 μ M TSA 1 h prior to IR exposure, in exponential and SD state. We monitored repair kinetics in Lig4^{-/-} MEFs up to 12 h. However, despite the expected chromatin relaxation, repair efficiency remained unaffected in all tested conditions (Figure 25).

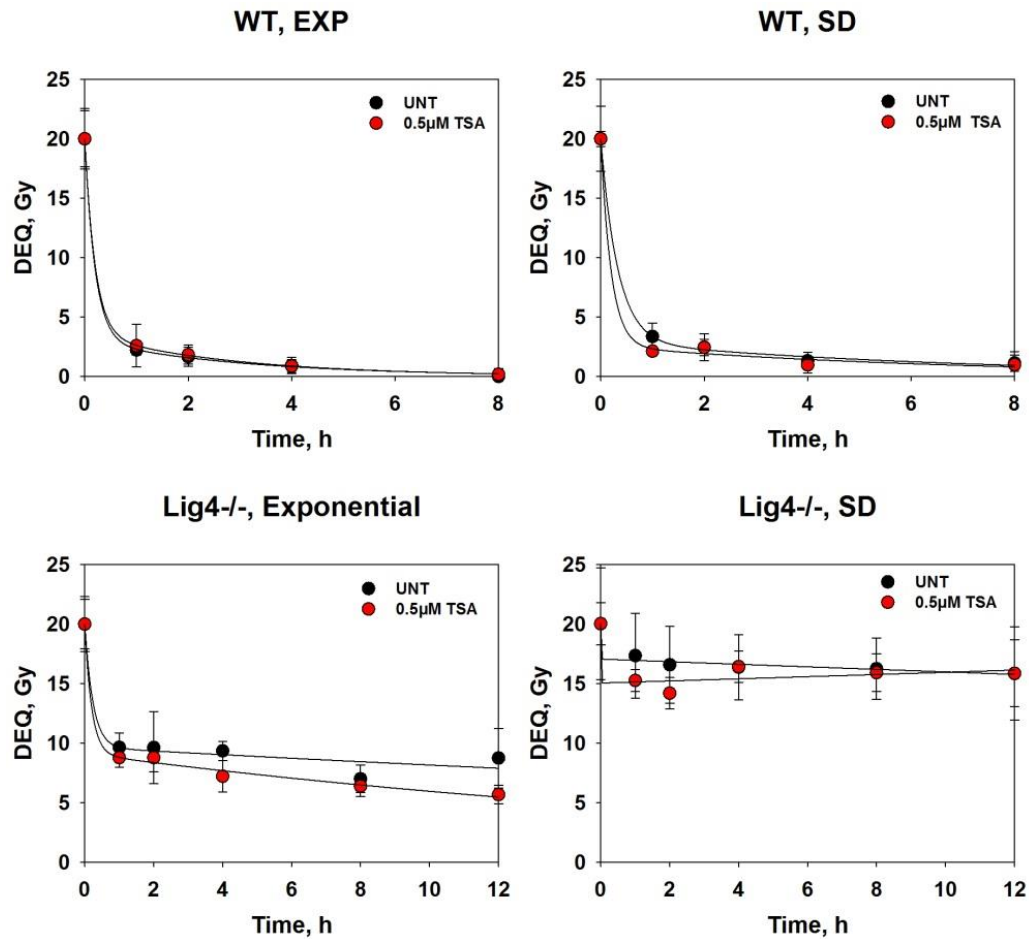


Figure 25. Repair kinetics of WT and Lig4^{-/-} MEFs treated with TSA.

WT and Lig4^{-/-} MEFs were treated with 0.5 μM TSA for 1 h. DMSO was added to untreated controls. DSB repair was measured by PFGE after 20 Gy of IR following TSA treatment. Results shown are from one experiment and error bars represent standard deviation calculated from four determinations.

We suspected that hyperacetylation may be reversible and therefore, we were not able to detect effects of hyperacetylation on repair efficiency. To rule out this possibility, we measured H3K9Ac levels after 0.5 μM TSA treatment at 2, 4, 8 and 12 h time points in Lig4^{-/-} MEFs with or without 20 Gy of IR. Results showed that H3K9 remained in hyperacetylated state up to 12 h, irrespectively of IR exposure (Figure 26). This finding confirmed that TSA remained effective during PFGE experiments that we measured repair efficiency.

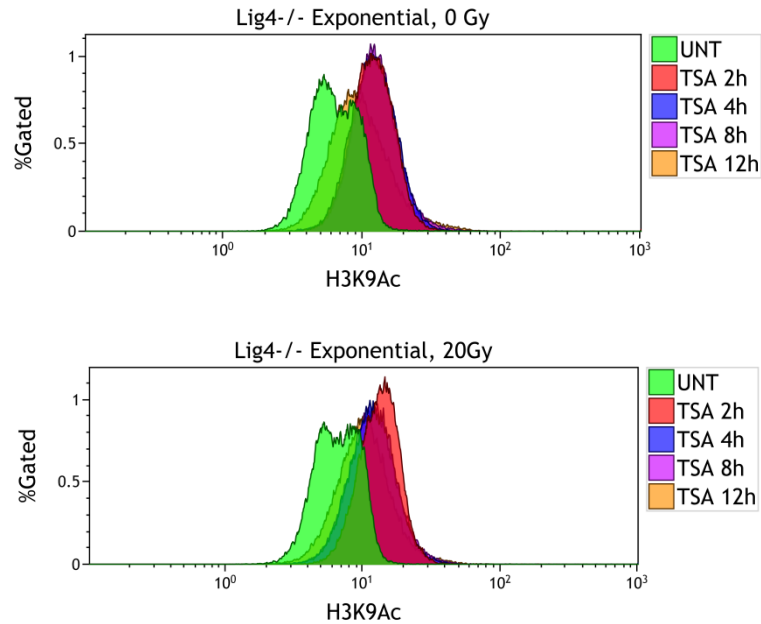


Figure 26. Acetylation status of Lig4^{-/-} MEFs after 2 to 12 h TSA treatment.

Lig4^{-/-} MEFs were treated with 0.5 μ M TSA. DMSO was added to untreated controls. After 1 h of incubation cells were exposed to 20 Gy of IR. Non-irradiated control samples were kept under the same conditions. Histogram plots indicate the mean fluorescence intensity of H3K9Ac in 5x10⁴ cells measured by flow cytometry at 2, 4, 8 and 12 h time points. Results shown are from one experiment.

We also tested the effects of increasing concentrations of TSA in repair efficiency of Lig4^{-/-} cells in SD state. Although there was a slight promotion in the repair efficiency when cells were treated with 5 and 7.5 μ M TSA, we were not able to reproduce these results in the repeated experiments and higher concentrations of TSA did not follow the similar trend (Figure 27). Therefore we concluded that this difference reflected variations in the experimental conditions and alt-EJ efficiency was not influenced by higher concentrations of TSA.

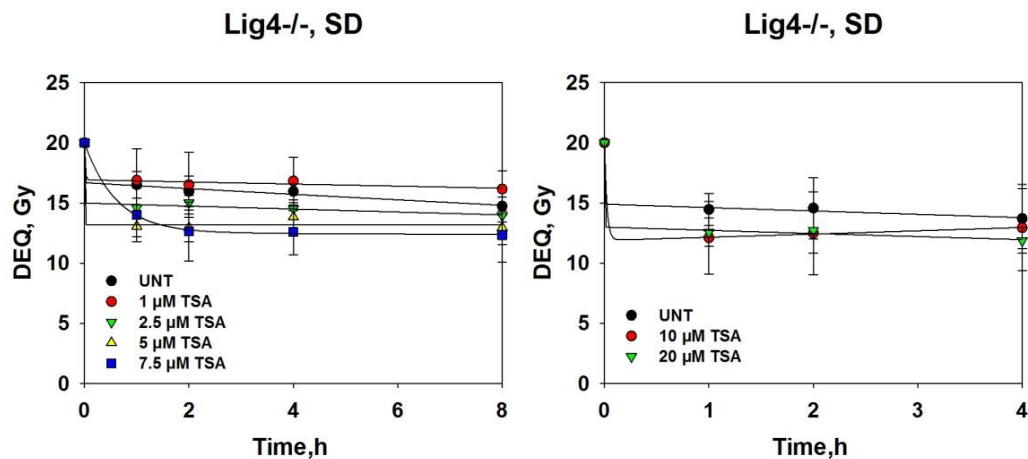


Figure 27. Repair kinetics of *Lig4*^{-/-} MEFs in SD state with increasing concentrations of TSA.

Lig4^{-/-} MEFs were treated with 1, 2.5, 5, 7.5, 10 and 20 μM TSA. DMSO was added to untreated controls. DSB repair was measured by PFGE after 20 Gy of IR following TSA treatment. Results shown are the average of at least three independent experiments and error bars represent standard deviation calculated from 12 determinations.

Next, we tested the effect of another HDAC inhibitor, Valproic Acid (VPA), alone or in combination with TSA. We treated *Lig4*^{-/-} MEFs with 1, 5 and 10 mM VPA or 10 mM VPA in combination with 10 μM TSA for 1 h. We observed that 10 μM TSA alone increased H3K9Ac levels to the maximum, whereas 10 mM VPA alone or in combination with TSA did not generate any further increase. In an independent experiment, we simultaneously deprived *Lig4*^{-/-} cells of serum and treated them with 1 mM VPA. After 3 days of incubation we performed PFGE experiment. We also combined this treatment with 10 μM post-IR TSA treatment. However, we did not observe any effect on abrogated alt-EJ with 3 days of VPA treatment alone or in combination with TSA (Figure 28).

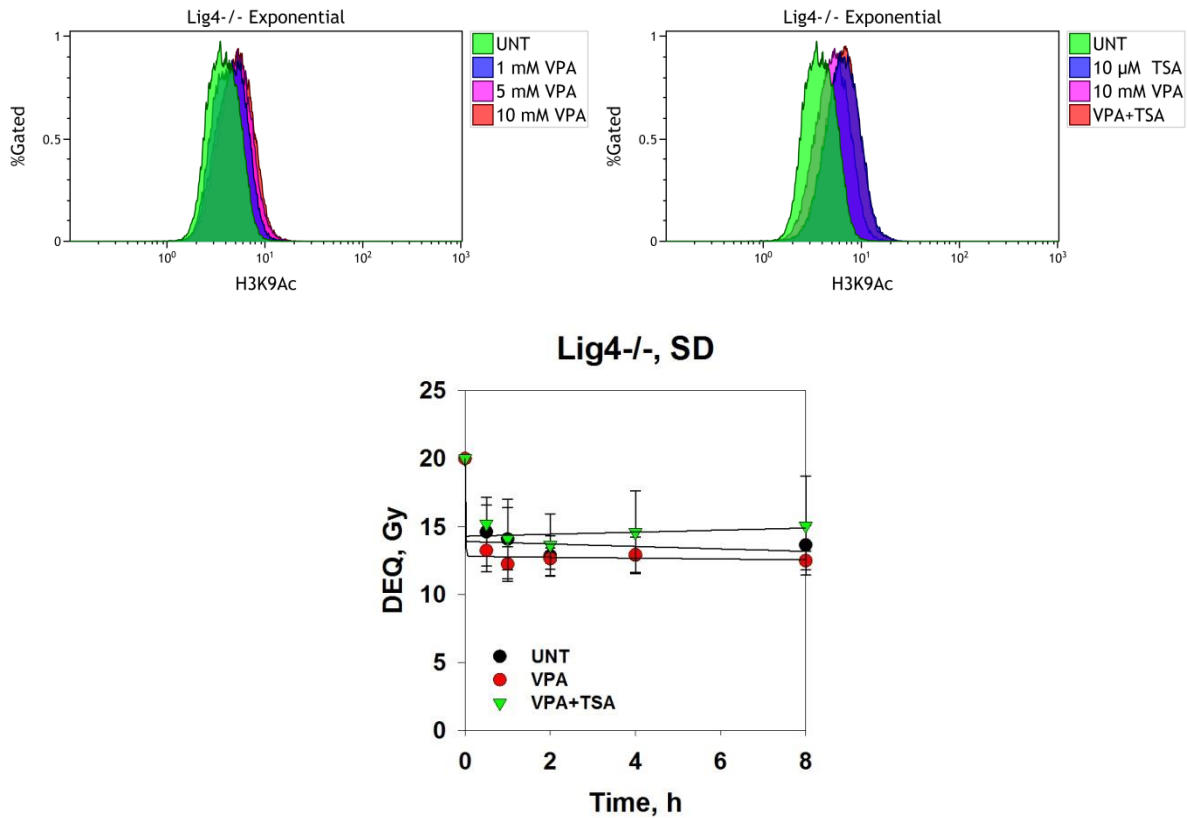


Figure 28. Lig4^{-/-} MEFs treated with VPA alone or in combination with TSA.

Lig4^{-/-} MEFs were treated with 1, 5, 10 mM VPA for 1 h. dH₂O was added to untreated controls (upper left panel). Lig4^{-/-} MEFs were treated with 10 μM TSA, 10 mM VPA and 10 μM TSA and 10 mM VPA in combination for 1 h. DMSO was added to untreated controls (upper right panel). Histogram plots indicate the mean fluorescence intensity of H3K9Ac in 5x10⁴ cells measured by flow cytometry (upper panel). Lig4^{-/-} MEFs were simultaneously deprived of serum and treated with 10 mM VPA for 3 days alone or in combination with post-IR TSA treatment (lower panel). Results shown are from one experiment and error bars represent standard deviation calculated from four determinations.

The first part of our study was designed with the purpose of analyzing the effect of the chromatin structure on the growth state dependence of alt-EJ. Therefore, particular emphasis was placed on investigating whether chromatin relaxing treatments influence the efficiency of alt-EJ in SD state. However, under the experimental conditions we applied here, chromatin relaxing treatments failed to promote compromised alt-EJ.

4.3. The role of DNA-PKcs in the DSB repair pathways

4.3.1. DNA end resection in DNA-PKcs deficient cells

Our findings in the previous sections led us search for further parameters that may underpin the growth state dependence of alt-EJ. As the next step, we focused on the unique response of DNA-PKcs^{-/-} cells in DSB repair by alt-EJ as it was shown in Figure 15. Indeed aforementioned experiments and previous data from our laboratory showed that DNA-PKcs deficient cells utilize alt-EJ independently of growth state. In addition, it has been shown that DNA-PKcs deficiency is associated with enhanced DNA end resection in G₂ phase of the cell cycle (Singh 2010, Dueva 2015). Based on these findings, we hypothesized that downregulation of DNA end resection in G₀ may also be DNA-PKcs dependent and the absence of DNA-PKcs may rescue DNA end resection, thus alt-EJ. Starting from this idea, we performed flow cytometry experiments to measure DNA end resection activity in DNA-PKcs^{-/-} cells, along with other c-NHEJ mutants in exponential and SD state in 1, 3 and 6 h time points following 20 Gy of IR exposure. Flow cytometry allows a quantitative measurement of the signal of interest. Moreover, cell cycle distribution by PI and EdU staining allows quantification of the signal in a selected cell cycle phase. We measured RPA signal as an indicator of DNA end resection (supplementary figures 1-5) and calculated the fold change in the RPA signal intensity between irradiated and non-irradiated samples. However, as seen in Figure 29, all cell lines showed detectable DNA end resection activity at 6 h time point after irradiation, only in the exponential phase of growth, which could be attributed to accumulation of cells in G₂ phase due to IR induced G₂ checkpoint activation (Dueva 2015). However, when we gated cells according to the cell cycle phases, it was evident that not only G₂, but also G₁ cells of an exponentially growing population exhibited DNA end resection activity (supplementary figures 6-15). Here we showed that DNA end resection could take place in the presence of DNA-PKcs and it was evidently not a privilege of DNA-PKcs deficient cells (Figure 29). We also employed a Ku80^{-/-} DNA-PKcs^{-/-} double mutant, along with Ku80^{-/-} single mutant cell line to rule out the potential inhibitory effect of DNA-PKcs on DNA end resection in a different c-NHEJ mutant. However, similar to other c-NHEJ mutants, DNA end resection activity was only detectable in exponentially growing state in Ku80^{-/-} DNA-PKcs^{-/-} double mutant as well (Figure 29). Interestingly, Ku80^{-/-} cells exhibited detectable DNA

end resection activity in SD state, which is suspected to be due to inefficient growth arrest, as seen in the PI histograms in Figure 30. Although, Ku80^{-/-} cells in SD state did not accumulate in G₂ upon 20 Gy of IR, unlike their exponential counterparts; when cells were gated according to cell cycle phases, it was shown that a high proportion of the RPA signal was observed in the G₂ population (supplementary figures 14-15).

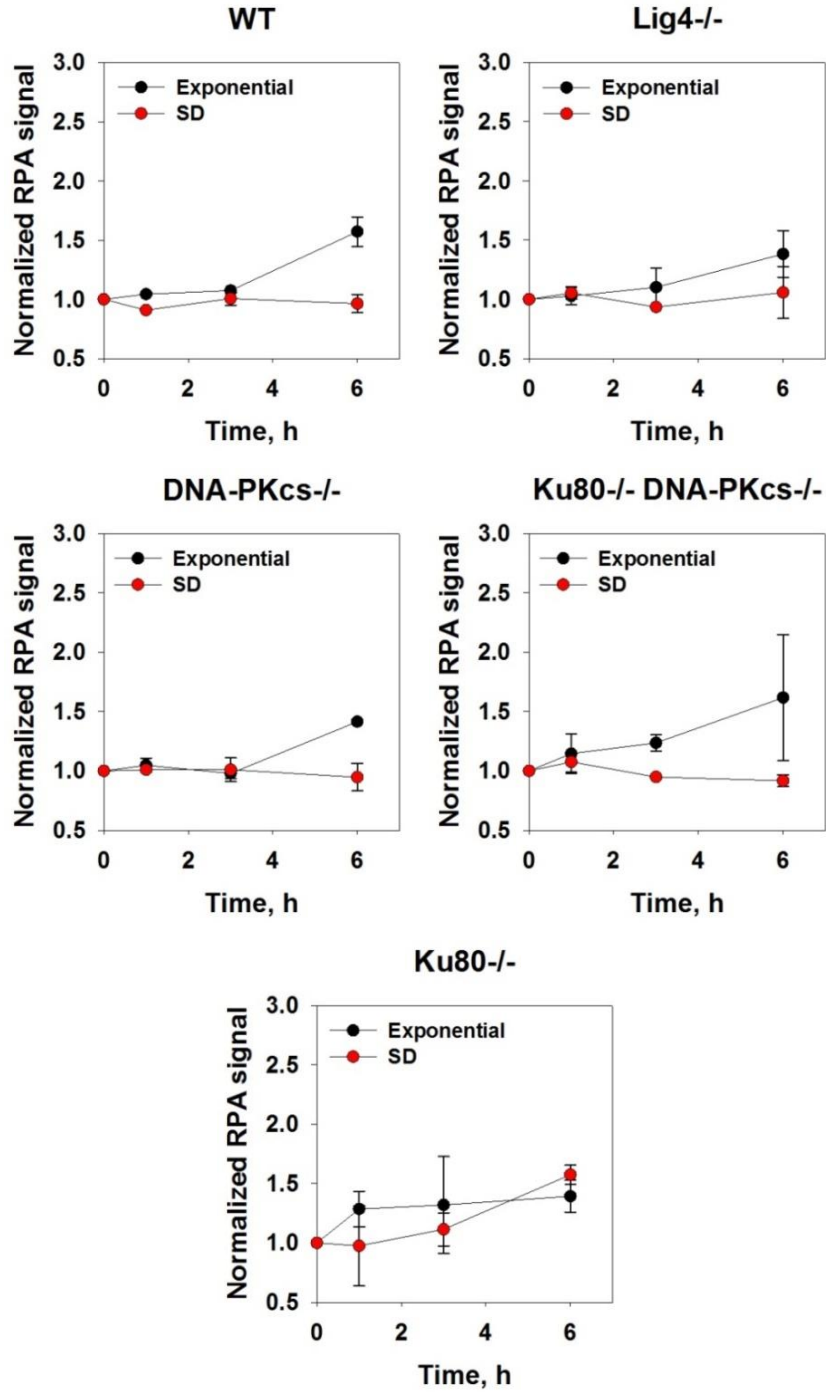


Figure 29. RPA levels induced by 20 Gy of IR in WT, Lig4^{-/-}, DNA-PKcs^{-/-}, Ku80^{-/-} DNA-PKcs^{-/-} and Ku80^{-/-} MEFs in exponential and SD state.

Graphs indicate fold change in the mean values of RPA signal in 5x10⁴ cells measured by flow cytometry and normalized to the non-irradiated control samples. Quantitative data is the average of two independent experiments. Error bars represent standard deviation. For the representative histogram plots see supplementary figures 1-5.

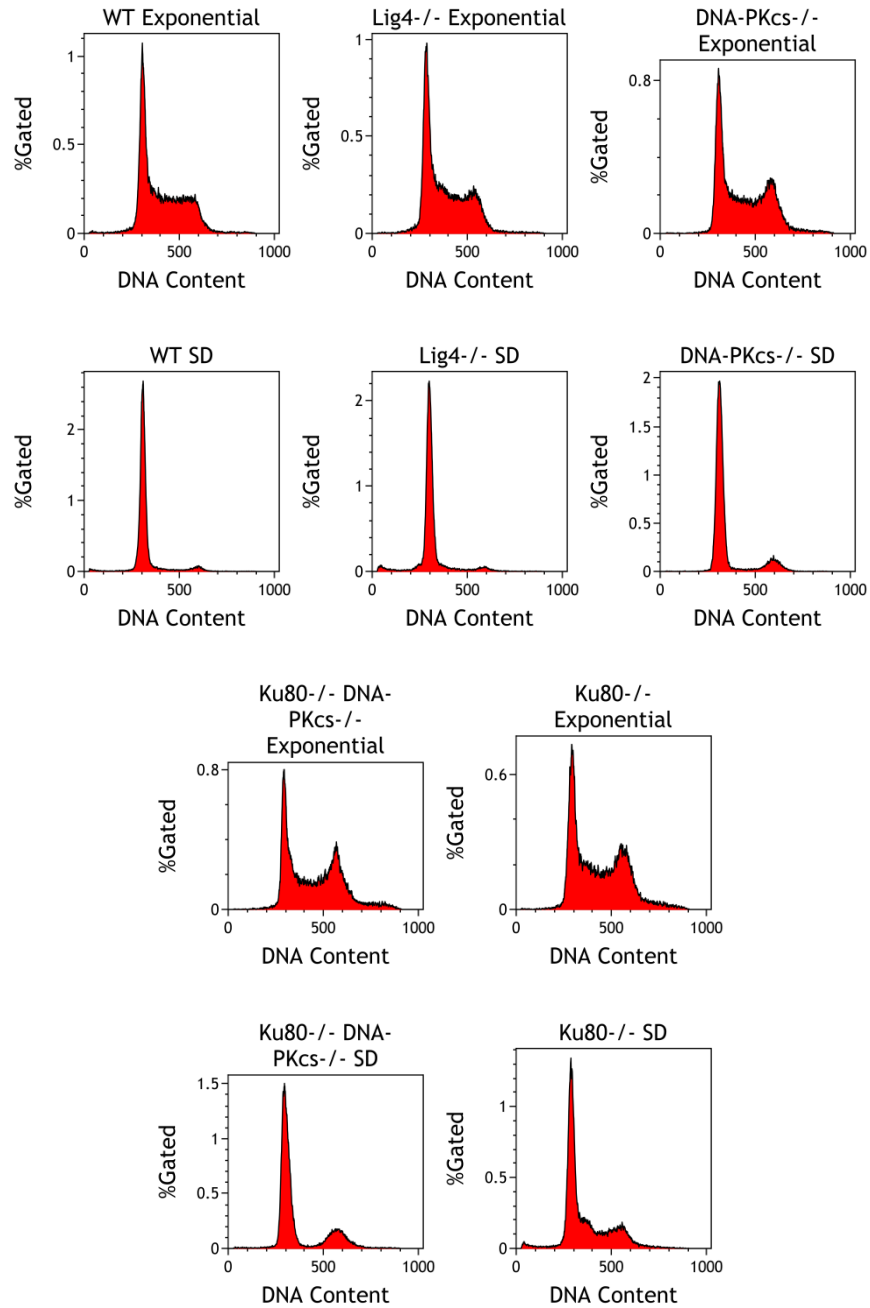


Figure 30. Cell cycle distribution of WT, Lig4^{-/-}, DNA-PKcs^{-/-}, Ku80^{-/-} DNA-PKcs^{-/-} and Ku80^{-/-} MEFs in exponential and SD state.

Representative PI histograms indicate the DNA content for MEFs that were shown in Figure 29.

It has been reported that CtIP regulates DNA end resection in alt-EJ (Lee-Theilen et al. 2011, Mladenov et al. 2013, Truong et al. 2013, Bakr A et al. 2016). Therefore, we performed western blot analysis to detect CtIP protein levels in WT, Lig4^{-/-} and DNA-PKcs^{-/-} cells in exponential

and SD state, at 6 h time point with or without 20 Gy of IR. In line with our data indicating that SD cells that are successfully accumulated in G₀ lack DNA end resection activity; CtIP levels were found to be very low in SD state for all tested cell lines. Irradiation did not influence CtIP protein levels in any of the growth states (Figure 31).

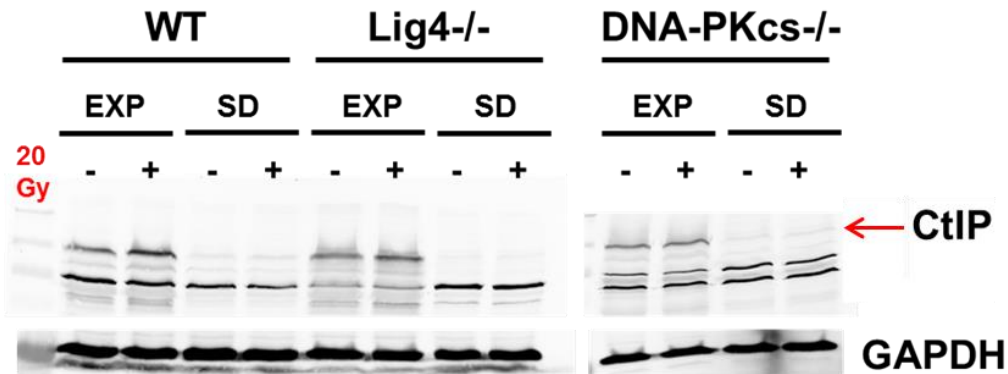


Figure 31. Total CtIP levels in WT, Lig4^{-/-} and DNA-PKcs^{-/-} cells in exponential and SD state.

CtIP protein levels detected by western blotting. Results shown are one out of at least three independent experiments with similar results. GAPDH was used as loading control.

4.3.2. Repair efficiency of Ku80^{-/-} DNA-PKcs^{-/-} double mutant MEFs

Furthermore, we measured the repair kinetics in Ku80^{-/-} DNA-PKcs^{-/-} double mutant, along with Ku80^{-/-} and DNA-PKcs^{-/-} single mutant MEFs in exponential and SD state. We inquired whether DNA-PKcs deficiency would rescue the abrogated alt-EJ in SD state in a different c-NHEJ mutant. Similar to other c-NHEJ mutants, repair was dramatically abrogated in Ku80^{-/-} MEFs in SD state. However, serum deprivation did not efficiently induce growth arrest (52.3% G₀/G₁, 39.2% S, 8.5% G₂) in Ku80^{-/-} MEFs. As we also showed in chapter 4.3.1, Ku80^{-/-} MEFs retained DNA end resection activity in SD state, possibly due to inefficient growth arrest. Repair abrogation despite the inefficient growth arrest and retained DNA end resection in the absence of serum may suggest a role for growth factors in the growth state dependence of alt-EJ. On the other hand, DNA-PKcs deficiency did not rescue the abrogated alt-EJ in SD state, indicating that Ku80 deficient phenotype was dominant under these conditions (Figure 32).

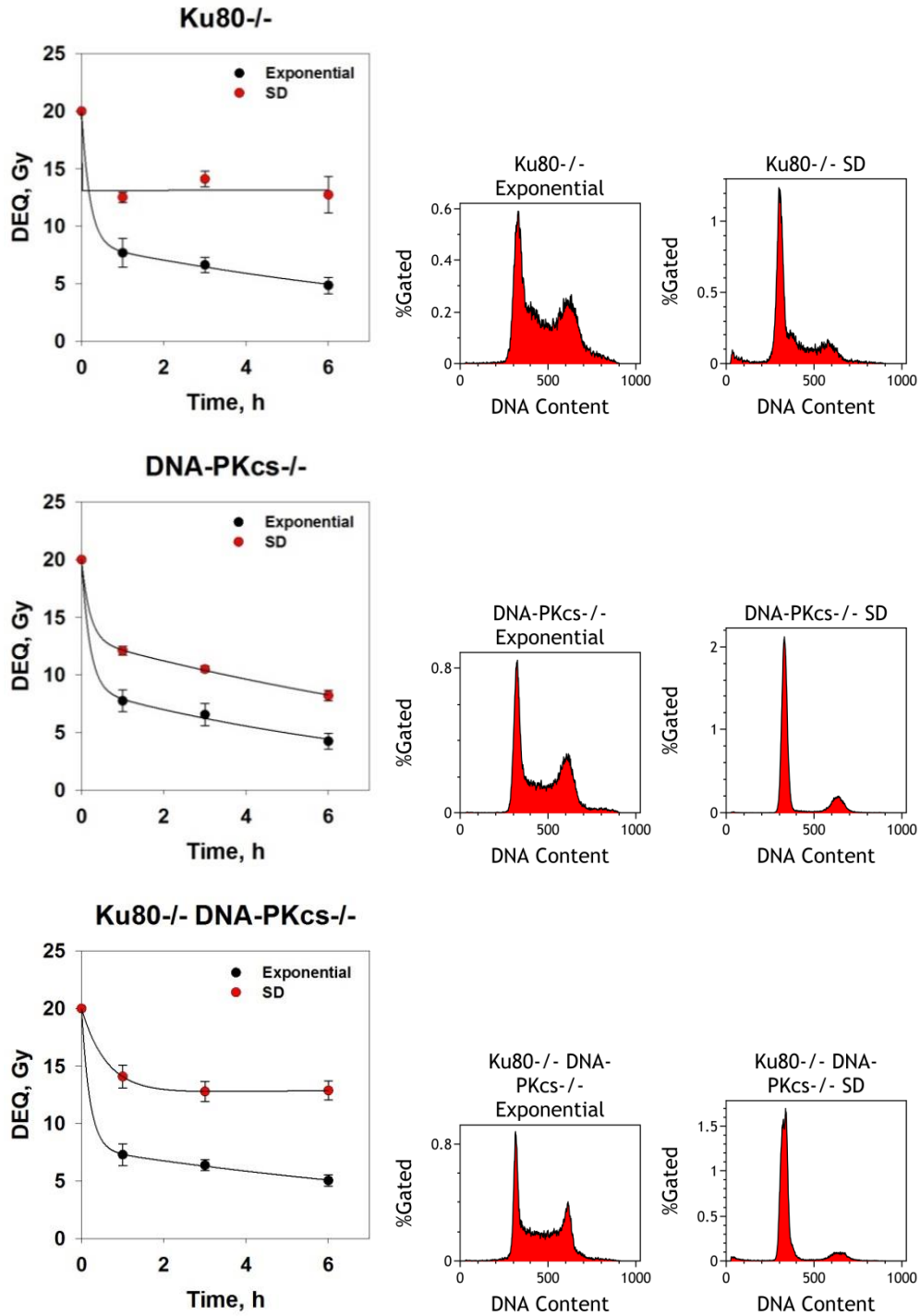


Figure 32. Repair kinetics of Ku80^{-/-}, DNA-PKcs^{-/-} and Ku80^{-/-} DNA-PKcs^{-/-} double mutant MEFs in exponential and SD state.

DSB repair was measured by PFGE after 20 Gy of IR in Ku80^{-/-} MEFs (upper panel), in DNA-PKcs^{-/-} MEFs (middle panel) and in Ku80^{-/-} DNA-PKcs^{-/-} double mutant MEFs (lower panel). Results shown are the average of two independent experiments and error bars represent standard deviation calculated from six determinations.

4.3.3. The effects of inhibition of PARP-1 and DNA ligases 1 and 3 on DSB repair in DNA-PKcs deficient cells

PARP-1 and DNA Ligases 1 and 3 are involved in DSB repair by alt-EJ (Wang et al. 2006, Soni et al. 2014). In order to obtain additional evidence confirming that DNA-PKcs^{-/-} cells repair IR induced DSBs via alt-EJ, we treated DNA-PKcs^{-/-} MEFs with PARP-1 inhibitor, PJ34, or the Ligase 1&3 inhibitor, L67. We added DMSO to untreated controls. However, unexpectedly, DNA-PKcs^{-/-} cells were not affected by these treatments. Although this data could suggest that DNA-PKcs^{-/-} cells repair via a pathway, which is independent of PARP-1 and Ligases 1 and 3, we suspected the effectiveness of these inhibitors as they were also ineffective in Lig4^{-/-} and Ku80^{-/-} cells (Figure 33).

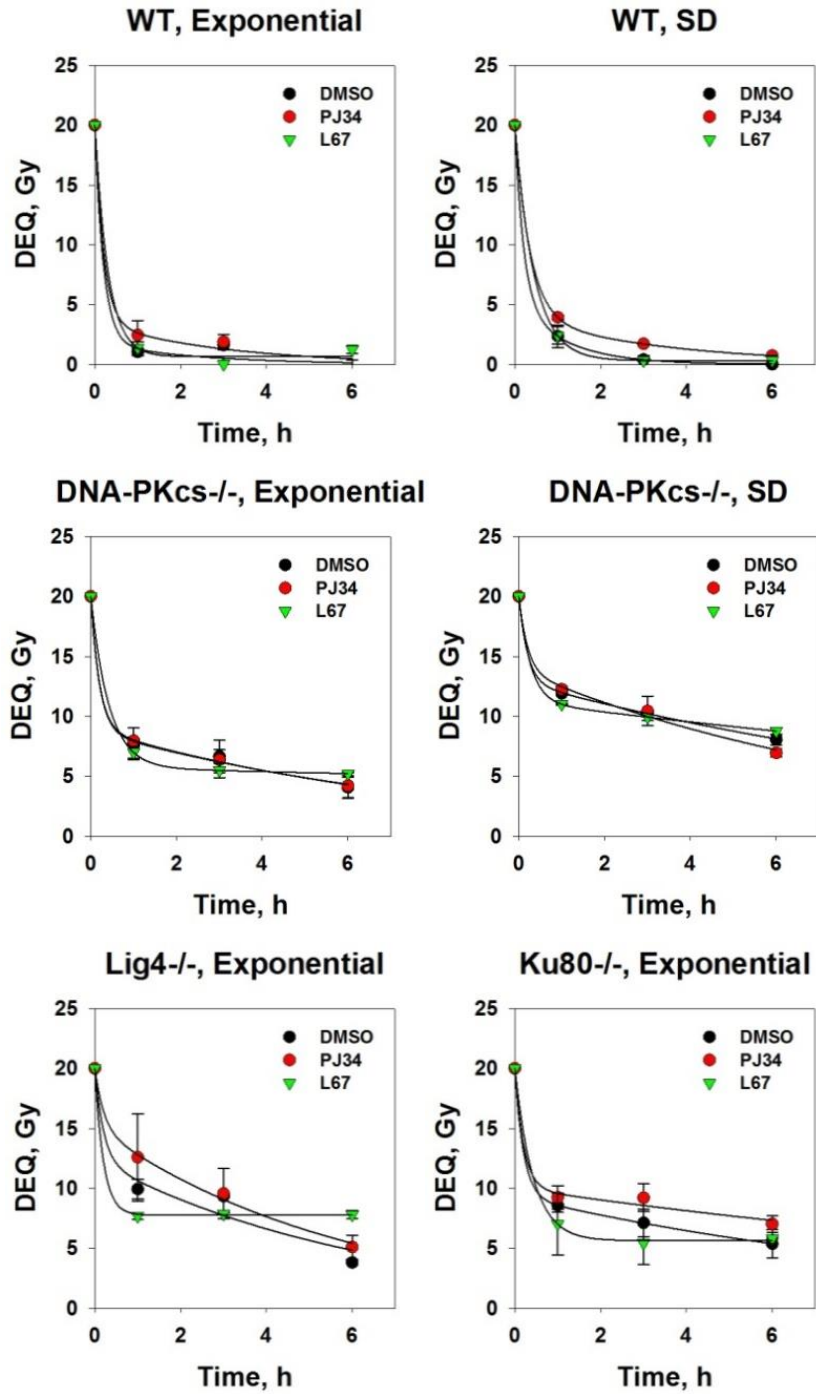


Figure 33. Repair kinetics of WT, DNA-PKcs^{-/-}, Lig4^{-/-} and Ku80^{-/-} MEFs after PJ34 and L67 treatment.

DSB repair was measured by PFGE after 20 Gy of IR following 5 μM PJ34 and 100 μM L67 treatments in WT MEFs (upper panel) and DNA-PKcs^{-/-} MEFs (middle panel) in exponential and SD state and in Lig4^{-/-} and Ku80^{-/-} MEFs (lower panel) in SD state. Results shown are the average of two independent experiments and error bars represent standard deviation calculated from six determinations.

Previously published work from our laboratory has clearly shown that inhibition of PARP-1 or Ligases 1 and 3, using the same inhibitors, significantly decreased the formation of translocations upon 1 Gy of IR in Lig4^{-/-}, DNA-PKcs^{-/-} and Ku80^{-/-} MEFs. As the formation of translocations is a typical feature of alt-EJ, these findings suggested that alt-EJ is suppressed by these treatments. Thus, not only was the efficiency of these inhibitors confirmed; but these findings also showed that DNA-PKcs^{-/-} cells require PARP-1 and Ligases 1 and 3 in order to perform DSB repair (Soni et al. 2014). However, we were not able to confirm these findings in PFGE experiments upon 20 Gy of IR. This discrepancy may suggest a dose dependent regulation regarding the mechanistic aspects of these factors, which require further investigations.

4.3.4. Chromatin structure and transcription related markers in different growth states

We showed in chapter 4.2 that chromatin structure is more compact in SD state as indicated by increased levels of H3K9me3 (Figure 19). Using additional histone and non-histone markers, we assessed the growth state dependent alterations in the chromatin structure and transcription in WT, Lig4^{-/-}, DNA-PKcs^{-/-} and Ku80^{-/-} cells (Figure 34 and supplementary figures 16-19).

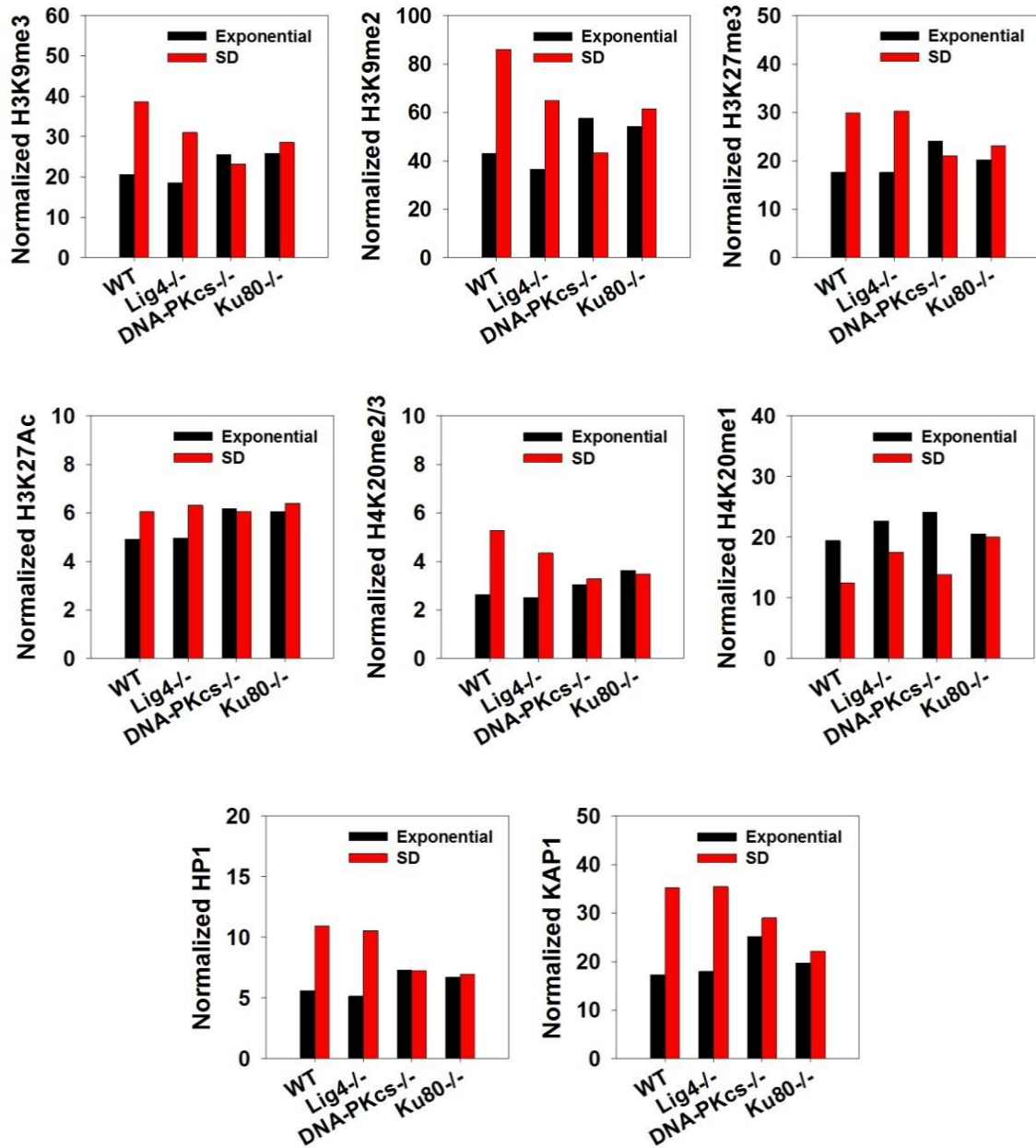


Figure 34. Flow cytometric analysis of heterochromatin and euchromatin related markers in WT, Lig4^{-/-}, DNA-PKcs^{-/-} and Ku80^{-/-} MEFs in exponential and SD state.

Quantification of the mean fluorescence intensity of corresponding markers in 5x10⁴ cells measured by flow cytometry. H3K9me3, H3K9me2, H3K27me3, H4K20me2/3, HP1 and KAP1 were used as heterochromatin markers. H3K27Ac was used as euchromatin marker. H4K20me1 indicated quiescent status. Results shown are from one to two independent experiments. For the representative histogram plots see supplementary figures 16-19.

Similar to our previous findings, H3K9me3 levels were found higher in SD state in WT and Lig4^{-/-} cells. Interestingly, DNA-PKcs^{-/-} and Ku80^{-/-} cells did not show significant alterations in

H3K9me3 levels in different growth states. Along these lines, other histone markers for heterochromatin and transcriptional repression, H3K9me2 and H3K27me3 followed the similar pattern as H3K9me3 for all cell lines. In contrast to these findings, H3K27Ac, which was expected to have a reciprocal relation to H3K27me3, showed a slight increase in SD state in WT and Lig4^{-/-} cells. We showed in chapter 4.2 that while H3K9me3 levels were significantly higher in SD state, H3K9Ac levels did not show the expected decrease. On the other hand, the methylation status of H4K20 showed reciprocal relation between mono- and di-/trimethylation. H4K20me2/3 showed an increase in SD state confirming more compact chromatin structure in WT and Lig4^{-/-} cells, while H4K20me1 showed decreased levels confirming the quiescent state of SD cells, except for Ku80^{-/-} cells. This finding confirmed the inefficient growth arrest in Ku80^{-/-} cells upon serum deprivation, as it was also shown in chapter 4.3.2. Cell cycle distribution of this cell line in SD state could also confirm the inefficient growth arrest as seen in Figure 35, and this may explain the unchanged levels of chromatin/transcription related markers in exponential and SD state. However, despite the efficient growth arrest in DNA-PKcs^{-/-} cells as confirmed by both decreased H4K20me1 levels (Figure 34) and cell cycle distribution (Figure 35), chromatin/transcription related markers did not show significant differences in exponential and SD state.

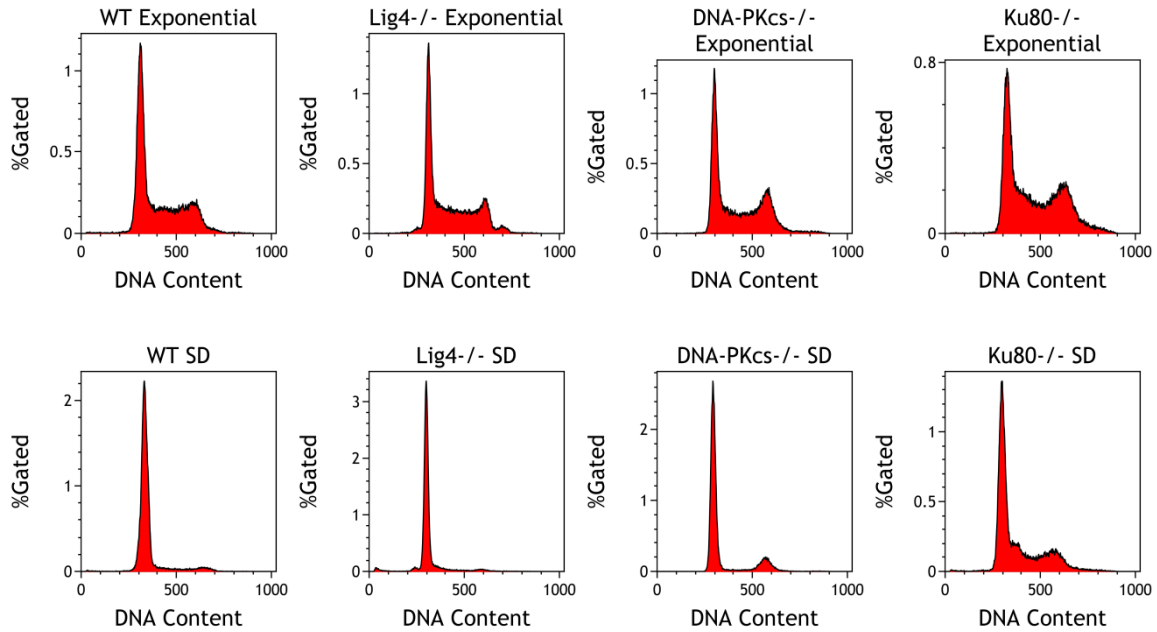


Figure 35. Cell cycle distribution of WT, Lig4^{-/-}, DNA-PKcs^{-/-} and Ku80^{-/-} MEFs in exponential and SD state. Representative PI histograms indicate the DNA content for MEFs that were shown in Figure 34.

We also measured the levels of two non-histone heterochromatin markers HP1 and KAP1 (Figure 34 lower panel). In line with increased levels of heterochromatin related histone markers, HP1 and KAP1 also showed increased levels in SD state in WT and Lig4^{-/-} cells, confirming more compact chromatin structure (Figure 34). These markers followed the similar pattern as heterochromatin related histone markers in DNA-PKcs^{-/-} and Ku80^{-/-} cells, showing only a slight increase in SD state. We also investigated HP1 and KAP1 protein levels in western blot, however as seen in Figure 36, protein levels did not show growth state dependent alterations in any of the cell lines. This may be simply explained by the experimental procedures we applied here. In the preparation of samples for flow cytometric measurements, we applied a permeabilization step that removes the unbound fraction of proteins and therefore only DNA and histone bound content was fixed during the fixation step (see chapter 3.2.6). Therefore, the protein levels measured by flow cytometry represent the DNA-histone bound fractions that reflect the chromatin status. On the other hand, as we prepared whole cell lysates for western blotting, as described in 3.2.10, it is not surprising that the overall protein levels remained similar in cells in different growth states, while their interaction with DNA and histones may change.

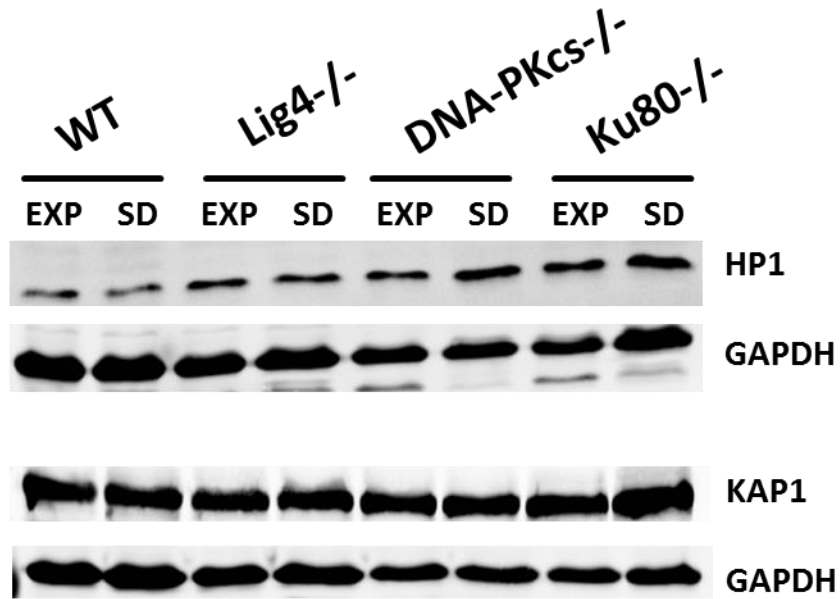


Figure 36. Total HP1 and KAP1 levels in WT, Lig4^{-/-}, DNA-PKcs^{-/-} and Ku80^{-/-} cells in exponential and SD state.

HP1 and KAP1 protein levels detected by western blotting. Results shown are one out of two independent experiments with similar results. GAPDH was used as loading control.

The overall findings suggested that in DNA-PKcs^{-/-} cells, growth state dependent chromatin structure alterations may be negligible. Further investigations are required to determine the role of DNA-PKcs in chromatin remodeling during the transition between G₀ and exponential growth state. In this study, we were not able to show that alterations in the chromatin structure had an impact on the growth state dependence of alt-EJ. However, our findings suggest that similar repair efficiency in DNA-PKcs^{-/-} cells in exponential and SD state may be a consequence of unchanged chromatin structure.

4.4. Alt-EJ in CHO cells expressing different mutant forms of DNA-PKcs

In the next step, we tested DNA-PKcs null, V3 CHO cells, transfected with several human cDNA of DNA-PKcs bearing different mutations in order to study the role of DNA-PKcs in the DSB repair pathway choice (cells were kindly provided by Dr. Kathryn Meek (Neal et al. 2014)).

Because the abundance of DNA-PKcs varies within mammals (primate cells express ~50 times more DNA-PKcs than rodent cells) (Meek et al. 2008); we employed cells expressing different levels of DNA-PKcs. A5 and A36 cells are V3 CHO cells corrected by transfection with wild type gene, expressing low and high levels of DNA-PKcs, respectively. ND5 and JKD2 cells mimic phosphorylated forms of DNA-PKcs. ND5 cells have two substitutions with aspartic acid at the extreme N-terminal region and they have very low kinase activity. JKD2 cells have aspartic acid substitutions at around amino acid 1000 at the N-terminus and they retain normal kinase activity. PQR and GG6 cells contain alanine substitutions in PQR and ABCDE clusters, respectively, and they have normal kinase activity. Vector A (VectA) is a control cell line generated by transfection of the DNA-PKcs deficient V3 CHO mutant with the empty vector used for the generation of the remaining DNA-PKcs mutants. K>R31 is a kinase dead mutant (Cui et al. 2005). A schematic diagram of DNA-PKcs structure and V3 CHO cells with the corresponding mutations are shown in Figure 37.

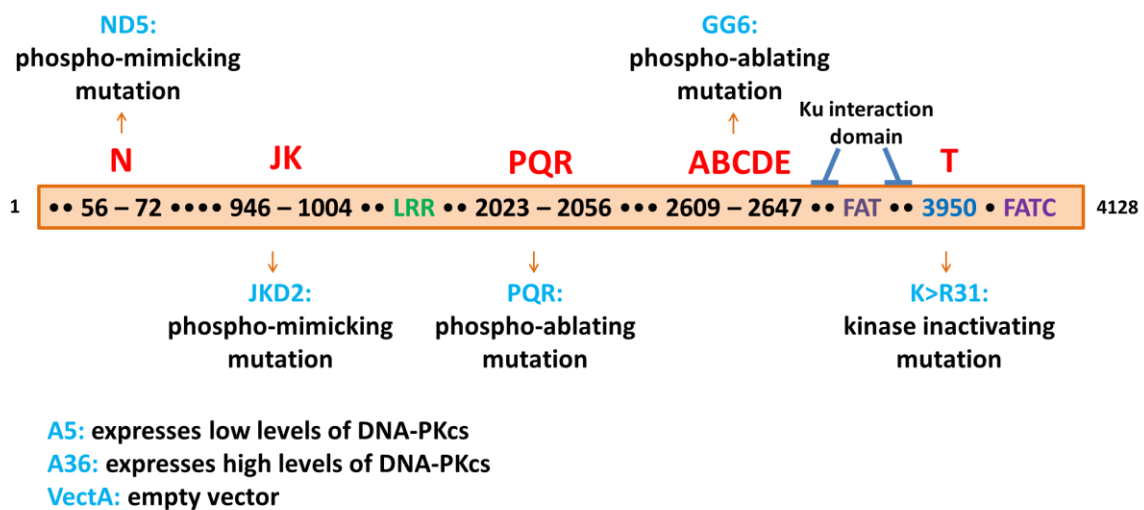


Figure 37. Schematic diagram of DNA-PKcs structure with major domains (red) and mutations in the corresponding CHO mutants (blue).

See text for more information. Figure adapted from Meek et al. 2008.

First of all, we standardized growth and serum deprivation conditions for V3 CHO cells in order to investigate growth state dependence of alt-EJ in DNA-PKcs mutants. We observed that 3 days of serum deprivation was sufficient to induce growth arrest in G₀/G₁ (Figure 38).

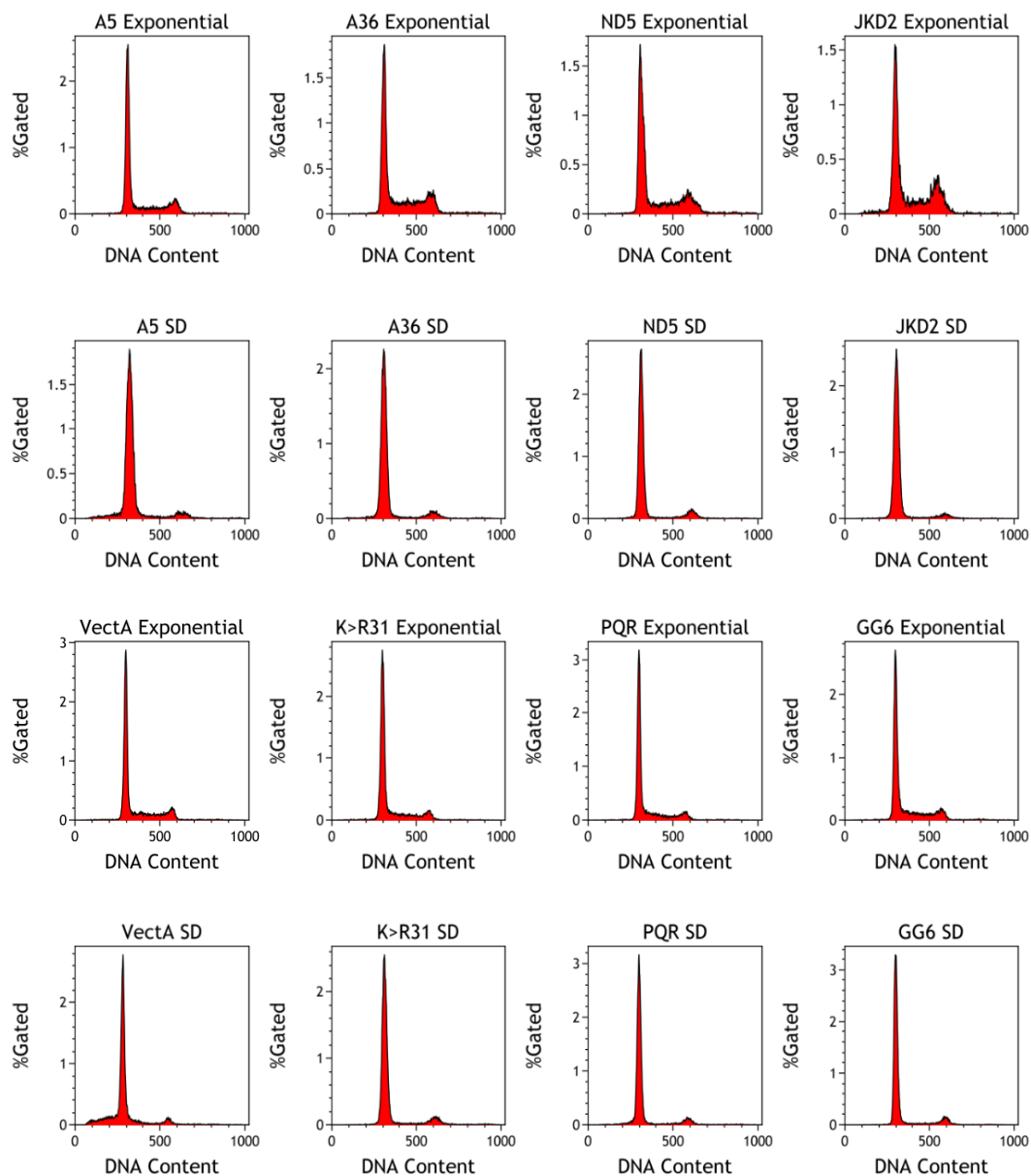


Figure 38. Cell cycle distribution of V3 CHO mutants in exponential and SD state.

Representative PI histograms indicate the DNA content of 1×10^4 cells measured by flow cytometry. Results shown are from one out of three independent experiments with similar results.

After standardizing growth conditions, we performed clonogenic survival assay to test the contribution of DNA-PKcs and its corresponding mutations (see Figure 37) to cellular radiosensitivity. We observed that A5, A36 and PQR cells were highly radioresistant in exponential, as well as in SD state. A5 and A36 cells express wild type DNA-PKcs in low and high levels, respectively. This finding showed that different levels of DNA-PKcs may not

influence radiosensitivity. PQR cells were suggested to have excessive DNA end resection activity, as opposite to GG6 cells that were suggested to have limited DNA end resection (Cui et al. 2005). We observed that GG6 cells were more radiosensitive than PQR cells, suggesting that DNA end resection may contribute to radioresistance. In both cell lines, radiosensitivity remained similar in exponential and SD state. ND5 cells that have very low kinase activity were relatively radiosensitive, however radiosensitivity was similar in exponential and SD state. Interestingly, JKD2 cells were more radiosensitive than ND5 cells and radiosensitivity increased in SD state, despite their wild type kinase activity. This finding suggests that in JKD2 cells DSB repair may be switched to alt-EJ, as it is growth state dependent. Moreover, this pathway switch may be independent of kinase activity of DNA-PKcs. Similar pattern was observed in VectA and K>R31 cells. VectA cells are deficient for DNA-PKcs and K>R31 lacks kinase activity. VectA and K>R31 cells were highly radiosensitive and radiosensitivity increased dramatically in SD state (Figure 39). This finding may confirm the growth state dependence of alt-EJ. However, we showed earlier that DNA-PKcs deficient cells repair DSBs induced by 20 Gy of IR independently of growth state (Figure 15, Figure 32). This discrepancy suggests that IR dose range may affect the response to DSBs. Previous studies from our laboratory have shown that contribution of HRR to DSB repair decreases with increasing IR dose (Demond 2016). Therefore, it is reasonable to assume that VectA and K>R31 cells may utilize HRR in exponential state upon low dose IR. However, another set of data from our laboratory has shown that, DSB repair in DNA-PKcs deficient MEFs markedly contributed to chromosome translocation formation (Soni et al. 2014). This finding is incompatible with the error-free nature of HRR and suggesting that repair may be operated by alt-EJ. However, further investigations are required to improve our understanding of the discrepancies between cellular responses to low and high dose IR.

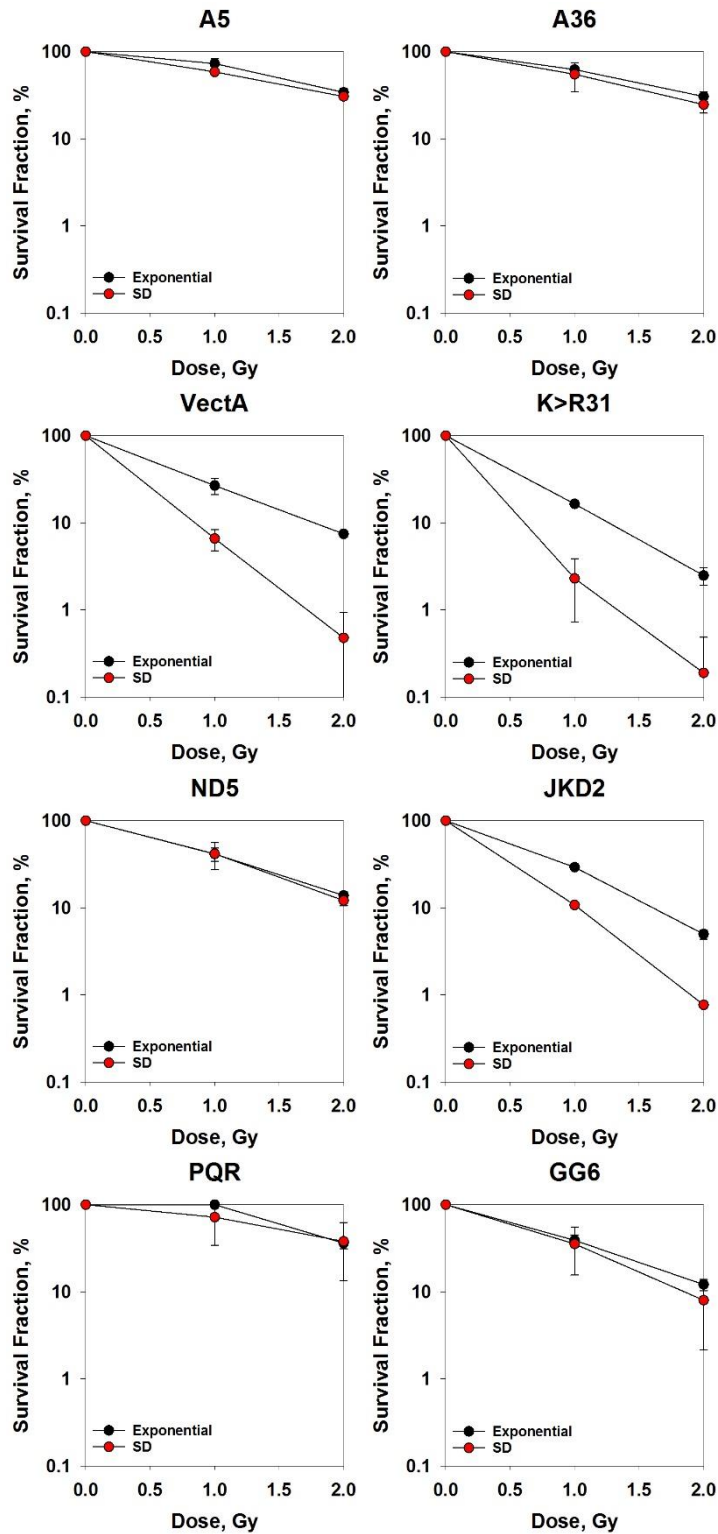


Figure 39. Survival curves of V3 CHO mutants in exponential and SD state.

Survival fraction was measured by clonogenic survival assay. Results shown are the average of two independent experiments and error bars represent standard deviation calculated from six determinations.

4.4.1. The effects of different DNA-PKcs levels on DSB repair

We measured the repair efficiency of two clones; A5, which express nearly normal levels of DNA-PKcs for CHO cells and A36, which express 20 fold higher levels of DNA-PKcs, similar to human cells. Both mutants repaired DSBs efficiently either in exponential or SD state, utilizing c-NHEJ (Figure 40).

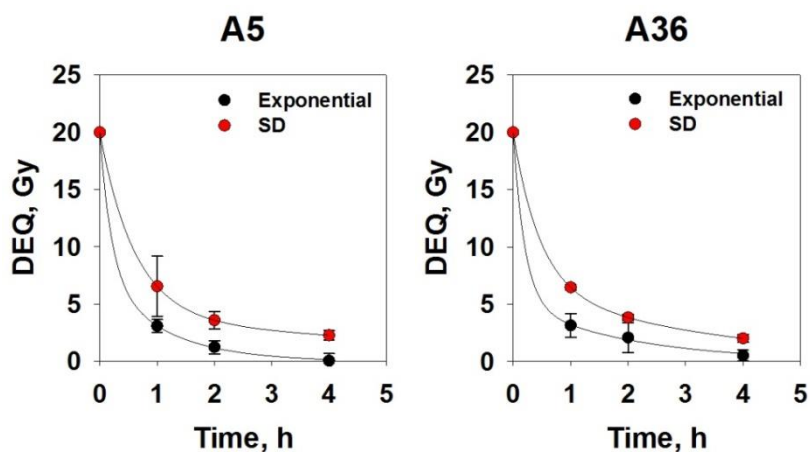


Figure 40. Repair kinetics of A5 and A36 cells in exponential and SD state.

DSB repair was measured by PFGE after 20 Gy of IR (A5: low levels of DNA-PKcs, A36: high levels of DNA-PKcs). Results shown are the average of two independent experiments and error bars represent standard deviation calculated from six determinations.

We also treated A5 and A36 cells with the DNA-PKcs inhibitor NU7441 in SD state in order to assess the role of DNA-PKcs abundance on alt-EJ. As seen in Figure 41, 5 μ M NU7441 treatment for 1 h only slightly decreased the repair efficiency in both cell lines. This finding suggests that upon inhibition of kinase activity, DNA-PKcs levels may not have an impact on alt-EJ efficiency.

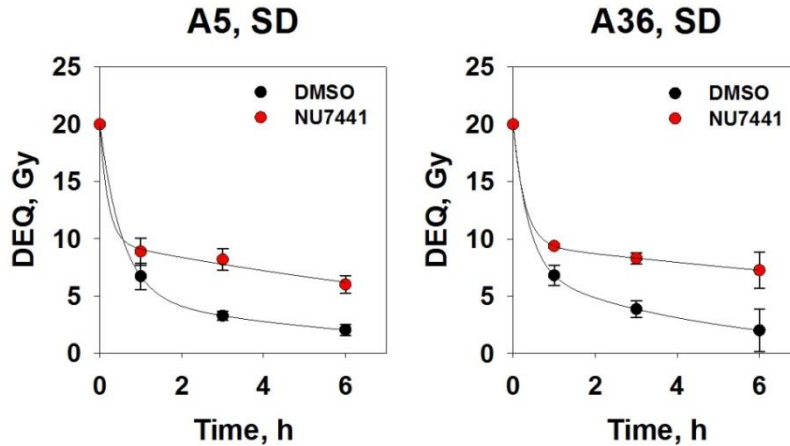


Figure 41. Repair kinetics of A5 and A36 cells in SD state treated with 5 μ M NU7441 for 1 h.

DSB repair was measured by PFGE after 20 Gy of IR following NU7441 treatment (A5: low levels of DNA-PKcs, A36: high levels of DNA-PKcs). DMSO was added to untreated controls. Results shown are the average of three independent experiments and error bars represent standard deviation calculated from nine determinations.

4.4.2. Different responses of DNA-PKcs knockout and kinase dead mutants

We next measured the repair efficiency of DNA-PKcs deficient (VectA) and kinase dead mutant (K>R31) in exponential and SD state. VectA cells showed similar repair efficiency regardless of growth state, confirming our data with DNA-PKcs^{-/-} MEFs as shown in chapter 4.1.2, Figure 15 and in chapter 4.3.2, Figure 32. Interestingly, the kinase dead mutant showed reduced repair efficiency in SD state (Figure 42). Different responses in DNA-PKcs deficiency and kinase inhibition may suggest a role for DNA-PKcs in DSB repair that is independent of kinase function.

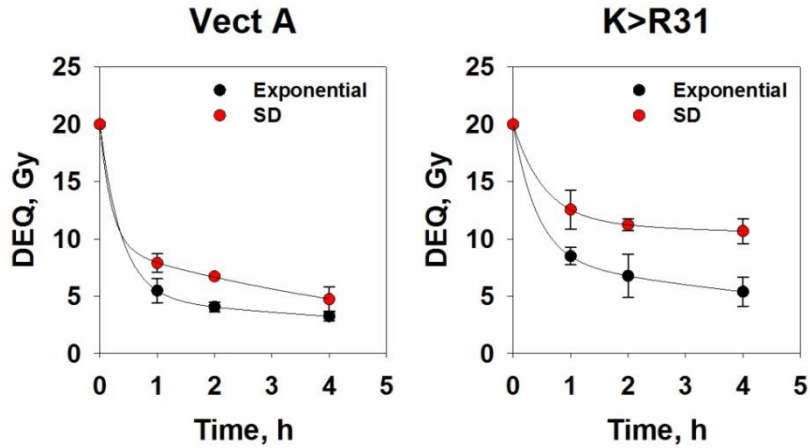


Figure 42. Repair kinetics of VectA and K>R31 cells in exponential and SD state.

DSB repair was measured by PFGE after 20 Gy of IR (VectA: empty vector, K>R31: kinase dead). Results shown are the average of three independent experiments and error bars represent standard deviation calculated from nine determinations.

To test whether NU7441 has a non-specific effect apart from inhibition of DNA-PKcs' kinase activity, we treated VectA and K>R31 cells with 5 μ M NU7441 for 1 h in SD state and measured the repair efficiency with PFGE. There was no additional effect of NU7441 on DNA-PKcs deficient or kinase dead mutants confirming the specificity of the inhibitor (Figure 43).

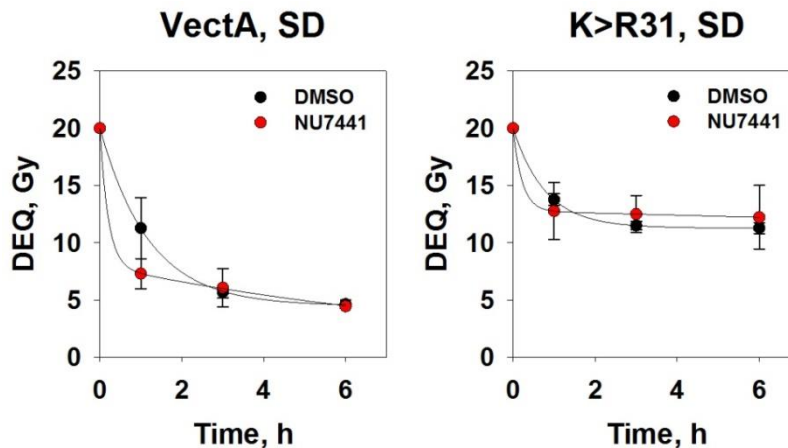


Figure 43. Repair kinetics of VectA and K>R31 cells in SD state treated with 5 μ M NU7441 for 1 h.

DSB repair was measured by PFGE after 20 Gy of IR following NU7441 treatment (VectA: empty vector, K>R31: kinase dead). DMSO was added to untreated controls. Results shown are the average of at least two independent experiments and error bars represent standard deviation calculated from six determinations.

4.4.3. The effects of phospho-mimicking mutations of DNA-PKcs on DSB repair

We measured the repair efficiency of two clones, ND5 and JKD2, which are phospho-mimicking forms of DNA-PKcs. The ND5 domain contains two conserved sites at the extreme N-terminus. This mutant interacts with Ku bound DNA and it has very low kinase activity. The JKD2 domain contains two completely conserved serine phosphorylation sites around amino acid 1000 from N-terminus; and this mutant retains wild type kinase activity (Singh 2010). In our PFGE experiments, we showed that ND5 cells repaired DSBs efficiently, either in exponential or SD state. JKD2 cells showed relatively slow repair kinetics in exponential state and repair efficiency decreased in SD state (Figure 44).

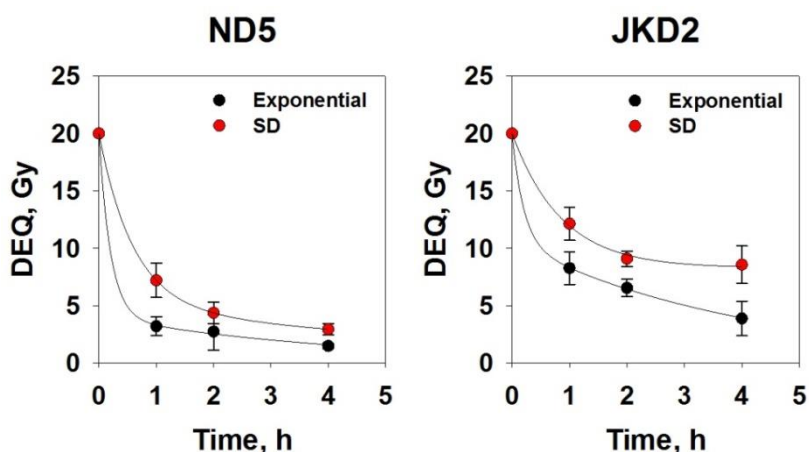


Figure 44. Repair kinetics of ND5 and JKD2 cells in exponential and SD state.

DSB repair was measured by PFGE after 20 Gy of IR (ND5: low kinase activity, JKD2: wild type kinase activity). Results shown are the average of three independent experiments and error bars represent standard deviation calculated from nine determinations.

We also treated ND5 and JKD2 mutants with the DNA-PKcs inhibitor NU7441 in exponential and SD state. Repair efficiency of both mutants was only very slightly affected by DNA-PKcs inhibition in exponential state. ND5 cells that have very low kinase activity showed reduction in repair upon DNA-PKcs inhibition. Interestingly, DNA-PKcs inhibition did not affect JKD2 cells that retain wild type kinase activity, in SD state (Figure 45). Slow repair kinetics and growth state dependence are typical features of alt-EJ. Along with the finding, which showed that JKD2 cells do not require DNA-PKcs for repair; these data may suggest that JKD2 phosphorylation plays an important role in the repair pathway choice between c-NHEJ and alt-

EJ. These hints are interesting mechanistic aspects of DNA-PKcs regulation and needs further elucidation.

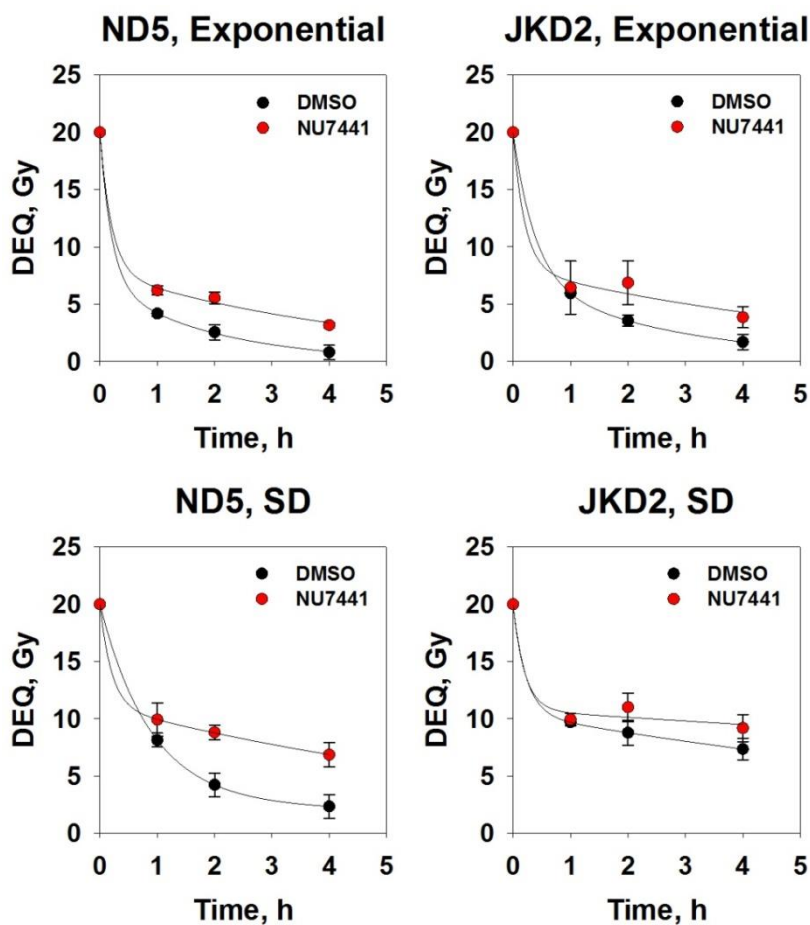


Figure 45. Repair kinetics of ND5 and JKD2 cells in exponential and SD state treated with 5 μ M NU7441 for 1 h.

DSB repair was measured by PFGE after 20 Gy of IR following NU7441 treatment (ND5: low kinase activity, JKD2: wild type kinase activity). DMSO was added to untreated controls. Results shown were obtained in one experiment and error bars represent standard deviation calculated from three determinations.

4.4.4. The effects of phospho-ablating mutations in the autophosphorylation sites of DNA-PKcs on DSB repair

We also measured the repair efficiency of two clones, PQR and GG6, which have serines and threonines substituted with alanine in PQR and ABCDE phosphorylation clusters, respectively. Autophosphorylation of PQR and ABCDE clusters is suggested to regulate DNA end resection in a reciprocal manner. While phosphorylation of the ABCDE cluster promotes DNA end

resection, phosphorylation of PQR cluster has an opposite effect. Alanine substitution in these clusters does not affect the kinase activity of DNA-PKcs, however DNA end resection is affected due to the inhibition of autophosphorylation (Cui et al. 2005). In our PFGE experiments, we observed that PQR cells repaired with similar efficiency in exponential and SD state, while GG6 cells showed only a very slight reduction in SD state (Figure 46).

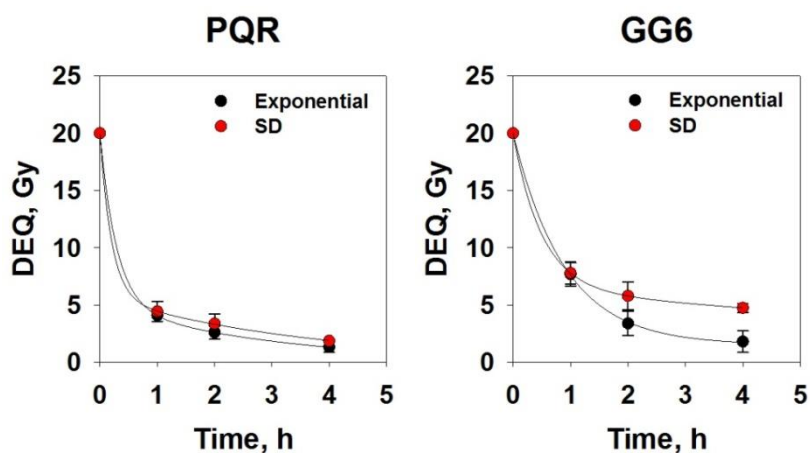


Figure 46. Repair kinetics of PQR and GG6 cells in exponential and SD state.

DSB repair was measured by PFGE after 20 Gy of IR (PQR: excessive DNA end resection, GG6: limited DNA end resection). Results shown are the average of three independent experiments and error bars represent standard deviation calculated from nine determinations.

We also treated PQR and GG6 cells with the DNA-PKcs inhibitor NU7441 in SD state. Interestingly, we found that repair efficiency of PQR cells was affected more dramatically compared to GG6 cells upon DNA-PKcs inhibition (Figure 47). Further experiments are required to elucidate whether this response is a consequence of different levels of DNA end resection activity or these autophosphorylation sites have additional roles in DSB repair pathways.

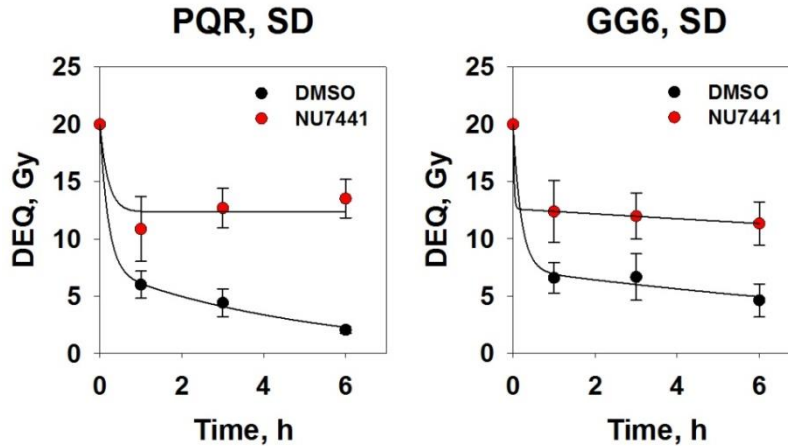


Figure 47. Repair kinetics of PQR and GG6 cells in SD state treated with 5 μ M NU7441 for 1 h.

DSB repair was measured by PFGE after 20 Gy of IR following NU7441 treatment (PQR: excessive DNA end resection, GG6: limited DNA end resection). DMSO was added to untreated controls. Results shown were obtained in one experiment and error bars represent standard deviation calculated from three determinations.

4.4.5. The role of DNA end resection in alt-EJ in DNA-PKcs mutants

Based on the previous data from our laboratory suggesting that DNA-PKcs deficiency is associated with enhanced DNA end resection (Dueva 2015), we measured DNA end resection in CHO cells expressing high levels of DNA-PKcs (A36), DNA-PKcs deficient (VectA), DNA-PKcs kinase dead mutant (K>R31) cell lines, along with PQR and ABCDE mutants with excessive and limited DNA end resection activity, PQR and GG6 cell lines, respectively (Cui et al. 2005). Similar to as explained in chapter 4.3.1, we measured RPA signal by flow cytometry to assess DNA end resection activity in 1, 3 and 6 h time points after 20 Gy of IR in exponential and SD state for each cell line. First, we showed the normalized RPA intensity, calculating the fold change between irradiated and non-irradiated samples from whole cell population. Similar to that observed in MEFs, DNA end resection activity was only detectable in exponential state, regardless of DNA-PKcs status. Neither DNA-PKcs deficient VectA cells, nor kinase dead mutant K>R31 cells showed DNA end resection activity in SD state. Similar to MEFs, in CHO cells, we were not able to correlate DNA-PKcs deficiency with increased DNA end resection activity. On the other hand, GG6 cells showed slightly lower rates of DNA end resection compared to other mutants, confirming that ABCDE site may be required for efficient DNA end resection (Figure 48).

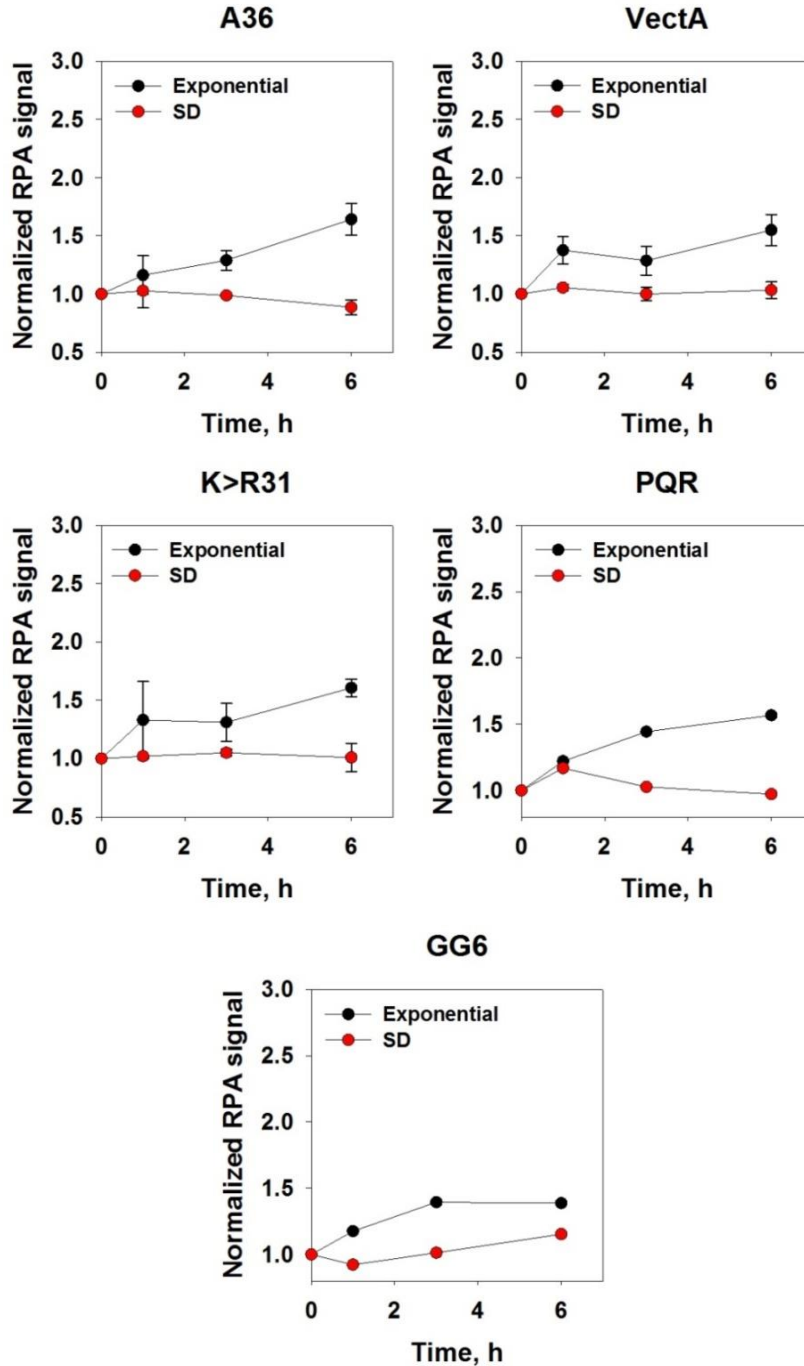


Figure 48. RPA levels induced by 20 Gy of IR in A36, VectA, K>R31, PQR and GG6 cells in exponential and SD state.

Graphs indicate fold change in the mean values of RPA signal in 5×10^4 cells measured by flow cytometry and normalized to the non-irradiated control samples. Quantitative data is the average of three independent experiments for A36 (high levels of DNA-PKcs), VectA (empty vector) and K>R31 (kinase dead) and error bars represent standard deviation. Quantitative data for PQR (excessive DNA end resection) and GG6 (limited DNA end resection) was obtained from one experiment. For the representative histogram plots see supplementary figures 20-24.

Flow cytometry histograms showed clearly separated peaks in RPA signal in exponential state, probably due to the formation of ssDNA during DNA replication in S and G₂ phases of the cell cycle and thus increased accumulation of RPA (Aylon et al. 2004, Zou et al. 2006, Daley and Sung 2014) (Supplementary figures 20-24). Interestingly, this separation was not prominent in MEF cells (Supplementary figures 1-5). This could be an interesting feature of MEFs, along with relatively lower rates of DNA end resection activity. However in order to rule out the possibility of different specificity of the antibody against mouse and CHO cells, further investigations are required. We gated G₁ and G₂ populations according to EdU incorporation and DNA content by combined EdU and PI staining, as described in chapter 3.2.6. We confirmed that G₁ and G₂ cells exhibited different levels of RPA signal. Similar to that observed in MEFs, not only in G₂, but also in G₁ phase of an exponential cell population, DNA end resection was detectable; however this was not restricted to DNA-PKcs deficient cells (Figure 49). Slightly lower rates of DNA end resection was observed in G₂ gated GG6 cells compared to G₂ gated PQR cells in exponential state, similar to that observed in whole cell population (Figure 50). As there was no detectable DNA end resection activity in SD state in any of the cell lines, except for G₂ gated GG6 cells with only a moderate DNA end resection activity, which presumably arose from inefficient growth arrest (Figure 51 and supplementary figure 34); we were not able to correlate the DNA end resection with repair efficiency of these cells in SD state. Although it is not surprising that lack of DNA end resection in SD state has no impact on the repair efficiency of A36, PQR and GG6 cell lines, as DSB repair is carried out by c-NHEJ, the observations regarding DSB repair in VectA cells that rely on alt-EJ regardless of growth state, cannot be linked to DNA end resection based on the results shown in Figure 48.

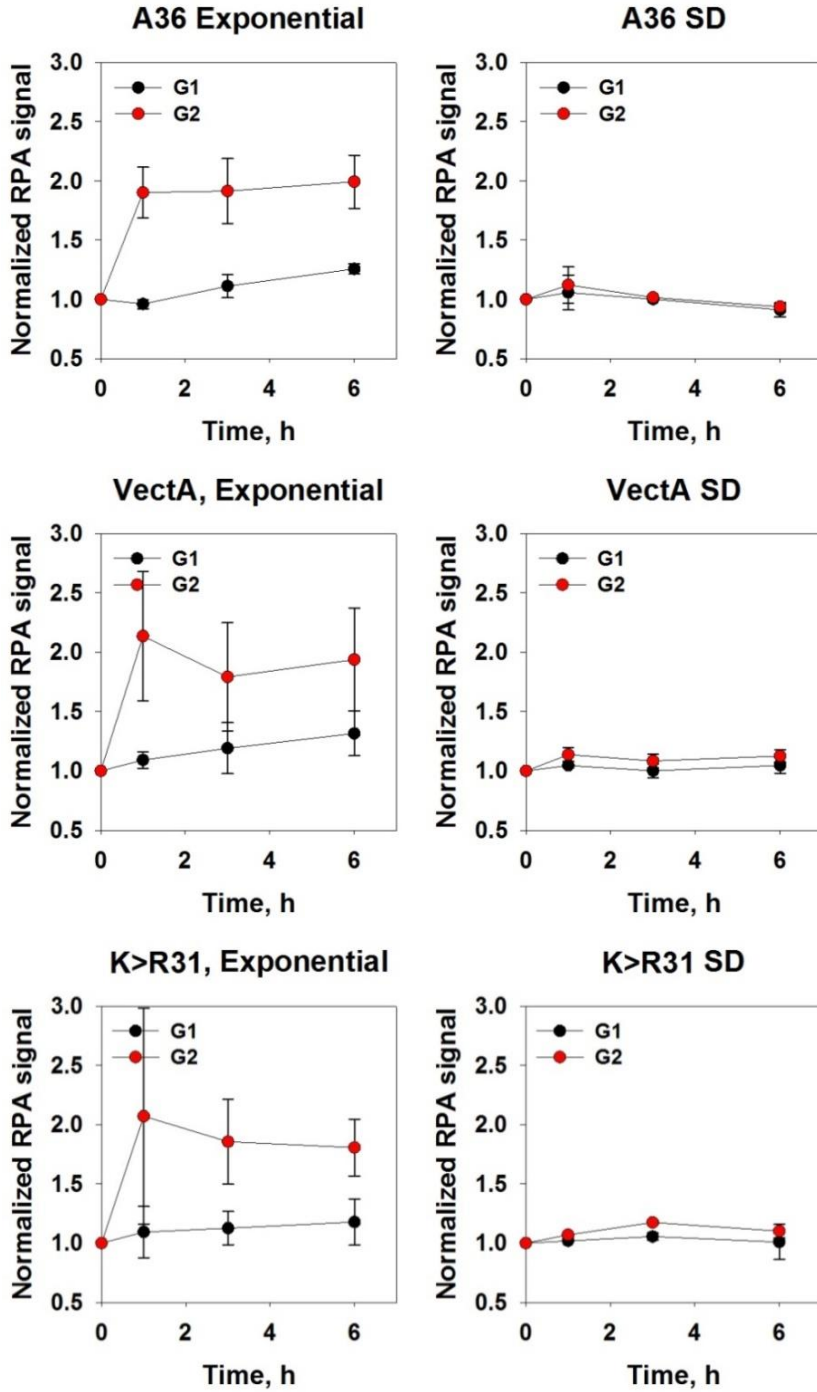


Figure 49. RPA levels induced by 20 Gy of IR in G₁ and G₂ phases in A36, VectA and K>R31 cells in exponential and SD state.

Graphs indicate fold change in the mean values of RPA signal in the gated cell populations according to combined EdU and PI staining (see supplementary figures 25-30). Quantitative data is the average of three independent experiments and error bars represent standard deviation.

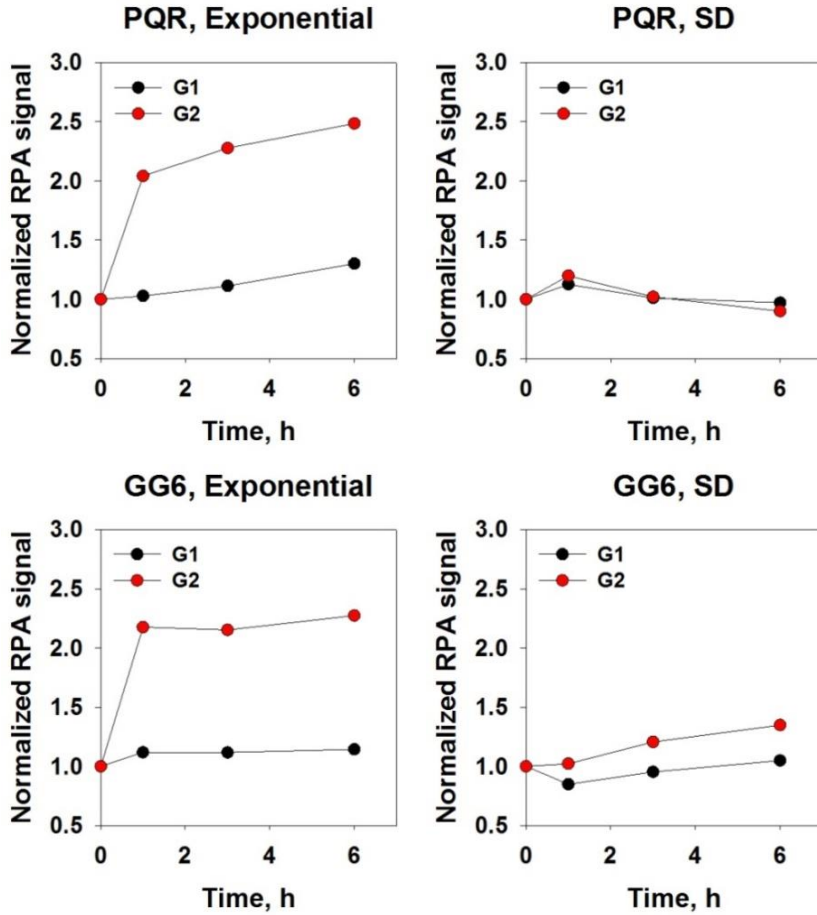


Figure 50. RPA levels induced by 20 Gy of IR in G₁ and G₂ phases in PQR and GG6 cells in exponential and SD state.

Graphs indicate fold change in the mean values of RPA signal in the gated cell populations according to combined EdU and PI staining (see supplementary figures 31-34). Quantitative data was obtained from one experiment.

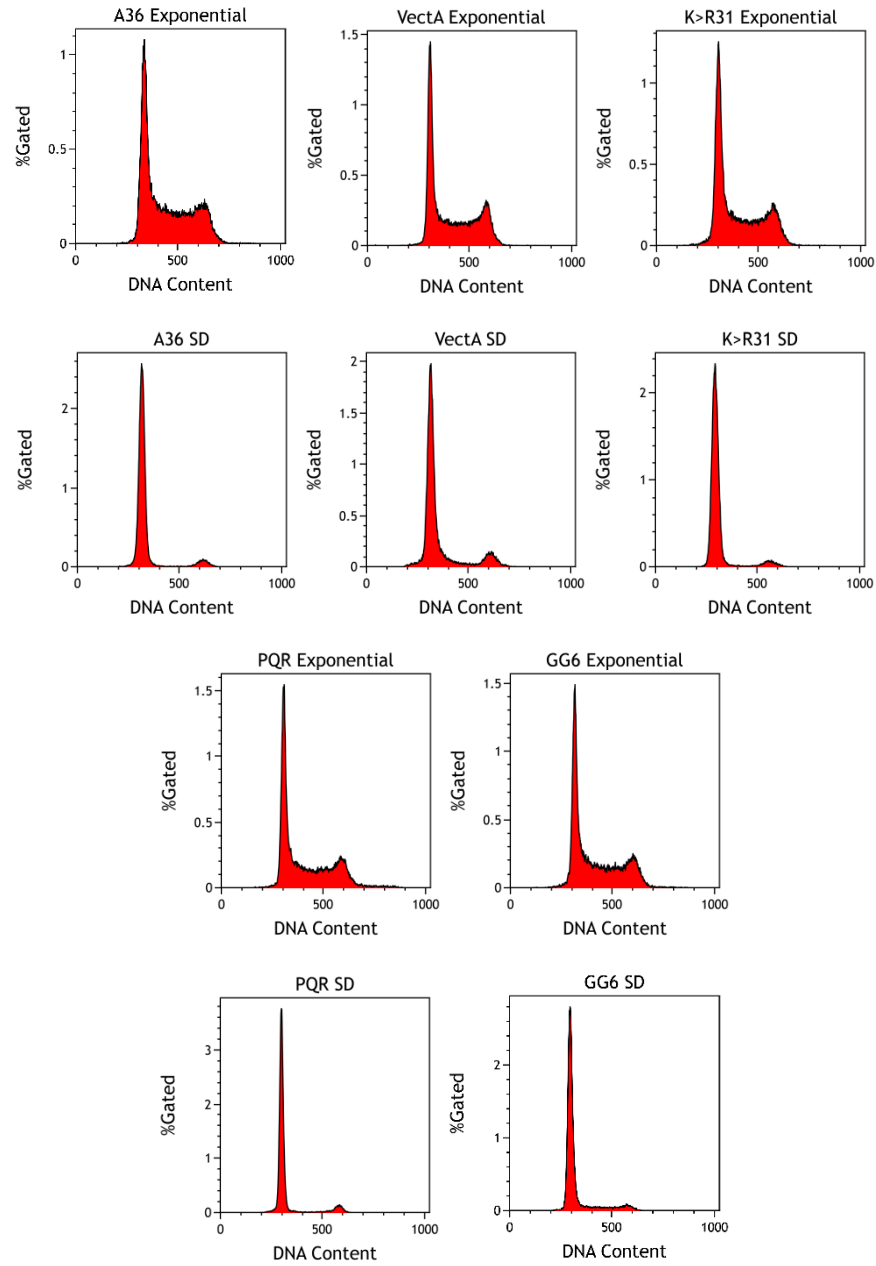


Figure 51. Cell cycle distribution of A36, VectA, K>R31, PQR and GG6 cells in exponential and SD state. Representative PI histograms indicate the DNA content for CHO cells that were shown in Figure 49 and Figure 50.

4.5. The role of 53BP1 in DSB repair pathway choice

53BP1 is known as a positive regulator of c-NHEJ by protecting DSBs from DNA end resection mediated by BRCA1 (Huertas 2010, Bunting et al. 2010, Liu and Huang 2016). Recent studies

suggested that, abrogated 53BP1 dependent end protection can stimulate BRCA1/CtIP dependent DNA end resection and switches the repair to alt-EJ in G₁ cells (Xiong et al. 2015, Bakr et al. 2016). These findings were in line with our hypothesis that DNA end resection may promote alt-EJ as stated in chapter 4.3.1. In order to confirm these data and test our hypothesis, we utilized 53BP1 deficient mouse embryonic stem cells (mESC) and measured the repair kinetics in the exponential and SD state. As expected, WT cells repaired with similar efficiency in exponential and SD state. In 53BP1^{-/-} cells, repair was moderately abrogated in SD state (Figure 52). However the PI histograms showed that the growth arrest was inefficient even after 5 days of serum deprivation (Figure 53).

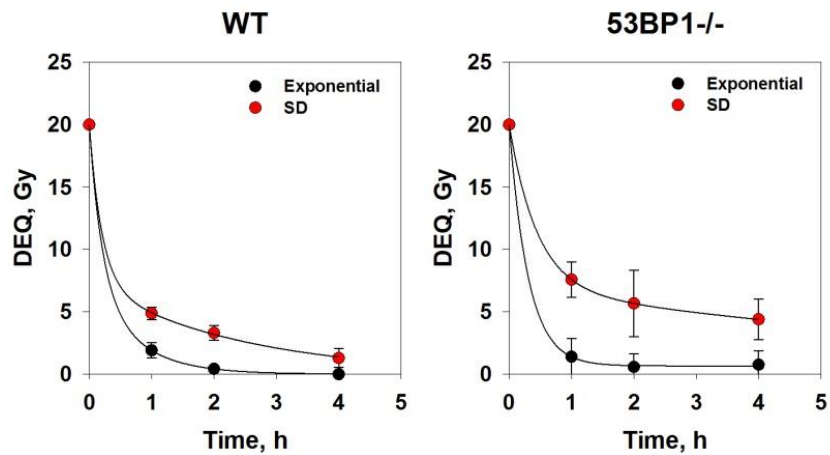


Figure 52. Repair kinetics of WT and 53BP1^{-/-} mESCs in exponential and SD state.

DSB repair was measured by PFGE after 20 Gy of IR. Results shown are the average of two independent experiments and error bars represent standard deviation calculated from eight determinations.

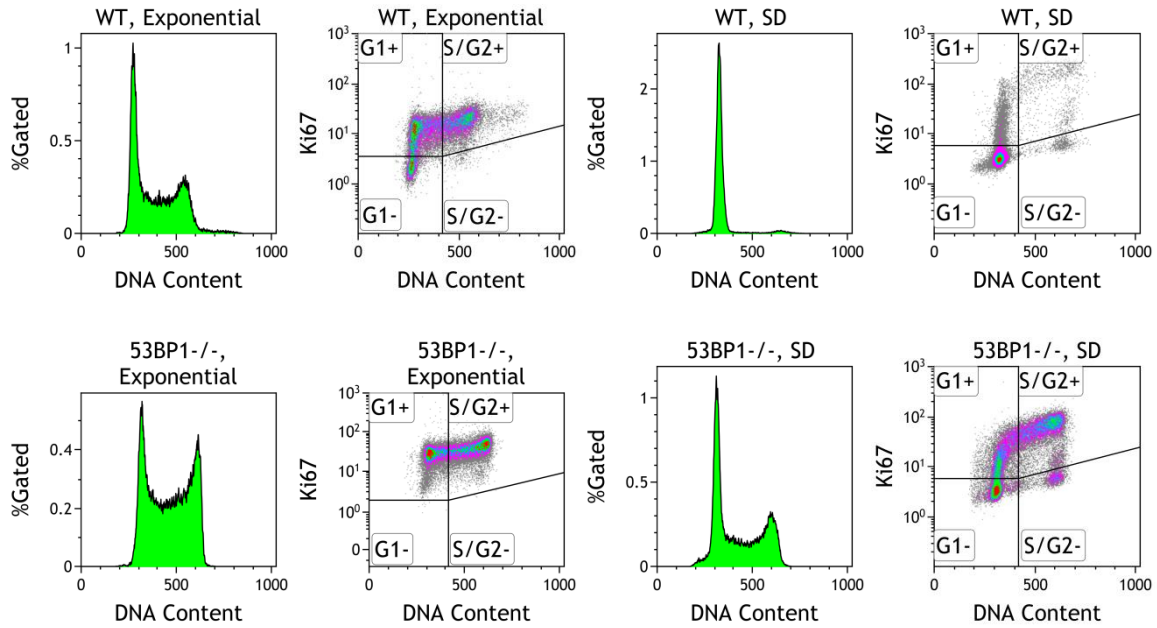


Figure 53. Cell cycle distribution and Ki67 levels in WT and 53BP1^{-/-} mESCs.

Representative PI histograms indicate the DNA content for mESCs that were shown in Figure 52. Dot plots indicate the distribution of Ki67 signal in 5×10^4 cells measured by flow cytometry. Gates were defined according to unstained negative controls.

Unlike $Ku80^{-/-}$ cells that showed dramatically abrogated repair efficiency upon serum deprivation despite inefficient growth arrest (see chapter 4.3.2), 53BP1^{-/-} cells repaired with high efficiency in the absence of serum. In order to investigate the efficiency of c-NHEJ and alt-EJ under these conditions, we treated cells with NU7441 to inhibit DNA-PKcs, thus c-NHEJ. Although, repair efficiency was slightly abrogated in exponential state upon 5 μ M NU7441 treatment for 1 h; in SD state we observed a dramatic abrogation of repair (Figure 54). These findings suggested that the repair in 53BP1^{-/-} cells is operated by c-NHEJ as it is DNA-PKcs dependent. Unexpectedly, 53BP1 deficiency did not rescue the abrogated alt-EJ when DNA-PKcs was inhibited. Moreover, repair abrogation in the absence of serum, despite the inefficient growth arrest was in line with our previous results with $Ku80^{-/-}$ cells (chapter 4.3.2), suggesting the importance of growth factors.

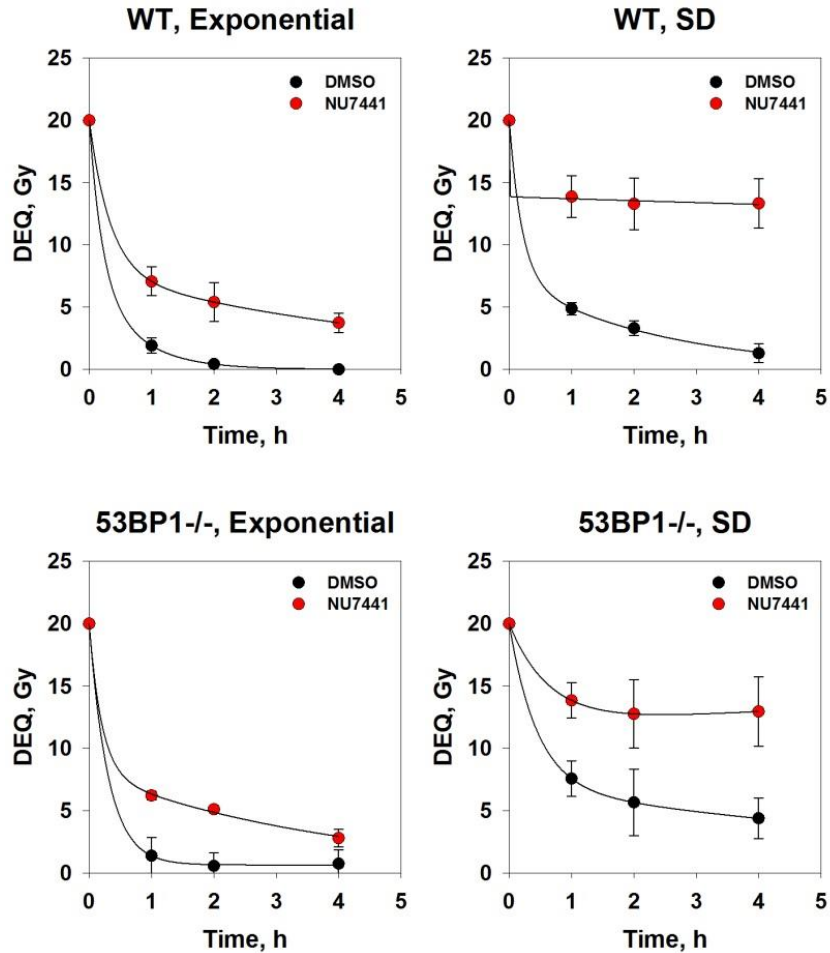


Figure 54. Repair kinetics of WT and 53BP1^{-/-} mESCs in exponential and SD state treated with 5 μ M NU7441 for 1 h.

DSB repair was measured by PFGE after 20 Gy of IR following NU7441 treatment. DMSO was added to untreated controls. Results shown are the average of three independent experiments and error bars represent standard deviation calculated from twelve determinations.

We next measured DNA end resection in WT and 53BP1^{-/-} mESCs in exponential and SD state in 1, 3 and 6 h time points following 20 Gy of IR. As seen in Figure 55, WT cells showed detectable DNA end resection activity only in the exponential phase of growth. However, in 53BP1^{-/-} cells, we observed relatively lower but detectable DNA end resection activity in SD

state, as well. Similar to $Ku80^{-/-}$ cells in SD state (chapter 4.3.1), this resection activity could also be attributed to the inefficient growth arrest as seen in the PI histograms in Figure 56.

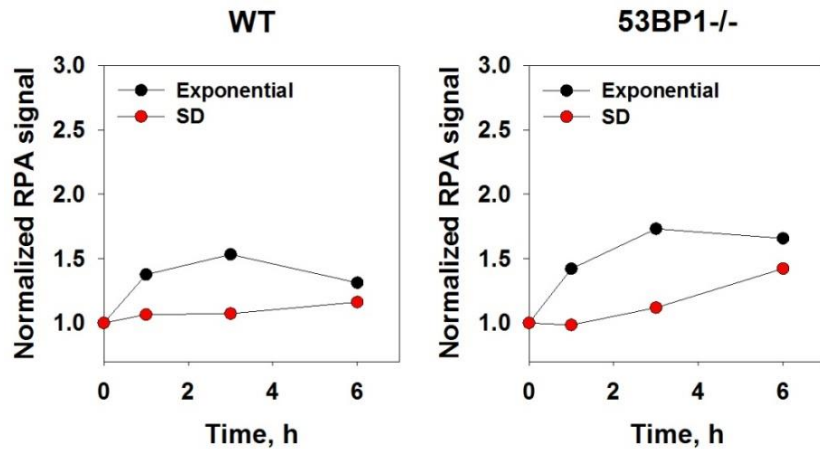


Figure 55. RPA levels induced by 20 Gy of IR in WT and 53BP1^{-/-} mESCs in exponential and SD state. Graphs indicate fold change in the mean values of RPA signal in 5×10^4 cells measured by flow cytometry and normalized to the non-irradiated control samples. Quantitative data was obtained from one experiment. For the representative flow cytometric histograms see supplementary figures 35-36.

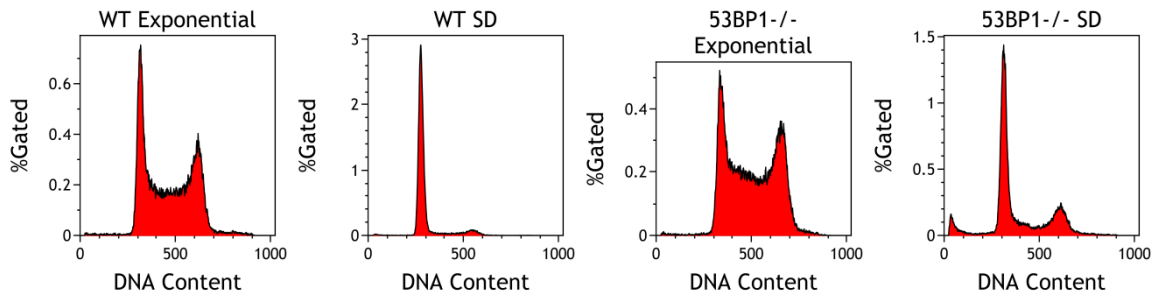


Figure 56. Cell cycle distribution of WT and 53BP1^{-/-} mESCs in exponential and SD state. Representative PI histograms indicate the DNA content for mESCs that were shown in Figure 55.

Similar to our findings from previous chapters, under the experimental conditions applied here, we were not able to correlate DNA end resection with growth state dependent feature of alt-EJ. It is very reasonable to speculate that the detectable DNA end resection measured in proliferating G₁ cells contributes to alt-EJ, and that the enhanced alt-EJ activity in G₂ could be explained by higher rates of DNA end resection in this phase of the cell cycle. Although downregulation of DNA end resection in G₀ could also explain the abrogation of alt-EJ, however similar repair efficiency of DNA-PKcs^{-/-} cells irrespectively of growth state could not be linked to DNA end resection according to our observations.

5. DISCUSSION

5.1. Global chromatin relaxation is not sufficient to promote alt-EJ in quiescent cells

DNA DSBs can arise from a variety of exogenous and endogenous sources. IR is one of the most important factors that can induce DSBs directly by energy deposition and indirectly by the generation of reactive oxygen species (ROS) (O'Driscoll and Jeggo 2006). Organisms have evolved sophisticated mechanisms to faithfully repair DSBs in order to protect genome integrity. Two main DSB repair pathways NHEJ and HRR have been extensively studied since many years; however how cells decide in the repair pathway choice is still a matter of debate (Kakaroukas and Jeggo 2014). In addition, the presence of a third pathway referred to as alternative end joining (alt-EJ) has been shown; however the mechanistic underpinnings of this pathway remain to be elucidated (Iliakis et al. 2004, Bennardo et al. 2008, Chiruvella et al. 2013, Dueva 2013, Frit et al. 2014). In this study, we focused on chromatin structure and DNA end resection as two potential parameters in the mechanistic regulation of alt-EJ.

We monitored alt-EJ activity in c-NHEJ mutant cell lines irradiated with 20 Gy of IR. Previous data from our laboratory has shown that in the repair of DSBs, the contribution of HRR is decreasing with the increasing dose of IR. Rad51 foci formation was measured in the late S and G₂ phases as an indicator of HRR and it was observed that Rad51 foci reach a maximum level at approximately 4 Gy and remain in plateau at higher doses. Moreover, the contribution of HRR in DSB repair of heterochromatic regions was found to be relatively low, suggesting that the chromatin structure may play an important role in DSB repair pathway choice (Kakaroukas and Jeggo 2014, Yao 2014, Demond 2016).

It has also been shown that repair kinetics in c-NHEJ deficient cells irradiated with high dose IR remain similar when these cells are also depleted for the genes of Rad52 epistasis group, which play a central role in HRR (Wang et al. 2001, Symington 2002). Along these lines, data from our laboratory has also shown that Lig4^{-/-} Rad54^{-/-} double mutant MEFs repair DSBs as efficiently as Lig4^{-/-} MEFs suggesting HRR does not contribute in the repair of DSBs induced by 20 Gy of IR (Wu et al. 2008). Another set of data from our laboratory has shown that CHO cells with mutations in the Rad51 paralogues XRCC2 and XRCC3 showed similar repair

kinetics with their WT counterparts, regardless of the cell cycle phase (Windhofer et al. 2007). Based on these findings we expected only a small contribution of HRR to the repair of DSBs induced by 20 Gy, and performed the experiments described here to monitor alt-EJ in c-NHEJ deficient cell lines. It is known that HRR is strictly cell cycle dependent and only active in late S and G₂ phases due to the requirement of a homologous sister chromatid (Hall and Giaccia 2006), while c-NHEJ is active throughout the cell cycle (Mladenov and Iliakis 2011). Wu et al. also showed that in CHO cells with mutations in Ku80 and DNA-PKcs, alt-EJ is active throughout the cell cycle; however, its activity is enhanced in G₂ phase (Wu et al. 2008).

As the vast majority of cells in human body is in a non-cycling quiescent state (Gerdes et al. 1983, Srivastava et al. 2010), in this study we focused on DSB repair in the quiescent state, often termed as G₀ cells. Using Ki67 as a widely accepted proliferation marker, we distinguished cycling (G₁, S and G₂) cells from putative G₀ cells (Figure 12) (Scholzen and Gerdes 2000, Falk et al. 2010, Sun and Kaufman 2018). Using WT MEFs we confirmed that c-NHEJ operates independently of growth state and repair efficiency in G₀ cells is similar to that of cycling cells. However, c-NHEJ mutant cells, with the exception of DNA-PKcs mutant, showed a strong growth state dependence and complete abrogation of repair in G₀ state, confirming previous findings (Figure 15) (Windhofer et al. 2007, Singh 2010, Mladenov et al. 2013).

Since many years, it has been accepted that DSB formation induces alterations in chromatin structure. Formation of γ H2AX foci with phosphorylation of histone variant H2AX at S139 residue by PIKK family members is the most intriguing example of alterations in the chromatin upon DSB formation. This modification is required to recruit DDR signaling and repair proteins at the site of DSBs and amplify the response signal (Elia and Bradley 1992, Kinner et al. 2008, Löbrich et al. 2010, Mah et al. 2010, Turinetto et al. 2015). It has also been shown that euchromatic regions, known as gene-rich and transcriptionally active, show higher sensitivity to DSB formation and higher occurrence of translocations (Folle et al. 1998, Feng et al. 2016). Previous data from our laboratory has also confirmed these findings, showing lower rates of γ H2AX foci formation in H3K9me3 positive regions as compared to H3K9me3 negative regions, indicating heterochromatic and euchromatic regions, respectively (Demond 2016).

Sensitivity of euchromatic regions to DSB formation is most likely a consequence of higher accessibility of the chromatin due to relaxed and open structure in these regions. Therefore, it is reasonable to expect that chromatin relaxation would facilitate DSB repair. It has been also shown by a wide range of studies that upon DSB formation, many chromatin remodeling factors and histone modifying enzymes act to promote chromatin relaxation and thus the accessibility of broken DNA ends (Ziv et al. 2006, Goodarzi et al. 2008, Srivastava et al. 2010, Cann and Dellaire 2011, Price and D'Andrea 2013). With such a great impact on DSB repair, chromatin structure was the first candidate to explain the growth state dependence of alt-EJ. It has been shown that quiescent cells typically have heterochromatic nuclei along with lower rates of transcription and metabolic activity. Given the importance of the chromatin structure, we hypothesized therefore that compact chromatin in G_0 cells may represent a barrier to alt-EJ (Tokuyasu et al. 1968, Sawicki 1979, Srivastava et al. 2010, Hauer and Gasser 2017).

First of all, we aimed to confirm the compact chromatin structure in G_0 state in MEFs. We measured levels of H3K9me3 as heterochromatin marker and H3K9Ac as euchromatin marker. We acquired G_0 -enriched cells with serum deprivation and compared the levels of these histone markers in exponential and SD state. While we could detect a statistically significant increase in H3K9me3 levels in SD cells, in line with the expected more compact chromatin structure, we were not able to detect a reciprocal correlation in H3K9Ac levels. Instead, H3K9Ac levels showed a slight increase in SD state; however this increase was negligible and it did not reach a statistical significance (Figure 19). Although it has been reported that modifications in different histone residues might be linked together such as H4K16 acetylation and H3S10 phosphorylation or H2B ubiquitination and H3K4 methylation, there is no evidence in the literature suggesting that H3K9 methylation and acetylation antagonize each other (Suganuma and Workman 2008, Lee et al. 2010, Bannister and Kouzarides 2011). An early study reported that in mitotic cells H3K9Ac levels decreased, while H3K9me3 levels increased. On the other hand, they stated that acetylation and methylation at H3K9 could not be simultaneously modified (Park et al. 2011). In view of these findings, our results are not surprising.

Furthermore, we applied a variety of treatments to induce chromatin relaxation in SD cells. It was previously reported that osmolarity of the environment influences the global chromatin

structure, and that hypotonic salt conditions induce global unfolding of the total nuclear chromatin (Klásterská and Ramel 1979, Delpire et al. 1985, Falk et al. 2008, Irianto et al. 2013, Lima et al. 2018). Therefore, we employed hypotonic treatment, which is acquired by dilution of the normal growth medium with dH₂O in 1:1 ratio and incubation of cells for 24 h. As it was reported that the osmotic alterations affect the folding of the global chromatin, it was not surprising that H3K9me3 and H3K9Ac levels, which are associated more with local changes in chromatin structure, were not influenced by this treatment. However, 24 h hypotonic treatment did not rescue the abrogated repair in Lig4^{-/-} SD cells. On the contrary, there was a slight reduction in repair efficiency of Lig4^{-/-} SD cells upon hypotonic treatment, and this reduction was more prominent in the exponential state of growth (Figure 20). Concerning the rapid and reversible effects of the hypotonic treatment (Falk et al. 2008, Irianto et al. 2013), we also employed a post-IR treatment, which involves the administration of pre-warmed hypotonic medium immediately after 20 Gy of IR was given. However, here again, there was no promotion of abrogated repair in Lig4^{-/-} SD cells (Figure 21).

Next, we employed a potent DNA methyltransferase inhibitor, 5'-aza-2'-deoxycytidine (AzadC) treatment. As DNA methylation is known to promote chromatin compaction, we aimed to inhibit DNA methylation and thus induce chromatin relaxation (Karymov et al. 2001, Christman 2002, Collings et al. 2013). First, we measured H3K9me3 levels in Lig4^{-/-} cells in exponential and SD state following incubation with AzadC. We expected that chromatin relaxation induced by inhibition of DNA methylation would impact overall chromatin compaction and thus heterochromatin markers. Although many studies suggested a cross-talk between chromatin compaction and histone methylation (Fischle 2008, Du et al. 2015, Duraisamy et al. 2017), our results showed that H3K9me3 levels increased upon AzadC treatment in both exponential and SD state cells. Interestingly, Komashko and Farnham also showed that 5-azacytidine induced a global increase in H3K9me3 and H3K27me3 levels, despite the specific loss of these markers from the promoters of the genes they investigated. Based on these findings they suggested that modified histones are not simply lost from chromatin, but rather they localize to different regions (Komashko and Farnham 2010). Nevertheless, we deprived Lig4^{-/-} cells of serum and simultaneously treated with AzadC. In this way, we allowed cells to progress through S phase before accumulating in G₀/G₁, allowing AzadC incorporation into DNA (Stresemann and Lyko

2008). However, AzadC treatment did not rescue the abrogated alt-EJ in Lig4^{-/-} cells (Figure 23).

Finally, we applied Trichostatin A (TSA) treatment, as it is a well-known HDAC inhibitor and HDAC inhibitors are known to induce chromatin relaxation by increasing the levels of histone acetylation (Tóth et al. 2004, Görisch et al. 2005, Shogren-Knaak et al. 2006, Lee et al. 2007, Carrier 2013). TSA treatment induced hyperacetylation of H3K9 in Lig4^{-/-} MEFs and WT controls in both exponential and SD state (Figure 24); however, neither in exponential nor in SD state was repair efficiency influenced by continuous treatment with TSA for 12 h (Figure 25). We also tested the durability of hyperacetylation effect of TSA in Lig4^{-/-} MEFs with or without 20 Gy of IR. Cells remained in the hyperacetylated state up to 12 h suggesting that the effect of TSA is not reversible within the duration of PFGE experiment (Figure 26). Nevertheless, neither increasing concentrations of TSA, nor 72 h treatment with Valproic acid, which is another global HDAC inhibitor, alone or in combination with TSA, influenced the abrogated alt-EJ in Lig4^{-/-} MEFs in SD state (Figure 27 and Figure 28). Our findings confirmed previously published data from our laboratory reporting that TSA induced hyperacetylation did not affect the kinetics of alt-EJ in Lig4^{-/-} MEFs, as well as Lig4^{-/-} human HCT116 cells or the human glioma cell line M059K treated with DNA-PKcs inhibitor Wortmannin (Manova et al. 2012).

In conclusion, under the experimental conditions applied here, we were not able to establish a link between chromatin relaxation induced by hypotonic treatment, inhibition of DNA methylation or inhibition of HDACs and the growth state dependent modulation of alt-EJ. However, one can question the efficiency of hypotonic treatment, as well as of AzadC treatment, to provoke the expected chromatin relaxation, as we were not able to confirm in every case the expected alterations in the chromatin structure. Nevertheless, we could clearly show that upon TSA treatment, histone H3K9 is hyperacetylated signifying chromatin relaxation. However, neither in exponential nor in SD state, is alt-EJ affected by TSA treatment. Our results suggest that parameters beyond global chromatin structure that can be altered by these treatments determine the growth state dependence of alt-EJ. Therefore, we focused next on the unique response of DNA-PKcs^{-/-} cells, as they repair with similar efficiency irrespectively of growth

state, unlike other c-NHEJ mutants. We also investigated the potential role of DNA end resection in this response.

5.2. Rescued alt-EJ in quiescence by DNA-PKcs deficiency may not be related to DNA end resection in rodent cells

Previous data from our laboratory has shown that the DNA-PKcs deficient cell line, M059J, exhibited dramatically higher number of RPA foci upon 4 Gy of IR in G₂, compared to their DNA-PKcs proficient counterparts, suggesting an excessive DNA end resection activity (Dueva 2015). This finding may suggest that DNA-PKcs suppresses DNA end resection in G₂. Therefore, we hypothesized that DNA-PKcs^{-/-} cells may retain DNA end resection activity in SD state and for this reason they may be able to perform alt-EJ, in contrast to other c-NHEJ mutants. We measured DNA end resection upon 20 Gy of IR at 1, 3 and 6 h in Lig4^{-/-} and DNA-PKcs^{-/-} MEFs along with WT controls. However, in all tested cell lines, DNA end resection was detectable only in exponential state and especially at the 6 h time point (Figure 29), which could be attributed to accumulation of cells in G₂ due to the IR induced G₂ checkpoint (Dueva 2015). On the other hand, our preliminary results showed that there was a detectable DNA end resection activity in G₁ phase of the cell cycle, and this activity was not restricted to DNA-PKcs deficient cells (supplementary figures 6-15). Moreover, we investigated DNA end resection in Ku80^{-/-} DNA-PKcs^{-/-} double mutant cells along with Ku80^{-/-} single mutants in order to assess the potential suppressor function of DNA-PKcs in a different c-NHEJ mutant. However, similar to other c-NHEJ mutants, DNA end resection was detectable and relatively higher only in the exponential phase of growth in Ku80^{-/-} DNA-PKcs^{-/-} double mutants (Figure 29). On the other hand, we observed that Ku80^{-/-} cells had detectable DNA end resection not only in the exponential, but also in the SD state (Figure 29), which could simply be explained by inefficient growth arrest despite 3 days of serum deprivation (Figure 30). Except for Ku80^{-/-} cells, none of the mutants showed a detectable DNA end resection in SD state. We also measured CtIP levels in Lig4^{-/-} and DNA-PKcs^{-/-} MEFs along with WT controls, as CtIP plays a regulatory role in DNA end resection and thus in alt-EJ (Lee-Theilen et al. 2011, Truong et al. 2013, Mladenov et al. 2013, Bakr et al. 2016). Consistent with results showing no detectable DNA end resection in SD state, CtIP was found to be significantly low in SD cells, with or without 20 Gy of IR (Figure

31). Our findings confirmed previously reported data showing that low CtIP expression in G₀ and early G₁ cells is enhanced as cells progress into the cell cycle (Liu and Lee 2006). These results may suggest that growth state dependence of alt-EJ is DNA end resection dependent, as it is downregulated while cells are in SD state. However, functioning of alt-EJ irrespectively of growth state in DNA-PKcs deficient cells cannot be explained by DNA end resection. Therefore, we placed more emphasis on DNA-PKcs deficiency and assessed the repair kinetics of Ku80^{-/-} DNA-PKcs^{-/-} double mutant, as we expected that in the absence of DNA-PKcs, alt-EJ would be promoted in a c-NHEJ deficient system. However, in the Ku80^{-/-} DNA-PKcs^{-/-} double mutant cells, the Ku80 deficient phenotype was dominant as the repair was abrogated in SD state, similar to what we observed in the Ku80^{-/-} single mutant (Figure 32). Consistent with our previous findings, SD state DNA-PKcs^{-/-} cells showed slightly slower but efficient repair, whereas the Ku80^{-/-} DNA-PKcs^{-/-} double mutant and the Ku80^{-/-} single mutant showed dramatically abrogated repair. One intriguing finding here was that despite the inefficient growth arrest and detectable DNA end resection in SD state, in Ku80^{-/-} cells, alt-EJ was abrogated. This finding suggests that, growth factors may be required for alt-EJ to perform its action, in addition to the general exponential growth state conditions and DNA end resection.

Although, DNA-PKcs is one of the central components of NHEJ, it was also suggested that c-NHEJ can operate independently of DNA-PKcs (Iliakis et al. 2004, Dobbs et al. 2010, Hendrickson et al. 2010, Davis et al. 2014, Dong et al. 2017). In order to examine this possibility, we performed PFGE experiments to confirm that DNA-PKcs deficient cells repair via alt-EJ, as efficiently as other c-NHEJ mutants. For this purpose, we employed inhibitors of PARP-1 and Ligases 1 and 3, as these factors are required for alt-EJ under some conditions (Wang et al. 2006, Paul et al. 2013, Soni et al. 2014, Bakr et al. 2016). Surprisingly, these treatments remained ineffective in all tested cell lines; despite previous findings from our laboratory showing that these inhibitors significantly decreased the formation of translocations (Figure 33) (Soni et al. 2014). Due to its involvement in formation of chromosome translocations, alt-EJ can be investigated by cytogenetic methods assessing chromosomal aberrations (Iliakis et al. 2015, Soni et al. 2015, Sallmyr and Tomkinson 2018). We infer therefore that rejoining of DSBs measured by PFGE at 20 Gy of IR exposure requires different mechanisms than chromosome translocations formation typically measured at ~1 Gy, however, this question remains to be

elucidated. Different experimental approaches such as genetic inhibition of PARP-1 and Ligases 1 and 3 via gene knockdown or knockout technologies may give more effective response in this direction as it was previously shown by our laboratory (Soni et al. 2015).

Despite the fact that, we were not able to establish a link between chromatin structure and growth state dependence of alt-EJ under the experimental conditions we examined here; the role of the chromatin structure in DSB repair is indisputable (Ziv et al. 2006, Falk et al. 2007, Srivastava et al. 2010, Goodarzi et al. 2010, Xu and Price 2011, Price and D'Andrea 2013, House et al. 2014, Taty-Taty et al. 2016, Hauer and Gasser 2017, Seeber and Gasser 2017). Not only it may represent a barrier to DSB repair via influencing lesion accessibility; but it may also affect other important processes such as DNA end resection and transcription (Ehrenhofer-Murray 2004, Li et al. 2007, Chen and Symington 2013, Voss and Hager 2014, Venkatesh and Workman 2015). We have shown that WT and Lig4^{-/-} MEFs exhibit higher levels of H3K9me3 in SD state suggesting a more compact chromatin structure. Regarding the importance of the chromatin structure, we employed additional markers such as, heterochromatin and transcriptional repression related histone markers H3K9me2, H3K27me3, H4K20me2/3 and non-histone markers HP1 and KAP1. We also examined euchromatin and transcriptional activation related histone markers H4K20me1 and H3K27Ac (Eberharter and Becker 2002, Bannister and Kouzarides 2011) and assessed the state of the chromatin structure in DNA-PKcs^{-/-} and Ku80^{-/-} cells in exponential and SD state in addition to WT and Lig4^{-/-} cells. Consistent with our previous results shown in Figure 19, WT and Lig4^{-/-} cells showed increased levels of all heterochromatin related markers. However, we also had unexpected findings, similar to those of H3K9Ac levels, a slight increase was observed in H3K27Ac levels in SD state in WT and Lig4^{-/-} cells. On the other hand, as expected H4K20me1 levels were found to be lower in SD state. DNA-PKcs^{-/-} and Ku80^{-/-} cells showed no detectable alterations in any of these markers, with the exception of lower levels of H4K20me1 in SD state in DNA-PKcs^{-/-} cells, confirming the quiescent state of the cells (Evertts et al. 2013). It may not be surprising that H4K20me1 levels remained similar in Ku80^{-/-} cells in the exponential and the SD state, as these cells did not completely accumulate in G₀/G₁ even 3 days after serum deprivation (Figure 35). Therefore, similar levels of these markers in Ku80^{-/-} cells may be simply explained by inefficient growth arrest. Intriguingly, despite the efficient growth arrest of DNA-PKcs^{-/-} cells, as confirmed by

both H4K20me1 levels (Figure 34) and PI histograms (Figure 35), all assessed markers exhibited similar levels in exponential and SD state. Previous reports have shown that, besides its function in DNA damage response and repair, DNA-PKcs regulates transcription, interacting with SP1 transcription factor and RNA Polymerases I and II (Jackson et al. 1990, Dvir et al. 1992, Kuhn et al. 1995, Labhart 1995, Maldonado et al. 1996, Liiv et al. 2008, Hill and Lee 2010, Pankotai et al. 2012). Together with these observations, our results suggest that DNA-PKcs may play a role in the regulation of chromatin structure and transcription. However, further investigations are required to elucidate this role of DNA-PKcs and its influence in the regulation of alt-EJ.

5.3. Mutations in the autophosphorylation sites or kinase inactivation may not mimic DNA-PKcs deficient phenotype

Given its importance in DNA damage signaling and DSB repair and its versatile functions, we placed more emphasis on DNA-PKcs. With this aim, we employed DNA-PKcs deficient V3 CHO cells, complemented with several mutants form of DNA-PKcs (Figure 37) (Neal et al. 2014). First, we examined two cell lines, A5 and A36, expressing nearly normal levels of wt DNA-PKcs in rodents, and 20-fold higher levels, similar to human cells, respectively. We used these mutants to investigate the effect of DNA-PKcs levels on DSB repair. However as seen in Figure 40, both mutants effectively repaired DSBs in both the exponential and the SD state. Inhibition of DNA-PKcs using NU7441 only slightly reduced the efficiency of repair in the SD state in both mutants (Figure 41). This finding may suggest that low levels of DNA-PKcs are sufficient for effective c-NHEJ. The VectA mutant, which was transfected with empty vector showed similar repair efficiency in both exponential and SD state. This finding confirms our previous results with DNA-PKcs^{-/-} MEF cells, suggesting that in the absence of DNA-PKcs, alt-EJ can operate irrespectively of growth state. Interestingly, the kinase dead mutant (K>R31) showed diminished repair efficiency in SD state, which is also in line with the studies suggesting that autphosphorylation of DNA-PKcs is required for detachment of DNA-PKcs from the DSB site to allow completion of repair (Figure 42) (Neal et al. 2014). To rule out the possibility of non-specific effects, we treated VectA and K>R31 cells with NU7441 and as expected there was no further effect of this treatment on the repair efficiency of both cell lines (Figure 43). We

tested the phospho-mimicking forms of DNA-PKcs; ND5 with very low kinase activity and JKD2 with wild type kinase activity. The ND5 mutant showed similar and efficient repair efficiency in both exponential and SD state. Interestingly, the JKD2 mutant showed slower repair kinetics in exponential state and repair efficiency was diminished in SD state, despite the wild type kinase activity (Figure 44). This finding may suggest that dephosphorylation of JKD2 domain is required to complete the repair process. On the other hand, while the repair efficiency of ND5 mutant in SD state was slightly diminished upon NU7441 treatment; there was no effect on the repair efficiency of JKD2 mutant in any of the growth states (Figure 45). This may suggest that phosphorylation of JKD2 domain shifts the repair pathway choice from c-NHEJ to alt-EJ upon 20 Gy IR. We also investigated autophosphorylation of DNA-PKcs on DSB repair. We tested phospho-ablating mutations in PQR and ABCDE sites in PQR and GG6 mutants, respectively. PFGE experiments showed that repair efficiency of PQR mutant was similar in the exponential and the SD state, whereas only a very slight decrease was observed in the repair efficiency of GG6 mutant in SD state (Figure 46). Repair efficiency of both mutants in SD state was dramatically abrogated upon NU7441 treatment (Figure 47). These results confirm previous findings suggesting that autophosphorylation of these sites is not required for efficient c-NHEJ (Meek et al. 2007, Dobbs et al. 2010).

We also studied the role of different levels of DNA-PKcs, along with DNA-PKcs deficiency and kinase dead mutation on DNA end resection. Different levels of DNA-PKcs did not influence DNA end resection activity (Supplementary Figure 37). Similar to DNA-PKcs^{-/-} MEFs, VectA mutant had detectable DNA end resection only in the exponential state. Similar results were obtained with other tested mutants (Figure 48). When cells were gated according to the cell cycle phase, we could confirm that in an exponentially growing population, not only G₂, but also G₁ cells show detectable DNA end resection activity, albeit at lower rates, especially at later time points compared to G₂ cells. In SD state, DNA end resection was detectable neither in G₁ nor in G₂ phases in any of the mutants (Figure 49-Figure 50). There was only barely detectable DNA end resection in G₂ phase of GG6 cells in SD state; however this could be attributed to inefficient arrest in G₀/G₁ as shown in Figure 51. Our overall findings showed that regardless of the status of DNA-PKcs, DNA end resection is downregulated when cells are in a quiescent state and DNA end resection can be rescued if the growth arrest is inefficient even in

the absence of serum. Based on our findings, DNA end resection is downregulated in G_0 , where alt-EJ is abrogated. However, the unique feature of DNA-PKcs deficient cells in the growth state dependence of alt-EJ is still a matter of debate and requires further investigations. Data from our laboratory has already shown that DNA-PKcs deficient cells of human and rodent origin exhibit similar DSB repair kinetics irrespectively of growth state (Singh 2010). Therefore, we could rule out the possibility that this response may be a consequence of the fact that rodent cells have ~50-fold lower levels of DNA-PKcs as compared to human cells (Finnie et al. 1995, Meek et al. 2008). We confirmed that different levels of DNA-PKcs influence neither DSB repair nor DNA end resection, using A5 and A36 CHO cells which express low and high levels of DNA-PKcs, respectively. However, we should consider that despite the similar response to DSBs in the absence of DNA-PKcs among species, cells may exhibit evolutionarily different forms of adaptation due to the different levels of DNA-PKcs, and it is possible that artificially generated cells do not reflect accurately these molecular mechanisms. Therefore, in future experiments, human cells should be included along with rodent cells to study the mechanistic underpinnings of alt-EJ in DNA-PKcs deficiency.

5.4. c-NHEJ could still operate in the absence of 53BP1

Another important factor which plays role in the DSB repair pathway choice is 53BP1 and it is known as a positive regulator of c-NHEJ. It suppresses DNA end resection and promotes c-NHEJ in G_1 cells. In S phase, BRCA1 antagonizes 53BP1 and mediates its removal from the break sites. Thus, BRCA1 promotes DNA end resection and the repair pathway shifts to HRR (Daley and Sung 2014, Zimmermann and de Lange 2014, Feng et al. 2015). Recent studies suggested that in the absence of 53BP1, DNA end resection is promoted and repair pathway shifts to alt-EJ in G_1 cells (Xiong et al. 2015, Bakr et al. 2016). Based on these findings and our hypothesis suggesting that DNA end resection could promote alt-EJ in SD state, we employed 53BP1 deficient mESCs and measured DSB repair kinetics. PFGE experiments showed that repair was not dramatically abrogated in 53BP1^{-/-} mESCs in SD state (Figure 52). Although PI histograms and Ki67 levels showed that these cells were still in a *quasi exponential* state despite 5 days of serum deprivation, we observed that in the absence of serum alt-EJ was abrogated. To investigate whether in the absence of 53BP1, c-NHEJ still operates; we used the DNA-PKcs

inhibitor NU7441. Unexpectedly, similar to WT controls, repair efficiency was dramatically abrogated in 53BP1^{-/-} mESCs in SD state, suggesting that DSB repair by c-NHEJ still occurred in the absence of 53BP1 (Figure 54). As we already discussed above the negligible contribution of HRR to DSB repair upon exposure of cells to high dose of IR, allows us to conclude that c-NHEJ is the main repair pathway throughout the cell cycle despite the activation of DNA end resection in S and G₂ phases. Moreover, it has been shown by our laboratory and others that there is detectable DNA end resection activity not only in S and G₂, but also in G₁ phase (Moscariello et al. 2015, Biehs et al. 2017, Löbrich and Jeggo 2017). As seen in Figure 55, we detected DNA end resection in WT cells only in exponential state, compatible with our previous findings. As seen in Figure 55, in 53BP1^{-/-} mESCs, DNA end resection could be detected at 6 h time point not only in the exponential but also in SD state. However, similar to Ku80^{-/-} MEFs, this resection activity may be due to inefficient growth arrest in SD state, as seen in the PI histograms in Figure 56. Based on these findings we can state that c-NHEJ operates efficiently and alt-EJ is not promoted in the absence of 53BP1. However in order to establish a link between 53BP1 deficiency and DNA end resection, optimization of the growth and serum deprivation conditions will be required.

6. SUMMARY

The main purpose of this study was to investigate the mechanistic underpinnings of the growth state dependence of alt-EJ. While HRR is strictly cell cycle dependent due to the requirement of a sister chromatid as template, c-NHEJ operates independently of the cell cycle and growth state. C-NHEJ does not use a template and therefore, it cannot restore the sequence around the DSBs. Moreover it can also lead to translocations. Alt-EJ operates on similar basic principles as c-NHEJ but it is even more prone to errors and chromosome translocations. However, unlike c-NHEJ, its efficiency fluctuates throughout the cell cycle and it is completely abrogated when cells are in G_0 .

In order to explore the mechanisms behind the growth state dependence of alt-EJ, we first inquired whether the chromatin structure is a determinant, as it was previously reported that G_0 cells have more compact and transcriptionally inactive chromatin. Our approach was to artificially modify chromatin structure and to measure the kinetics of alt-EJ, particularly following chromatin relaxation. However, under the experimental conditions applied in this study, we were not able to show that chromatin relaxation promoted abrogated alt-EJ in G_0 cells. Nevertheless, one intriguing finding was that DNA-PKcs deficient cells exhibited similar chromatin structure related signature of H3K9me2, H3K9me3, H3K27Ac, H3K27me3, H4K20me2/3, HP1 and KAP1 in both cycling and G_0 phase. As DNA-PKcs deficient cells do not show typical growth state dependent fluctuations of alt-EJ, this finding suggests that chromatin structure may be the determinant in the growth state dependence of alt-EJ. However, it could be that treatments with limited effects on chromatin structure fail to revert this phenotype of alt-EJ. It is well established that chromatin structure is highly dynamic and plays a central role in DSB repair. Therefore, further investigations in this context are required.

Another prime candidate to explain the growth state dependence of alt-EJ was DNA end resection, as unpublished data from our laboratory has shown that DNA-PKcs deficient human glioblastoma cells, M059J, retain DNA end resection activity in G_0 . While DNA end resection is typically downregulated in G_0/G_1 phases of the cell cycle, persistent DNA end resection activity in G_0 could explain why DNA-PKcs deficient cells efficiently utilize alt-EJ in G_0 , in contrast to other c-NHEJ mutants. Our investigations could confirm that, in DNA-PKcs

proficient status, DNA end resection is only detectable in exponentially growing cells with an enhanced activity in G₂ and it is downregulated in G₀ phase. Indeed, cell cycle and growth state dependent fluctuations of DNA end resection parallel the kinetics of alt-EJ and suggest that abrogation of alt-EJ in G₀ may be due to lack of DNA end resection. However, unlike DNA-PKcs deficient human glioblastoma cells, we were not able to detect DNA end resection activity in DNA-PKcs deficient MEF and CHO cells in G₀. Moreover, we observed that alt-EJ was abrogated in Ku80 deficient MEFs despite detectable DNA end resection activity, which is possibly a consequence of inefficient growth arrest in G₀. Yet the response of the latter cell line suggests that growth factors may also be regulating alt-EJ. Here we conclude that, DNA end resection alone may not be responsible for the growth state dependence of alt-EJ. Future studies should be designed with the purpose of analyzing the combined contributions of DNA end resection and other parameters such as chromatin structure, growth factors and transcriptional regulation in the growth state dependence of alt-EJ.

7. ZUSAMMENFASSUNG

Das Ziel dieser Arbeit war es, die mechanistischen Grundlagen der Wachstumsphasenabhängigkeit von alt-EJ zu untersuchen. Während die HRR stark vom Zellzyklus abhängt, da hier das Schwesterchromatid als Vorlage für die Reparatur dient, arbeitet c-NHEJ unabhängig sowohl von der Zellzyklusphase als auch von der Wachstumsphase. C-NHEJ benötigt keine Vorlage, was allerdings dazu führt, dass die Originalsequenzen um die DSBs nicht wiederhergestellt werden können. Darüber hinaus kann es auch zu Translokationen führen. Alt-EJ arbeitet nach ähnlichen Prinzipien wie c-NHEJ, ist aber noch anfälliger für Fehler und Chromosomentranslokationen. Im Gegensatz zu c-NHEJ schwankt seine Reparatureffizienz jedoch während des gesamten Zellzyklus und wird vollständig inaktiv, sobald sich die Zellen in G_0 befinden.

Um die Mechanismen der Wachstumsphasenabhängigkeit von alt-EJ zu erforschen, haben wir uns zuerst gefragt, ob die Chromatinstruktur ein möglicher Faktor ist, da zuvor berichtet wurde, dass das Chromatin in G_0 -Zellen kompakter und transkriptionell inaktiv ist. Unser Ansatz bestand also darin, die Chromatinstruktur künstlich zu modifizieren und die Kinetik von alt-EJ insbesondere nach der Chromatinrelaxierung zu messen. Unter den experimentellen Bedingungen, die in dieser Studie angewandt wurden, konnten wir jedoch nicht zeigen, dass die Chromatinrelaxierung in den G_0 -Zellen die Inhibierung des alt-EJ verhinderte. Ein bemerkenswertes Ergebnis war jedoch, dass DNA-PKcs-defiziente Zellen eine ähnliche Chromatinstrukturbezogene Signatur von H3K9me₂, H3K9me₃, H3K27Ac, H3K27me₃, H4K20me_{2/3}, HP1 und KAP1 sowohl in der exponentiellen Wachstumsphase als auch in der G_0 -Phase aufwiesen. Da DNA-PKcs-defiziente Zellen keine typischen wachstumsphasenabhängigen Fluktuationen von alt-EJ zeigen, deutet dieses Ergebnis darauf hin, dass die Chromatinstruktur hier der bestimmende Faktor für die Wachstumsphasenabhängigkeit von alt-EJ sein könnte. Es ist jedoch möglich, dass Behandlungen von begrenzter Auswirkung auf die Chromatinstruktur diesen Phänotyp von alt-EJ nicht umkehren können. Wir wissen, dass die Chromatinstruktur sehr dynamisch ist und eine zentrale Rolle bei der DSB-Reparatur spielt. Daher sind weitere Untersuchungen in diesem Zusammenhang erforderlich.

Ein weiterer wichtiger Kandidat zur Erklärung der Wachstumsphasenabhängigkeit von alt-EJ war die DNA-Endresektion, da nicht veröffentlichte Daten aus unserem Labor zeigten, dass DNA-PKcs-defiziente humane Glioblastomzellen (M059J) die DNA-Endresektionsaktivität in G_0 behalten. Während die DNA-Endresektion typischerweise in G_0 / G_1 -Phasen des Zellzyklus herunterreguliert wird, könnte die erhöhte DNA-Endresektionsaktivität in G_0 erklären, warum bei DNA-PKcs-defizienten Zellen im Gegensatz zu anderen c-NHEJ-Mutanten alt-EJ in G_0 effizient genutzt wird. Unsere Untersuchungen konnten bestätigen, dass die DNA-Endresektion in DNA-PKcs-profizienten Zellen nur in der exponentiellen Phase, mit erhöhter Aktivität in G_2 , nachweisbar ist und in der G_0 -Phase herunterreguliert wird. In der Tat korrelieren die Zellzyklus- und Wachstumsphasenabhängigen Schwankungen der DNA-Endresektion mit den Kinetiken von alt-EJ und legen nahe, dass die Aufhebung von alt-EJ in G_0 auf mangelnde Endresektionsaktivität zurückzuführen sein könnte. Im Gegensatz zu DNA-PKcs-defizienten humanen Glioblastomzellen konnten wir jedoch keine DNA-Endresektionsaktivität in DNA-PKcs-defizienten MEF- und CHO-Zellen in G_0 nachweisen. Darüber hinaus beobachteten wir, dass alt-EJ trotz nachweisbarer DNA-Endresektionsaktivität in Ku80-defizienten MEFs inhibiert wurde, was möglicherweise eine Folge eines ineffizienten Wachstumsstopps in G_0 ist. Die Reaktion der letzteren Zelllinie legt damit nahe, dass auch Wachstumsfaktoren alt-EJ regulieren könnten. Wir schließen daraus, dass die DNA-Endresektion möglicherweise nicht allein für die Wachstumsphasenabhängigkeit von alt-EJ verantwortlich ist. Zukünftige Studien sollten mit dem Ziel entworfen werden, die kombinierten Beiträge der DNA-Endresektion und anderer Parameter wie Chromatinstruktur, Wachstumsfaktoren und Transkriptionsregulation in der Wachstumsphasenabhängigkeit von alt-EJ zu analysieren.

8. REFERENCES

- Alberts B, Johnson A, Lewis J, et al. *Molecular Biology of the Cell*. 4th edition. New York: Garland Science; 2002.
- Albiez H, Cremer M, Tiberi C, Vecchio L, Schermelleh L, Dittrich S, Küpper K, Joffe B, Thormeyer T, von Hase J, Yang S, Rohr K, Leonhardt H, Solovei I, Cremer C, Fakan S, Cremer T. Chromatin domains and the interchromatin compartment form structurally defined and functionally interacting nuclear networks. *Chromosome Res*. 2006. 14(7):707-33.
- Anderson L, Henderson C, Adachi Y. Phosphorylation and rapid relocalization of 53BP1 to nuclear foci upon DNA damage. *Mol Cell Biol*. 2001. 21(5):1719-29.
- Aylon Y, Liefshitz B, Kupiec M. The CDK regulates repair of double-strand breaks by homologous recombination during the cell cycle. *EMBO J*. 2004. 23(24):4868-75.
- Bakr A, Köcher S, Volquardsen J, Petersen C, Borgmann K, Dikomey E, Rothkamm K, Mansour WY. Impaired 53BP1/RIF1 DSB mediated end-protection stimulates CtIP-dependent end resection and switches the repair to PARP1-dependent end joining in G1. *Oncotarget*. 2016. 7(36):57679-57693.
- Bannister AJ, Kouzarides T. Regulation of chromatin by histone modifications. *Cell Res*. 2011. 21(3):381-95.
- Barski A, Cuddapah S, Cui K, Roh TY, Schones DE, Wang Z, Wei G, Chepelev I, Zhao K. High-resolution profiling of histone methylations in the human genome. *Cell*. 2007. 129(4):823-37.
- Bártová E1, Krejčí J, Harnicarová A, Galiová G, Kozubek S. Histone modifications and nuclear architecture: a review. *J Histochem Cytochem*. 2008. 56(8):711-21.
- Bennardo N, Cheng A, Huang N, Stark JM. Alternative-NHEJ is a mechanistically distinct pathway of mammalian chromosome break repair. *PLoS Genet*. 2008. 4(6):e1000110.
- Biehs R, Steinlage M, Barton O, Juhász S, Künzel J, Spies J, Shibata A, Jeggo PA, Löbrich M. DNA Double-Strand Break Resection Occurs during Non-homologous End Joining in G1 but Is Distinct from Resection during Homologous Recombination. *Mol Cell*. 2017. 65(4):671-684.
- Bulger M. Hyperacetylated chromatin domains: lessons from heterochromatin. *J Biol Chem*. 2005. 280(23):21689-92.
- Bunting SF, Callén E, Wong N, Chen HT, Polato F, Gunn A, Bothmer A, Feldhahn N, Fernandez-Capetillo O, Cao L, Xu X, Deng CX, Finkel T, Nussenzweig M, Stark JM,

Nussenzweig A. 53BP1 inhibits homologous recombination in Brca1-deficient cells by blocking resection of DNA breaks. *Cell*. 2010. 141(2):243-54.

Cann KL, Dellaire G. Heterochromatin and the DNA damage response: the need to relax. *Biochem Cell Biol*. 2011. 89: 45–60.

Carrier F. Chromatin Modulation by Histone Deacetylase Inhibitors: Impact on Cellular Sensitivity to Ionizing Radiation. *Mol Cell Pharmacol*. 2013. 5(1):51-59.

Chang HHY, Pannunzio NR, Adachi N, Lieber MR. Non-homologous DNA end joining and alternative pathways to double-strand break repair. *Nat Rev Mol Cell Biol*. 2017. 18(8):495-506.

Chapman JR, Taylor MR, Boulton SJ. Playing the end game: DNA double-strand break repair pathway choice. *Mol Cell*. 2012. 47(4):497-510.

Chen BP, Uematsu N, Kobayashi J, Lerenthal Y, Krempler A, Yajima H, Löbrich M, Shiloh Y, Chen DJ. Ataxia telangiectasia mutated (ATM) is essential for DNA-PKcs phosphorylations at the Thr-2609 cluster upon DNA double strand break. *J Biol Chem*. 2007. 282(9):6582-7.

Chen H, Symington LS. Overcoming the chromatin barrier to end resection. *Cell Res*. 2013. 317–319.

Chiruvella KK, Liang Z, Wilson TE. Repair of double-strand breaks by end joining. *Cold Spring Harb Perspect Biol*. 2013. 5(5):a012757.

Christman JK. 5-Azacytidine and 5-aza-2'-deoxycytidine as inhibitors of DNA methylation: mechanistic studies and their implications for cancer therapy. *Oncogene*. 2002. 21(35):5483-95.

Clouaire T, Legube G. DNA double strand break repair pathway choice: a chromatin based decision? *Nucleus*. 2015. 107-13.

Collings CK, Waddell PJ, Anderson JN. Effects of DNA methylation on nucleosome stability. *Nucleic Acids Res*. 2013. 41(5):2918-31.

Cooper GM. *The Cell: A Molecular Approach*. 2nd edition. Sunderland (MA): Sinauer Associates; 2000.

Cui X, Yu Y, Gupta S, Cho YM, Lees-Miller SP, Meek K. Autophosphorylation of DNA-dependent protein kinase regulates DNA end processing and may also alter double-strand break repair pathway choice. *Mol Cell Biol*. 2005. 25(24):10842-52.

Daley JM, Niu H, Miller AS, Sung P. Biochemical mechanism of DSB end resection and its regulation. *DNA Repair (Amst)*. 2015. 32:66-74.

- Daley JM, Sung P. 53BP1, BRCA1, and the choice between recombination and end joining at DNA double-strand breaks. *Mol Cell Biol.* 2014. 34(8):1380-8.
- Davis AJ, Chen BP, Chen DJ. DNA-PK: a dynamic enzyme in a versatile DSB repair pathway. *DNA Repair (Amst).* 2014. 17:21-9.
- Davis AJ, Chen DJ. DNA double strand break repair via non-homologous end-joining. *Transl Cancer Res.* 2013. 2(3):130-143.
- DeFazio LG, Stansel RM, Griffith JD, Chu G. Synapsis of DNA ends by DNA-dependent protein kinase. *EMBO J.* 2002. 21(12):3192-200.
- Delpire E, Duchêne C, Goessens G, Gilles R. Effects of osmotic shocks on the ultrastructure of different tissues and cell types. *Exp Cell Res.* 1985. 160(1):106-16.
- Demond M. The influence of chromatin structure on DNA double strand break repair pathway choice (PhD Thesis). *DuEPublico.* 2016.
- DiBiase SJ, Zeng ZC, Chen R, Hyslop T, Curran WJ Jr, Iliakis G. DNA-dependent protein kinase stimulates an independently active, nonhomologous, end-joining apparatus. *Cancer Res.* 2000. 60(5):1245-53.
- Dobbs TA, Tainer JA, Lees-Miller SP. A structural model for regulation of NHEJ by DNA-PKcs autophosphorylation. *DNA Repair (Amst).* 2010. 9(12):1307-14.
- Dong J, Zhang T, Ren Y, Wang Z, Ling CC, He F, Li GC, Wang C, Wen B. Inhibiting DNA-PKcs in a non-homologous end-joining pathway in response to DNA double-strand breaks. *Oncotarget.* 2017. 8(14):22662-22673.
- Du J, Johnson LM, Jacobsen SE, Patel DJ. DNA methylation pathways and their crosstalk with histone methylation. *Nat Rev Mol Cell Biol.* 2015. 16(9):519-32.
- Dueva R, Iliakis G. Alternative pathways of non-homologous end joining (NHEJ) in genomic instability and cancer. *Transl Cancer Res.* 2013;2(3):163-77.
- Dueva RK. A role for DNA-PKcs in G2 checkpoint response and DNA end resection after exposure to ionizing radiation (PhD Thesis). *DuEPublico.* 2015.
- Duraisamy AJ, Mishra M, Kowluru RA. Crosstalk Between Histone and DNA Methylation in Regulation of Retinal Matrix Metalloproteinase-9 in Diabetes. *Invest Ophthalmol Vis Sci.* 2017. 58(14):6440-6448.

Dvir A, Peterson SR, Knuth MW, Lu H, Dynan WS. Ku autoantigen is the regulatory component of a template-associated protein kinase that phosphorylates RNA polymerase II. *Proc Natl Acad Sci U S A*. 1992. 89(24):11920-4.

Eberharter A, Becker PB. Histone acetylation: a switch between repressive and permissive chromatin. Second in review series on chromatin dynamics. *EMBO Rep*. 2002. 3(3):224-9.

Ehrenhofer-Murray AE. Chromatin dynamics at DNA replication, transcription and repair. *Eur J Biochem*. 2004. 271(12):2335-49.

Elia MC, Bradley MO. Influence of chromatin structure on the induction of DNA double strand breaks by ionizing radiation. *Cancer Res*. 1992. 52(6):1580-6.

Evertts AG, Manning AL, Wang X, Dyson NJ, Garcia BA, Collier HA. H4K20 methylation regulates quiescence and chromatin compaction. *Mol Biol Cell*. 2013. 24(19):3025-37.

Falk M, Lukasova E, Gabrielova B, Ondrej V, Kozubek S. Chromatin dynamics during DSB repair. *Biochim Biophys Acta*. 2007. 1773(10):1534-45.

Falk M, Lukášová E, Kozubek S. Chromatin structure influences the sensitivity of DNA to gamma-radiation. *Biochim Biophys Acta*. 2008. 1783(12):2398-414.

Falk M, Lukasova E, Kozubek S. Higher-order chromatin structure in DSB induction, repair and misrepair. *Mutat Res*. 2010. 704(1-3):88-100.

Feng L, Li N, Li Y, Wang J, Gao M, Wang W, Chen J. Cell cycle-dependent inhibition of 53BP1 signaling by BRCA1. *Cell Discov*. 2015. 1:15019.

Feng YL, Xiang JF, Kong N, Cai XJ, Xie AY. Buried territories: heterochromatic response to DNA double-strand breaks. *Acta Biochim Biophys Sin (Shanghai)*. 2016. 48(7):594-602.

Finnie NJ, Gottlieb TM, Blunt T, Jeggo PA, Jackson SP. DNA-dependent protein kinase activity is absent in xrs-6 cells: implications for site-specific recombination and DNA double-strand break repair. *Proc Natl Acad Sci U S A*. 1995. 92(1):320-4.

Fischle W. Talk is cheap—cross-talk in establishment, maintenance, and readout of chromatin modifications. *Genes Dev*. 2008. 22(24):3375-82.

Folle GA, Martínez-López W, Boccardo E, Obe G. Localization of chromosome breakpoints: implication of the chromatin structure and nuclear architecture. *Mutat Res*. 1998. 404(1-2):17-26

Frank KM, Sharpless NE, Gao Y, Sekiguchi JM, Ferguson DO, Zhu C, Manis JP, Horner J, DePinho RA, Alt FW. DNA ligase IV deficiency in mice leads to defective neurogenesis and embryonic lethality via the p53 pathway. *Mol Cell*. 2000. 5(6):993-1002.

Frit P, Barboule N, Yuan Y, Gomez D, Calsou P. Alternative end-joining pathway(s): bricolage at DNA breaks. *DNA Repair (Amst)*. 2014. 17:81-97.

Gerdes J, Schwab U, Lemke H, Stein H. Production of a mouse monoclonal antibody reactive with a human nuclear antigen associated with cell proliferation. *Int J Cancer*. 1983. 31(1):13-20.

Goodarzi AA, Jeggo P, Lobrich M. The influence of heterochromatin on DNA double strand break repair: Getting the strong, silent type to relax. *DNA Repair (Amst)*. 2010. 9(12):1273-82.

Goodarzi AA, Noon AT, Deckbar D, Ziv Y, Shiloh Y, Löbrich M, Jeggo PA. ATM signaling facilitates repair of DNA double-strand breaks associated with heterochromatin. *Mol Cell*. 2008. 31: 167–177.

Goodarzi AA, Yu Y, Riballo E, Douglas P, Walker SA, Ye R, Härer C, Marchetti C, Morrice N, Jeggo PA, Lees-Miller SP. DNA-PK autophosphorylation facilitates Artemis endonuclease activity. *EMBO J*. 2006. 25(16):3880-9.

Görisch SM, Wachsmuth M, Tóth KF, Lichter P, Rippe K. Histone acetylation increases chromatin accessibility. *J Cell Sci*. 2005. 118(Pt 24):5825-34.

Haaf T. The effects of 5-azacytidine and 5-azadeoxycytidine on chromosome structure and function: implications for methylation-associated cellular processes. *Pharmacol Ther*. 1995. 65(1):19-46.

Hall EJ, Giaccia AJ. *Radiobiology for the Radiologist*. 6th Edition ed. Philadelphia, Baltimore, New York, London, Buenos Aires, Hong Kong, Sydney, Tokyo: Lippincott Williams & Wilkins; 2006.

Harper JV, Brooks G. The mammalian cell cycle: an overview. *Methods Mol Biol*. 2005. 296:113-53.

Hauer MH, Gasser SM. Chromatin and nucleosome dynamics in DNA damage and repair. *Genes Dev*. 2017. 31(22):2204-2221.

Helleday T, Lo J, van Gent DC, Engelward BP. DNA double-strand break repair: from mechanistic understanding to cancer treatment. *DNA Repair (Amst)*. 2007. 6(7):923-35.

Hendrickson CL, Purkayastha S, Pastwa E, Neumann RD, Winters TA. Coincident In Vitro Analysis of DNA-PK-Dependent and -Independent Nonhomologous End Joining. *J Nucleic Acids*. 2010. 2010:823917.

Heyer WD. Biochemistry of eukaryotic homologous recombination. *Top Curr Genet*. 2007. 17:95-133.

Hill MA. Radiation damage to DNA: the importance of track structure. *Radiat Meas*. 1999. 31(1-6):15-23.

Hill R, Lee PW. The DNA-dependent protein kinase (DNA-PK): More than just a case of making ends meet? *Cell Cycle*. 2010. 9(17):3460-9.

House NC, Koch MR, Freudenreich CH. Chromatin modifications and DNA repair: beyond double-strand breaks. *Front Genet*. 2014. 5:296.

Hübner B, Cremer T, Neumann J. Correlative microscopy of individual cells: sequential application of microscopic systems with increasing resolution to study the nuclear landscape. *Methods Mol Biol*. 2013. 1042:299-336.

Hübner B, Lomiento M, Mammoli F, Illner D, Markaki Y, Ferrari S, Cremer M, Cremer T. Remodeling of nuclear landscapes during human myelopoietic cell differentiation maintains co-aligned active and inactive nuclear compartments. *Epigenetics Chromatin*. 2015. 8:47.

Huertas P. DNA resection in eukaryotes: deciding how to fix the break. *Nat Struct Mol Biol*. 2010. 17(1):11-6

Iliakis G, Murmann T, Soni A. Alternative end-joining repair pathways are the ultimate backup for abrogated classical non-homologous end-joining and homologous recombination repair: Implications for the formation of chromosome translocations. *Mutat Res Genet Toxicol Environ Mutagen*. 2015. 793:166-75.

Iliakis G, Nüsse M. Evidence that repair and expression of potentially lethal damage cause the variations in cell survival after X irradiation observed through the cell cycle in Ehrlich ascites tumor cells. *Radiat Res*. 1983. 95(1):87-107.

Iliakis G, Wang H, Perrault AR, Boecker W, Rosidi B, Windhofer F, Wu W, Guan J, Terzoudi G, Pantelias G. Mechanisms of DNA double strand break repair and chromosome aberration formation. *Cytogenet Genome Res*. 2004. 104(1-4):14-20.

Iliakis G. Backup pathways of NHEJ in cells of higher eukaryotes: cell cycle dependence. *Radiother Oncol*. 2009. 92(3):310-5.

- Iliakis GE, Cicilioni O, Metzger L. Measurement of DNA double-strand breaks in CHO cells at various stages of the cell cycle using pulsed field gel electrophoresis: calibration by means of ¹²⁵I decay. *Int J Radiat Biol.* 1991. 59(2):343-57.
- Irianto J, Swift J, Martins RP, McPhail GD, Knight MM, Discher DE, Lee DA. Osmotic challenge drives rapid and reversible chromatin condensation in chondrocytes. *Biophys J.* 2013. 104(4):759-69.
- Jackson SP, MacDonald JJ, Lees-Miller S, Tjian R. GC box binding induces phosphorylation of Sp1 by a DNA-dependent protein kinase. *Cell.* 1990. 63(1):155-65.
- Kabotyanski EB, Gomelsky L, Han JO, Stamato TD, Roth DB. Double-strand break repair in Ku86- and XRCC4-deficient cells. *Nucleic Acids Res.* 1998. 26(23):5333-42.
- Kakarougkas A, Jeggo PA. DNA DSB repair pathway choice: an orchestrated handover mechanism. *Br J Radiol.* 2014. 87(1035):20130685.
- Karymov MA, Tomschik M, Leuba SH, Caiafa P, Zlatanova J. DNA methylation-dependent chromatin fiber compaction in vivo and in vitro: requirement for linker histone. *FASEB J.* 2001. 15(14):2631-41.
- Kastan MB, Bartek J. Cell-cycle checkpoints and cancer. *Nature.* 2004. 432(7015):316-23.
- Kinner A, Wu W, Staudt C, Iliakis G. Gamma-H2AX in recognition and signaling of DNA double-strand breaks in the context of chromatin. *Nucleic Acids Res.* 2008. 36(17):5678-94.
- Kinner A, Wu W, Staudt C, Iliakis G. Gamma-H2AX in recognition and signaling of DNA double-strand breaks in the context of chromatin. *Nucleic Acids Res.* 2008. 36(17):5678-94.
- Klásterská I, Ramel C. The hypotonic pretreatment in mammalian cytology: its function and effect on the aspect of meiotic chromosomes. *Hereditas.* 1979. 90(1):21-9.
- Komashko VM, Farnham PJ. 5-azacytidine treatment reorganizes genomic histone modification patterns. *Epigenetics.* 2010. 5(3):229-40.
- Kuhn A, Gottlieb TM, Jackson SP, Grummt I. DNA-dependent protein kinase: a potent inhibitor of transcription by RNA polymerase I. *Genes Dev.* 1995. 9(2):193-203.
- Kumar R, Horikoshi N, Singh M, Gupta A, Misra HS, Albuquerque K, Hunt CR, Pandita TK. Chromatin modifications and the DNA damage response to ionizing radiation. *Front Oncol.* 2013. 2:214.
- Labhart P. DNA-dependent protein kinase specifically represses promoter-directed transcription initiation by RNA polymerase I. *Proc Natl Acad Sci U S A.* 1995. 92(7):2934-8.

- Lee HB, Noh H, Seo JY, Yu MR, Ha H. Histone deacetylase inhibitors: a novel class of therapeutic agents in diabetic nephropathy. *Kidney Int Suppl.* 2007. (106):S61-6.
- Lee JS, Smith E, Shilatifard A. The language of histone crosstalk. *Cell.* 2010. 142(5):682-5.
- Lee-Theilen M, Matthews AJ, Kelly D, Zheng S, Chaudhuri J. CtIP promotes microhomology-mediated alternative end joining during class-switch recombination. *Nat Struct Mol Biol.* 2011. 18(1):75-9.
- Leitch AR. Higher levels of organization in the interphase nucleus of cycling and differentiated cells. *Microbiol Mol Biol Rev.* 2000. 64(1):138-52.
- Lemaître C, Soutoglou E. Double strand break (DSB) repair in heterochromatin and heterochromatin proteins in DSB repair. *DNA Repair (Amst).* 2014. 19:163-8.
- Li B, Carey M, Workman JL. The role of chromatin during transcription. *Cell.* 2007. 128(4):707-19.
- Li Y, Dilworth FJ. Compacting Chromatin to Ensure Muscle Satellite Cell Quiescence. *Cell Stem Cell.* 2016. 18(2):162-4.
- Liiv I, Rebane A, Org T, Saare M, Maslovskaja J, Kisand K, Juronen E, Valmu L, Bottomley MJ, Kalkkinen N, Peterson P. DNA-PK contributes to the phosphorylation of AIRE: importance in transcriptional activity. *Biochim Biophys Acta.* 2008. 1783(1):74-83.
- Lima AF, May G, Díaz-Colunga J, Pedreiro S, Paiva A, Ferreira L, Enver T, Iborra FJ, Pires das Neves R. Osmotic modulation of chromatin impacts on efficiency and kinetics of cell fate modulation. *Sci Rep.* 2018. 8(1):7210.
- Liu F, Lee WH. CtIP activates its own and cyclin D1 promoters via the E2F/RB pathway during G1/S progression. *Mol Cell Biol.* 2006. 26(8):3124-34.
- Liu L, Cheung TH, Charville GW, Hurgu BM, Leavitt T, Shih J, Brunet A, Rando TA. Chromatin modifications as determinants of muscle stem cell quiescence and chronological aging. *Cell Rep.* 2013. 4(1):189-204.
- Liu T, Huang J. DNA End Resection: Facts and Mechanisms. *Genomics Proteomics Bioinformatics.* 2016. 14(3):126-130.
- Löbrich M, Jeggo P. A Process of Resection-Dependent Nonhomologous End Joining Involving the Goddess Artemis. *Trends Biochem Sci.* 2017. 42(9):690-701.

Löbrich M, Shibata A, Beucher A, Fisher A, Ensminger M, Goodarzi AA, Barton O, Jeggo PA. gammaH2AX foci analysis for monitoring DNA double-strand break repair: strengths, limitations and optimization. *Cell Cycle*. 2010. 9(4):662-9.

Lodish H, Berk A, Zipursky SL, et al. *Molecular Cell Biology*. 4th edition. New York: W. H. Freeman; 2000.

Lopez-Contreras AJ, Fernandez-Capetillo O. Signalling DNA damage. *Protein Phosphorylation in Human Health*, Huang C (Ed.) InTech; 2012.

Ma Y, Kanakousaki K, Buttitta L. How the cell cycle impacts chromatin architecture and influences cell fate. *Front Genet*. 2015. 6:19.

Mah LJ, El-Osta A, Karagiannis TC. gammaH2AX: a sensitive molecular marker of DNA damage and repair. *Leukemia*. 2010. 24(4):679-86.

Maldonado E, Shiekhhattar R, Sheldon M, Cho H, Drapkin R, Rickert P, Lees E, Anderson CW, Linn S, Reinberg D. A human RNA polymerase II complex associated with SRB and DNA-repair proteins. *Nature*. 1996. 381(6577):86-9.

Manova V, Singh SK, Iliakis G. Processing of DNA double strand breaks by alternative non-homologous end-joining in hyperacetylated chromatin. *Genome Integr*. 2012. 3(1):4.

McKnight JN, Boerma JW, Breeden LL, Tsukiyama T. Global Promoter Targeting of a Conserved Lysine Deacetylase for Transcriptional Shutoff during Quiescence Entry. *Mol Cell*. 2015. 59(5):732-43.

Meek K, Dang V, Lees-Miller SP. DNA-PK: the means to justify the ends? *Adv Immunol*. 2008. 99:33-58.

Meek K, Douglas P, Cui X, Ding Q, Lees-Miller SP. Trans Autophosphorylation at DNA-dependent protein kinase's two major autophosphorylation site clusters facilitates end processing but not end joining. *Mol Cell Biol*. 2007. 27(10):3881-90.

Mehta A, Haber JE. Sources of DNA double-strand breaks and models of recombinational DNA repair. *Cold Spring Harb Perspect Biol*. 2014. 6(9):a016428.

Mladenov E, Iliakis G. Induction and repair of DNA double strand breaks: the increasing spectrum of non-homologous end joining pathways. *Mutat Res*. 2011. 711(1-2):61-72.

Mladenov E, Magin S, Soni A, Iliakis G. DNA double-strand break repair as determinant of cellular radiosensitivity to killing and target in radiation therapy. *Front Oncol*. 2013. 3:113.

- Mladenov E, Magin S, Soni A, Iliakis G. DNA double-strand-break repair in higher eukaryotes and its role in genomic instability and cancer: Cell cycle and proliferation-dependent regulation. *Semin Cancer Biol.* 2016. 37-38:51-64.
- Morriscal SW. DNA-pairing and annealing processes in homologous recombination and homology-directed repair. *Cold Spring Harb Perspect Biol.* 2015. 7(2):a016444.
- Moscariello M, Wieloch R, Kurosawa A, Li F, Adachi N, Mladenov E, Iliakis G. Role for Artemis nuclease in the repair of radiation-induced DNA double strand breaks by alternative end joining. *DNA Repair (Amst).* 2015. 31:29-40.
- Murmann-Konda TTY. The contribution of DNA DSB repair pathways to the repair of chromosome breaks throughout the cell cycle (PhD Thesis). DuEPublico. 2016.
- Neal JA, Meek K. Choosing the right path: does DNA-PK help make the decision? *Mutat Res.* 2011. 711(1-2):73-86.
- Neal JA, Sugiman-Marangos S, VanderVere-Carozza P, Wagner M, Turchi J, Lees-Miller SP, Junop MS, Meek K. Unraveling the complexities of DNA-dependent protein kinase autophosphorylation. *Mol Cell Biol.* 2014. 34(12):2162-75.
- Nevaldine B, Longo JA, Hahn PJ. The scid defect results in much slower repair of DNA double-strand breaks but not high levels of residual breaks. *Radiat Res.* 1997. 147(5):535-40.
- O'Driscoll M, Jeggo PA. The role of double-strand break repair — insights from human genetics. *Nat Rev Genet.* 2006. 7(1):45-54.
- Pankotai T, Bonhomme C, Chen D, Soutoglou E. DNAPKcs-dependent arrest of RNA polymerase II transcription in the presence of DNA breaks. *Nat Struct Mol Biol.* 2012. 19(3):276-82.
- Park JA, Kim AJ, Kang Y, Jung YJ, Kim HK, Kim KC. Deacetylation and methylation at histone H3 lysine 9 (H3K9) coordinate chromosome condensation during cell cycle progression. *Mol Cells.* 2011. 34:3-9.
- Paudyal SC, You Z. Sharpening the ends for repair: mechanisms and regulation of DNA resection. *Acta Biochim Biophys Sin (Shanghai).* 2016. 48(7):647-57.
- Paul K, Wang M, Mladenov E, Bencsik-Theilen AA, Bednar T, Wu W, Arakawa H, Iliakis G. DNA ligases I and III cooperate in alternative non-homologous end-joining in vertebrates. *PLoS One.* 2013. 8(3): e59505.

- Pei H, Zhang L, Luo K, Qin Y, Chesi M, Fei F, Bergsagel PL, Wang L, You Z, Lou Z. MMSET regulates histone H4K20 methylation and 53BP1 accumulation at DNA damage sites. *Nature*. 2011. 470(7332):124-8.
- Price BD, D'Andrea AD. Chromatin remodeling at DNA double-strand breaks. *Cell*. 2013. 152(6):1344-54.
- Rosidi B, Wang M, Wu W, Sharma A, Wang H, Iliakis G. Histone H1 functions as a stimulatory factor in backup pathways of NHEJ. *Nucleic Acids Res*. 2008. 36(5):1610-23.
- Rossetto D, Avvakumov N, Côté J. Histone phosphorylation: a chromatin modification involved in diverse nuclear events. *Epigenetics*. 2012. 7(10):1098-108.
- Rothkamm K, Löbrich M. Misrepair of radiation-induced DNA double-strand breaks and its relevance for tumorigenesis and cancer treatment (review). *Int J Oncol*. 2002. 21(2):433-40.
- Sallmyr A, Tomkinson AE. Repair of DNA double-strand breaks by mammalian alternative end-joining pathways. *J Biol Chem*. 2018. 293(27):10536-10546.
- San Filippo J, Sung P, Klein H. Mechanism of eukaryotic homologous recombination. *Annu Rev Biochem*. 2008. 77:229-57.
- Satyanarayana A, Kaldis P. Mammalian cell-cycle regulation: several Cdks, numerous cyclins and diverse compensatory mechanisms. *Oncogene*. 2009. 28(33):2925-39.
- Sawicki W. Chromatin Pattern in Situ: Dependence upon Cell Cycle, Preimplantation Development and Cellular Aging in Vitro. In: Nicolini C.A. (eds) *Chromatin Structure and Function*. NATO Advanced Study Institutes Series (Series A: Life Sciences), vol 21b. 1979. Springer, Boston, MA.
- Schipler A, Iliakis G. DNA double-strand-break complexity levels and their possible contributions to the probability for error-prone processing and repair pathway choice. *Nucleic Acids Res*. 2013. 41(16):7589-605.
- Scholzen T, Gerdes J. The Ki-67 protein: from the known and the unknown. *J Cell Physiol*. 2000. 182(3):311-22.
- Seeber A, Gasser SM. Chromatin organization and dynamics in double-strand break repair. *Curr Opin Genet Dev*. 2017. 43:9-16.
- Shogren-Knaak M, Ishii H, Sun JM, Pazin MJ, Davie JR, Peterson CL. Histone H4-K16 acetylation controls chromatin structure and protein interactions. *Science*. 2006; 311:844-847.

Sims RJ 3rd, Nishioka K, Reinberg D. Histone lysine methylation: a signature for chromatin function. *Trends Genet.* 2003. 19(11):629-39.

Singh SK, Bednar T, Zhang L, Wu W, Mladenov E, Iliakis G. Inhibition of B-NHEJ in plateau-phase cells is not a direct consequence of suppressed growth factor signaling. *Int J Radiat Oncol Biol Phys.* 2012. 84(2):e237-43.

Singh SK. The Function of Backup Pathways of Non-Homologous End Joining in Relation to Growth State and Lesion Quality in Cells of Higher Eukaryotes (PhD Thesis). DuEPublico. 2010.

Soni A, Siemann M, Grabos M, Murmann T, Pantelias GE, Iliakis G. Requirement for Parp-1 and DNA ligases 1 or 3 but not of Xrcc1 in chromosomal translocation formation by backup end joining. *Nucleic Acids Res.* 2014. 42(10):6380-92.

Soni A, Siemann M, Pantelias GE, Iliakis G. Marked contribution of alternative end-joining to chromosome-translocation-formation by stochastically induced DNA double-strand-breaks in G2-phase human cells. *Mutat Res Genet Toxicol Environ Mutagen.* 2015. 793:2-8

Srivastava S, Mishra RK, Dhawan J. Regulation of cellular chromatin state: insights from quiescence and differentiation. *Organogenesis.* 2010. 6(1):37-47.

Stresemann C, Lyko F. Modes of action of the DNA methyltransferase inhibitors azacytidine and decitabine. *Int J Cancer.* 2008. 123(1):8-13.

Suganuma T, Workman JL. Crosstalk among Histone Modifications. *Cell.* 2008. 135(4):604-7.

Sun X, Kaufman PD. Ki-67: more than a proliferation marker. *Chromosoma.* 2018. 127(2):175-186.

Suryadinata R, Sadowski M, Sarcevic B. Control of cell cycle progression by phosphorylation of cyclin-dependent kinase (CDK) substrates. *Biosci Rep.* 2010. 30(4):243-55.

Swygert SG, Kim S, Wu X, Fu T, Hsieh TH, Rando OJ, Eisenman RN, Shendure J, McKnight JN, Tsukiyama T. Condensin-Dependent Chromatin Compaction Represses Transcription Globally during Quiescence. *Mol Cell.* 2019. 73(3):533-546.

Symington LS, Role of RAD52 epistasis group genes in homologous recombination and double-strand break repair. *Microbiol Mol Biol Rev.* 2002. 66(4):630-70,

Tamulevicius P, Wang M, Iliakis G. Homology-directed repair is required for the development of radioresistance during S phase: interplay between double-strand break repair and checkpoint response. *Radiat Res.* 2007. 167(1):1-11.

Taty-Taty GC, Chailleux C, Quaranta M, So A, Guirouilh-Barbat J, Lopez BS, Bertrand P, Trouche D, Canitrot Y. Control of alternative end joining by the chromatin remodeler p400 ATPase. *Nucleic Acids Res.* 2016. 44(4):1657-68.

Tokuyasu K, Madden SC, Zeldis LJ. Fine structural alterations of interphase nuclei of lymphocytes stimulated to growth activity in vitro. *J Cell Biol.* 1968. 39(3): 630–660.

Tóth KF, Knoch TA, Wachsmuth M, Frank-Stöhr M, Stöhr M, Bacher CP, Müller G, Rippe K. Trichostatin A-induced histone acetylation causes decondensation of interphase chromatin. *J Cell Sci.* 2004 Aug 15;117(Pt 18):4277-87.

Truong LN, Li Y, Shi LZ, Hwang PY, He J, Wang H, Razavian N, Berns MW, Wu X. Microhomology-mediated End Joining and Homologous Recombination share the initial end resection step to repair DNA double-strand breaks in mammalian cells. *Proc Natl Acad Sci U S A.* 2013. 110(19):7720-5.

Tubbs A, Nussenzweig A. Endogenous DNA Damage as a Source of Genomic Instability in Cancer. *Cell.* 2017. 168(4):644-656.

Turinetto V, Giachino C. Multiple facets of histone variant H2AX: a DNA double-strand-break marker with several biological functions. *Nucleic Acids Res.* 2015. 43(5):2489-98.

Venkatesh S, Workman JL. Histone exchange, chromatin structure and the regulation of transcription. *Nat Rev Mol Cell Biol.* 2015. 16(3):178-89.

Voss TC, Hager GL. Dynamic regulation of transcriptional states by chromatin and transcription factors. *Nat Rev Genet.* 2014. 15(2):69-81.

Walker JR, Corpina RA, Goldberg J. Structure of the Ku heterodimer bound to DNA and its implications for double-strand break repair. *Nature.* 2001. 412(6847):607-14.

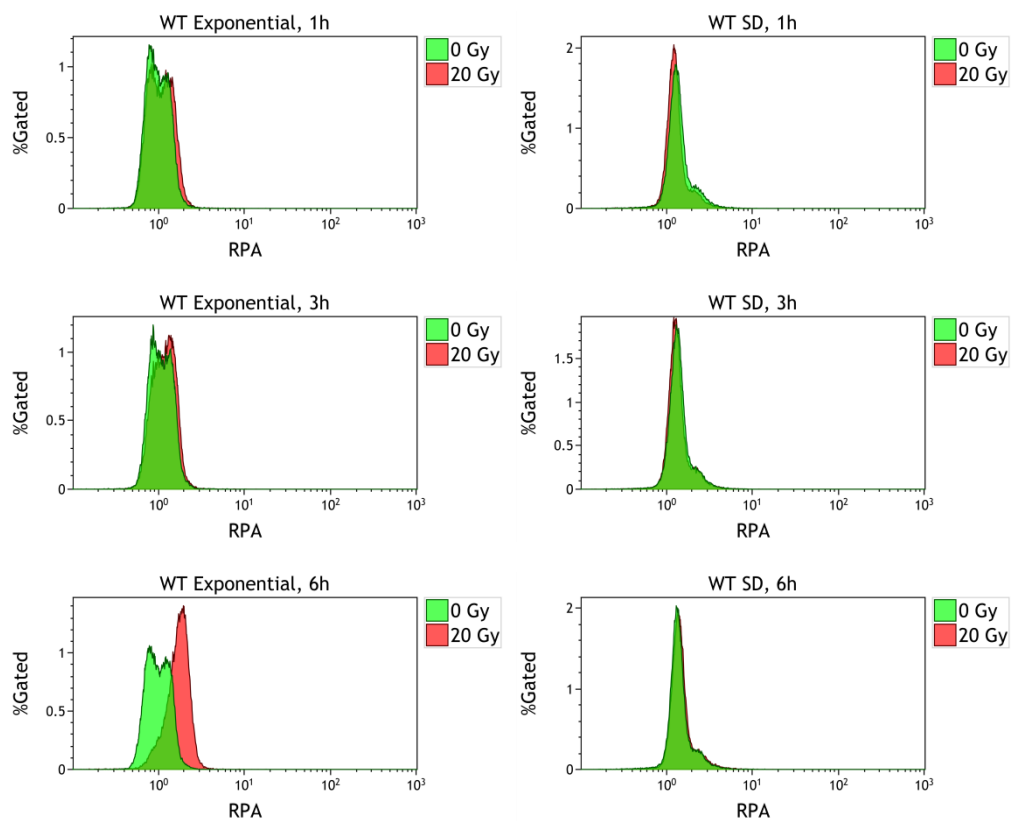
Wang H, Perrault AR, Takeda Y, Qin W, Wang H, Iliakis G. Biochemical evidence for Ku-independent backup pathways of NHEJ. *Nucleic Acids Res.* 2003. 31(18):5377-88.

Wang H, Zeng ZC, Bui TA, Sonoda E, Takata M, Takeda S, Iliakis G. Efficient rejoining of radiation-induced DNA double-strand breaks in vertebrate cells deficient in genes of the RAD52 epistasis group. *Oncogene.* 2001. 20(18):2212-24.

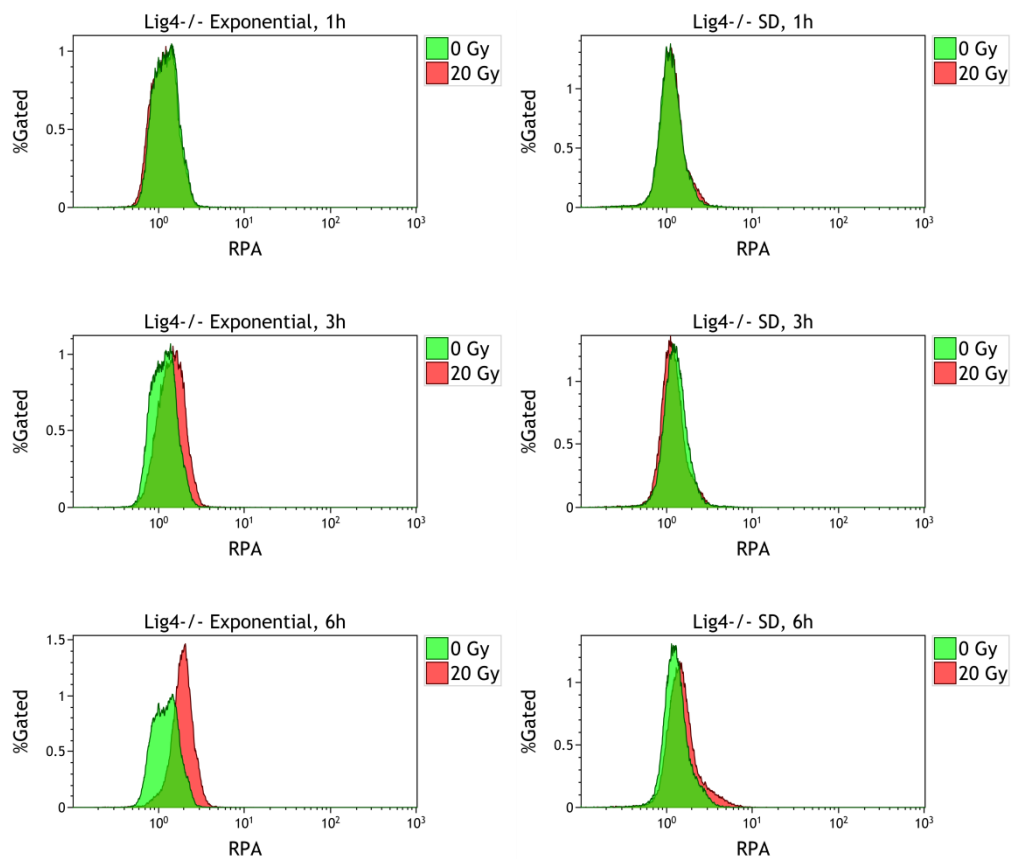
Wang H, Zeng ZC, Perrault AR, Cheng X, Qin W, Iliakis G. Genetic evidence for the involvement of DNA ligase IV in the DNA-PK-dependent pathway of non-homologous end joining in mammalian cells. *Nucleic Acids Res.* 2001. 29(8):1653-60.

- Wang M, Wu W, Wu W, Rosidi B, Zhang L, Wang H, Iliakis G. PARP-1 and Ku compete for repair of DNA double strand breaks by distinct NHEJ pathways. *Nucleic Acids Res.* 2006. 34(21):6170-82.
- Ward IM, Minn K, Jorda KG, Chen J. Accumulation of checkpoint protein 53BP1 at DNA breaks involves its binding to phosphorylated histone H2AX. *J Biol Chem.* 2003. 278(22):19579-82.
- Weterings E, Chen DJ. DNA-dependent protein kinase in nonhomologous end joining: a lock with multiple keys? *J Cell Biol.* 2007. 179(2):183-6.
- Windhofer F, Wu W, Wang M, Singh SK, Saha J, Rosidi B, Iliakis G. Marked dependence on growth state of backup pathways of NHEJ. *Int J Radiat Oncol Biol Phys.* 2007. 68(5):1462-70.
- Wu W, Wang M, Mussfeldt T, Iliakis G. Enhanced use of backup pathways of NHEJ in G2 in Chinese hamster mutant cells with defects in the classical pathway of NHEJ. *Radiat Res.* 2008. 170(4):512-20.
- Wu W, Wang M, Wu W, Singh SK, Mussfeldt T, Iliakis G. Repair of radiation induced DNA double strand breaks by backup NHEJ is enhanced in G2. *DNA Repair (Amst).* 2008. 7(2):329-38.
- Xiong X, Du Z, Wang Y, Feng Z, Fan P, Yan C, Willers H, Zhang J. 53BP1 promotes microhomology-mediated end-joining in G1-phase cells. *Nucleic Acids Res.* 2015. 43(3):1659-70.
- Xu Y, Price BD. Chromatin dynamics and the repair of DNA double strand breaks. *Cell Cycle.* 2011. 10(2):261-7.
- Yao G. Modelling mammalian cellular quiescence. *Interface Focus.* 2014. 4(3):20130074.
- Zimmermann M, de Lange T. 53BP1: pro choice in DNA repair. *Trends Cell Biol.* 2014. 24(2):108-17.
- Ziv Y, Bielopolski D, Galanty Y, Lukas C, Taya Y, Schultz DC, Lukas J, Bekker-Jensen S, Bartek J, Shiloh Y. Chromatin relaxation in response to DNA double-strand breaks is modulated by a novel ATM- and KAP-1 dependent pathway. *Nat Cell Biol.* 2006. 8(8):870-6.
- Zou Y, Liu Y, Wu X, Shell SM. Functions of human replication protein A (RPA): from DNA replication to DNA damage and stress responses. *J Cell Physiol.* 2006. 208(2):267-73.

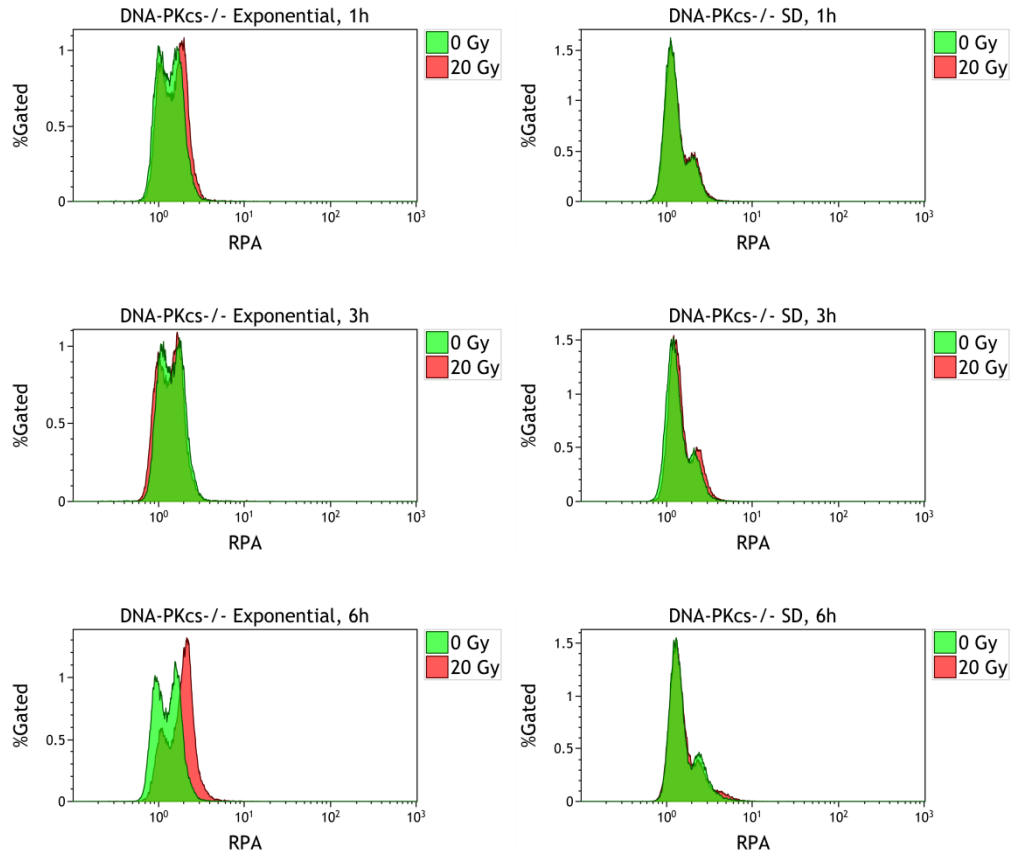
9. SUPPLEMENTARY DATA



Supplementary Figure 1. RPA levels induced by 20 Gy of IR in WT cells in exponential and SD state. Histogram plots indicate the mean fluorescence intensity of RPA signal in 5×10^4 cells measured by flow cytometry.

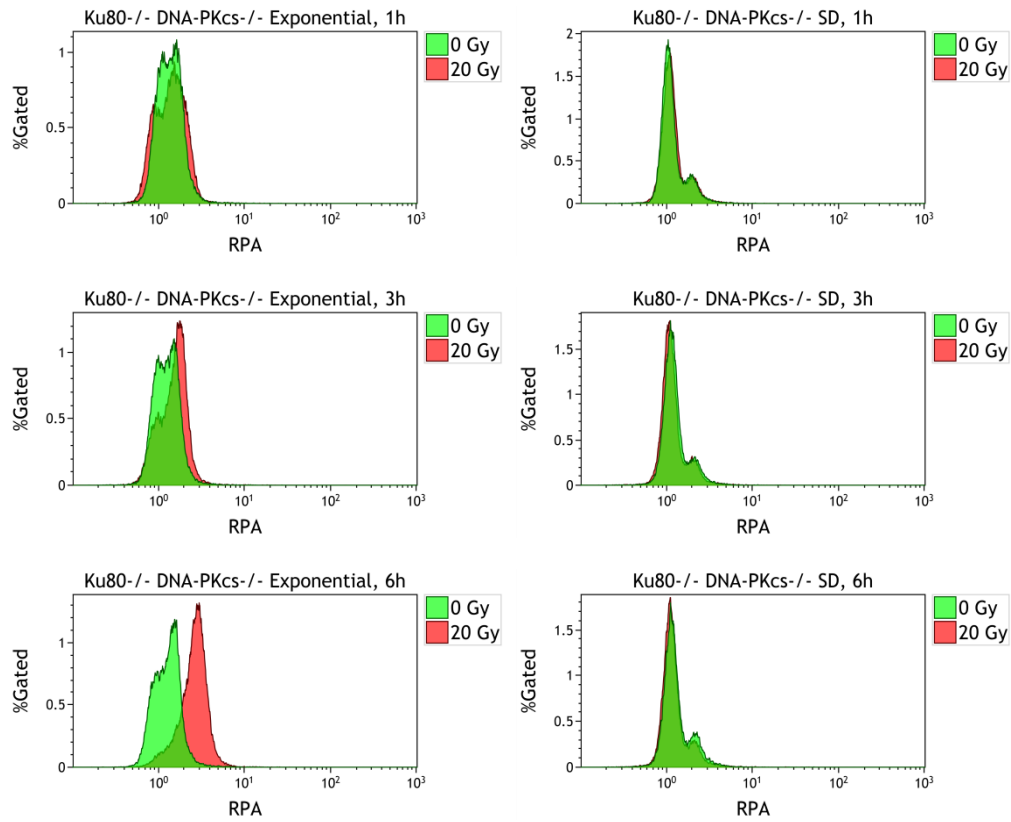


Supplementary Figure 2. RPA levels induced by 20 Gy of IR in Lig4^{-/-} cells in exponential and SD state. Histogram plots indicate the mean fluorescence intensity of RPA signal in 5x10⁴ cells measured by flow cytometry.



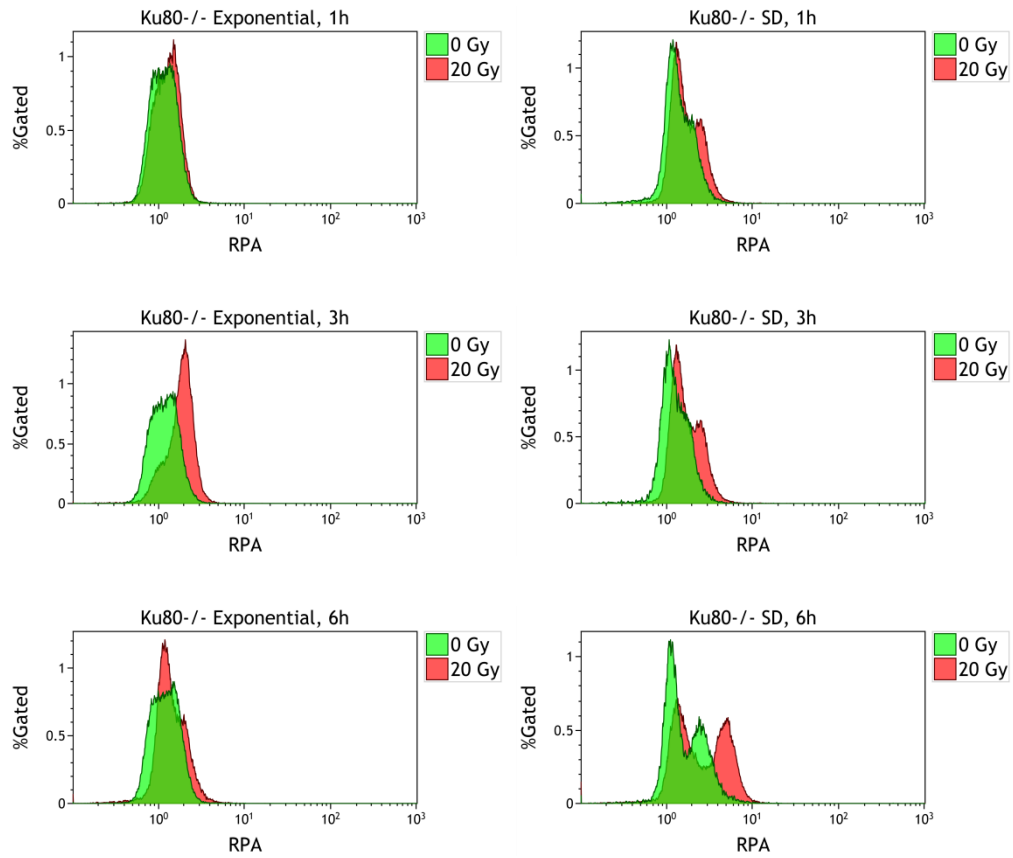
Supplementary Figure 3. RPA levels induced by 20 Gy of IR in DNA-PKcs^{-/-} cells in exponential and SD state.

Histogram plots indicate the mean fluorescence intensity of RPA signal in 5x10⁴ cells measured by flow cytometry.

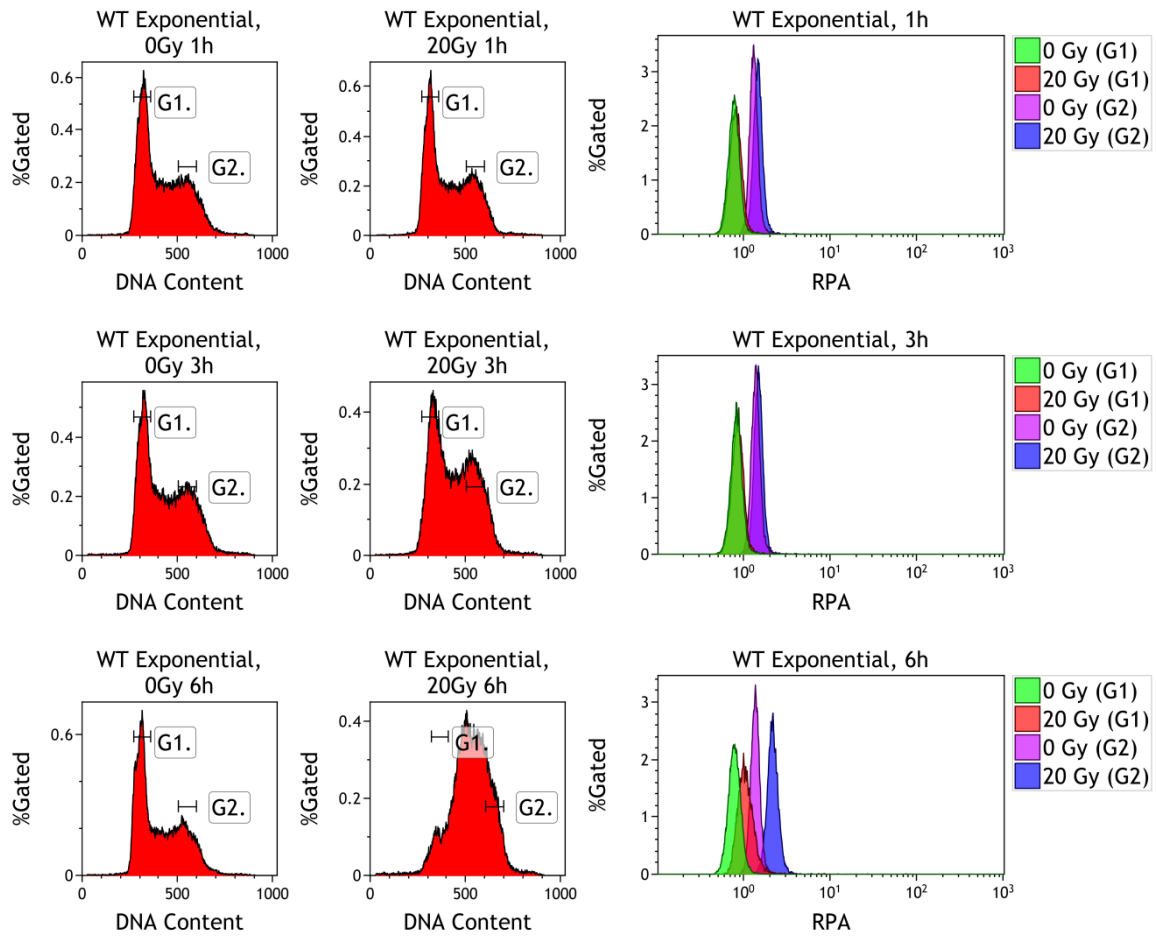


Supplementary Figure 4. RPA levels induced by 20 Gy of IR in Ku80^{-/-} DNA-PKcs^{-/-} cells in exponential and SD state.

Histogram plots indicate the mean fluorescence intensity of RPA signal in 5x10⁴ cells measured by flow cytometry.

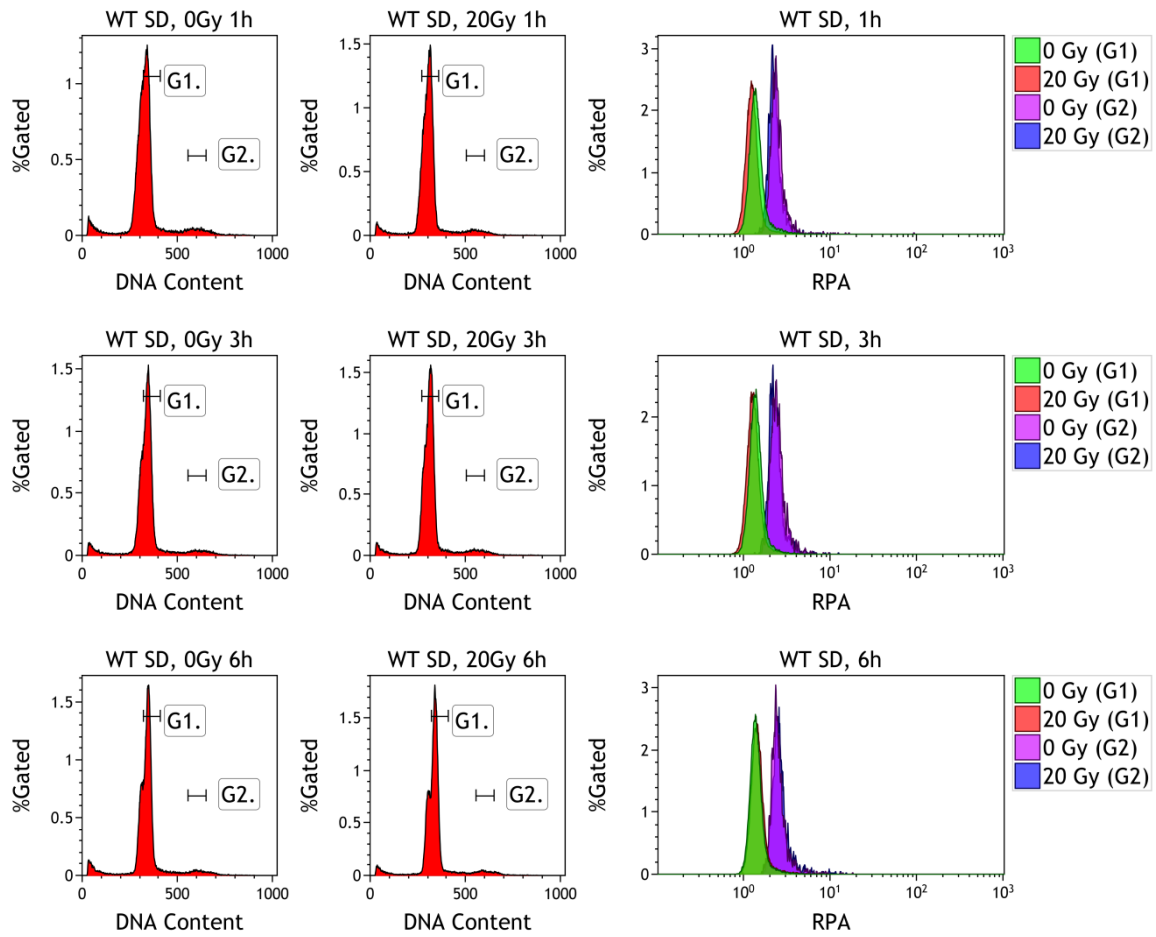


Supplementary Figure 5. RPA levels induced by 20 Gy of IR in Ku80^{-/-} cells in exponential and SD state. Histogram plots indicate the mean fluorescence intensity of RPA signal in 5x10⁴ cells measured by flow cytometry.



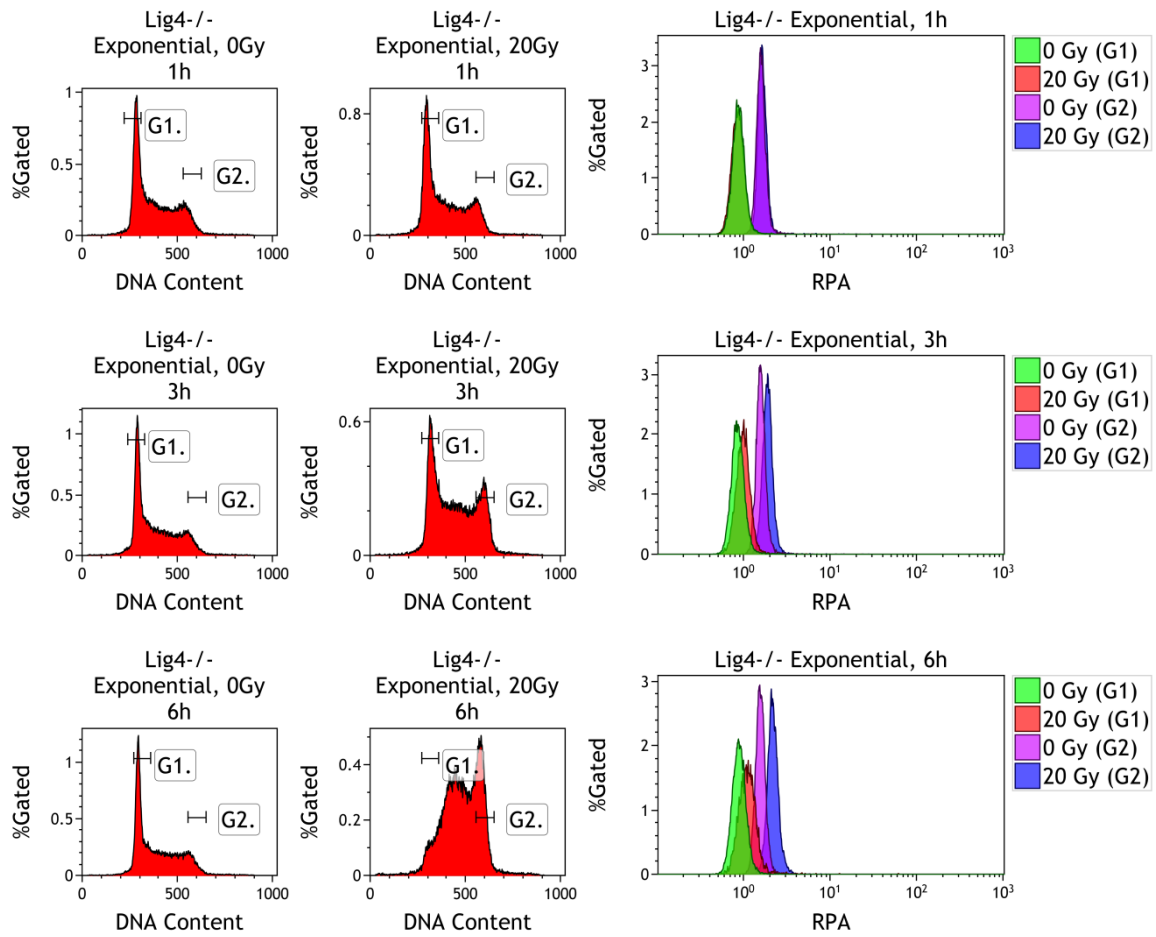
Supplementary Figure 6. DNA end resection in G₁ and G₂ phases in WT cells in exponential state.

Cells were gated in G₁ and G₂ phases according to PI histograms and RPA signal was plotted for each cell cycle phase.



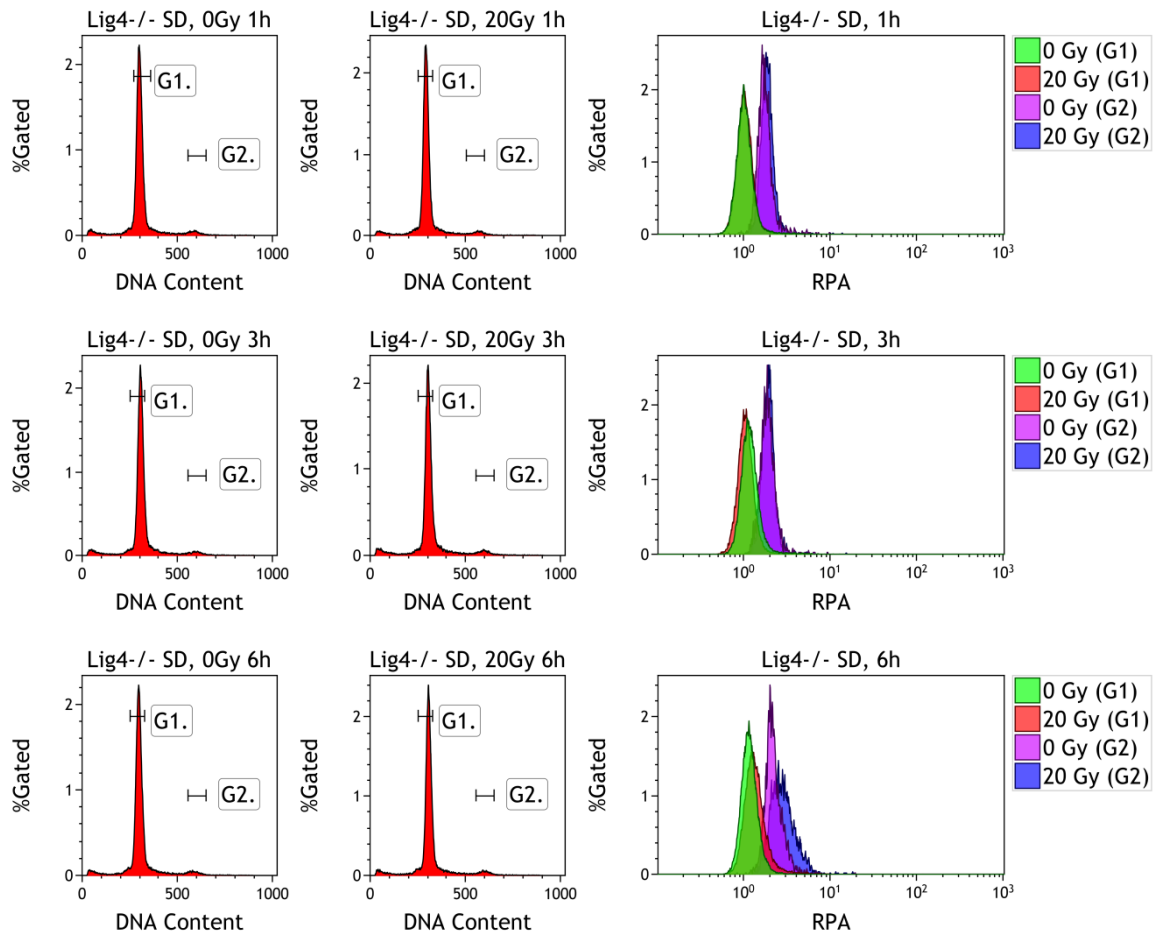
Supplementary Figure 7. DNA end resection in G₁ and G₂ phases in WT cells in SD state.

Cells were gated in G₁ and G₂ phases according to PI histograms and RPA signal was plotted for each cell cycle phase.



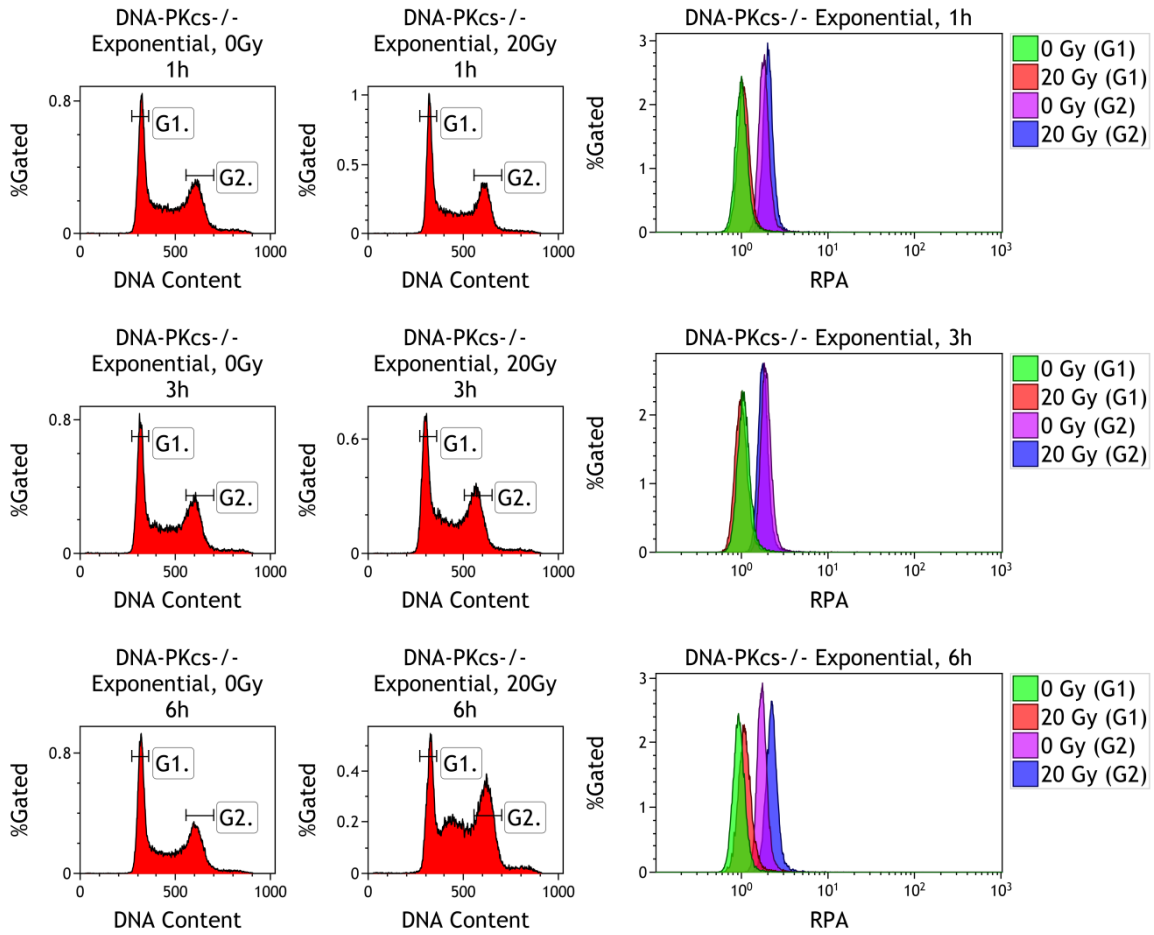
Supplementary Figure 8. DNA end resection in G₁ and G₂ phases in *Lig4*^{-/-} cells in exponential state.

Cells were gated in G₁ and G₂ phases according to PI histograms and RPA signal was plotted for each cell cycle phase.

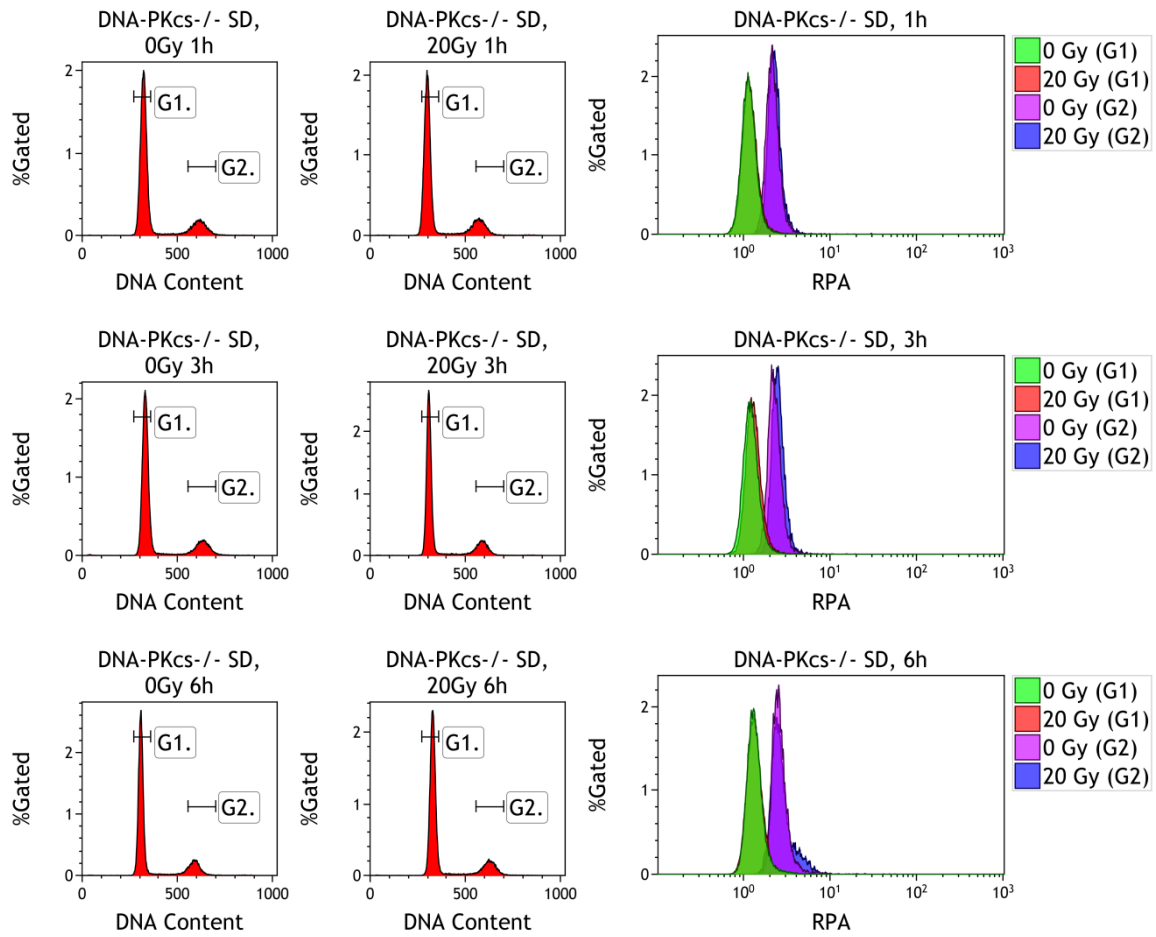


Supplementary Figure 9. DNA end resection in G₁ and G₂ phases in *Lig4*^{-/-} cells in SD state.

Cells were gated in G₁ and G₂ phases according to PI histograms and RPA signal was plotted for each cell cycle phase.

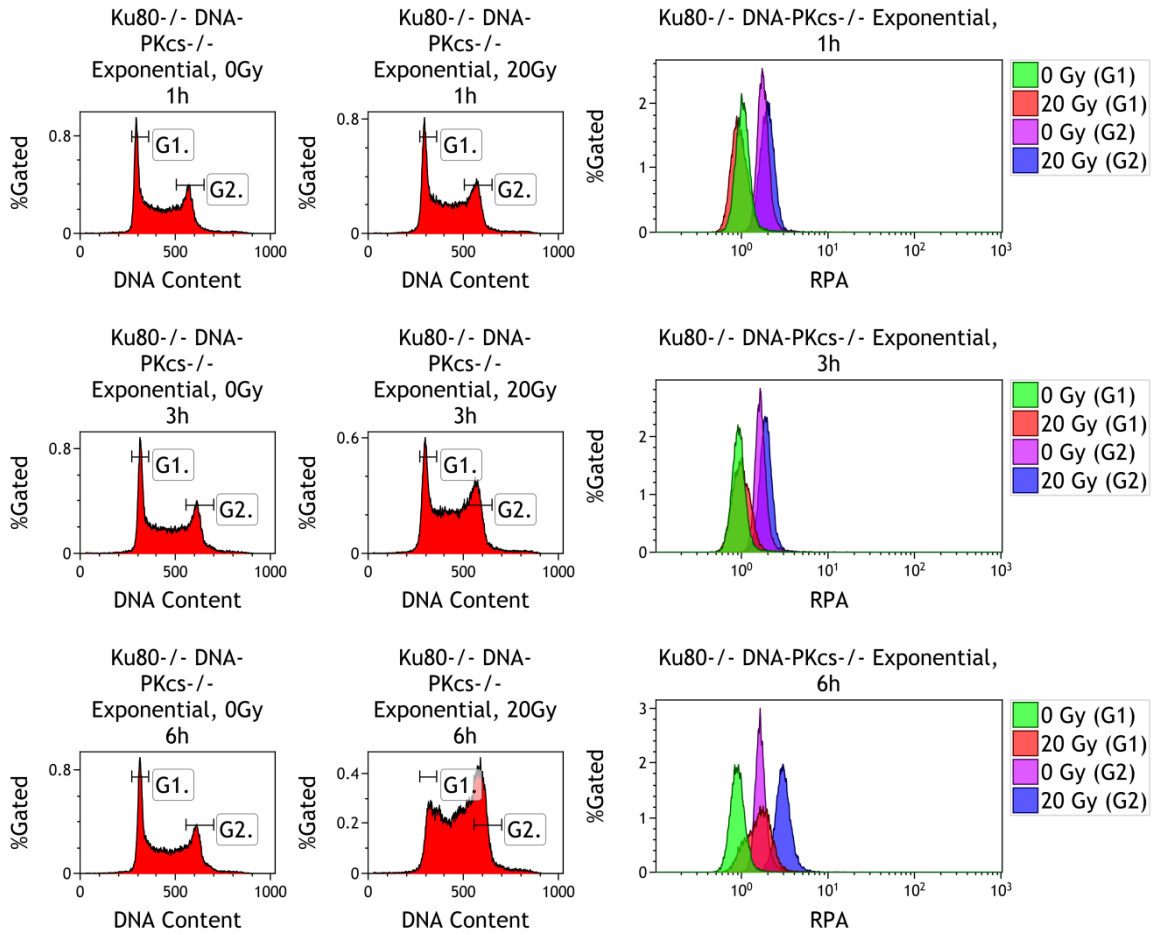


Supplementary Figure 10. DNA end resection in G₁ and G₂ phases in DNA-PKcs^{-/-} cells in exponential state. Cells were gated in G₁ and G₂ phases according to PI histograms and RPA signal was plotted for each cell cycle phase.



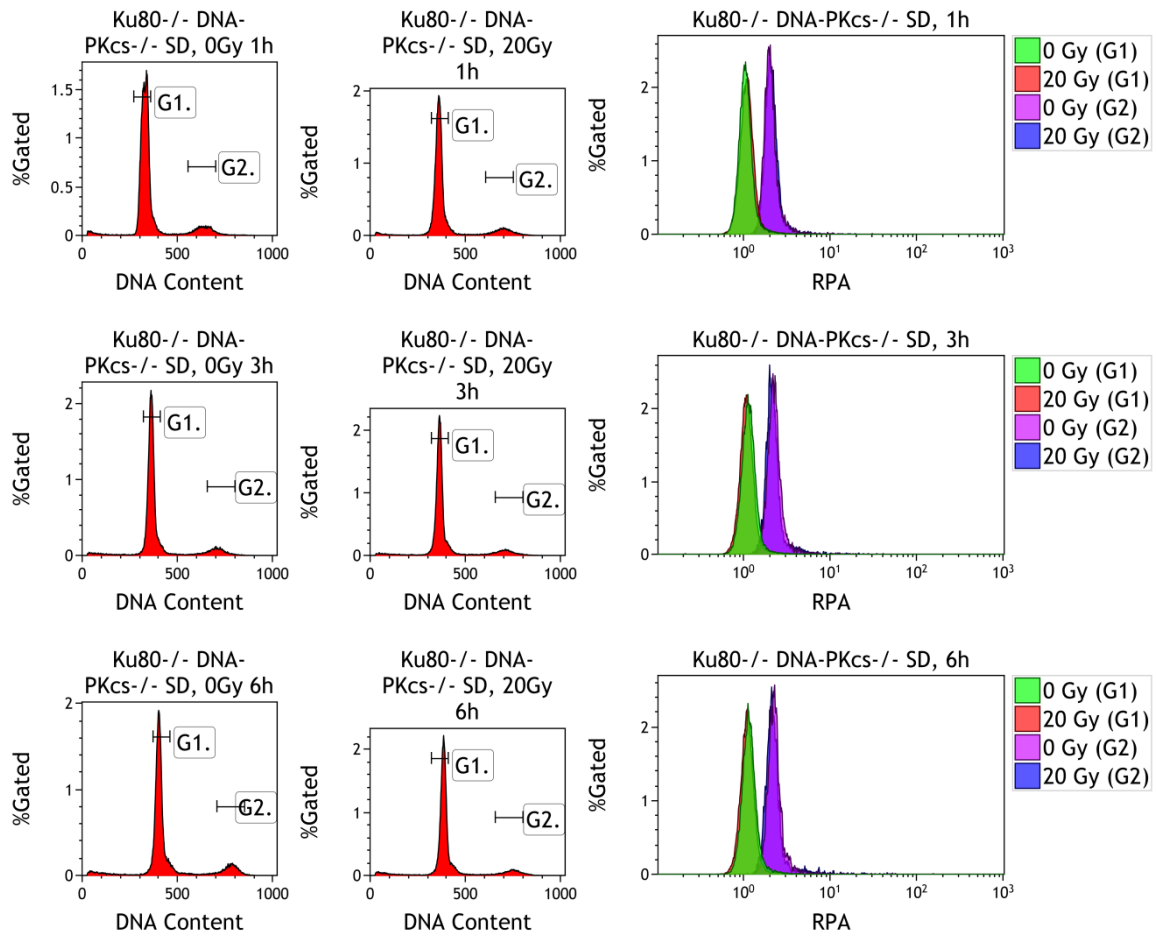
Supplementary Figure 11. DNA end resection in G₁ and G₂ phases in DNA-PKcs^{-/-} cells in SD state.

Cells were gated in G₁ and G₂ phases according to PI histograms and RPA signal was plotted for each cell cycle phase.

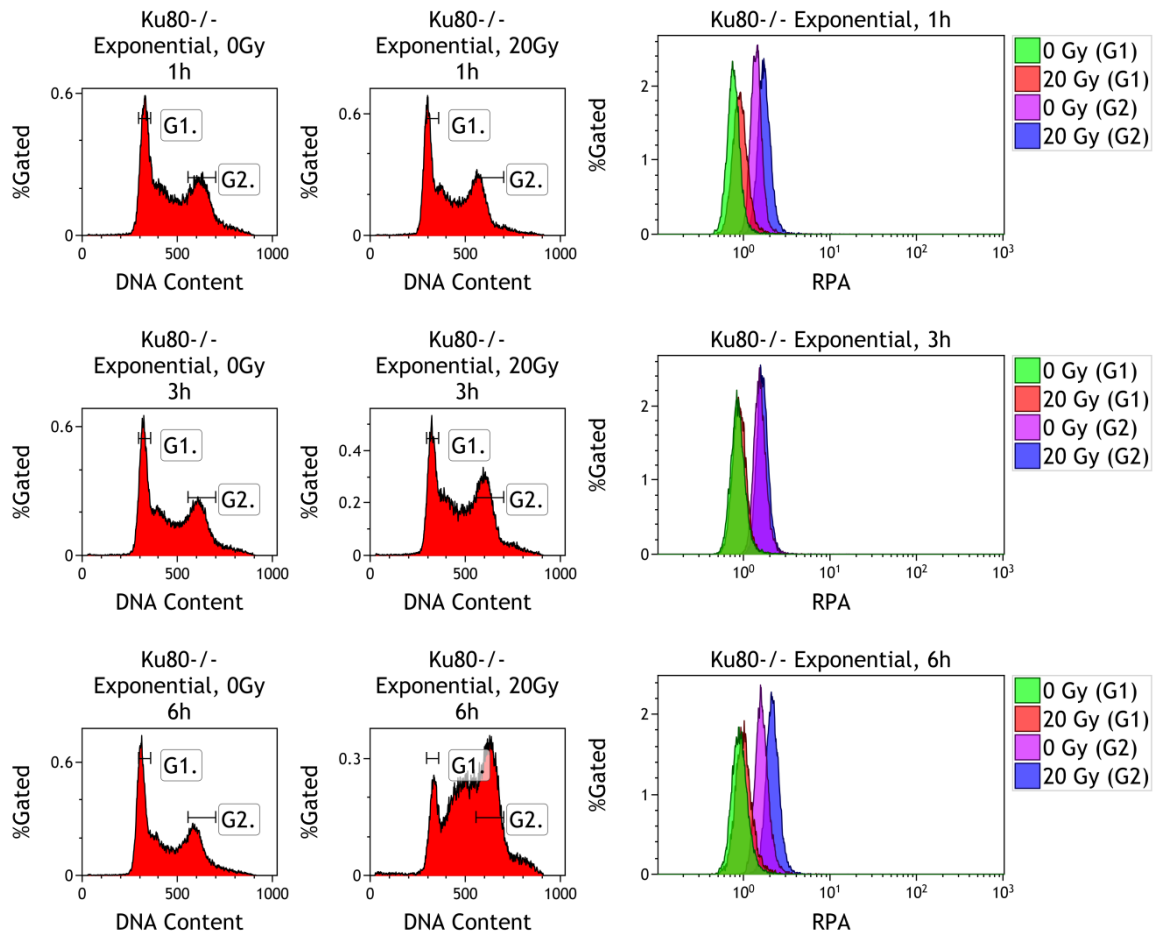


Supplementary Figure 12. DNA end resection in G₁ and G₂ phases in *Ku80^{-/-} DNA-PKcs^{-/-}* cells in exponential state.

Cells were gated in G₁ and G₂ phases according to PI histograms and RPA signal was plotted for each cell cycle phase.

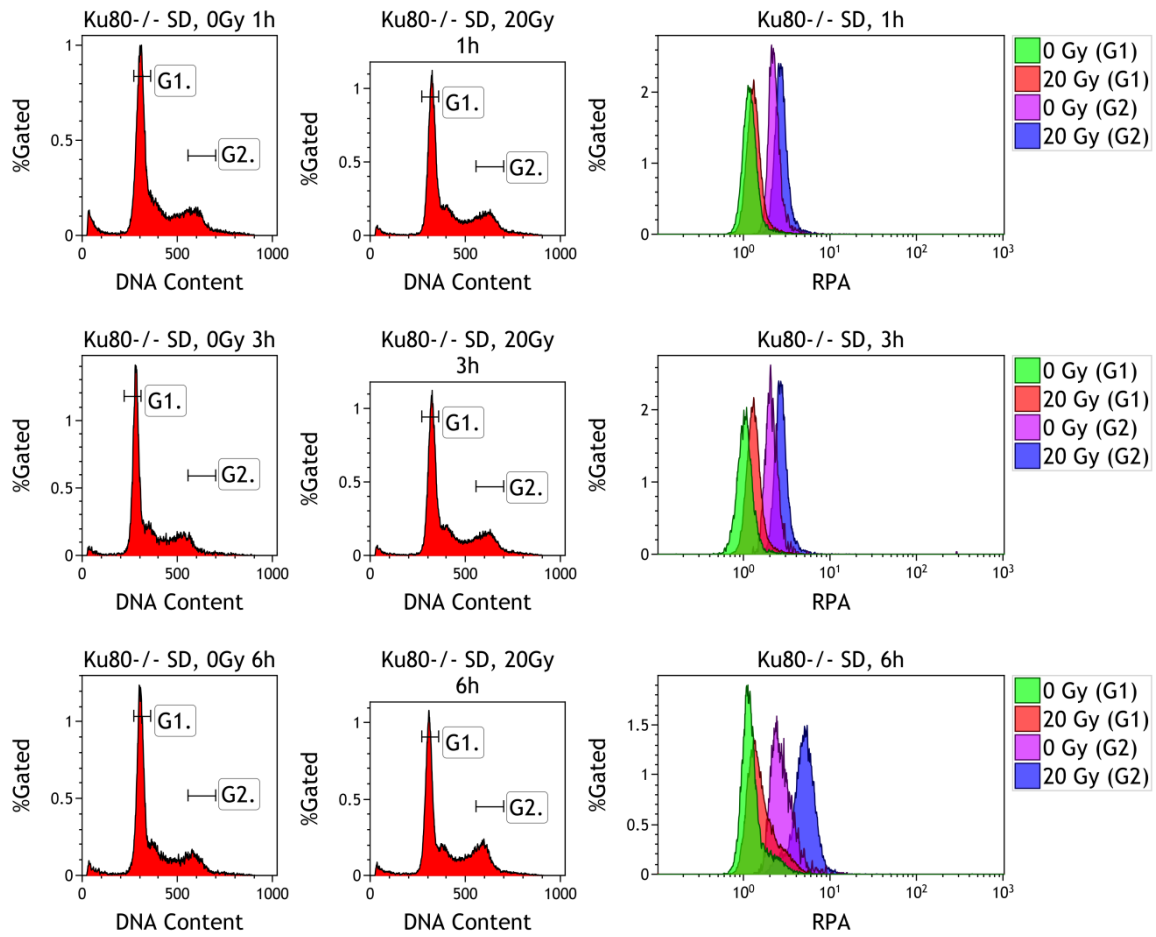


Supplementary Figure 13. DNA end resection in G₁ and G₂ phases in Ku80^{-/-} DNA-PKcs^{-/-} cells in SD state. Cells were gated in G₁ and G₂ phases according to PI histograms and RPA signal was plotted for each cell cycle phase.



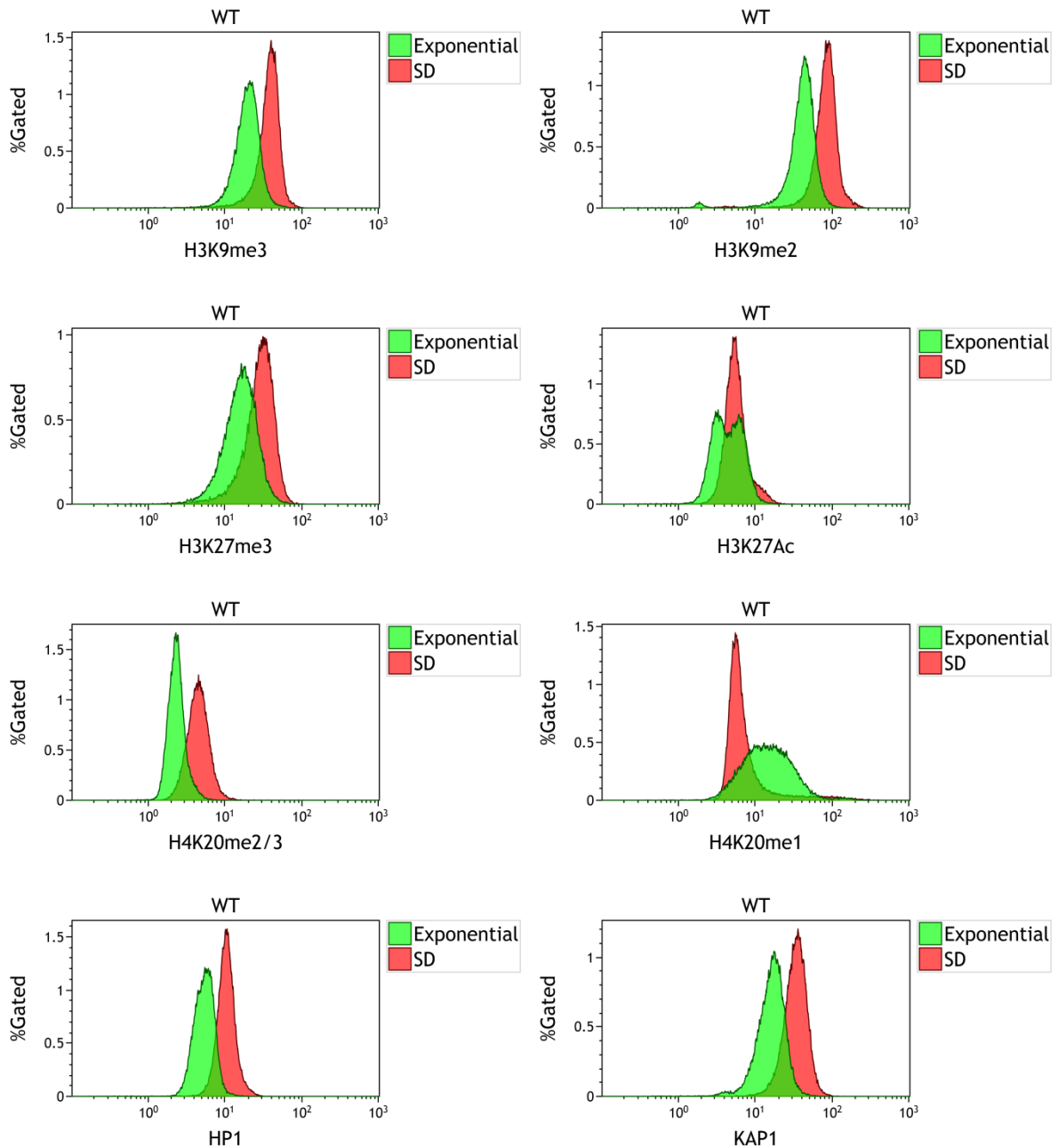
Supplementary Figure 14. DNA end resection in G₁ and G₂ phases in $Ku80^{-/-}$ cells in exponential state.

Cells were gated in G₁ and G₂ phases according to PI histograms and RPA signal was plotted for each cell cycle phase.



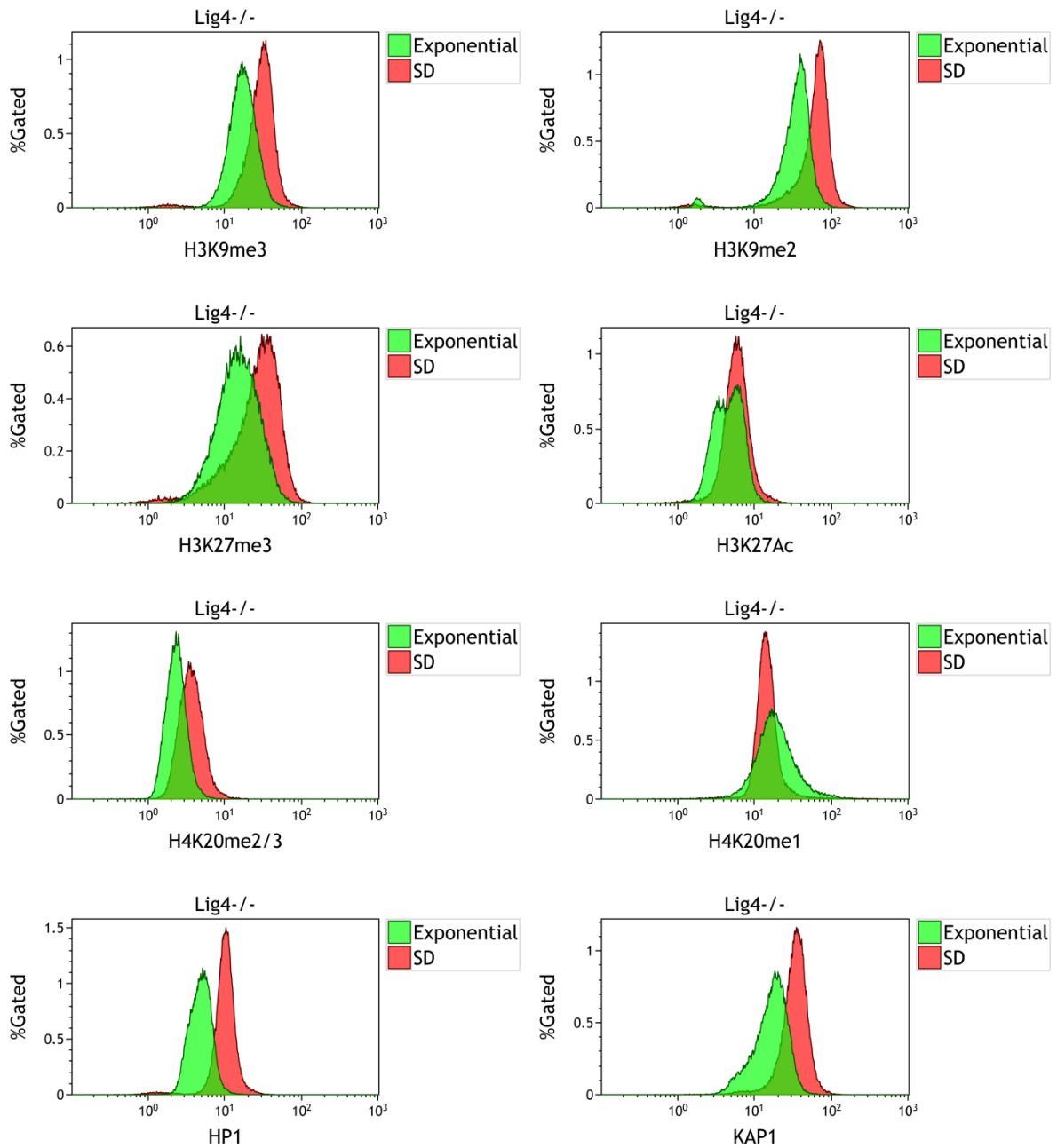
Supplementary Figure 15. DNA end resection in G₁ and G₂ phases in $Ku80^{-/-}$ cells in SD state.

Cells were gated in G₁ and G₂ phases according to PI histograms and RPA signal was plotted for each cell cycle phase.



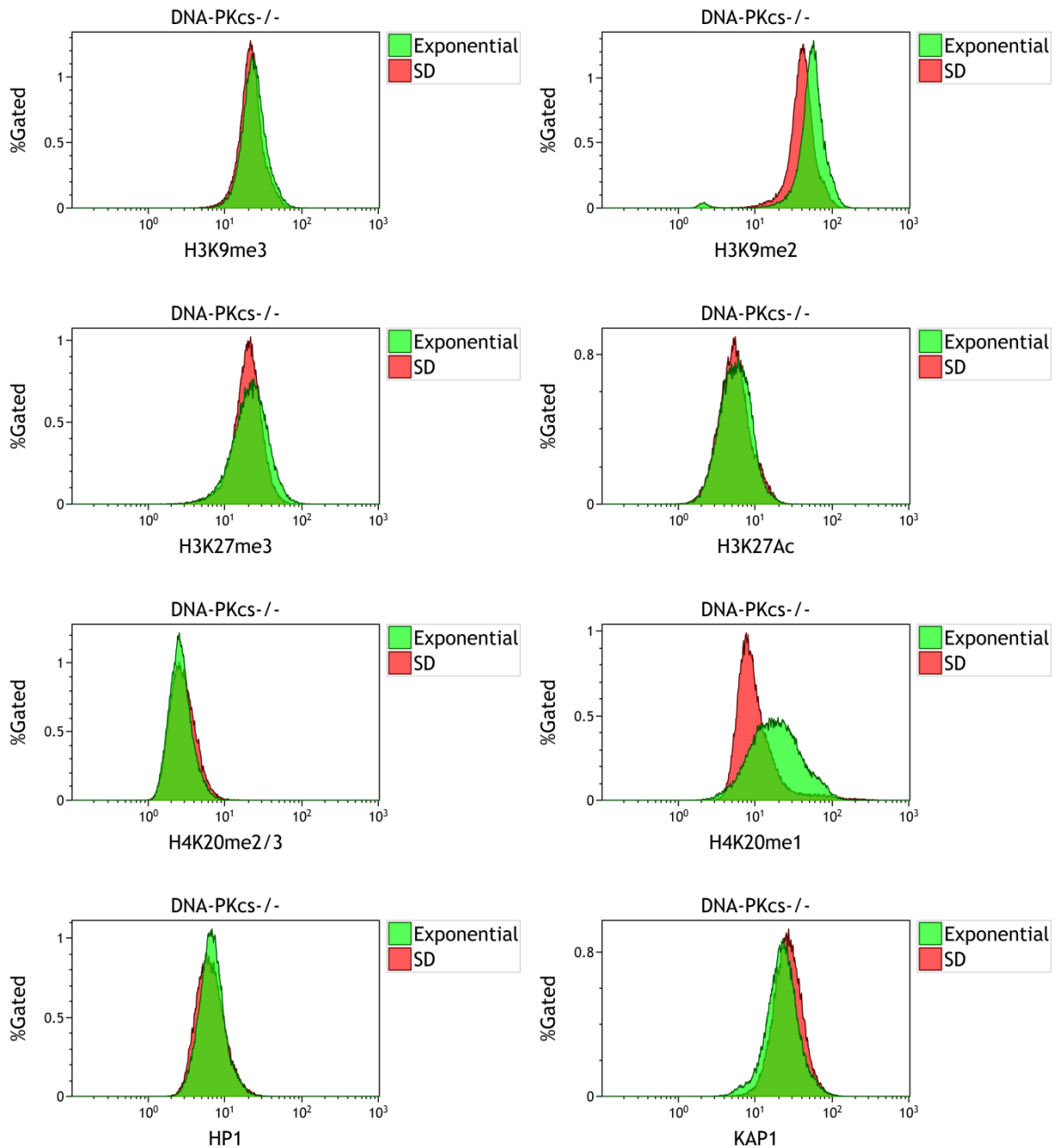
Supplementary Figure 16. Chromatin structure and transcription related markers in WT MEFs.

Representative histogram plots indicate the mean fluorescence intensity of corresponding marker in 5x10⁴ cells measured by flow cytometry.

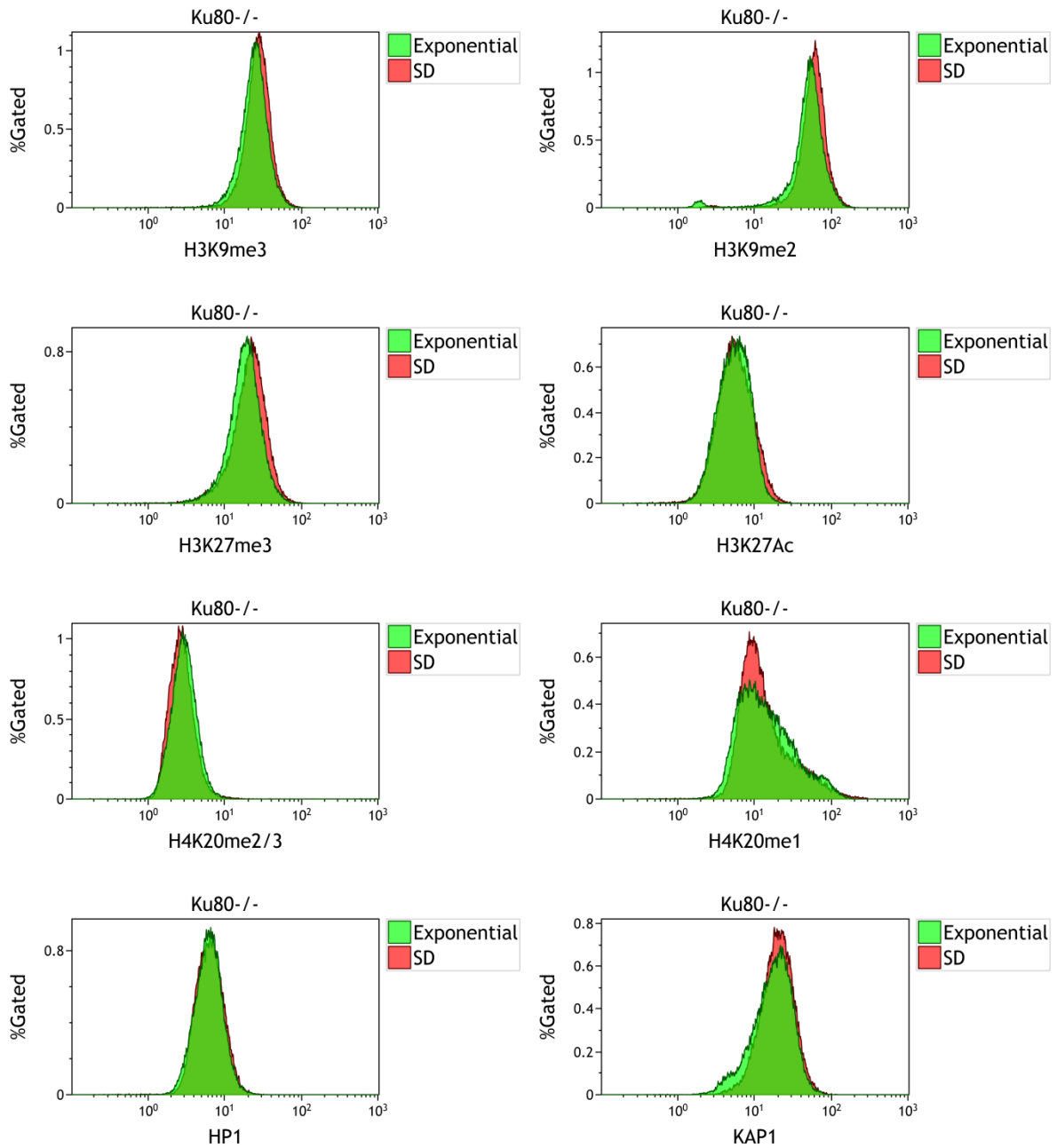


Supplementary Figure 17. Chromatin structure and transcription related markers in *Lig4*^{-/-} MEFs.

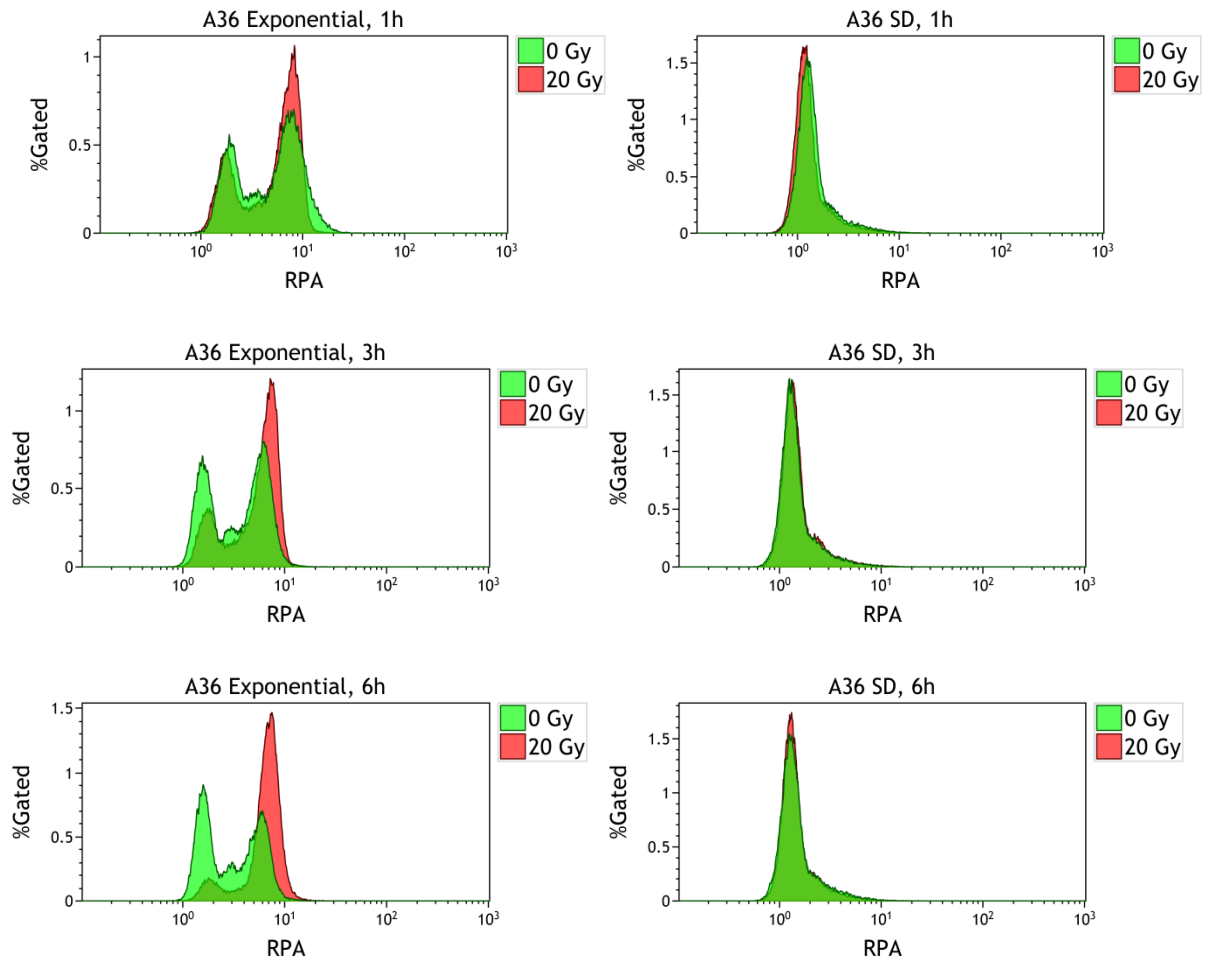
Representative histogram plots indicate the mean fluorescence intensity of corresponding marker in 5×10^4 cells measured by flow cytometry.



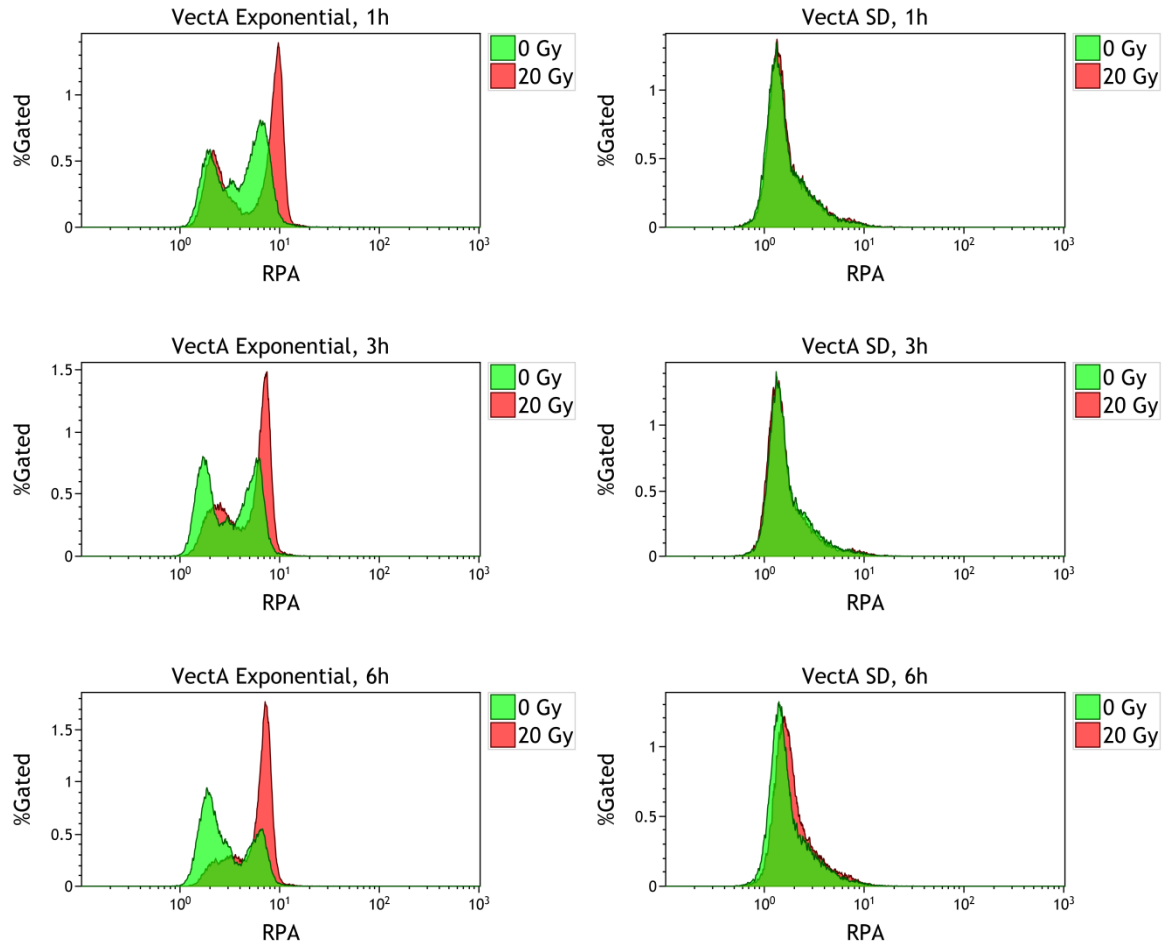
Supplementary Figure 18. Chromatin structure and transcription related markers in DNA-PKcs^{-/-} MEFs. Representative histogram plots indicate the mean fluorescence intensity of corresponding marker in 5x10⁴ cells measured by flow cytometry.



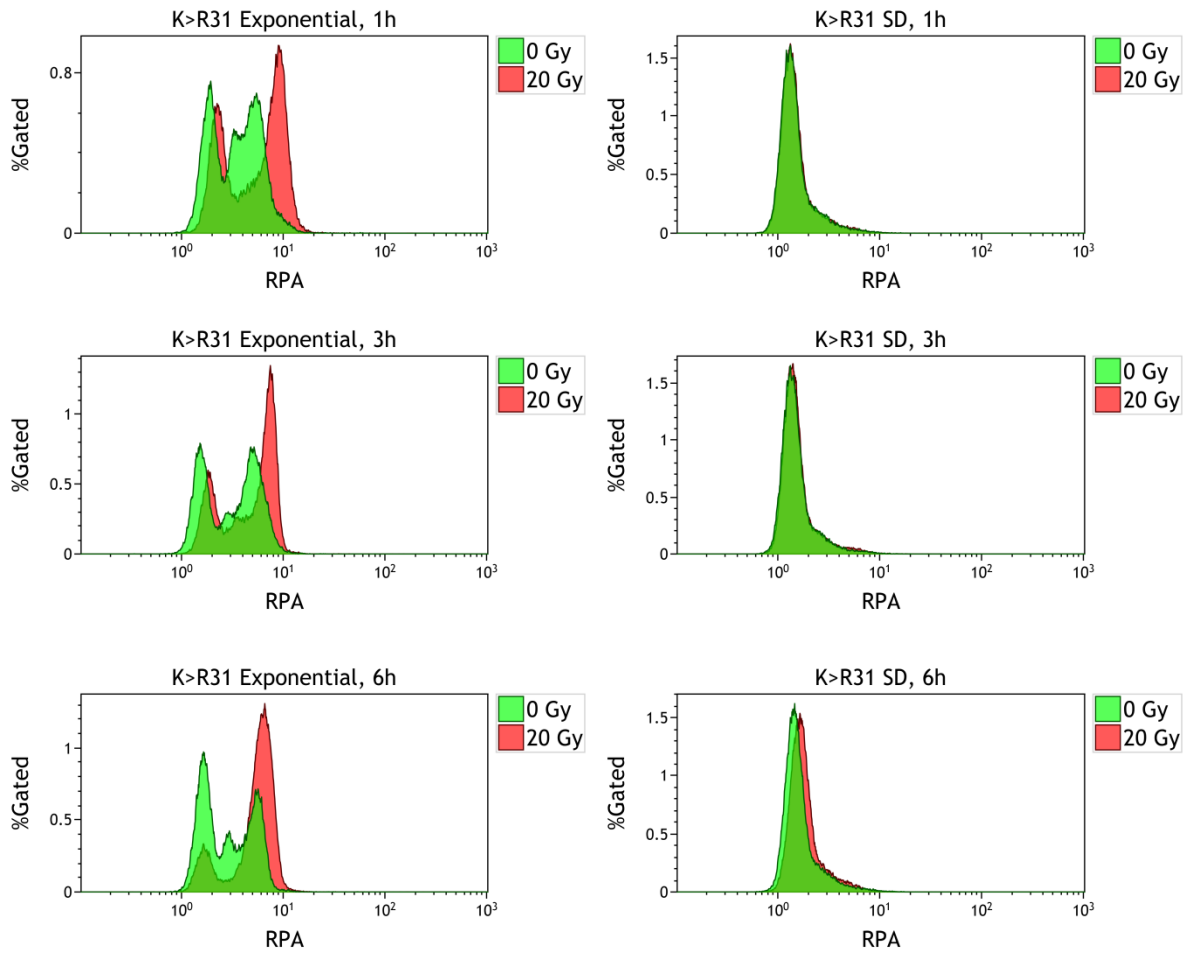
Supplementary Figure 19. Chromatin structure and transcription related markers in *Ku80*^{-/-} MEFs. Representative histogram plots indicate the mean fluorescence intensity of corresponding marker in 5×10^4 cells measured by flow cytometry.



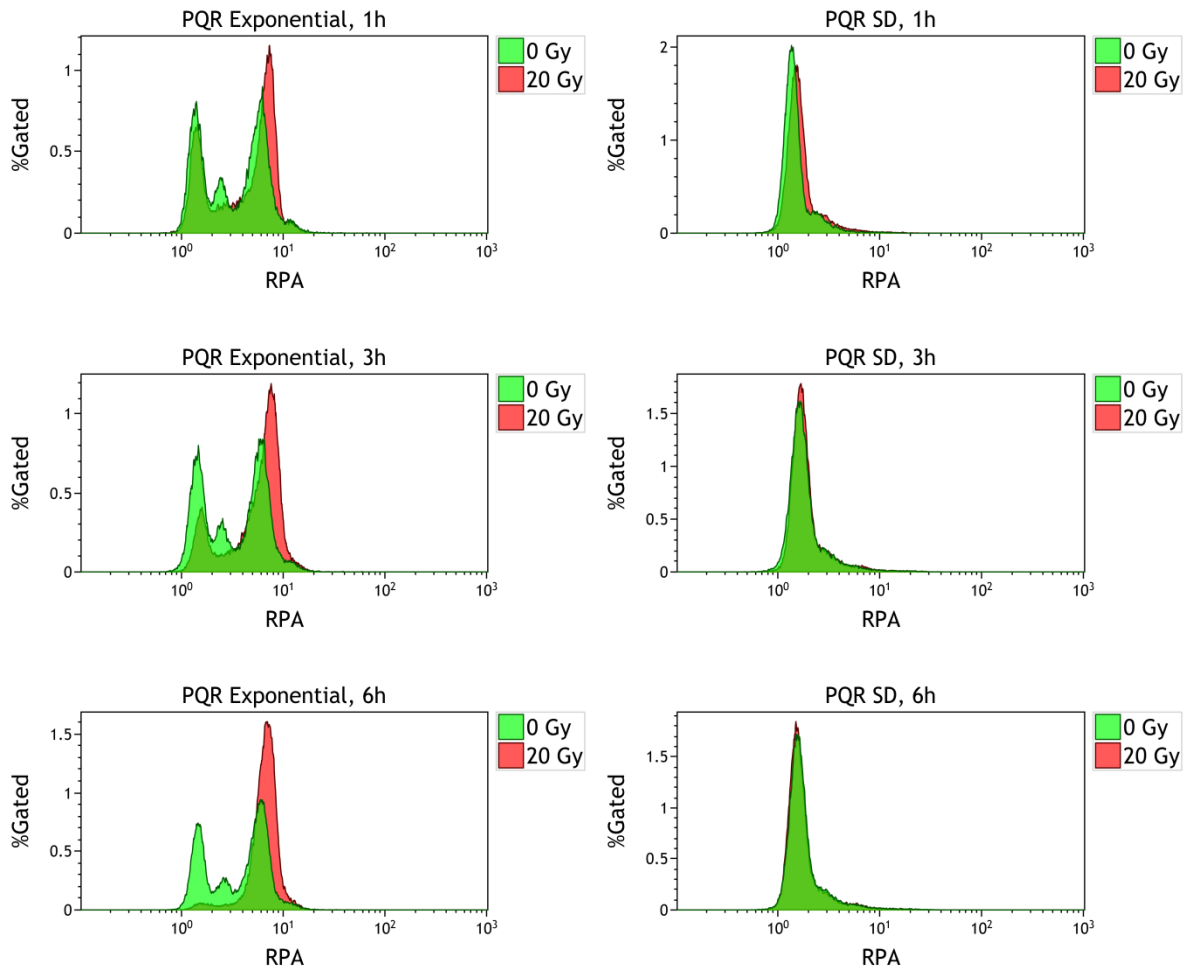
Supplementary Figure 20. RPA levels induced by 20 Gy of IR in A36 cells in exponential and SD state. Histogram plots indicate the mean fluorescence intensity of RPA signal in 5×10^4 cells measured by flow cytometry.



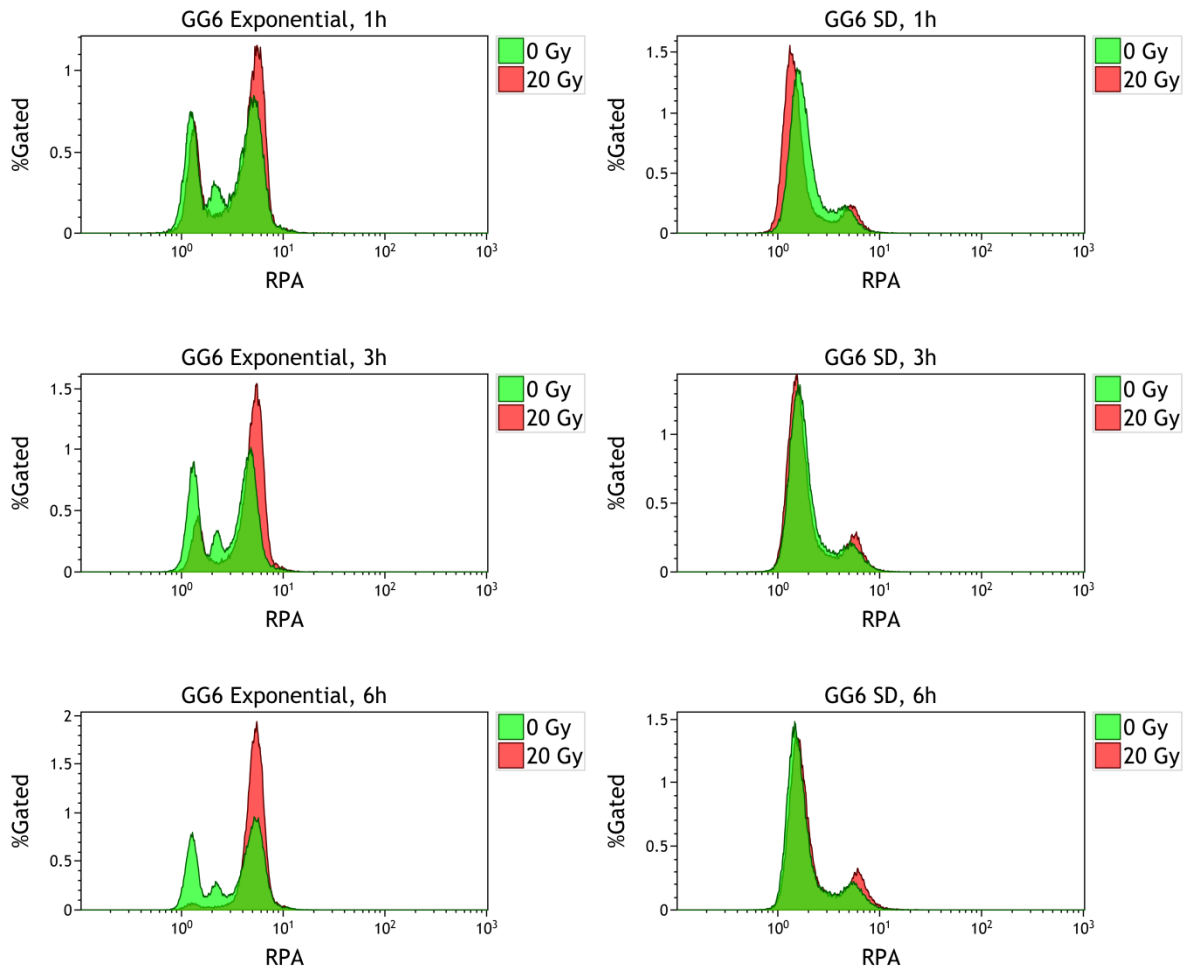
Supplementary Figure 21. RPA levels induced by 20 Gy of IR in VectA cells in exponential and SD state. Histogram plots indicate the mean fluorescence intensity of RPA signal in 5×10^4 cells measured by flow cytometry.



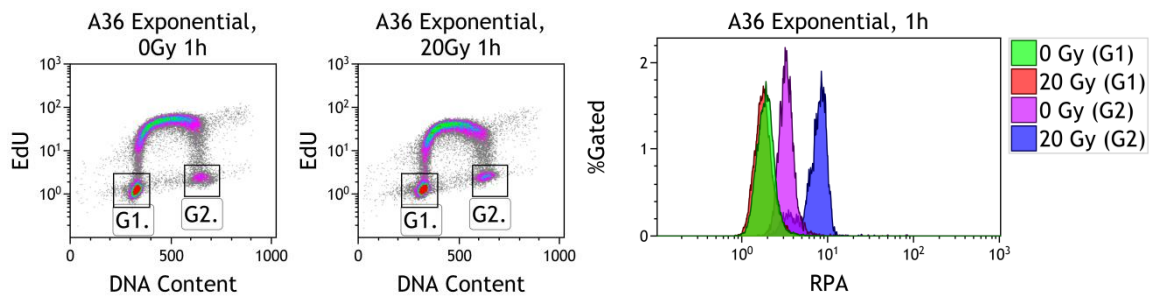
Supplementary Figure 22. RPA levels induced by 20 Gy of IR in K>R31 cells in exponential and SD state. Histogram plots indicate the mean fluorescence intensity of RPA signal in 5×10^4 cells measured by flow cytometry.

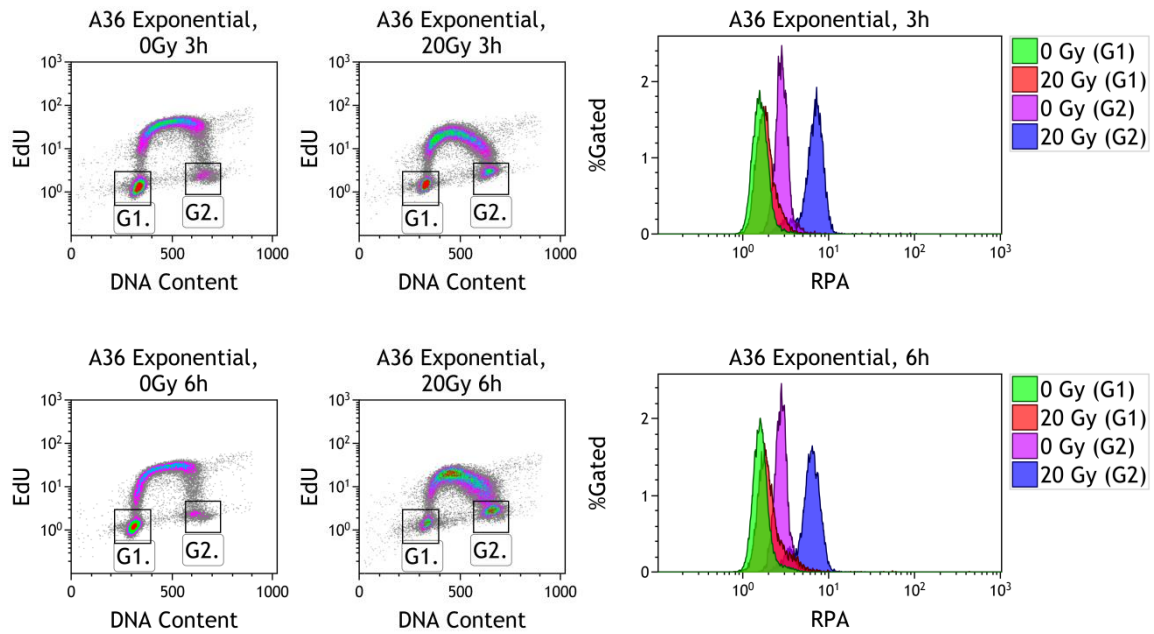


Supplementary Figure 23. RPA levels induced by 20 Gy of IR in PQR cells in exponential and SD state. Histogram plots indicate the mean fluorescence intensity of RPA signal in 5×10^4 cells measured by flow cytometry.



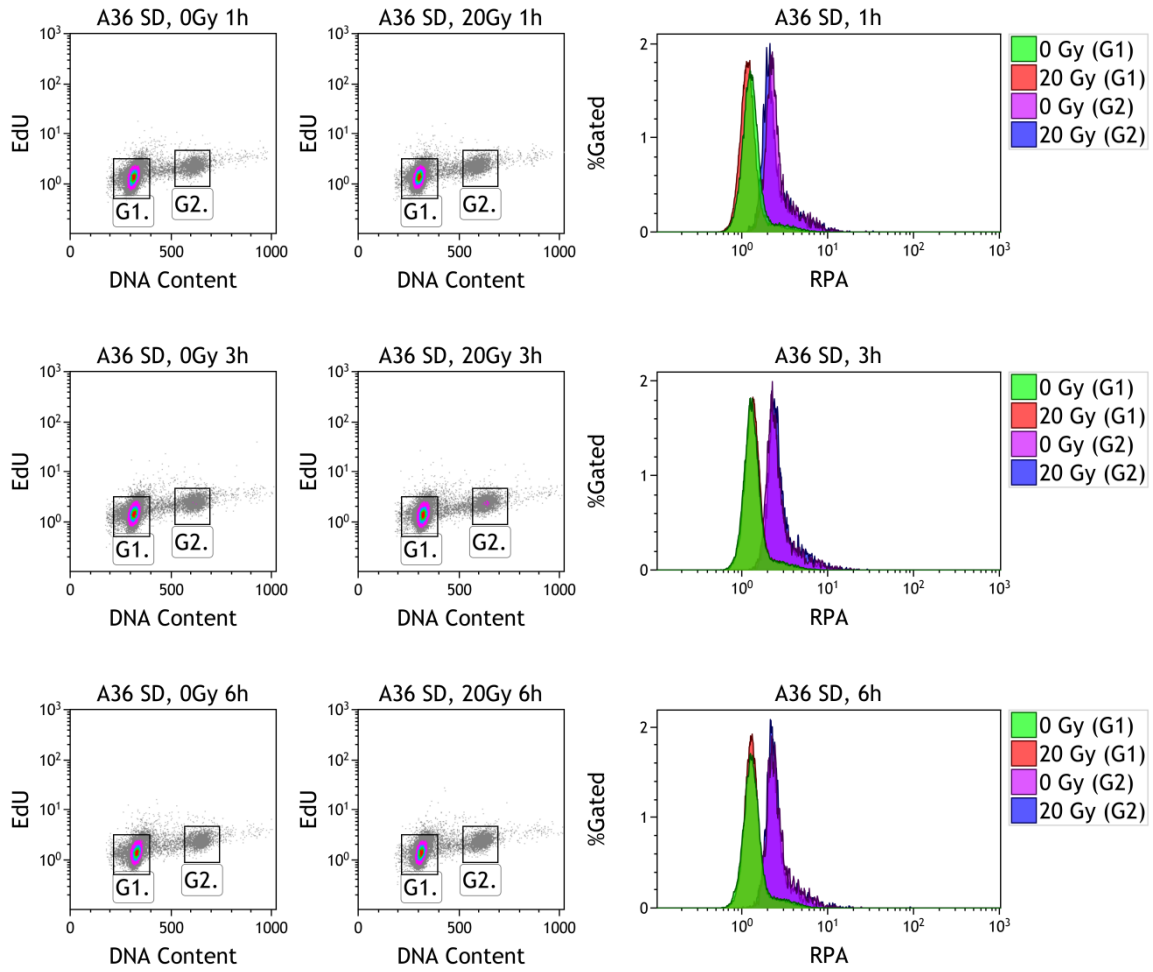
Supplementary Figure 24. RPA levels induced by 20 Gy of IR in GG6 cells in exponential and SD state. Histogram plots indicate the mean fluorescence intensity of RPA signal in 5×10^4 cells measured by flow cytometry.





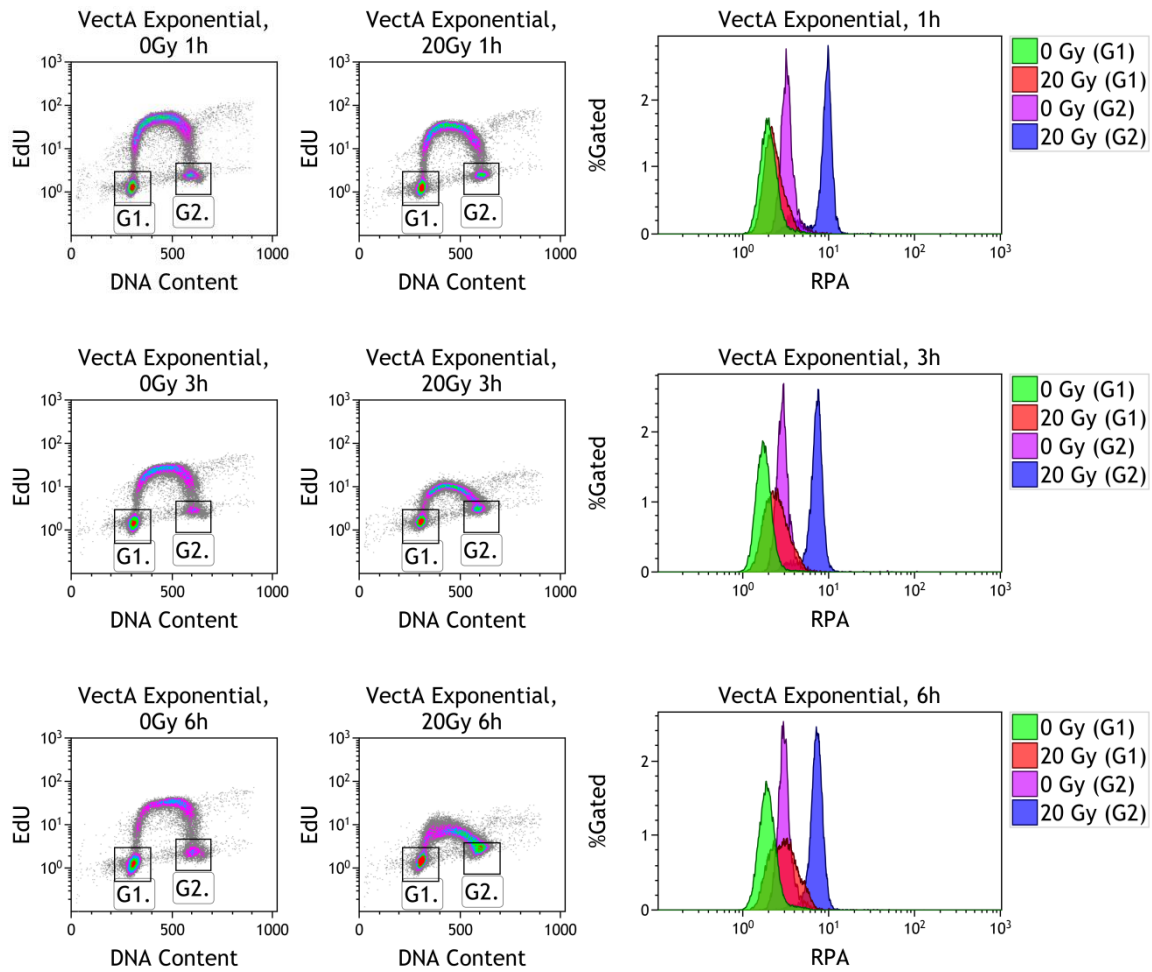
Supplementary Figure 25. DNA end resection in G₁ and G₂ phases in A36 cells in exponential state.

Cells were gated in G₁ and G₂ phases according to EdU staining and RPA signal was plotted for each cell cycle phase.

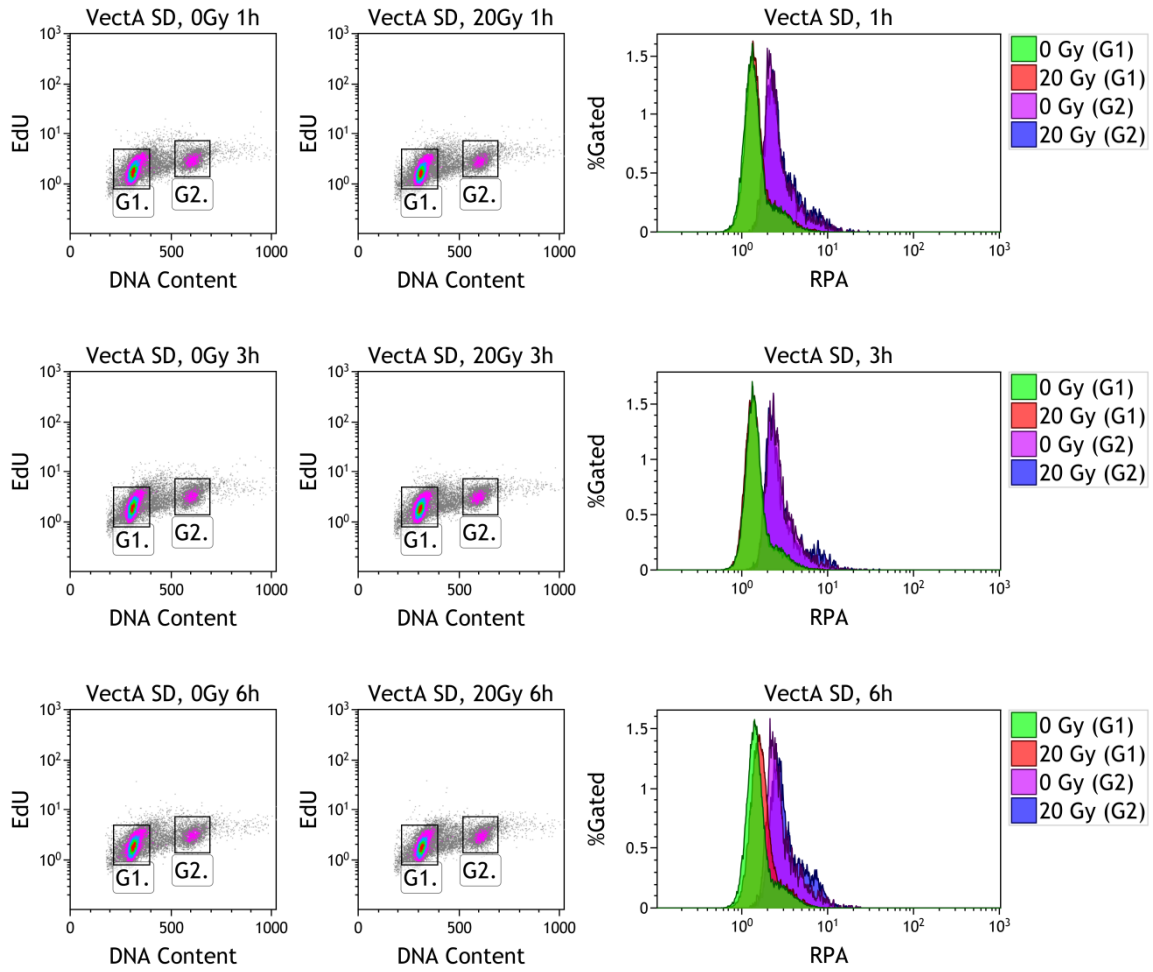


Supplementary Figure 26. DNA end resection in G₁ and G₂ phases in A36 cells in SD state.

Cells were gated in G₁ and G₂ phases according to EdU staining and RPA signal was plotted for each cell cycle phase.

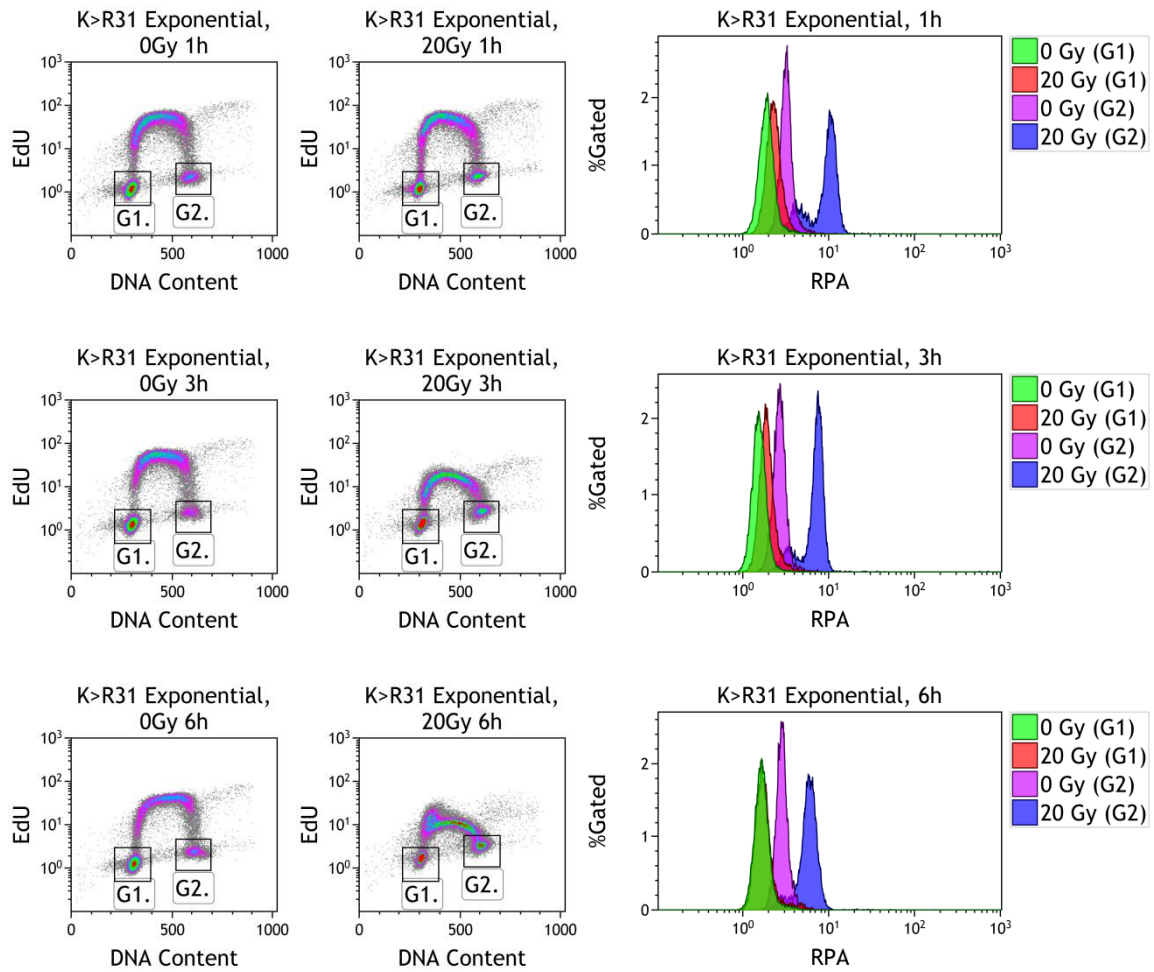


Supplementary Figure 27. DNA end resection in G₁ and G₂ phases in VectA cells in exponential state. Cells were gated in G₁ and G₂ phases according to EdU staining and RPA signal was plotted for each cell cycle phase.



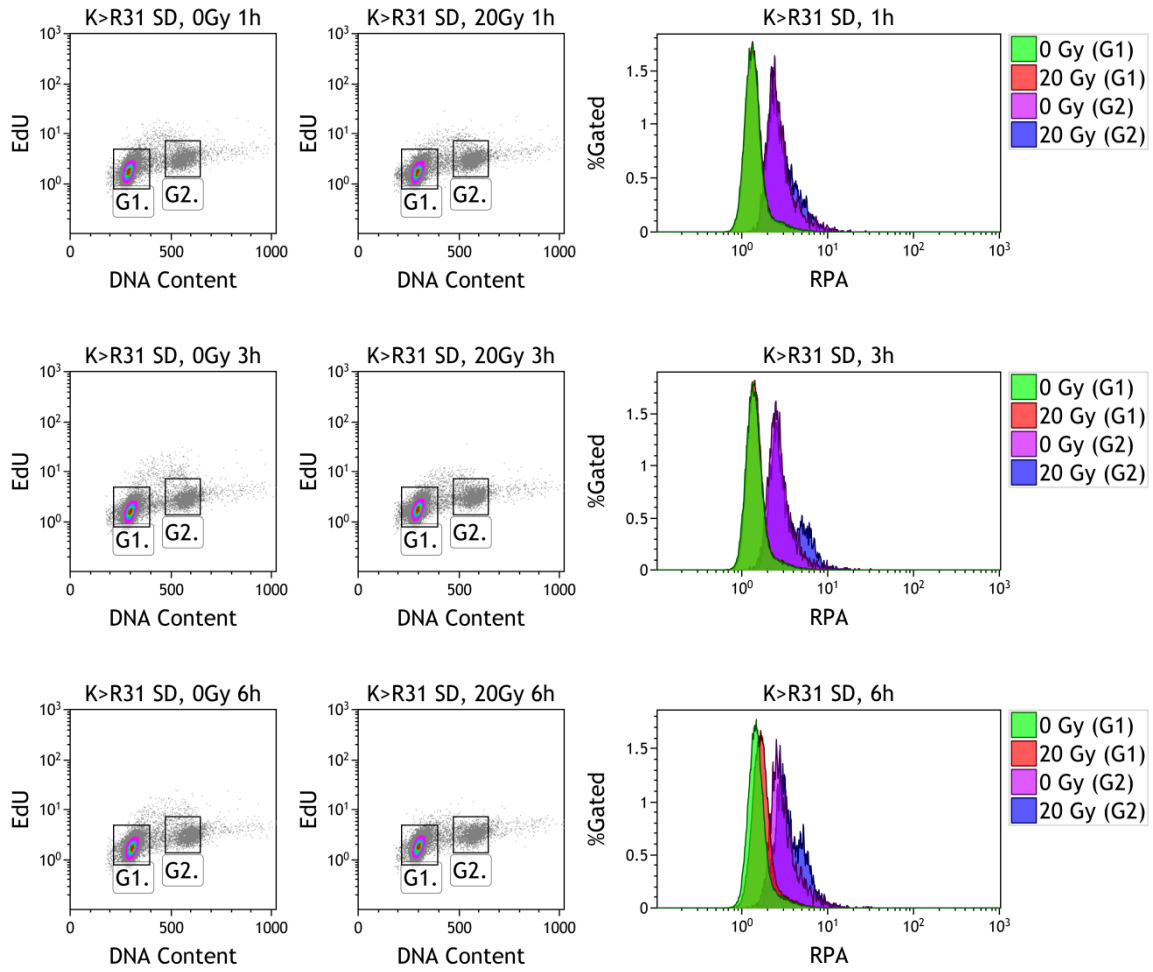
Supplementary Figure 28. DNA end resection in G₁ and G₂ phases in VectA cells in SD state

Cells were gated in G₁ and G₂ phases according to EdU staining and RPA signal was plotted for each cell cycle phase.



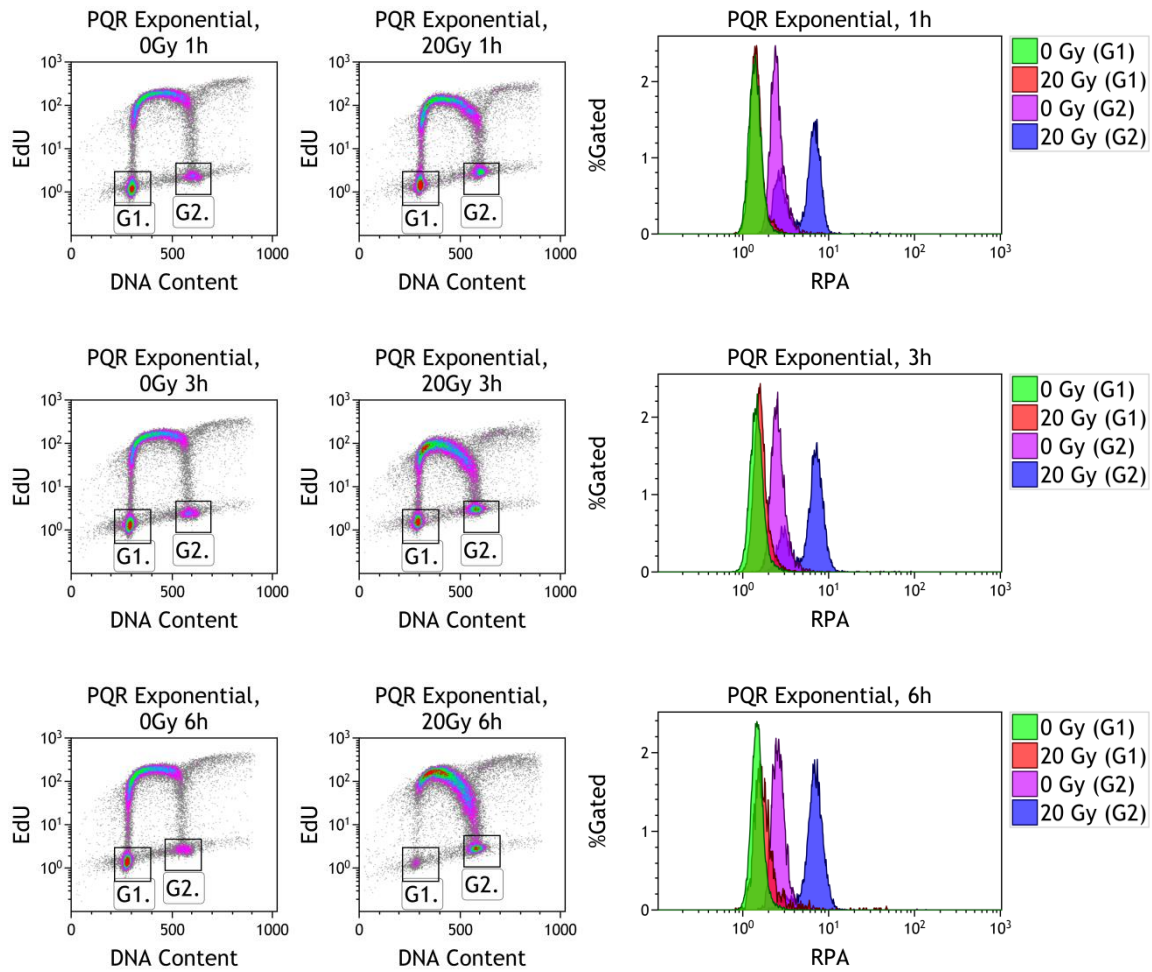
Supplementary Figure 29. DNA end resection in G₁ and G₂ phases in K>R31 cells in exponential state.

Cells were gated in G₁ and G₂ phases according to EdU staining and RPA signal was plotted for each cell cycle phase.

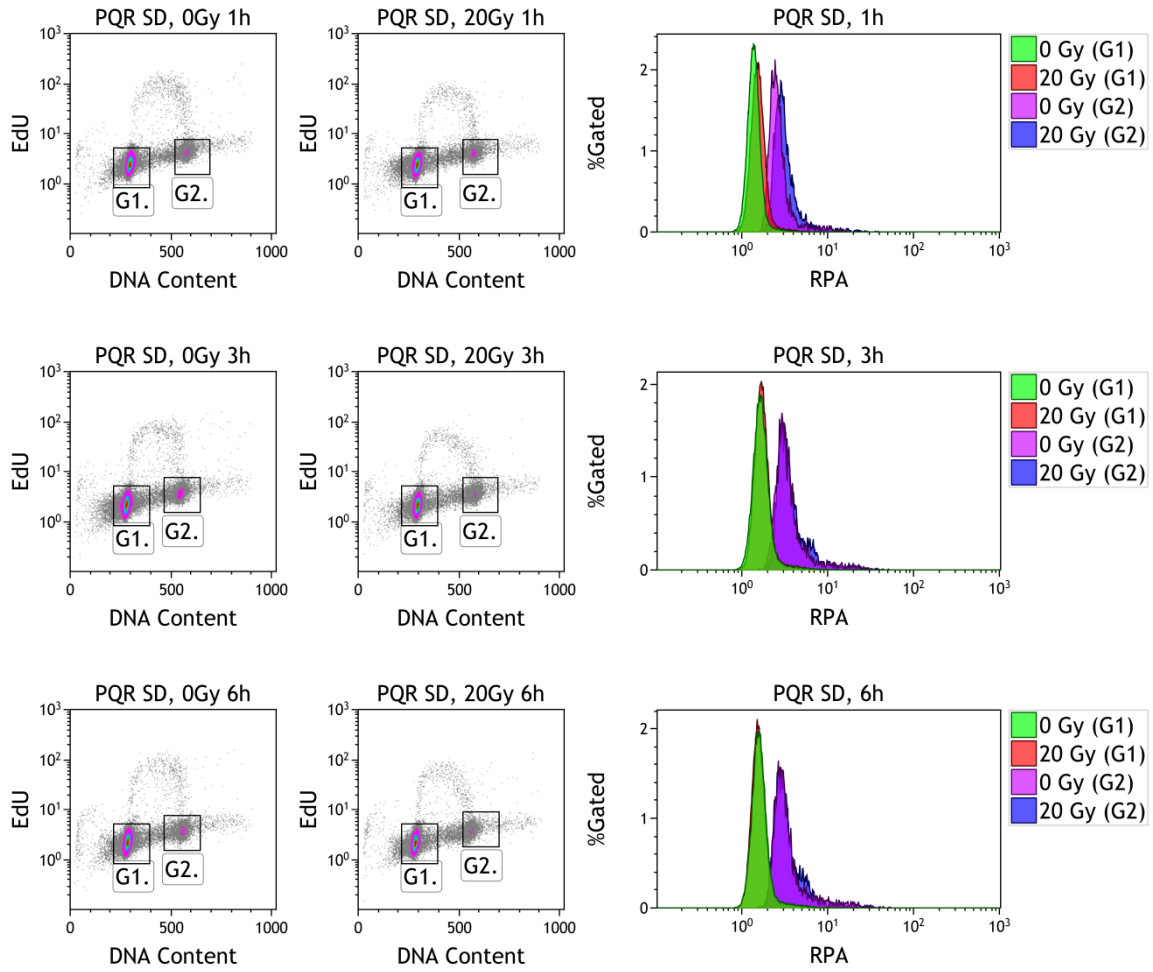


Supplementary Figure 30. DNA end resection in G₁ and G₂ phases in K>R31 cells in SD state.

Cells were gated in G₁ and G₂ phases according to EdU staining and RPA signal was plotted for each cell cycle phase.

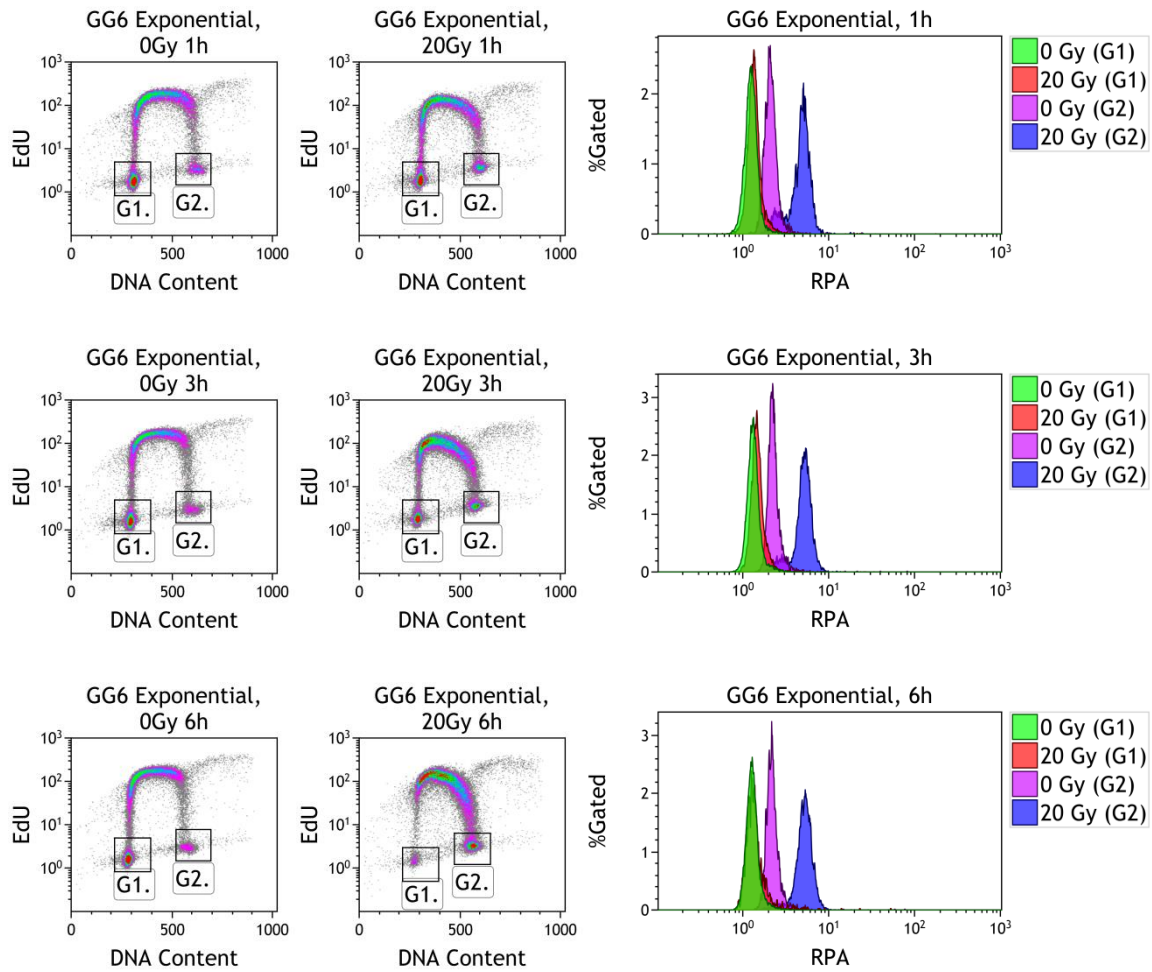


Supplementary Figure 31. DNA end resection in G₁ and G₂ phases in PQR cells in exponential state. Cells were gated in G₁ and G₂ phases according to EdU staining and RPA signal was plotted for each cell cycle phase.

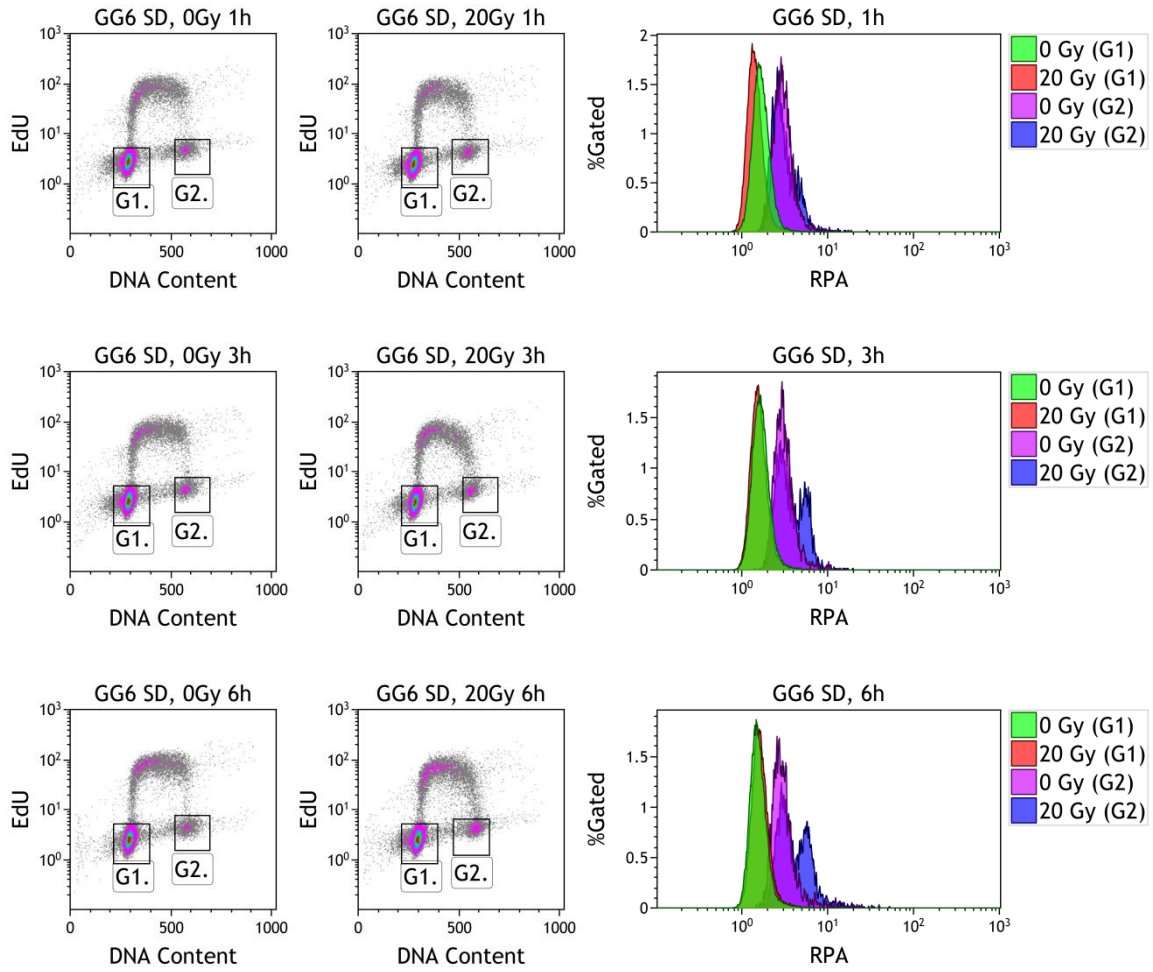


Supplementary Figure 32. DNA end resection in G₁ and G₂ phases in PQR cells in SD state.

Cells were gated in G₁ and G₂ phases according to EdU staining and RPA signal was plotted for each cell cycle phase.

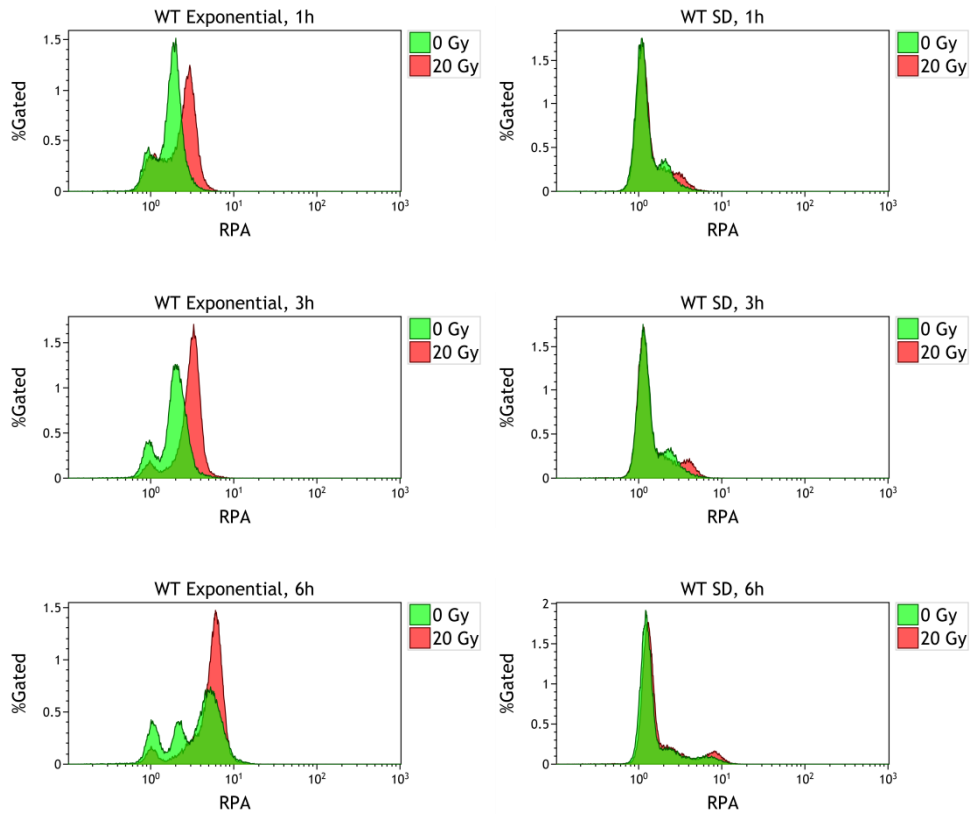


Supplementary Figure 33. DNA end resection in G₁ and G₂ phases in GG6 cells in exponential state. Cells were gated in G₁ and G₂ phases according to EdU staining and RPA signal was plotted for each cell cycle phase.

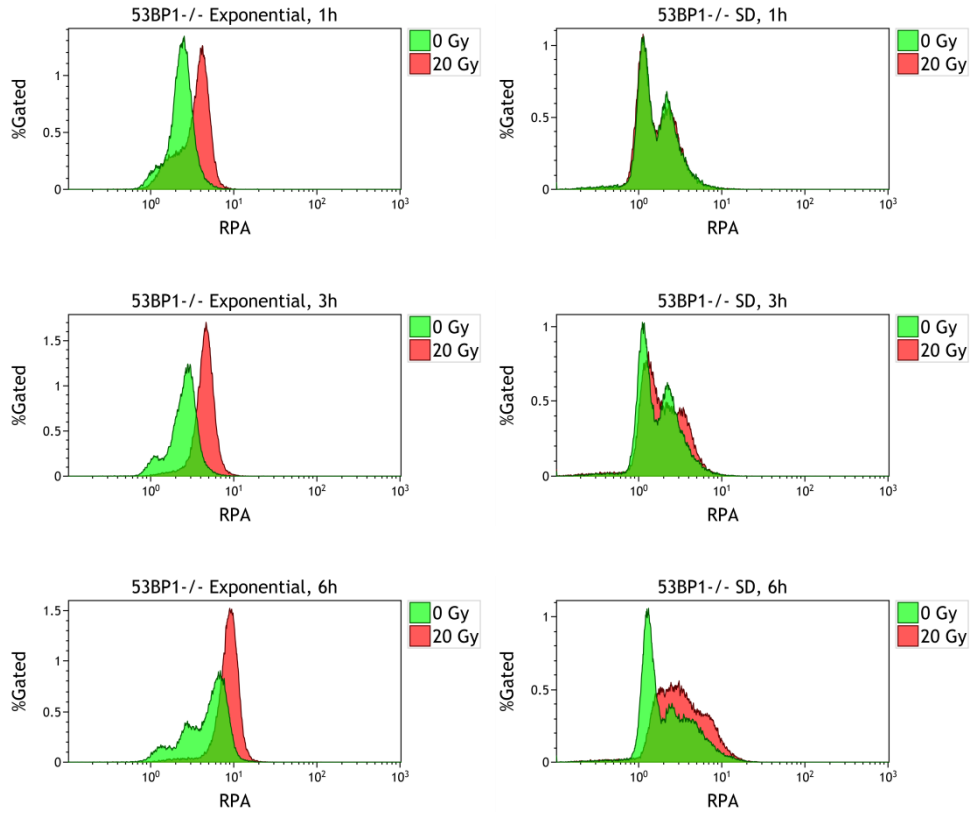


Supplementary Figure 34. DNA end resection in G₁ and G₂ phases in GG6 cells in SD state.

Cells were gated in G₁ and G₂ phases according to EdU staining and RPA signal was plotted for each cell cycle phase.

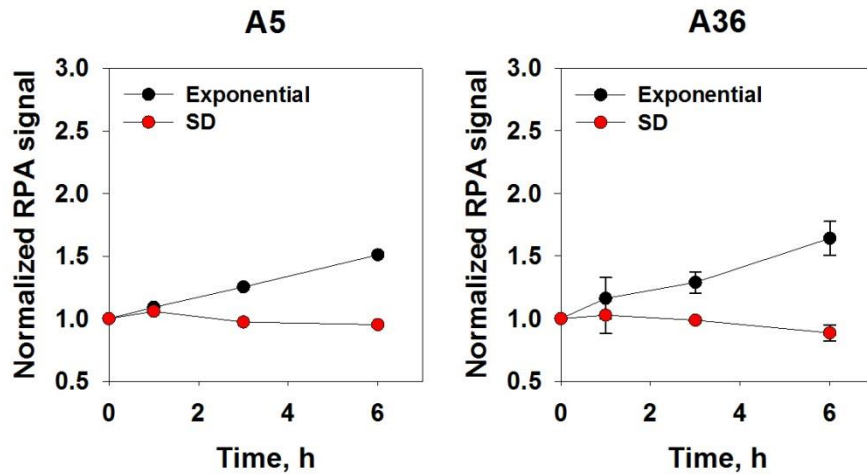


Supplementary Figure 35. RPA levels induced by 20 Gy of IR in WT mESCs in exponential and SD state. Histogram plots indicate the mean fluorescence intensity of RPA signal in 5×10^4 cells measured by flow cytometry.



Supplementary Figure 36. RPA levels induced by 20 Gy of IR in 53BP1^{-/-} mESCs in exponential and SD state.

Histogram plots indicate the mean fluorescence intensity of RPA signal in 5×10^4 cells measured by flow cytometry.



Supplementary Figure 37. RPA levels induced by 20 Gy of IR in CHO cells in exponential and SD state.

DNA end resection in CHO cells expressing low levels of DNA-PKcs (A5) and high levels of DNA-PKcs (A36). Quantitative data was obtained from one experiment for A5 and three independent experiments for A36 cells. Error bars represent standard deviation.

10. ACKNOWLEDGEMENTS

First of all, I would like to express my sincere thanks to Prof. Dr. George Iliakis for giving me the opportunity to perform my PhD as a part of his team. His great enthusiasm in science has always been inspiring. His continuous support not only in scientific but also in personal matters helped me through a challenging PhD.

I would like to particularly thank Dr. Fanghua Li, Dr. Emil Mladenov and Dr. Simon Magin for their scientific contribution and all other colleagues for their patience and support when I had gone through hard times. Many thanks to each member of the Institute of Medical Radiation Biology for maintaining a friendly and peaceful environment. Special thanks to Vasiliki Tasiou and Shipra Chaudhary for always being there in good or bad times; your friendship is precious. Thanks to Dr. Veronika Mladenova, Christian Möllers and Malihe Mesbah, with whom I really enjoyed sharing an office and Dr. Lisa Krieger, who has always been very helpful.

I would like to express my deepest gratitude to my parents, especially my mother who has always been patient and supportive whenever I needed. Thanks to Adem Yıldırım for his encouragement and guidance for a PhD in Germany. Thanks to Yasin Bahadır Erol for always being there, especially at hard times.

Special thanks to my husband Bilal Tetik and our little Ege; your presence is irreplaceable.

The work presented in this thesis was funded by Bundesministerium für Bildung und Forschung (BMBF) 02NUK037B entitled “VERCHROMT: Erkennung, Verarbeitung und biologische Konsequenzen von Chromatinschäden nach Teilchenbestrahlung”.

11. CURRICULUM VITAE

Der Lebenslauf ist in der veröffentlichten Version aus Gründen des Datenschutzes nicht enthalten.

Der Lebenslauf ist in der veröffentlichten Version aus Gründen des Datenschutzes nicht enthalten.

Der Lebenslauf ist in der veröffentlichten Version aus Gründen des Datenschutzes nicht enthalten.

12. DECLARATIONS

Erklärung:

Hiermit erkläre ich, gem. §7 Abs. (2) d) + f) der Promotionsordnung der Fakultät für Biologie zur Erlangung des Dr. rer. nat., dass ich die vorliegende Dissertation selbstständig verfasst und mich keiner anderen als der angegebenen Hilfsmittel bedient, bei der Abfassung der Dissertation nur die angegebenen Hilfsmittel benutzt und alle wörtlich oder inhaltlich übernommenen Stellen als solche gekennzeichnet habe.

Essen, den _____

Unterschrift der Doktorandin

Erklärung:

Hiermit erkläre ich, gem. § 7 Abs. (2) e) + g) der Promotionsordnung der Fakultät für Biologie zur Erlangung des Dr. rer. nat., dass ich keine anderen Promotionen bzw. Promotionsversuche in der Vergangenheit durchgeführt habe und dass diese Arbeit von keiner anderen Fakultät/Fachbereich abgelehnt worden ist.

Essen, den _____

Unterschrift der Doktorandin

Erklärung:

Hiermit erkläre ich, gem. § 6 Abs. (2) g) der Promotionsordnung der Fakultät für Biologie zur Erlangung des Dr. rer. nat., dass ich das Arbeitsgebiet, dem das Thema „*The role of chromatin structure and DNA end resection in the growth-state dependence of alternative end joining (alt-EJ)*“ zuzuordnen ist, in Forschung und Lehre vertrete und den Antrag von Pelin Küçük befürworte und die Betreuung auch im Falle eines Weggangs, wenn nicht wichtige Gründe dem entgegenstehen, weiterführen werde.

Essen, den _____

Unterschrift eines Mitgliedes der Universität Duisburg-Essen